Physics Library
QC
1
.U56

Volume 65A
Number 4
July–August 1961

OF MICHIGAN
AUG 11 1961
PHYSICS
LIBRARY

Physics and Chemistry

U.S. DEPARTMENT OF COMMERCE

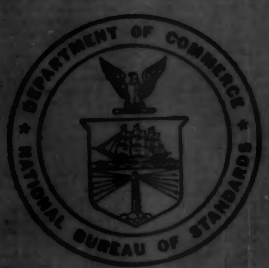

SECTION A

JOURNAL OF RESEARCH

NATIONAL BUREAU OF STANDARDS

Journal of Research
of the
National Bureau of Standards

A. Physics and Chemistry

JULY–AUG. • 1961

VOLUME • 65A

NUMBER • 4

Editor: U. Fano

Associate Editors: L. M. Kushner
J. M. Richardson

Publication dates:
Feb. 1, Apr. 1, June 1, Aug. 1, Oct. 1, Dec. 1, 1961.

JOURNAL OF RESEARCH

The National Bureau of Standards Journal of Research reports research and development in the fields of activity shown at right. Also included from time to time are survey articles on topics closely related to the Bureau's scientific and technical program.

The Journal is published in four separate sections as follows:

A. Physics and Chemistry

Contains papers of interest primarily to scientists working in these fields. Issued six times a year. Annual subscription: domestic, $4.00; foreign, $4.75.

B. Mathematics and Mathematical Physics

Presents studies and compilations designed mainly for the mathematician and the theoretical physicist. Issued quarterly. Annual subscription: domestic, $2.25; foreign, $2.75.

C. Engineering and Instrumentation

Reports research and development results of interest chiefly to the engineer and the applied scientist. Issued quarterly. Annual subscription: domestic, $2.25; foreign, $2.75.

D. Radio Propagation

Reports work in radio propagation, upper atmospheric physics, and communications. Issued six times a year. Annual subscription: domestic, $4.00; foreign, $4.75.

U.S. DEPARTMENT OF COMMERCE
Luther H. Hodges, Secretary

NATIONAL BUREAU OF STANDARDS
A. V. Astin, Director

Functions and Activities

The functions of the National Bureau of Standards are set forth in the Act of Congress, March 3, 1901, as amended. These include the development and maintenance of the national standards of measurement and the provision of means and methods for making measurements consistent with these standards; the determination of physical constants and properties of materials; the development of methods and instruments for testing materials, devices, and structures; advisory services to government agencies on scientific and technical problems; invention and development of devices to serve special needs of the Government; and the development of standard practices, codes, and specifications. The work includes basic and applied research, development, engineering, instrumentation, testing, evaluation, calibration services, and various consultation and information services. The Bureau also serves as the Federal technical research center in a number of specialized fields. The scope of activities of the National Bureau of Standards is suggested in the following listing of the divisions and sections engaged in technical work.

Washington, D.C.

Electricity. Resistance and Reactance. Electrochemistry. Electrical Instruments. Magnetic Measurements. Dielectrics.

Metrology. Photometry and Colorimetry. Refractometry. Photographic Research. Length. Engineering Metrology. Mass and Scale. Volumetry and Densimetry.

Heat. Temperature Physics. Heat Measurement. Cryogenic Physics. Equation of State. Statistical Physics.

Radiation Physics. X-ray. Radioactivity. Radiation Theory. High Energy Radiation. Radiological Equipment. Nucleonic Instrumentation. Neutron Physics.

Analytical and Inorganic Chemistry. Pure Substances. Spectrochemistry. Solution Chemistry. Standard Reference Materials. Applied Analytical Research.

Mechanics. Sound. Pressure and Vacuum. Fluid Mechanics. Engineering Mechanics. Rheology. Combustion Controls.

Organic and Fibrous Materials. Rubber. Textiles. Paper. Leather. Testing and Specifications. Polymer Structure. Plastics. Dental Research.

Metallurgy. Thermal Metallurgy. Chemical Metallurgy. Mechanical Metallurgy. Corrosion. Metal Physics. Electrodeposition.

Mineral Products. Engineering Ceramics. Glass. Refractories. Enameled Metals. Crystal Growth. Physical Properties. Constitution and Microstructure.

Building Research. Structural Engineering. Fire Research. Mechanical Systems. Organic Building Materials. Codes and Safety Standards. Heat Transfer. Inorganic Building Materials.

Applied Mathematics. Numerical Analysis Computation. Statistical Engineering. Mathematical Physics.

Data Processing Systems. SEAC Engineering Group. Components and Techniques. Digital Circuitry. Digital Systems. Analog Systems. Applications Engineering.

Atomic Physics. Spectroscopy. Radiometry. Solid State Physics. Electron Physics. Atomic Physics.

Instrumentation. Engineering Electronics. Electron Devices. Electronic Instrumentation. Mechanical Instruments. Basic Instrumentation.

Physical Chemistry. Thermochemistry. Surface Chemistry. Organic Chemistry. Molecular Spectroscopy. Molecular Kinetics. Mass Spectrometry. Molecular Structure and Radiation Chemistry.

• Office of Weights and Measures.

Boulder, Colorado

Cryogenic Engineering. Cryogenic Equipment. Cryogenic Processes. Properties of Materials. Gas Liquefaction.

Ionosphere Research and Propagation. Low Frequency and Very Low Frequency Research. Ionosphere Research. Prediction Services. Sun-Earth Relationships. Field Engineering. Radio Warning Services.

Radio Propagation Engineering. Data Reduction Instrumentation. Radio Noise. Tropospheric Measurements. Tropospheric Analysis. Propagation-Terrain Effects. Radio-Meteorology. Lower Atmosphere Physics.

Radio Standards. High Frequency Electrical Standards. Radio Broadcast Service. Radio and Microwave Materials. Atomic Frequency and Time Interval Standards. Electronic Calibration Center. Millimeter-Wave Research. Microwave Circuit Standards.

Radio Systems. High Frequency and Very High Frequency Research. Modulation Research. Antenna Research. Navigation Systems. Space Telecommunications.

Upper Atmosphere and Space Physics. Upper Atmosphere and Plasma Physics. Ionosphere and Exosphere Scatter. Airglow and Aurora. Ionospheric Radio Astronomy.

Order all publications from the Superintendent of Documents
U.S. Government Printing Office, Washington 25, D.C.

Use of funds for printing this publication approved by the Director of the Bureau of the Budget (June 19, 1961).

JOURNAL OF RESEARCH of the National Bureau of Standards—A. Physics and Chemistry
Vol. 65A, No. 4, July–August 1961

Electrical Properties and Kinetics of Electrode Reactions

Ralph J. Brodd

(April 12, 1961)

A common basis for investigations of the properties of electrode reactions is provided. The basic equations of electrostatics and electrodynamics and the assumption that electrode reactions are relaxation processes, are used to develop the equations for the electrical behavior of electrode systems. Thus electrode reaction processes are characterized as two states separated by an energy barrier. The application of static and alternating fields to electrode systems is interpreted in terms of the kinetic parameters of the electrode reactions. The equations for impedance are applied to silver and cadium electrode systems reported in the literature. The agreement of experiment and theoretical expectation is excellent. The equations are also applied to the interpretation of the impedance of LeClanché cells. The kinetic analysis of a simple unimolecular reaction is used to illustrate the kinetic interpretation of experimental information. This simple analysis may be extended to more complex reactions.

1. Introduction

The experimental investigation of electrode reaction mechanisms has followed four schemes of attack: (a) the determination of the steady state electrode potential as a function of current, (b) the voltage-step or potentiostatic method where the current density is measured as a function of time at constant electrode potential, (c) the current-step or galvanostatic method where the electrode potential is measured as a function of time at constant current density, and (d) the measurement of the impedance of the electrode system as a function of the frequency of an applied alternating field. The analysis of method (a) has been summarized in great detail by Bockris [1].[1] The theoretical basis for analysis of methods (b), (c), and (d), however, is not complete and in many cases the fundamental relationship between these methods is not recognized.

Method (d), in spite of its wide application, has suffered in the past from several disadvantages. Contamination problems especially on solid electrodes are intensified as adsorption and desorption of solution impurities give rise to an impedance in parallel with the electrode impedance. Corrosion reactions at metal electrodes give rise to impedances which also contribute to the overall electrode impedance. The measurement of the high capacitance and low resistance of electrode processes also presents some experimental difficulties.

Over the past sixty years the accepted theory for the prediction of the electrical properties of electrode systems has been based primarily on the work of Warburg [2]. Other theories which postulate either that the electrode capacitance is a power function of the frequency [3] or that a special circuit element of constant phase angle θ is present [4] do not conform with experimental evidence [5]. Warburg assumed that diffusion of the reacting species to the electrode surface was the cause of electrode polarization. His theory predicted that the phase angle was 45° and that the series resistance and capacitance of the electrode varied as $\omega^{-1/2}$ where $\omega=2\pi f$ with f the frequency of the alternating field. The mathematics of the original theory of Warburg has been improved by many people. The most significant improvement in recent years removed the restriction of a constant phase angle [6]. However, even with this restriction removed there are serious discrepancies between the theory and experiment.

These developments all predict a linear dependence of the resistance and reactance with $\omega^{-1/2}$. While this relation is obeyed in many instances, frequent references are found to "anomalous" dispersions and absorptions. The cause of the disagreement between experiment and theory has been suggested to be surface roughness, adsorption and desorption of solution impurities or the presence of a corrosion process. The point of view in this paper is that the basis of earlier theories is unsatisfactory. A new representation for the consideration of electrode processes which includes the earlier theories will be set forth in this paper.

Since electrode processes may be described as involving two equilibrium states separated by an energy barrier [7], it is convenient to treat electrode reactions as relaxation processes. The controlling relaxation process may be either a charge transfer reaction ($Ag=Ag^{+}+e$), a chemical reaction simultaneous with, preceding, or succeeding, the charge transfer reaction, or a diffusional process of one or more of the participants in the reactions at the electrode-solution interface. Data from the existing literature will be used as a test for the treatment of electrode processes given below. It is the main purpose of this paper to demonstrate the application of relaxation theory and methods to impedance measurements of the electrode-solution interface.

2. General Relaxation Theory

2.1. Electrical Theory

Recently there has been increased interest in the electrostatic approach to electrochemical kinetics [8]. In particular, an attempt to relate atomic and elec-

[1] Figures in the brackets indicate the literature references at the end of this paper.

tronic polarizations to the calculation of oxidation-reduction reaction rates has been made by Marcus [9] with some success. Relaxation theory has been applied to evaluate the reaction rate constants of ionization reactions in aqueous solutions with good success [10].

As a result of these successes in applying relaxation theory to electrolytic systems it is appropriate to attempt to apply the same theoretical consideration to the electrode-solution interface. Both the Debye theory [11] which treats polarization arising from the orientation of permanent dipoles and the Wagner-Maxwell theory [12] which treats polarization arising from the accumulation of charges at the interface in heterogeneous dielectrics, lead to energy absorption as characterized in figure 1 for a hypothetical case. Electrode processes also lead to energy adsorption at the electrode-solution interface, often in the power frequency range.

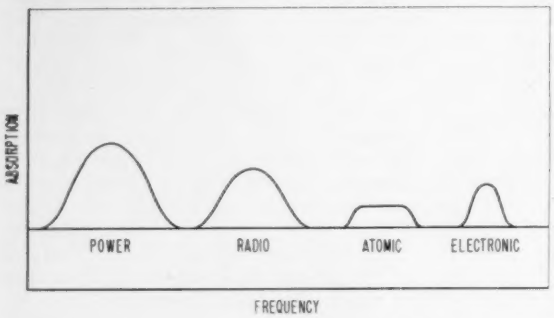

FIGURE 1. *Energy absorption as a function of frequency for a hypothetical system.*

While the derivation of the equations for relaxation processes are well known and are available elsewhere [12], a brief account of the development is in order.

We will define the field quantity **E** by

$$\mathbf{E}=-\nabla V \text{ (v/m)}, \tag{1}$$

where V is electric potential. The vector polarization, **P**, is defined by

$$\mathbf{P}=\mathbf{D}-\epsilon_0\mathbf{E} \text{ (coulombs/m}^2\text{)}, \tag{2}$$

where ϵ_0 is the permittivity of a vacuum and **D** is the displacement. The relationship between **E** and **D** is given by

$$\mathbf{D}=\epsilon\mathbf{E} \text{ (coulombs/m}^2\text{)}, \tag{3}$$

where ϵ is the permittivity.

When the electrode-solution interface is subjected to an alternating field, two possibilities arise which depend on the frequency of the field, the temperature, and the nature of the electrode-solution interface. In the first case there is no measurable phase difference between **D** and **E** and the polarization is in phase with the alternating field. In the other case there is a measurable phase difference between **D** and **E**. A phase difference between **D** and **E** can be due to any of three factors: d-c conductivity, relaxation effects, and resonance effects.

We will examine now in more detail relaxation effects as they affect the energy absorption at the electrode solution interface. A simple model that may be used for the description of this effect is that of a process in which the energy absorption is characterized by a relaxation time. If a constant electric field is applied at the electrode-solution interface we assume that a polarization will result from a disturbance of the equilibrium distribution of the participants in the electrode reactions at the electrode-solution interface. We will also assume as in other relaxation phenomena that the time rate of change $\frac{dP}{dt}$ of **P** is proportional to the difference between the final value, P_s, and the actual value P [11, 12]:

$$\frac{dP}{dt}=\frac{1}{\tau}(P_s-P) \text{ (coulombs/m}^2\text{/sec)}, \tag{4}$$

where τ is a constant with the dimensions of time. Since τ is a measure of the time lag, it is called the relaxation time. Integrating eq (4) using the condition $P_{t=0}=P_\infty$ (i.e., P_∞ is the instantaneous contribution to the polarization) we obtain

$$P=P_\infty+(P_s-P_\infty)\ (1-\epsilon^{-t/\tau}) \text{ (coulombs/m}^2\text{)}. \tag{5}$$

In the opposite condition where a static field is suddenly taken away we have

$$\frac{dP}{dt}=-\frac{1}{\tau}P \text{ (coulombs/m}^2\text{/sec)}. \tag{6}$$

Here we have $P_{t=0}=P_s-P_\infty$. Integration gives:

$$P=(P_s-P_\infty)e^{-t/\tau} \text{ (coulombs/m}^2\text{)}. \tag{7}$$

A description of relaxation effects by equations similar to eqs (5) and (7) was first given by Pellat [13]. The subscripts ∞ and s refer to the values of the quantities at times much less or much greater than τ.

For alternating field when there is a phase difference between **D** and **E**, it is useful to express D and E as complex numbers,

$$E=E_0e^{+j\omega t} \text{ (v/m)} \tag{8}$$

$$D=D_0e^{+j(\omega t-\delta)} \text{ (coulombs/m}^2\text{)} \tag{9}$$

where j is $\sqrt{-1}$, $\omega=2\pi\times$ the frequency f of the alternating field, t is the time, and δ is the phase angle between **D** and **E**.

When δ is independent of **E** we can write

$$D=\epsilon^*E \text{ (coulombs/m}^2\text{)}. \tag{10}$$

where ϵ^* is the complex permittivity. Here we

will be most interested in the impedance, Z of the electrode-solution interface,

$$Z=R-jX_c \text{ (ohms)}, \tag{11}$$

in which R is the resistance and X_c is the capacitive reactance.

In relaxation theory it is generally assumed that eq (4) is valid for alternating as well as static fields, and hence it can be shown that [2]

$$Z=R_\infty+\frac{R_s-R_\infty}{1+j\omega\tau} \text{ (ohms)}. \tag{12}$$

As a result

$$R=R_\infty+\frac{R_s-R_\infty}{1+\omega^2\tau^2} \text{ (ohms)}, \tag{13}$$

and

$$X_c=(R_s-R_\infty)\frac{\omega\tau}{1+\omega^2\tau^2} \text{ (ohms)}. \tag{14}$$

By plotting the left hand side of eqs (13) and (14) against log ω we obtain the plots shown in figures 2 and 3. The maximum in the X_c—log ω plot is reached when log $\omega\tau=0$. Thus

$$\omega_{max}=\frac{1}{\tau} \text{ (sec}^{-1}\text{)}. \tag{15}$$

We have

$$R_{(max)}=\frac{R_s+R_\infty}{2} \text{ (ohms)}, \tag{16}$$

$$X_{c(max)}=\frac{R_s-R_\infty}{2} \text{ (ohms)}. \tag{17}$$

The use of a logarithmic scale has the advantage that the curves in figures 2a and b are symmetrical about $\omega\tau=1$.

Another method of representing the curves is to construct an Argand diagram or complex plane locus in which the imaginary part X_c of the impedance is plotted against the real part R, each point corresponding to one frequency (13). From eqs (13) and (14) we obtain

$$\left[R-\frac{R_s+R_\infty}{2}\right]^2+X_c^2=\left[\frac{R_s-R_\infty}{2}\right]^2. \tag{18}$$

By plotting R versus X_c a semicircle must be obtained with a radius $(R_s-R_\infty)/2$, its center on the abscissa at a distance $(R_s+R_\infty)/2$ from the origin. The semicircle in figure 3 corresponds to values taken from figure 2. For given values of R_s and R_∞ the R, X_c curve is completely defined provided the equations are valid. The frequency range in which the absorption occurs has no influence on the R, X_c curve. Thus, this method of representation is independent of the relaxation time, and reveals the inherent simplicity of the relaxation process.

[2] The subscripts ∞ and s refer to the value of the quantities at frequencies far above or far below $1/2\pi\tau$ respectively. The definition $Z=1/(j\omega\epsilon^*)$ was used to relate the complex permittivity to the impedance.

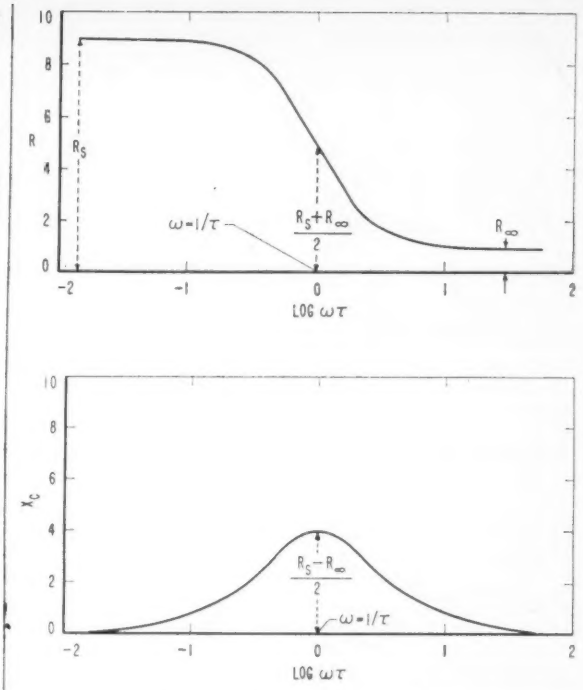

FIGURE 2. *a. The dependence of R on frequency according to eq (13) assuming $R_s=9$, $R_\infty=1$ and $\tau=10^{-3}$ sec.*
b. The dependence of X_c on frequency according to eq (14), assuming $R_s=9$, $R_\infty=1$ and $\tau=10^{-3}$ sec.

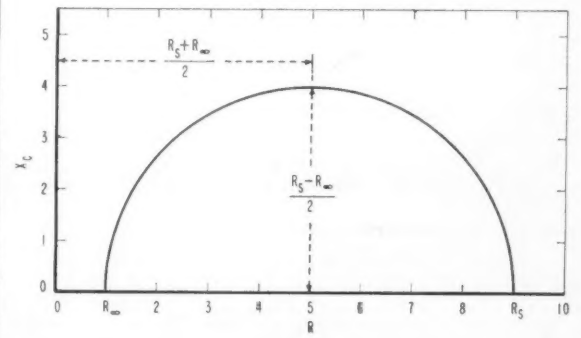

FIGURE 3. *Relationship between R and X_c according to eq (18), for R_s, R_∞ and τ given in figure 2.*

An experimental quantity of interest is tan θ where $\theta=90°-\delta$. From eqs (13) and (14) we find

$$-\tan\theta=\frac{X_c}{R}=\frac{(R_s-R_\infty)\omega\tau}{R_s+R_\infty\omega^2\tau^2}. \tag{19}$$

Taking $(\partial \tan\theta/\partial\omega)=0$ we find the maximum value of tan θ is obtained at the frequency

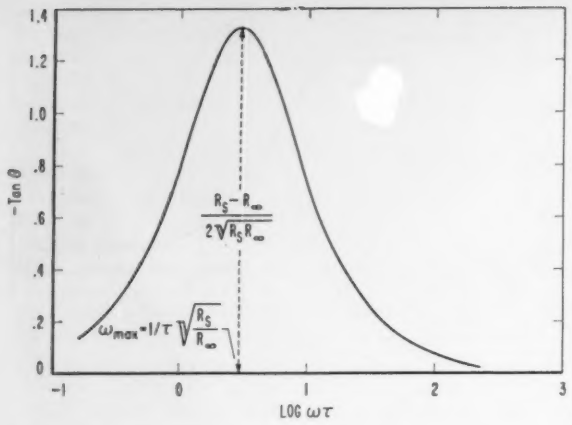

FIGURE 4. *The dependence of tan θ on frequency according to eq (19) for R_s, R_∞ and τ given in figure 2.*

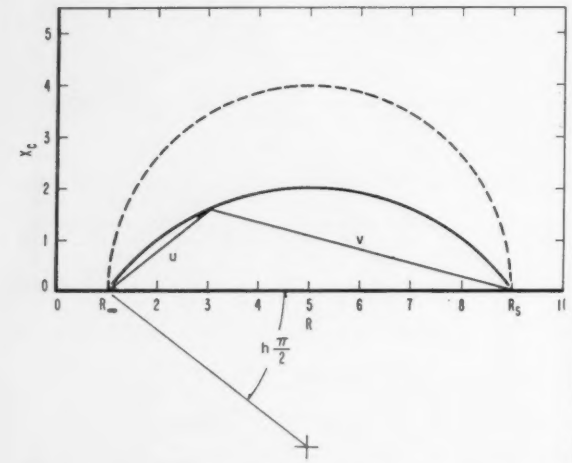

FIGURE 5. *Relationship between R and X_c according to eq (26), defining the parameter, h for R_s, R_∞ and τ given in figure 3.*

The curve for $h=0$ is drawn in with dashed lines.

$$\omega'_{max} = \frac{1}{\tau}\sqrt{\frac{R_s}{R_\infty}}\ (\text{sec}^{-1}) \tag{20}$$

$$-\tan\theta_{(max)} = \frac{R_s - R_\infty}{2\sqrt{R_s R_\infty}}. \tag{21}$$

In figure 4 the dependence of tan θ on log ω is shown for the values of R_s, R_∞ and τ used in figures 2 and 3.

In some cases [14] τ may have a distribution of values about a most probable value. The fact that τ may have a distribution of values in no way invalidates the equations or graphical representations given previously. Rather it throws eq (12) into a more general form:

$$Z = R_\infty + \frac{R_s - R_\infty}{1 + j(\omega\tau)^{1-h}}\ (\text{ohms}) \tag{22}$$

where h is identified with the angle defined in figure 5. When $h=0$ eq (22) is reduced to eq (12). The distribution function for the case where $h=0$ is closely approximated by a Boltzman distribution function for τ.

A point is chosen on the R, X_c curve in figure 5 corresponding to a measurement at a certain frequency ω_1. The distances u and v from this point to the intersection points R_∞ and R_s of the curve with the abscissa respectively are determined as shown in figure 5. The equation

$$u/v = (\omega_1/\omega_{max})^{1-h} \tag{23}$$

may be used to evaluate ω_{max} if u, v, ω_1, and h are known. To determine h a plot of the quantity log (u/v) versus log ω is constructed. The result must be a straight line with the slope $(1-h)$ in order that eq (22) be applicable.

In this discussion only one process was assumed to be occurring. Wherever more than one relaxation process is occurring simultaneously, the total polarization is assumed to be the sum of the different polarization contributions. As a result eq (5) is written in the form

$$P_t = P_\infty + \sum_r (P_s - P_\infty)_r (1 - e^{-t/\tau_r})\ (\text{coulombs/m}^2) \tag{24}$$

and eq (12) is written as

$$Z = R_\infty + \sum_r \frac{(R_s - R_\infty)_r}{1 + (j\omega\tau_r)}\ (\text{ohms}) \tag{25}$$

with

$$R = R_\infty + \sum_r \frac{R_a}{1 + \omega^2\tau_r^2}\ (\text{ohms}) \tag{26}$$

and

$$X_c = \sum_r \frac{R_a \omega\tau_r}{1 + \omega^2\tau_r^2}\ (\text{ohms}) \tag{27}$$

where

$$R_a = (R_s - R_\infty)_r \tag{28}$$

is the contribution to the resistance by the r-th relaxation process. If eq (25) does not apply, a more powerful means of combining the impedance of the various processes must be found.

2.2. Kinetic Theory

In section 2.1, it was assumed that polarization is the result of a disturbance of the equilibrium distribution of the participants in the electrode reaction. An alternate and sometimes more illuminating approach to the properties of the electrode-solution interface is based on the kinetic behavior of the various processes at the electrode-solution interface. In order to discuss the kinetics of an

electrode process, it is necessary first to formulate a reaction mechanism. If the electrode process is a simple unimolecular reaction [3] given by

$$A \underset{k_2}{\overset{k_1}{\rightleftharpoons}} A^* \tag{29}$$

the reaction may be depicted in terms of free energy and reaction coordinates as shown in figure 6 [15].

The reaction rate constants are related to the free energy of activation and the field strength by

$$k_1 = G_0 \exp -\left[\frac{\Delta F^{\ddagger} + \lambda\beta\Delta\phi F}{RT}\right] (\text{sec}^{-1}) \tag{30}$$

and

$$k_2 = G_{0'} \exp -\left[\frac{(\Delta F^{\ddagger} + \Delta F) - \lambda(1-\beta)\Delta\phi F}{RT}\right] (\text{sec}^{-1}) \tag{31}$$

where G_0 and $G_{0'}$ are constants for a given system, $\Delta F^{\ddagger}$ is the free energy of activation, ΔF is the free energy change for the process, λ is the number of charges transferred in the process, R is the gas constant, T is the temperature in degrees Kelvin, F is Faraday's constant, β is the symmetry factor, usually assumed to be ½ [17] and $\Delta\phi$ is the difference in the inner potentials of the solution and electrode. We may write the kinetic equations for the reaction directly.

$$dN_1/dt = k_2 N_2 - k_1 N_1 \tag{32}$$

$$dN_2/dt = -k_2 N_2 + k_1 N_1 \tag{33}$$

where N_1 and N_2 are the concentrations of A and A^* respectively. If $N = \sum_r N_r$, it can be shown that solution of eqs (32) and (33) takes the form

$$N_1 = N_{01} + C_{11} e^{-\alpha t} \tag{34}$$

and

$$N_2 = N_{02} + C_{12} e^{-\alpha t} \tag{35}$$

where

$$\alpha = k_1 + k_2 \ (\text{sec}^{-1}) \tag{36}$$

and N_{01} and N_{02} are the equilibrium values of N_1 and N_2 respectively. Also we note that $C_{11} = -C_{12}$. C_{11} is directly proportional to the relaxation time and conductance of the process and the potential drop at the electrode surface. Since $N_2 - N_1$ is proportional to the polarization we note the exponential approach to equilibrium as required in relaxation theory. When a field is suddenly removed, it follows that

$$P = (P_s - P_\infty) e^{-\alpha t} \ (\text{coulombs/m}^2), \tag{37}$$

or

$$P = (P_s - P_\infty) e^{-t/\tau} \ (\text{coulombs/m}^2), \tag{38}$$

[3] The analysis of more complex reactions will not be considered here. The reader is referred to the available literature for several treatments of complex reaction kinetics [16].

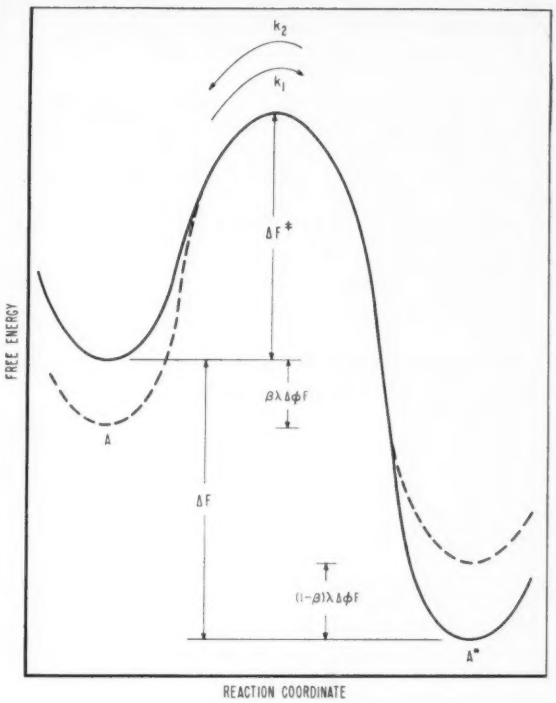

FIGURE 6. *Details of the free energy of activation barrier for a simple unimolecular process.*

which is identical with eq (7) and

$$\tau = 1/(k_1 + k_2) \ (\text{sec}). \tag{39}$$

Thus τ is related directly to the reaction rate constants for the process. The relaxation time τ depends on ΔF and $\Delta F^{\ddagger}$ as well as $\Delta\phi$. As a result τ may be expected to be a function of temperature and electrode potential.

The resistance $R_s - R_\infty$ in eqs (12) and (25) is the resistance associated with the given relaxation process. This resistance will be the resistance of the electrode process, $R_a = (R_s - R_\infty)$; R_a may be substituted directly into the equation for exchange current density, J_0,

$$J_0 = (RT/\lambda F)(1/AR_a) \ (\text{amp/m}^2) \tag{40}$$

where $[RT/\lambda F]$ is thermal potential expressed in volts and A is the area.

Either the Argand diagram or the log plots also may be used to evaluate the resistance of the electrode process, R_a, and the relaxation time, τ. In figures 2b and 3, $R_a/2$ is the maximum height of the curve. The frequency at the maximum is related to τ by eq (15). In figure 2a, R_a is the height of the step and τ is found from the frequency at the midpoint of the step.

The equation from older theories (2, 6)

$$R-X_c=R_a \tag{41}$$

is not a reliable method for determining R_a for an electrode process. From eqs (13) and (14) we see that the difference $R-X_c$ may vary from R_∞ to R_s depending on whether ω is far removed above or below ω_{max}. Thus the use of eq (41) in the older theories is valid only at frequencies far below ω_{max} and if R_∞ is zero.

At equilibrium

$$dN_1/dt=dN_2/dt=0. \tag{42}$$

The rate of the process at equilibrium is the exchange current. Therefore, we may write

$$J_0=k_1N_{01}=k_2N_{02} \text{ (amp/m}^2\text{)} \tag{43}$$

and

$$k_1/k_2=N_{02}/N_{01}. \tag{44}$$

From eqs (30) and (31) we can also write

$$k_1/k_2=\exp[(\Delta F-\lambda\Delta\phi F)/RT]. \tag{45}$$

Unfortunately even if the free energy change is known, it is not possible at present to evaluate $\Delta\phi$ for electrochemical processes. In certain circumstances a good approximation for $\Delta\phi$ is given by

$$V_e-V_{zpc}=\Delta\phi \text{ (v)} \tag{46}$$

where V_e-V_{zpc} is the electrode potential with respect to the electrode potential at zero point of charge [18]. The zero point of charge is very difficult to evaluate.

An alternate and possibly more fruitful approach to the ratio k_1/k_2 may be to determine the ratio N_{02}/N_{01} as noted in eq (44). The concentrations of the elements of the process may be found by the analysis of the charge distributions. This type of calculation has been given for mercury electrode interfaces by Grahame [19]. At present, it is not possible to extend the analysis of charge distribution to other electrode interfaces except by inference as the zero point of charge for most metal electrodes cannot be accurately evaluated.

If one of the elements of the process is a metal, say A, the concentration of A, N_{01}, may be taken as the number of surface atoms. Using eq (43) and the exchange current, k_1 can be found immediately. Then substituting k_1 and τ into eq (39), k_2 can be evaluated. Likewise if N_{02}, but not N_{01} may be determined, eqs (39) and (43) can be used to evaluate k_1 and k_2.

Once the ratio k_1/k_2 has been evaluated at one potential the rate constants for the process may be determined at any other potential by

$$k_1'/k_2'=(k_1/k_2)\exp(-\Delta\phi'\lambda F)/RT \tag{47}$$

where $\Delta\phi'$ is the change in $\Delta\phi$ from the old to the new electrode potential and k_1'/k_2' is the ratio of rate constants at the new electrode potential.

3. Applications

Since equations describing the kinetic and electrical properties of the electrode-solution interface are now available, the application of the various equations will be illustrated with data obtained from real electrode systems. The impedance of a D-size LeClanché cell constructed at NBS is shown in figure 7. The cell has a paste liner and a bobbin composition by weight of 8 parts African MnO_2 ore, 1.24 parts ammonium chloride and 1 part acetylene black. The impedance of the cell was measured on a substitution type Wien bridge described by Vinal [20]. The values of the resistance, capacitance, and reactance of 4 cells are reported in table 1 for the frequency range 50 c/s to 50 kc/s at room temperature. From these data the values of R_a, ω_m and R_∞ are given in table 2. Only data for cell 1 is shown in figure 7 for illustration. The introduction of three absorption regions was required to reproduce the impedance of LeClanché cells as a function of frequency. The three regions of energy absorption or dispersion were found in figure 7b by curve fitting using the theoretical behavior of the imaginary part of the impedance given by eq (27). These three curves are drawn in lightly in figure 7. It was necessary to introduce three relaxation processes in order to fit the experimental curve. The analysis of data by curve fitting is a necessity in the absence of other information on the location of the absorption regions.

Experiments using pairs of either zinc or manganese oxide electrodes established that the dispersion with ω_{max}=600 c/s was associated with the zinc electrode while the other dispersions were associated with processes at the manganese oxide electrodes. Euler and Dehmelt [21] reached the same conclusions except they did not report the dispersion centered about ω_{max}=180 kc/s. A summary of the results from other cells in the group manufactured at NBS is given in table 1. In all cases the sum of the theoretical curves for three absorption regions fit the experimental behavior of the impedance.

Figure 7 illustrates the usefulness of the various types of data representation. The Argand diagram (fig. 7a) immediately reveals the complete behavior of the impedance. The plot of log ω (fig. 7b) reveals the additivity of the imaingary part of the impedance as assumed in eq (27). Each type of data representation has its usefulness and applications.

The silver-silver ion and cadmium-cadmium ion electrode systems illustrate the use of eq (13) to represent the behavior of the resistive portion of the electrode impedance [22]. In figure 8 the electrode resistance versus log ω for both systems is shown. The results of the analysis of these graphs is given in table 3. The theoretical curves included for comparative purposes were calculated assuming that the values of R_s and R_∞ and τ given in the caption of the figure. The agreement of theoretical calculation and experiment is excellent.

To illustrate the calculations of k_1 and k_2 for unimolecular reactions the analysis of the silver-silver ion system in figure 8a will be given. Examination

TABLE 1. *Resistance, capacitance, and reactance of D-size LeClanché cells*

Cell	$f=\omega/2\pi$	50	100	200	500	1.0 k	2.0 k	5.0 k	10 k	20 k	50 k
1	R ohm	0.623	0.453	0.219	0.228	0.203	0.185	0.176	0.171	0.166	0.164
	C μF	15100	6110	3815	2740	2262	1812	1320	946	648	298
	X ohm	0.211	0.261	0.209	0 116	0.070	0.044	0.024	0.017	0.012	0.011
2	R ohm	0.642	0.439	0.306	0.218	0.191	0.175	0.167	0.156	0.154	0.153
	C μF	12100	5435	3568	2632	2153	1697	1241	929.8	652.0	260.2
	X ohm	0.263	0.294	0.223	0.121	0.074	0.047	0.026	0.017	0.012	0.009
3	R ohm	0.942	0.519	0.378	0.250	0.210	0.186	0.171	0.163	0.160	0.161
	C μF	9350	3962	2510	1829	1495	1211	931.0	926.9	534.4	297.7
	X ohm	0.431	0.402	0.317	0.174	0.106	0.066	0.034	0.022	0.015	0.011
4	R ohm	0.488	0.355	0.260	0.180	0.167	0.159	0.150	0.145	0.142	0.142
	C μF	16700	7361	4843	3580	2893	2227	1580	1139	805.0	360.2
	X ohm	0.191	0.216	0.165	0.089	0.055	0.036	0.020	0.014	0.010	0.009

TABLE 2. *Interpretation of data from table 1*

Cell	R_∞	Ra_1	ω_{max}	Ra_2	ω_{max}	Ra_3	ω_{max}
	Ohm	*Ohm*	*sec*$^{-1}$	*Ohm*	*sec*$^{-1}$	*Ohm*	*sec*$^{-1}$
1	0.159	0.518	596	0.054	6.9 k	0.020	210 k
2	.151	.602	502	.058	6.3 k	.014	190 k
3	.160	.608	583	.060	8.2 k	.020	190 k
4	.136	.420	690	.050	3.1 k	.010	170 k

of figure 8a shows only one dispersion region. Therefore we need consider only one reaction. It is very unlikely that two reactions in the silver system would have the same relaxation time. We will assume that the process at the Ag electrode is:

$$Ag \underset{k_2}{\overset{k_1}{\rightleftharpoons}} Ag^+ + e. \tag{48}$$

We will assume that the concentration of electrons is very large compared to the other concentrations and that the concentration of electrons remains constant. Thus, eq (48) may be assumed to be a unimolecular reaction. The concentration of silver atoms will be taken as the number of surface atoms, approximately 6.0×10^{18} atoms/m^2, calculated from the silver metal lattice dimensions [23]. Using eq (43) and data from Table 3 with $J_0=1.1\times10^2$ amp/m^2 or a particle flow of 6.9×10^{20} particles/m^2/sec.

$$6.9\times10^{20}=(6\times10^{18})k_1 \text{ (particles/m}^2\text{/sec)}$$

$$k_1=115 \text{ sec}^{-1}.$$

From eq (39) with $\tau=1/8100$

$$8100=115+k_2 \text{ (sec}^{-1}\text{)}$$

$$k_2=7985 \text{ (sec}^{-1}\text{)}.$$

From eq (44) the concentration of silver ions, N_2, is

$$115/7985=N_2/(6.0\times10^{18})$$

$$N_2=8.6_4\times10^{16} \text{ (ions/m}^2\text{)}.$$

Other investigations of the silver-silver ion system have reported the presence of a low frequency

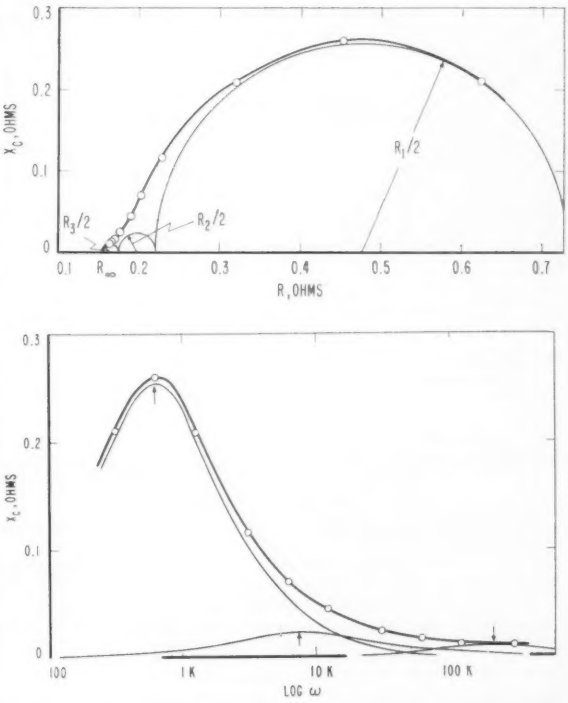

FIGURE 7. *a. Argand diagram of the impedance of a LeClanché cell.*
b. The dependence of X_c on frequency for a LeClanché cell.

TABLE 3. *Summary of data from figure 9*

Electrode System	R_∞	Ra[1]	τ	Electrode area	I_0
	Ohms	*Ohms*	*sec*	*m*$^2\times10^4$	*amp/m*^{2}
Ag−Ag$^+$ [10 g $AgNO_3$ per 100 cm^2 water]	130	112	$1.2_3\times10^{-4}$	0.04	1.1×10^2
Cd−Cd^{++} [15 g $CdSO_4$ per 100 cm^2 water]	230	90	6.4×10^{-5}	.04	1.4×10^2

[1] The experimental cell was composed of two identical electrodes separated by a solution containing ions of the electrode material. The total resistance associated with the electrode reaction is the sum of the resistance contribution of each electrode. As a result the resistance used in calculation is $R_a/2$.

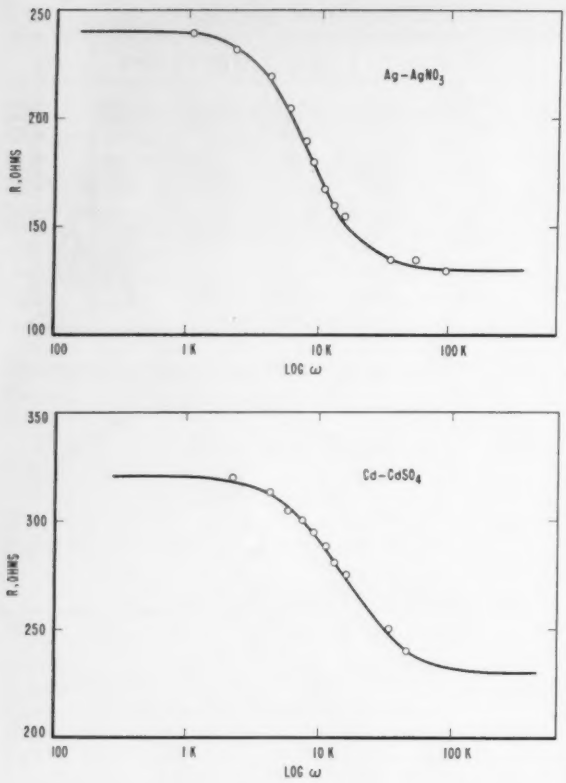

FIGURE 8. *a. The dependence of resistance, R, on frequency for the silver-silver ion (10 g $AgNO_3$ per 100 cm^3 of solution) electrode system.*

The solid line was calculated using eq (25) and assuming that $R_s=242$, $R_\infty=130$ and $\tau=1.23\times10^{-4}$. The circles are the experimental data [23].

b. The dependence of resistance, R, on frequency for the cadmium ion (15 g $CdSO_4$ per 100 cm^3 of solution) electrode system.

The solid line was calculated using eq (25) and assuming that $R_s=320$, $R_\infty=230$ and $\tau=6.4\times10^{-3}$. The circles are the experimental data [23].

dispersion [24] associated with a diffusion process. This is not noticed in Banerji's work, figure 8a, used here for illustration [22]. A similar analysis may be made for the cadmium-cadmium ion system.

4. Concluding Remarks

In this paper a point of view of the kinetics and electrical properties of electrode systems has been taken that differs from previous theories. The description of electrode reactions as relaxation processes, which includes charge-transfer, and chemical and diffusion processes, is very general in nature. Since diffusion processes may be classified as relaxation processes, the representation given in this paper will include previous theories. Equations for the prediction of the electrical behavior of electrode processes have been given. The representation given in this paper based on relaxation phenomena was applied to the electrical behavior of electrodes previously reported in the literature, namely, Ag, Ag^+ and Cd, Cd^+; conformity with theoretical predictions was obtained. The representation was also applied successfully to the electrical behavior of LeClanché cells. Only cursory observations on the galvanostatic and potentiostatic methods have been made and the problem of nonlinear combinations of electrode processes has not been considered. Also, resonance effects have not been treated in this paper.

The author thanks M. G. Broadhurst, J. I. Lauritzen, Jr., J. D. Hoffman, and F. B. Silsbee for making a number of helpful suggestions during the course of this work.

5. References

[1] J. O'M. Bockris, Modern aspects of electrochemistry, ch IV. (Academic Press, Inc., New York, N.Y., 1955.)
[2] E. Warburg, Wied Ann. **67,** 493 (1899).
[3] I. Wolff, Phys. Rev. **27,** 755 (1926).
[4] H. Fricke, Phil. Mag. [7] **14,** 310 (1932).
[5] Summary: C. Jones and S. M. Christian, J. Am. Chem. Soc. **57,** 272 (1935).
[6] J. E. B. Randles, Disc. Faraday Soc. **1,** 11 (1947).
B. V. Ershler, Disc. Faraday Soc. **1,** 269 (1947).
B. V. Ershler, Zhur. Fiz. Khim. **22,** 683 (1948).
D. C. Grahame, J. Electrochem. Soc. **99,** 370C (1952).
H. Gerischer, Z. Physik. Chem. **198,** 286 (1951).
[7] R. W. Gurney and R. H. Fowler, Proc. Roy. Soc. **136A,** 378 (1932).
[8] H. Chang and G. Jaffe, J. Chem. Phys. **20,** 107 (1953).
J. R. Macdonald, J. Chem. Phys. **22,** 1857 (1954).
[9] R. A. Marcus, Can. J. Chem. **37,** 155 (1959).
[10] R. G. Pearson, Disc. Faraday Soc. **17,** 187 (1954).
M. Eigen, Disc. Faraday Soc. **24,** 25 (1957).
[11] P. Debye, Polar molecules, ch V (Dover Publications, New York, N.Y., 1945).
[12] C. J. F. Böttcher, Theory of electric polarization (Elsevier Publishing Co., Houston, 1952).
H. Fröhlich, Theory of dielectrics (Oxford University Press, London, 1958).
C. P. Smyth, Dielectric behavior and structure (McGraw-Hill Book Co., Inc., New York, 1955).
[13] H. Pellat, Ann. Chim. Phys. **18,** 150 (1899).
K. S. Cole and R. H. Cole, J. Chem. Phys. **9,** 341 (1941).
[14] R. M. Fuoss and J. G. Kirkwood, J. Am. Chem. Soc. **63,** 385 (1941).
[15] H. Eyring, J. Chem. Phys. **4,** 283 (1936).
S. Glasstone, K. J. Laidler and H. Eyring, The theory of rate processes (McGraw-Hill Book Co., New York, N.Y., 1941).
[16] E. W. Montroll and K. G. Shuler, Advances in chemical physics, Vol. I, p 361 (Interscience Publishers, Inc., New York, N.Y., 1958).
S. H. Bauer, J. Chem. Phys. **21,** 1888 (1953).
J. D. Hoffman and B. M. Axilrod, J. Research, NBS **54,** 357 (1955).
[17] J. O'M. Bockris, Electrochemical Constants, Circular 524, National Bureau of Standards, p. 243.
[18] R. J. Brodd, J. Electrochem. Soc. **106,** 74 (1959).
[19] D. C. Grahame, Chem. Rev. **41,** 441 (1947).
[20] G. W. Vinal, Storage Batteries, 4th Ed., p. 328 (John Wiley and Sons, New York, N.Y., 1955).
[21] J. Euler and K. Dahmelt, Z. Elektrochem. **61,** 1200 (1957).
[22] B. Banerji, Trans. Faraday Soc. **22,** 112 (1926).
[23] F. Seitz, Modern theory of solids, p. 6 (McGraw-Hill Book Co., Inc., New York, N.Y., 1940).
[24] A. R. Despic and J. O'M. Bockris, J. Chem. Phys. **32,** 389 (1960); also W. Lorentz, Z. physic. Chem., Frankfort **17,** 136 (1958).

(Paper 65A4–111)

JOURNAL OF RESEARCH of the National Bureau of Standards—A. Physics and Chemistry
Vol. 65A, No. 4, July–August 1961

Effect of Hydrostatic Pressure Upon the Relaxation of Birefringence in Amorphous Solids

Roy M. Waxler and Leason H. Adams

(March 28, 1961)

A study was made of the effect of hydrostatic pressure upon the relaxation of birefringence in two commercial plastics which were glasslike in nature. The birefringence was introduced into the materials by loading in uniaxial compression, and the decay of birefringence with time was measured using a polarimeter. The rate at which the optical path-difference disappeared was greatly inhibited by the hydrostatic pressure, and a pressure of 10,000 bars was found to be sufficient to stop the release completely. The results are interpreted as the effect of hydrostatic pressure upon the mobility of the materials. Some experiments were conducted to determine the effect of temperature upon the relaxation, that the effects of pressure and temperature might be compared.

1. Introduction

When an amorphous solid is subjected to a uniaxial stress, it becomes birefringent, and the subsequent decay of this birefringence is associated with a relaxation of the stress. This phenomenon is attributed to flow in the material. The relaxation of internal stress in glass as a function of temperature was investigated some years ago by Adams and Williamson [1] [1] in their work on annealing. Investigations by Lillie [2] and Isard and Douglas [3] give evidence that in the annealing of silicate glasses, the release is accomplished essentially by viscous flow. Regardless of the mechanism by which the stress is released, the influence of hydrostatic pressure upon this mobility is of general interest in solid state physics. The hydrostatic pressure of itself does not introduce any double refraction into the material, as will be shown.

2. Measurement of Optical Path-Difference

In measuring optical path-difference it is customary to use a Babinet compensator or a graduated quartz wedge, which instruments afford a sensitivity of about ± 5 mμ. A polarimeter developed by Goranson and Adams [4] affords a sensitivity of ± 0.05 mμ, and the measurements may be made easily.[2] Plane-polarized light is rotated through an angle equal to one-half the phase lag produced by double refraction in the specimen by this instrument. Since the measurements were of angular displacement, it was found to be convenient and adequate to express the optical path-difference as phase lag in the specimen in degrees, this value being twice the measured value of the rotation. The instrument is equipped with a graduated quartz wedge used in determining the multiples of 360° when the phase lag in the specimen exceeds one whole wavelength. A high pressure mercury arc lamp was used with optical filters to isolate the green line of 5461A.

[1] Figures in brackets indicate the literature references at the end of this paper.
[2] The authors are indebted to the Geophysical Laboratory of the Carnegie Institute of Washington for the loan of this instrument.

3. Pressure Apparatus

The apparatus and techniques for obtaining high hydrostatic pressures have been described in detail by Weir [5]. Briefly, a heavy-walled pressure vessel has a smooth bore which contains a light petroleum distillate. By means of a hydraulic press, a leak-proof piston is forced into the bore of the vessel thereby compressing the liquid and generating hydrostatic pressure. The apparatus is designed for pressures up to 10,000 bars, and the pressure is measured internally by means of a manganin pressure gage to a precision of $\pm \frac{1}{8}$ bar.

4. Choice of Material and Method of Introducing Optical Path Difference

It was convenient to select a glass such as glucose, or polybutyl methacrylate, that would anneal around room temperature. It was planned to introduce double refraction into a specimen by plunging it into a bath at low temperature, and then to observe the relaxation at room temperature. Some polybutyl methacrylate was polymerized and molded into blocks. The dimensions of these blocks were reduced to $1\frac{1}{2} \times \frac{9}{16} \times \frac{3}{8}$ in. to permit them to enter the bore of the pressure vessel. The amount of double refraction introduced into one of these small specimens by quenching varied markedly so that it was impossible to find an area with sufficient uniformity to allow a good measurement.

Considering the difficulties with temperature-induced photoelastic effects, a method was sought that would introduce into a specimen a uniform birefringence that would decay with time. It has been found in early work on photoelastic stress analysis [6] that when a transparent plastic is loaded and the load held constant over a period of time, the optical path difference caused by the stress does not remain constant but increases with time. Likewise, when the load is removed, the optical path difference does not go to zero immediately but decays gradually. These effects are shown very roughly for allyl

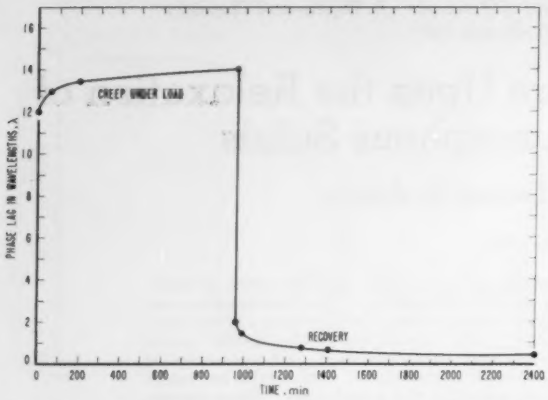

FIGURE 1. *Birefringence in a specimen of allyl diglycol carbonate when loaded to 350 kg/cm² for 960 minutes and then unloaded.*

diglycol carbonate in figure 1, where a specimen in the form of a block $1\frac{1}{2} \times \frac{9}{16} \times \frac{3}{8}$ in. was loaded lengthwise in uniaxial compression. Allyl diglycol carbonate is widely used in stress analysis, having a stress-optical coefficient of 26.5 brewsters, where 1 brewster $= 10^{-13}$ (cm)²/dyne. It is available in large clear sheets that give excellent transmission of light in the visible region.

A small loading mechanism which has been described previously [7] was employed to insure a uniform and uniaxial compression of the specimen. This device was modified for the present work, so that instead of using suspended weights, the load was applied by means of a testing machine. A specimen of allyl diglycol carbonate with the same dimensions as used previously was loaded to 350 kg/cm², and the platens of the testing machine were then held in this fixed spatial position for a period of 16 hr. Upon removing the residual load, measurement of the specimen in the polarimeter showed that there was a phase lag of about 720°, or two wavelengths of the 5461 A line. This residual phase lag reduced to about 20 percent of its original value in the course of a day, and when a plot was made of the phase lag in the specimen versus time, the points fell on a smooth curve.

Change in birefringence under load was also observed in commercial polymethyl methacrylate. Like allyl diglycol carbonate, this material is available in large, clear sheets, and affords excellent transmission in the visible region of the spectrum. However, polymethyl methacrylate has a much smaller stress-optical coefficient (about 3.75 brewsters). A specimen of this plastic, with the same dimensions as used previously, was loaded in uniaxial compression to 700 kg/cm², and the platens of the testing machine were then held in this fixed spatial position for a period of 16 hr. Upon removal of the residual load, the specimen exhibited a residual phase lag corresponding to three-quarters of a wavelength of mercury green light, and this lag gradually reduced to about 20 percent of its original value in the course of a day.

For both allyl diglycol carbonate and polymethyl methacrylate, X-ray diffraction patterns obtained from a Geiger counter diffractometer showed the presence of broad peaks typical of amorphous materials.

A piece of allyl diglycol carbonate which showed no evidence of double refraction when examined in polarized light was placed in the pressure bomb and subjected to a pressure of 10,000 bars for a period of 10 min. The pressure was then released, and the specimen, upon removal from the bomb, still showed no sign of double refraction after temperature equilibrium had been established. The result of this experiment was taken as verification of the statement in the introduction that hydrostatic pressure of itself does not introduce any double refraction into an amorphous solid.

Since the relaxation curve for allyl diglycol carbonate was not closely reproducible for specimens treated in the same way, it was decided to load a specimen double the usual length, one half to be placed in the pressure bomb at elevated pressure, and the other half to be used as a reference specimen at atmospheric pressure. Upon removal from the loading apparatus, examination in polarized light showed that the optical path-difference in each half was the same.

5. Experimental Procedure

The above approach was followed in an experiment where the pressure bomb was raised to 10,000 bars, this pressure being selected because a large effect was sought. Making allowances for the time spent in raising and lowering the pressure in the bomb, the results of the experiment indicated that there was no relaxation of the specimen at all during the time it was under the pressure of 10,000 bars. This initial experiment was followed by similar ones using pressures of 2,100 bars, 1,000 bars, and 500 bars, and it could be seen, qualitatively, that the relaxation proceeded at a greater rate at each succeedingly lower pressure.

To ascertain that this inhibiting of the relaxation was not unique for allyl diglycol carbonate, two experiments of a similar nature were conducted with polymethyl methacrylate at pressures of 2,000 bars and 1,000 bars. It was necessary to enclose a polymethyl methacrylate specimen in a polyethylene bag in order to protect it from attack by the petroleum fraction used in the pressure bomb. The results of the experiments agreed qualitatively with earlier results, that the relaxation proceeded at a greater rate at lower pressure. Since the relaxation curves for polymethyl methacrylate had been found to be reproducible at atmospheric pressure, it was not necessary to have an individual reference specimen for each test, as with allyl diglycol carbonate.

All these experiments on both plastics were conducted at a temperature of 24 °C.

6. Calculation of Relative Mobilities

In studying the relaxation of each amorphous solid,

an empirical relationship between the variables was sought for greater convenience in handling the data. It was found that the data could be fitted very well to the equation

$$\frac{d\phi}{dt}=-A\phi^4 \tag{1}$$

where ϕ represents the phase lag in a specimen, t represents the time, and A is a constant for a given temperature and pressure. Integrating equation (1) one obtains

$$\frac{1}{\phi^3}-\frac{1}{\phi_0^3}=3At, \tag{2}$$

ϕ_0 being the initial phase lag in the specimen. It can be seen that by plotting the reciprocal cubed of phase lag versus time that a straight line results. Furthermore, knowing the time and amount of phase lag in the specimen when it was put into the pressure bomb, and the time and amount of phase lag when it was removed, it was possible to infer the rate of the relaxation under pressure. This is shown in figure 2 for allyl diglycol carbonate subjected to a pressure of 1,000 bars.

It was assumed that the constant, $3A$, was a measure of the tendency to flow in the material, or of its mobility in the most general sense. The ratio of the slopes of the two straight lines shown in figure 2 was taken as an expression of the mobility at elevated pressure relative to the mobility at atmospheric pressure; i.e., the relative mobility was taken as A_p/A_0 where $3A_0$ and $3A_p$ are respectively the slopes at atmospheric pressure and at elevated pressure. The data for each experiment were treated in this manner, and relative mobilities were calculated in each case.

7. A New Experimental Method

There were several objections to making measurements in the foregoing manner: (1) Only a rough estimate could be made of the time that a specimen was affected by the pressure, because 10 min would elapse in bringing the bomb up to pressure, and about the same time would elapse in releasing the pressure; (2) it was known that there was a temperature rise due to adiabatic compression, and a lowering of temperature due to adiabatic expansion; (3) one could see that the fourth power relationship for the relaxation (eq 1) held at atmospheric pressure, but there was no assurance that the same law applied while a specimen was under pressure.

These considerations made it desirable to observe the relaxation while a specimen was under pressure. Fortunately, for this purpose, it was possible to utilize a pressure vessel equipped with glass windows [3] [8]. The windows were supported by hardened stainless steel plugs, the contacting faces being ground optically flat. The combination of window and supporting steel plug made a Bridgman seal [9] according to a design proposed by Poulter [10]. The vessel was capable of supporting pressures up to 1,500 bars, and had been built with a surrounding oil bath for temperature control.

In order to observe relaxation under pressure, the polarimeter of Goranson and Adams was disassembled and remounted on a large optical bench. The pressure vessel was placed at such a position in the optical train that it enclosed the specimen. As a safety measure against possible failure of the window, a total reflection prism was placed in the optical train immediately after the specimen, so that the light beam was turned through 90°. The light beam then passed through the quarter-wave plate and analyzer which were placed at right angles to the rest of the optical train (fig. 3). With this arrangement, the reflection of the polarized light had no effect upon the measurement of phase lag in the specimen beyond changing the zero point in taking readings.

Photoelastic effects caused by hydrostatic pressure were observed in the glass windows of the vessel, and these effects increased in magnitude with increasing pressure. A black cross typical of a radial distribution of stress appeared when the windows were examined between crossed polaroids with white light. With the aid of a sensitive red tint plate,

[3] This pressure vessel was kindly loaned by Dr. R. E. Gibson, Director of the Applied Physics Laboratory of the Johns Hopkins University.

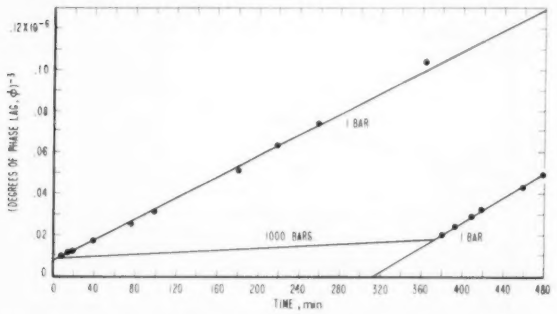

FIGURE 2. *The reciprocal cubed of phase lag in allyl diglycol carbonate as a function of time, showing the effect of a hydrostatic pressure of 1,000 bars in comparison with that of 1 bar, the plot at 1,000 bars being inferred.*

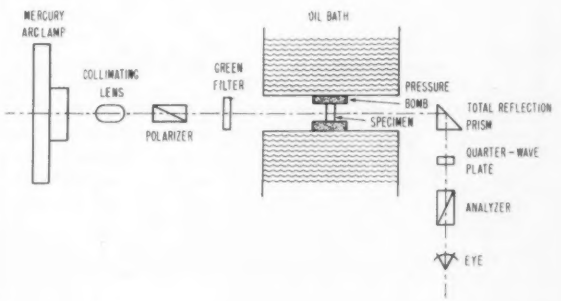

FIGURE 3. *Arrangement of optical system to measure optical path-difference.*

it was estimated that at a pressure of 1,000 bars, the optical path-difference varied from zero at the center of the aperture to about 50 $m\mu$ at the edge. This maximum was reduced to about 25 $m\mu$ by placing a diaphragm at the window. Using the polarimeter with monochromatic light produced an integrated effect of this variation so that it was slightly more difficult to make a photometric match at the higher pressures.

The pressure in the bomb was measured by means of a calibrated Bourdon gage to the nearest 7 bars. A mercury contact thermoregulator held the temperature in the oil bath surrounding the bomb to within ± 0.02 °C.

Measurements were then made of relaxation while a specimen was under hydrostatic pressure, and the results of a typical experiment are shown in figure 4. The specimen was first allowed to relax at atmospheric pressure for a period of 120 min, and then the hydrostatic pressure was applied and held for a period of 240 min.

The reciprocal cubed of phase lag was plotted against time in minutes and it can be seen from figure 4 that the fourth power relationship for relaxation (1) really holds at elevated pressure. The irregularities in the points immediately after changes in pressure are attributable to associated, adiabatic temperature changes. The slope of the straight line which represents the parameter, $3A_p$, was found, therefore, from direct measurements rather than by determining the slope by inference, as had been done before a pressure bomb with windows was available. The parameter, $3A_0$, was found from the slope of the straight line in the first, 120-min period, when the specimen was at atmospheric pressure, and the relative mobility was calculated.

Experiments at 24 °C were conducted on allyl diglycol carbonate at pressures of 162, 430, and 869 bars. Relative mobilities were calculated and these data were combined with data obtained by the old method of estimating the relaxation under pressure (see fig. 2). The relative mobilities versus pressure at 24 °C are shown in figure 5 for both allyl diglycol carbonate and polymethyl methacrylate.

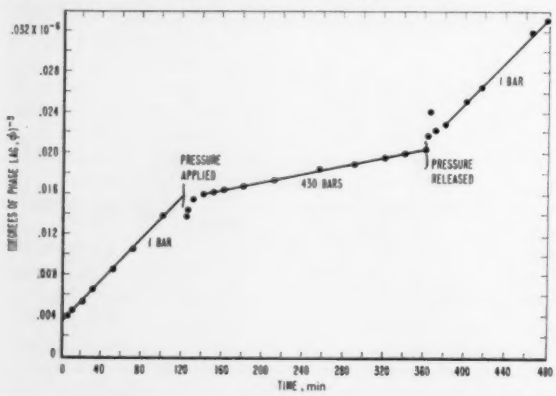

FIGURE 4. *The reciprocal cubed of phase lag in allyl diglycol carbonate as a function of time, showing the effect of a hydrostatic pressure of 430 bars in comparison with that of 1 bar.*

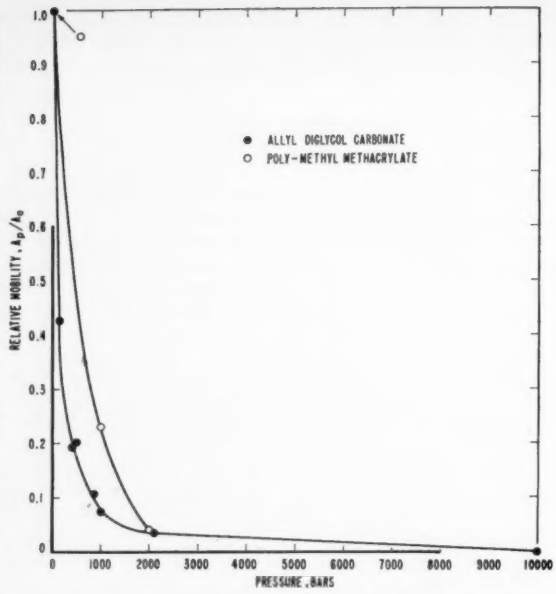

FIGURE 5. *Relative mobility as a function of pressure at 24 °C.*

8. Effect of Temperature

In order to gain some conception of the relative effects of temperature and pressure upon the relaxation of allyl diglycol carbonate, additional experiments were conducted at 20 °C and 30 °C. The observations were made, as nearly as possible, at pressures of 200, 500, and 1,000 bars, a freshly cut specimen being used each time. When relative mobilities were calculated from the data, it was found that a straight line represented the relationship 1/(relative mobility) versus pressure at a given temperature, and this is shown in figure 6. The data for all the relative mobilities resulting from change in pressure are given in table 1.

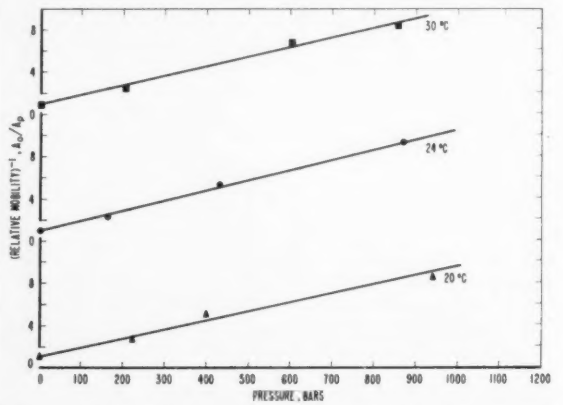

FIGURE 6. *(Relative mobility)$^{-1}$ in allyl diglycol carbonate as a function of pressure at 3 temperatures.*

TABLE 1. *Dependence of relative mobility upon pressure at constant temperature*

Material	Temperature	Pressure bars	Relative mobility A_p/A_0
	°C		
Allyl diglycol carbonate	20	1	1.000
		223	0.357
		397	.198
		941	.115
	24	1	1.000
		162	0.427
		430	.193
		500	.203
		869	.107
		1,000	.0746
		2,100	.0364
		10,000	0.0
	30	1	1.000
		204	0.405
		601	.145
		855	.117
Polymethyl methacrylate	24	1	1.000
		1,000	0.230
		2,000	.0403

One experiment was conducted at atmospheric pressure to determine the value of 3 A for the same specimen of allyl diglycol carbonate at 20, 24, and 30 °C. Using the slope of the straight line at 20 °C as a basis, relative mobilities were determined, and they appeared to vary exponentially with temperature according to the equation

$$\text{Log}\,\frac{A_\theta}{A_{20}}=0.106\,\theta-2.120 \qquad (3)$$

where A_θ is the mobility at the given temperature, θ, and A_{20} is the mobility at 20 °C. This relationship is shown in figure 7, and the data are shown in table 2.

9. Discussion

As can be seen in figure 5, the flow in amorphous solids is very sensitive to the effect of hydrostatic pressure and even the comparatively low pressure of 162 bars is sufficient to reduce the relative mobility of allyl diglycol carbonate to less than half its value at atmospheric pressure. The effect becomes less pronounced at higher pressures, but a pressure of 10,000 bars is sufficient to inhibit the flow completely. The effect in polymethyl methacrylate is comparable, but not as great as in allyl diglycol carbonate.

At pressures below 1,000 bars a linear relationship appears to hold for 1/(relative mobility) versus pressure for allyl diglycol carbonate as shown in figure 6. At higher pressures the relationship ceases to be linear and, as the pressure increases, 1/(relative mobility) increases rapidly. Since the slopes of the straight lines in figure 6 are nearly the same, it appears that the pressure dependence of 1/(relative mobility) is not affected by temperature, at least not over the range of pressure and temperature investigated.

If this variable, 1/(relative mobility), or relative resistance to flow is considered, it is interesting to compare the results of the present investigation with

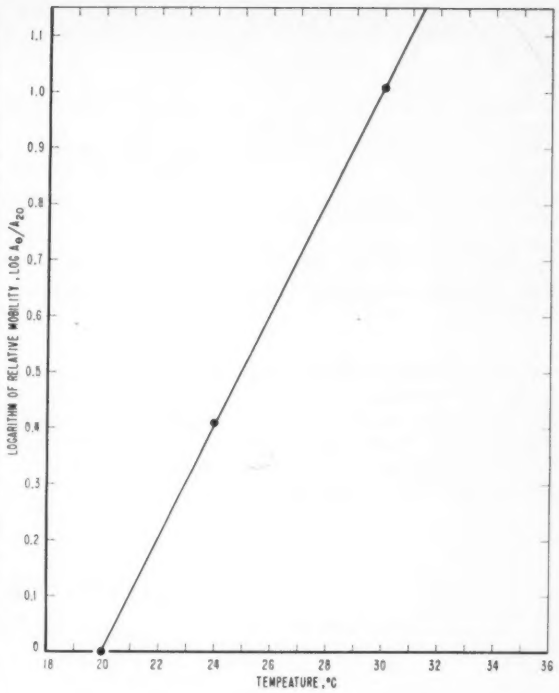

FIGURE 7. *Effect of temperature upon the relative mobility of allyl diglycol carbonate at atmospheric pressure.*

TABLE 2. *Dependence of relative mobility upon temperature at atmospheric pressure*

Material	Pressure bars	Temperature	Relative mobility A_θ/A_{20}	Logarithm of relative mobility Log A_θ/A_{20}
		°C		
Allyl diglycol carbonate	1	20	1.0	0.0
		24	2.56	.409
		30	11.49	1.060

those of Bridgman [9] in his work on the viscosity of liquids under pressure. Bridgman points out that the viscosity of a liquid increases with pressure at a rapidly increasing rate. He also shows that the relative change of viscosity with temperature becomes markedly greater at high pressure, whereas most temperature effects become less at high pressures. Bridgman comments on the large magnitude of the pressure effect, and the large variation from liquid to liquid, and these observations apply generally to all the liquids studied, although water is somewhat abnormal in its behavior, and shows the effect of association at low temperatures and pressures.

From Bridgman's tabulated data it can be seen that oleic acid showed an increase of fourfold in relative viscosity upon increasing the pressure from

1 bar to 1,000 bars at 30 °C. Allyl diglycol carbonate showed a ninefold increase in relative resistance to flow for the same pressure change at the same temperature. Of all the liquids investigated by Bridgman, oleic acid showed the greatest pressure dependence of relative viscosity for pressures up to 1,000 bars. Eugenol showed the greatest pressure dependence up to 12,000 bars, and Bridgman calculated that this increase of pressure at 30 °C would increase the relative viscosity by 10^7. Although measurements were made at a slightly lower temperature (24 °C), the relative resistance to flow of allyl diglycol carbonate became infinitely great at 10,000 bars.

The authors thank Charles E. Weir of the National Bureau of Standards for his advice and material assistance in conducting the experiments. The authors also thank the members of the Bureau's Structural Engineering Section for their cooperation and the use of their equipment.

(Paper 65A4–112)

10. References

[1] L. H. Adams and E. D. Williamson, The annealing of glass, J. Franklin Inst. **190,** 597, 835 (1920).
[2] H. R. Lillie, Stress release in glass a phenomenon involving viscosity as a variable with time, J. Am. Ceram. Soc. **19,** 45 (1936).
[3] J. O. Isard and R. W. Douglas, The relaxation of stress in fused silica. Part I. Experimental., J. Soc. Glass Tech. **39,** 61 T. (1955). Part II. Theoretical., J. Soc. Glass Tech. **39,** 83 T. (1955).
[4] R. W. Goranson and L. H. Adams, A method for the precise measurement of optical path-difference especially in stressed glass, J. Franklin Inst. **216,** 475 (1933).
[5] Charles E. Weir, High-pressure apparatus for compressibility studies and its application to measurements on leather and collagen, J. Research NBS **45,** 6 (1950) RP 2160.
[6] E. G. Coker and L. N. G. Filon, A treatise on photoelasticity, pp. 263, 267, 275 (Univ. Press, Cambridge, 1931).
[7] Roy M. Waxler and Albert Napolitano, Relative stress-optical coefficients of some National Bureau of Standards optical glasses, J. Research NBS **59,** 2 (1957) RP 2779.
[8] R. E. Gibson, The compressions of certain salts in water, glycol and methanol, J. Am. Chem. Soc. **59,** 1521 (1937).
[9] P. W. Bridgman, The physics of high pressure, pp. 32, 330 (G. Bell and Sons, Ltd., London, 1931).
[10] T. C. Poulter, Apparatus for optical studies at high pressure, Phys. Rev. **40,** 860 (1932).

JOURNAL OF RESEARCH of the National Bureau of Standards—A. Physics and Chemistry
Vol. 65A, No. 4, July–August 1961

Vapor Pressures of Platinum, Iridium, and Rhodium

R. F. Hampson, Jr., and R. F. Walker

(April 4, 1961)

The vapor pressures of platinum, iridium, and rhodium have been measured using a microbalance technique based on the Langmuir method. Heats of sublimation at 298 °K were calculated with the aid of free energy functions. The least square lines for the vapor pressure data, the heats of sublimation, and the normal boiling points obtained were as follows:

(1) Platinum:

$$\text{Log } P_{\text{atm}} = 6.761 - \frac{27{,}575}{T} \qquad (1{,}916 \text{ to } 2{,}042 \text{ °K})$$

$$\Delta H_s^\circ(298) = 134.9 \pm 1.0 \text{ kcal/mole}$$

$$\text{bp} = 4{,}100 \pm 100 \text{ °K}$$

(2) Iridium:

$$\text{Log } P_{\text{atm}} = 7.139 - \frac{33{,}337}{T} \qquad (1{,}986 \text{ to } 2{,}260 \text{ °K})$$

$$\Delta H_s^\circ(298) = 159.9 \pm 2.0 \text{ kcal/mole}$$

$$\text{bp} = 4{,}800 \pm 100 \text{ °K}$$

(3) Rhodium:

$$\text{Log } P_{\text{atm}} = 6.894 - \frac{27{,}276}{T} \qquad (1{,}709 \text{ to } 2{,}075 \text{ °K})$$

$$\Delta H_s^\circ(298) = 132.5 \pm 2.0 \text{ kcal/mole}$$

$$\text{bp} = 4{,}000 \pm 100 \text{ °K}.$$

The indicated uncertainties are estimates of the overall limits of error. The value of the gas constant R used in the calculation of ΔH_s° is 1.98726 cal/degree mole.

1. Introduction

Systematic measurements of the vapor pressure of iridium and rhodium over a wide temperature range have not been published previously. A summary of previous estimates or observations of their normal boiling points and values of their heats of sublimation, $\Delta H_s^\circ(298)$, is given in table 1.

The vapor pressure of platinum was calculated by Langmuir and Mackay from measurements of the rate of sublimation in vacuum [5].[1] Subsequently, Jones, Langmuir, and Mackay [6] adjusted these data in accordance with a revised temperature scale. Stull and Sinke used tabulated thermal functions and the adjusted data to calculate a $\Delta H_s^\circ(298)$ of 134.8 kcal/mole and a boiling point of 4,100 °K [4].

Simultaneously with the present investigation, Dreger and Margrave [7] at the University of Wisconsin and Hasapis, Panish and Rosen [8] at the AVCO Corp., Wilmington, Mass., have been measuring vapor pressures of the pertinent substances.

Dreger and Margrave measured rates of sublimation of iridium, rhodium, and platinum samples suspended in a graphite tube furnace. Their data for iridium and rhodium as reported are subject to an additional correction and will not, therefore, be quoted in detail. The data on platinum have just been published [9]. Over the temperature range of 1,571 to 1,786 °K, the vapor pressure of the solid platinum was given by: $\log P_{\text{mm}} = 10.362 - \frac{29{,}100}{T}$, which leads to a normal boiling point of 4,100 ± 100 °K. The mean $\Delta H_s^\circ(298)$ was 135.2 kcal/mole, with a mean deviation of 0.85 kcal/mole.

TABLE 1. *Summary of published data on volatilization of iridium and rhodium*

Substance	Normal boiling point	$\Delta H_s^\circ(298)$	Reference
	°K	kcal/mole	
Iridium	4673	----	Mott [1].
	5573	----	Richardson [2].
	4800	165	Brewer [3].
	4400	150	Stull, Sinke [4].
Rhodium	4273	----	Mott [1].
	4773	----	Richardson [2].
	4150	138	Brewer [3].
	4000	133	Stull, Sinke [4].

[1] Figures in brackets indicate the literature references at the end of this paper.

Hasapis, Panish, and Rosen have given preliminary data on the vapor pressure of iridium over the temperature range 2,100 to 2,600 °K. A thoria effusion cell was used for these measurements, and the slope of a Clausius-Clapeyron plot of the data yielded a tentative ΔH_s° of 155 ± 5 kcal/mole over this range of measurement. More recently, Panish and Reif have made measurements of the rates of sublimation of iridium and have used the effusion method to obtain rhodium vapor pressures [10]. For iridium they give ΔH_s° (298) = 158.4 kcal/mole with a mean deviation of 0.4 kcal/mole and an estimated boiling point of 4,800 °K. The corresponding values for rhodium are 132.8 and 0.3 kcal/mole and 3,980 °K.

In all the foregoing measurements it was assumed that the substances sublime to monatomic gaseous species. It was further assumed that the coefficients of sublimation are unity, when calculating vapor pressures from the rate measurements. The lack of agreement among different observations or measurements may be broadly attributed to differences and uncertainties in the experimental techniques.

2. Experimental Technique

The experimental technique used in the current investigation was based on the Langmuir method for determining the equilibrium vapor pressure (P) from measurements of the rate of sublimation (m) at absolute temperature T, in accordance with the equation:

$$P = \left(\frac{m}{\alpha}\right)\sqrt{\frac{2\pi RT}{M}}.$$

The rate of sublimation was measured in terms of the mass of material leaving unit area of the subliming surface per unit of time, in vacuum. A value of unity has been adopted for the coefficient of sublimation (α) for all calculations of vapor pressures. However, as discussed later, it is probable that this represented an upper limiting value that was not always appropriate under the experimental conditions.[2] It has also been assumed that the appropriate value of the molecular weight of the vapor species (M) is that of the monomeric species. Actual vapor pressures would be somewhat lower than calculated, if polymeric vapor species were involved.

2.1. Apparatus

The apparatus used has been described in some detail previously [11, 12]. Briefly, the sample was suspended from an equi-arm, quartz beam microbalance into a water-cooled, glass furnace chamber and heated by induction. The microbalance had a sensitivity of about 1 μg. The sample was attached to the balance by drilling a narrow (0.010 in. diam) hole through the sample and looping a short length of fine (0.002 in. diam) wire of the same substance through the hole. The loop was then placed over a hook on the balance suspension, which consisted of a chain of 0.010 in. diam sapphire rods. The presence of the hole and the loop (which was not heated significantly by the induction field) was ignored when calculating the effective surface area of the load.

The radiofrequency induction field from an external coil was concentrated in the region of the sample with the aid of a water-cooled, copper concentrator held within the furnace chamber. The concentrator had a vertical, uniform bore, ½ in. diam x 1½ in. long, into which the sample was suspended. Water-cooled copper, therefore, enclosed the sample throughout each run, except for the open ends of the bore.

The furnace chamber and the microbalance housing were continuously pumped throughout each run with a liquid-nitrogen-trapped, oil diffusion pump. Pressures within the system were measured with an ionization gauge attached at the vacuum port of the furnace chamber.

2.2. Samples

The samples consisted of short rods, approximately ¾ in. long x 0.085 in. diam, and were suspended with their axes vertical. The surface areas at the run temperatures were determined by correcting the room temperature areas of about 1.3 cm^2 using literature values for the thermal expansion coefficients. No corrections were applied for the slight change in surface area of each sample due to sublimation. Assuming each sample sublimed uniformly over its surface area, the error introduced by neglecting the change in surface area was less than 0.3 percent.

The purity of the samples was estimated from general qualitative spectrochemical analyses. The iridium sample was estimated to be at least 99.99 percent pure, the only major impurity being Rh at the 0.001 to 0.01 percent level; traces of Al, Fe, and Pd, in amounts less than 0.001 percent, were the only other elements detected in the sample. Estimated impurities in the rhodium sample were: Fe, Ir, Pd, Pt, 0.1 to 1 percent; Al, Ca, Cr, Cu, Ni, Ru, 0.01 to 0.1 percent; and B, Si, Ti 0.001 to 0.01 percent. It may have contained less than 98 percent rhodium. Pd, Ir, Rh, at the 0.01 to 0.1 percent level, were the major impurities in the platinum sample. Cu and Fe were each estimated to be in the range 0.001 to 0.01 percent and Ag as less than 0.001 percent. The platinum sample was, therefore, probably better than 99.7 percent purity.

2.3. Procedure

The microbalance was used as a deflection instrument, deflections of its beam being directly proportional to changes in mass of the sample. Beam deflections were measured with a cathetometer readable to 1 μ displacement. The microbalance was calibrated, with each sample *in situ*, using Class M microbalance weights previously calibrated by the Mass Section of NBS.

Interaction between the rf field and the sample caused the balance to be deflected increasingly as the output of the rf generator was increased. By start-

[2] It is often the case that the effects of α varying within the limits 0.5 and 1.0 would not be detected in the course of measurements, due to the imprecision of our knowledge of such factors as temperature differences.

ing with the sample close to the center of the bore in the concentrator in a vertical direction, the deflection could be reduced to a minimum; however, a continuous record of the change in mass of the sample was still not obtainable with reliability. The balance was, therefore, first read with the sample at room temperature. The sample was then heated rapidly according to a predetermined schedule, held at constant temperature for a given period of time, then cooled rapidly. When the sample had returned to room temperature, the balance was then read again to obtain the total mass change during the course of each run.

The procedure adopted raises a question as to the extent to which mass changes occurring during heating and cooling contributed to the total observed mass change. The variation of vapor pressures with temperature was such that the mass-loss rates occurring 50 to 100 °K below the constant temperature were generally of the order of 1 percent of that occurring at the constant temperature. On heating, the last 300 to 400 °K of the temperature rise was accomplished in less than 15 sec. The relatively low-heat content of the hot system also resulted in an even more rapid rate of cooling over the first few hundred degrees when the power was turned off. Thus, even though a sample was held at a constant temperature for a period as short as ½ min, the observed mass change could be attributed entirely to the constant temperature period without introducing gross errors. In fact, no systematic decrease in the scatter of the data was detected as the length of runs increased from ½ min to 3 hr.

For each substance the duration of the runs was increased from about 1 min at the highest temperatures to about 2 or 3 hr at the lowest temperatures, to yield weight losses of about 100 micrograms. The uncertainty in the measurement of the weight loss during each run was less than ±2 percent.

No special procedure was used to clean the samples after handling. It was assumed that outgassing and cleanup of the surface would occur during the first few runs and that, if there were significant surface contamination, the data would appear to be sufficiently anomalous to justify their rejection. Samples were not normally exposed to atmospheric pressure between runs. Due consideration was given to possible recontamination of the surface whenever it became necessary to open up the evacuated system to add a tare weight to the balance or to examine the sample.

Pressures within the system were in the range 2×10^{-6} to 8×10^{-5} mm Hg throughout each run. Due to outgassing, pressures tended to rise to the upper portion of this range during the first runs after the system was exposed to atmosphere pressure. Subsequent runs yielded successively lower maximum pressures. No trends in the data with changes of pressure in the system were detected.

2.4. Temperature Measurement and Control

Brightness temperatures were measured by sighting with an optical pyrometer having an effective wavelength of about 0.660 to 0.665 μ, about midway down the length of the sample. Pyrometer readings were corrected by comparing the scale of the pyrometer with that of a similar pyrometer calibrated on the International Temperature Scale by the Temperature Physics Section of NBS. A correction was then applied for the absorption by a window in the furnace chamber.

The angle of sighting was 75° to the normal; separate calibrations were, therefore, also obtained for each sample to correct brightness temperatures for the angle of sighting. These calibrations were undertaken as the samples were heated in air. Under these conditions the rhodium sample appeared to acquire and retain an oxide coating throughout the pertinent temperature range, and the sign of the temperature correction was characteristic of a nonmetal rather than of a metal. Consequently, the corrections obtained for the platinum sample were also applied to the rhodium sample, and an additional uncertainty of ±5 °C was assigned to the final brightness temperatures of the rhodium.

Corrected brightness temperatures were converted to thermodynamic temperatures with the aid of literature values for the normal spectral emissivities, $\epsilon\lambda$, at the wavelength, λ, given by the respective authors.

Stephens [13] gives values for the emissivity of platinum for $\lambda=0.660$ μ. An extrapolation of his data yields values of ϵ_λ increasing linearly from 0.293 at 1,700 °K to 0.300 at 2,050 °K. The data of Worthing [14] have approximately the same temperature dependence, but are significantly higher, yielding (when extrapolated) ϵ_λ rising from 0.307 at 1,700 °K to 0.315 at 2,050 °K ($\lambda=0.665$ μ). A check on the appropriate values to be used in the present work was made by observing the brightness temperature at the onset of surface melting of the platinum sample under the experimental conditions. The results of the observations are summarized in table 2. Using $\lambda=0.660$ μ, a value of $\epsilon_\lambda=0.308$ was calculated from these observations and the known melting point of platinum. A temperature dependence was assigned to this value, yielding a normal emissivity rising linearly from 0.304 at 1,850 °K to 0.308 at 2,050 °K. These values are about the mean of those given by Stephens and Worthing, and have been used in the present work.

TABLE 2. *Observations of melting point of platinum under experimental conditions* ($\epsilon_\lambda=0.308$)

Brightness temperature	Thermodynamic temperature	Evidence of surface melting
°C	°K	
1567±5	2043	Not melted.
1575±5	2053	Melted.
1570±5	2047	Possibly melted slightly; evidence masked by preceding run.
1562±5	2037	Not melted.
1562±5	2037	Not melted.
1565±5	2041	Partially melted.
	2042±1	Accepted melting point of Pt.

The emissivities of iridium and rhodium are not well established; in particular, no data for the dependence of their emissivities on temperature are available. An additional uncertainty, upon which it is not possible to place close limits, is, therefore, involved in the temperatures of these substances. Goldwater and Danforth [15] found the mean spectral emissivity of iridium to be 0.33 (λ=0.65 μ) for measurements over the 1,000 to 1,750 °C range. Whitney [16] observed the emissivity of rhodium to increase with temperature over the range 1,700 to 2,200 °K, for a sample subjected to only limited heat treatment. However, after 700 hr of heat treatment a constant value of ϵ_λ=0.242 (λ=0.667 μ) was obtained for the entire range of 1,300 to 2,000 °K.

The foregoing values of ϵ_λ have been used to obtain the thermodynamic temperatures of iridium and rhodium in the present work.

Constant temperatures were maintained to within ±5 °C or better by manual control of the output of the rf generator. No significant temperature gradients could be observed down the length of samples. Sightings on the top or upper end of the rod as suspended gave temperatures which were consistent with those observed down the length when the different angle of sighting was taken into consideration (the angle was about 15° to the normal for the top of the sample).

3. Results and Discussion

3.1. Platinum

In table 3 are given the vapor pressures calculated from measurements of the rate of mass loss of platinum and the corresponding values of $\Delta H_s^\circ(298)$ calculated using the free energy functions of Stull and Sinke [4].

An original purpose of the measurements with platinum was to check the apparatus and technique using a substance whose vapor pressures had been previously measured. It was unfortunate, therefore, that the data obtained for this substance showed the least internal consistency. Several runs yielded unexpectedly low rates of sublimation. As indicated in table 3, some of the rates were too low to detect significant mass losses during the period of the runs; other low rates were measurable, but scattered and have been rejected as being clearly inconsistent with the bulk of the data. The rejected data have been marked with an asterisk in table 3. As far as could be ascertained, the anomalous data were not due to any misbehavior of the balance or of other components of the apparatus. They occurred below some critical temperature, which apparently increased with more extensive heat-treatment at higher temperatures. During the course of one run in which the sample was vaporizing at a very low rate, the temperature was raised rapidly just a few degrees, and the "normal" rate of sublimation was immediately restored for the remainder of the run.

It has not yet been possible to identify the cause of the low rates of sublimation. The two most likely possibilities are contamination of the surface of the sample either from its surroundings or by migration of impurities to the surface of the sample, and significant changes in the crystal structure of the sample with progressive heat treatment. Nevertheless, the results suggest that platinum may acquire a coefficient of sublimation considerably less than unity under the experimental conditions.

Apart from the anomalous data discussed, the remainder of the data had sufficient internal consistency to justify their acceptance. These data are compared with the results of Jones, Langmuir, and Mackay, and of Dreger and Margrave in figure 1. The first two runs shown in table 3 have been rejected because they were the initial runs, and because the values of $\Delta H_s^\circ(298)$ differed significantly from the mean of the accepted runs. Nevertheless, they yield values of $\Delta H_s^\circ(298)$ which are within the range of those of Dreger and Margrave, obtained in the same low temperature region. Furthermore, their data also have more than the usual amount of scatter in this region. Using free-energy functions, the data of Jones et al., yield heats of sublimation which show a slight increase with temperature, from which we calculate a mean $\Delta H_s^\circ(298)$ of 134.6 kcal/mole. Nevertheless, it is interesting to note that the three sets of measurements lead to mean heats which agree within the limits of experimental error.

TABLE 3. *Vapor pressures and heats of sublimation of platinum*

Temperature	Duration of run	Weight loss	Vapor pressure	$\Delta H_s^\circ(298)$
°K	min	μg	mm Hg	kcal/mole
1710	130	37	1.68×10^{-7}	*136.3
1822	36	103	1.74×10^{-6}	*136.6
1764	85			
2043	10	1798	1.16×10^{-4}	135.8
1990	2	214	6.85×10^{-5}	134.4
1962	2	126	3.99×10^{-5}	134.7
1926	3	92	1.93×10^{-5}	135.0
1916	6	198	2.07×10^{-5}	134.1
1917	25	75	1.88×10^{-6}	*143.3
1909	30	23	4.74×10^{-7}	*147.9
1917	28	20	4.44×10^{-7}	*148.8
1842	29			
1955	4	215	3.41×10^{-5}	134.8
1928	10			
1968	4	244	3.88×10^{-5}	135.2
1951	5			
1980	2	158	5.03×10^{-5}	134.9
1949	20			
1970	7	25	2.24×10^{-6}	*146.5
1976	4.5	68	9.58×10^{-6}	*141.2
1986	3.5	276	5.03×10^{-5}	135.4
2000	2	231	7.39×10^{-5}	134.8
2025	2	269	8.68×10^{-5}	135.8
2034	2	374	1.21×10^{-4}	135.0
2053	.5	174	2.25×10^{-4}	**133.7
2047	1	267	1.73×10^{-4}	134.4
2037	1	205	1.32×10^{-4}	134.9
2037	1	206	1.33×10^{-4}	134.8
2023	1	178	1.15×10^{-4}	134.5
2016	1	170	1.09×10^{-4}	134.3
2003	1	109	6.98×10^{-5}	135.2
Mean $\Delta H_s^\circ(298)$				134.9
Standard deviation				0.5

Data are presented in experimental sequence, a dashed entry indicating that no significant weight loss was detected during a run.
*Rejected.
**Sample partially melted; data rejected.

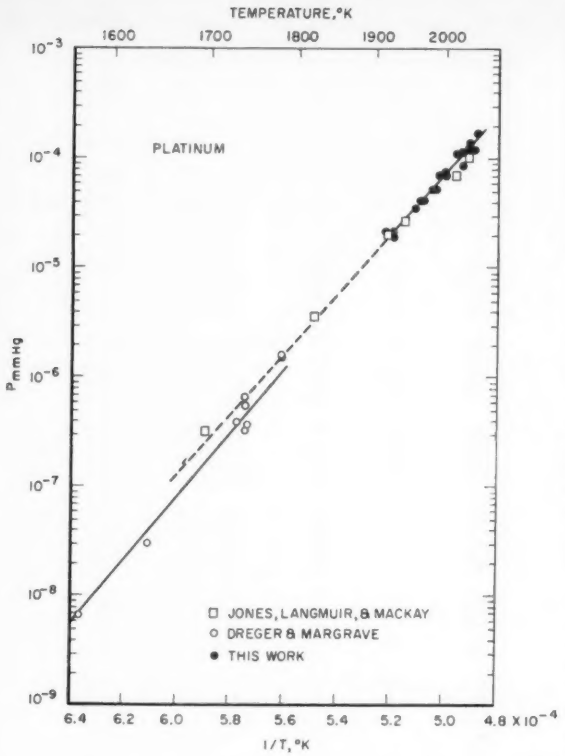

FIGURE 1. *Vapor pressure of platinum versus reciprocal of absolute temperature, for different investigators.*

The least-squares line representing this work is shown extrapolated with a broken line. The other line is that given by Dreger and Margrave.

The overall limits of error of the absolute value of $\Delta H_s^\circ(298)$ were estimated by taking into account the scatter of the data, the uncertainty in the temperature ($\pm 10°$ K), and the uncertainty in the weight-loss measurements. No allowance was made for the uncertainty in the free-energy functions or in the sublimation coefficient. The overall limits of error of the absolute value were estimated to be ± 1.0 kcal/mole. The corresponding overall limits of error of the vapor pressures are about ± 25 percent.

The mean "third law" value of ΔH_s° (298) from table 4 is 134.9 ± 1.0 kcal/mole, from which we estimate a normal boiling point of 4,100 ± 100 °K by extrapolating Stull and Sinke's tables. The least-squares line through the accepted data for the temperature range 1,916 °K to the melting point is given by:

$$\text{Log } P_{atm} = 6.761 - \frac{27{,}575}{T}$$

or

$$\text{Log } P_{mm} = 9.642 - \frac{27{,}575}{T}.$$

This line is drawn in figure 1.

3.2. Iridium

Iridium vapor pressures and the corresponding values of ΔH_s° (298) calculated from tabulated free energy functions [4] are given in table 4.

TABLE 4.—*Vapor pressures and heats of sublimation of iridium*

Temperature **	Duration of run	Weight loss	Vapor pressure	ΔH_s° (298)
°K	min	μg	mm Hg	kcal/mole
1964	1	60	3.98×10^{-4}	*136.6
1990	1	11	7.11×10^{-6}	*145.2
2029	1	4	2.94×10^{-6}	*151.5
2059	1	1	3.28×10^{-7}	*162.7
2134	1	4	3.00×10^{-6}	*159.1
2185	1	9	6.08×10^{-6}	159.8
2016	22	8	2.29×10^{-7}	160.8
2077	75	3	3.07×10^{-8}	*173.9
2190	12	108	6.26×10^{-6}	160.1
2190	13	109	5.80×10^{-6}	160.4
2260	9	192	1.50×10^{-5}	161.1
2257	12	277	1.62×10^{-5}	160.6
2211	9	110	8.48×10^{-6}	160.2
2179	12	103	5.96×10^{-6}	159.5
2249	8	172	1.51×10^{-5}	160.3
2190	11	120	7.59×10^{-6}	159.2
2178	10	88	6.11×10^{-6}	159.3
2161	10	62	4.30×10^{-6}	159.6
2150	30	142	3.26×10^{-6}	160.0
2160	20	108	3.71×10^{-6}	160.2
2130	40	131	2.23×10^{-6}	160.1
2121	45	130	1.98×10^{-6}	160.0
2120	42	127	2.06×10^{-6}	159.7
2088	58	105	1.23×10^{-6}	159.5
2060	50	54	7.28×10^{-7}	159.5
2021	90	46	3.44×10^{-7}	159.6
1986	180	48	1.78×10^{-7}	159.5
Mean ΔH_s° (298)				159.9
Standard deviation				0.5

Data are presented in experimental sequence.
*Rejected.
**Emissivity, ϵ_λ, assumed to be 0.33 at $\lambda = 0.65\mu$.

The iridium data had the best internal consistency, and this may have been a result of the greater purity of the sample. The results of the first four runs in table 4 were partially attributed to the cleanup of the sample and were rejected. Barely significant mass changes were recorded during the period of the fifth and eighth runs, and the results of these runs were also rejected.

The overall limits of error of the absolute value of ΔH_s° (298) were estimated by taking into account the scatter of the data, the uncertainty in the temperature (± 25 °K), and the uncertainty in the weight-loss measurements. No allowance was made for the uncertainty in the free-energy functions or in the sublimation coefficient. The overall limits of error of the absolute value were estimated to be ± 2.0 kcal/mole. The corresponding overall limits of error of the vapor pressures are about ± 60 percent.

In figure 2 the accepted experimental data are plotted, and the least-squares line for the data is shown. The equation of the line, which applies to the temperature range 1,986 to 2,260 °K, is:

$$\text{Log } P_{\text{atm}} = 7.139 - \frac{33{,}337}{T}$$

or

$$\text{Log } P_{\text{mm}} = 10.02\,) - \frac{33{,}337}{T}.$$

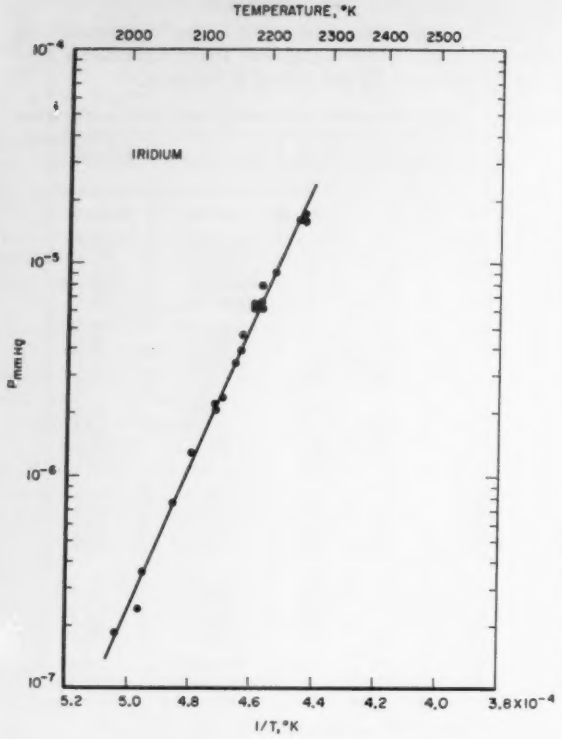

FIGURE 2. *Vapor pressure of iridium versus reciprocal of absolute temperature.*

The mean $\Delta H_s^\circ(298)$ is 159.9 ± 2.0 kcal/mole from which a boiling point of $4{,}800 \pm 100$ °K is estimated. These results are in agreement with those of Panish and Reif [10] within the limits of experimental error.

3.3. Rhodium

Rhodium vapor pressures and the heats of sublimation based on Stull and Sinke's tabulated free energy functions [4] are given in table 5. The vapor pressures over the range 1,709 to 2,075 °K are plotted in figure 3, together with the least-squares line through the experimental points.

The rhodium data had more general scatter than the iridium; in particular, some of the earlier runs (see table 5) yielded lower heats of sublimation than were obtained towards the end of the sequence of runs, over the same temperature range. It is possible that the more volatile impurities in the sample were contributing to the scatter, but the deviations of the experimental points from their mean did not justify the rejection of any of the data. During a long sequence of runs on the same sample, the surface becomes thermally etched, leading to an increase in the emissivity. Such an effect would also contribute to an apparent increase in the heats of sublimation as the sequence progressed.

The mean ΔH_s° (298) is 132.5 ± 2.0 kcal/mole from which a normal boiling point of $4{,}000 \pm 100$ °K is estimated. The least squares fit to the data is given by:

$$\text{Log } P_{\text{atm}} = 6.894 - \frac{27{,}276}{T}$$

or

$$\text{Log } P_{\text{mm}} = 9.775 - \frac{27{,}276}{T}.$$

The mean heat of sublimation agrees with that of Panish and Reif within the limits of experimental error.

The overall limits of error of the absolute value of ΔH_s° (298) were estimated by taking into account the scatter of the data, the uncertainty in the temperature (± 20 °K), and the uncertainty in the weight-loss measurements. No allowance was made for the uncertainty in the free-energy functions or in the sublimation coefficient. The overall limits of error of the absolute value were estimated to be ± 2.0 kcal/mole. The corresponding overall limits of error of the vapor pressures are about ± 65 percent.

TABLE 5. *Vapor pressure and heats of sublimation of rhodium*

Temperature**	Duration of run	Weight loss	Vapor pressure	$\Delta H_s^\circ(298)$
°K	min	μg	mm Hg	kcal/mole
1708	25	90	3.15×10^{-6}	*126.4
1774	80	82	9.16×10^{-7}	*135.7
1851	40	417	9.43×10^{-6}	132.9
1859	5	89	1.62×10^{-5}	131.5
1851	6	101	1.52×10^{-5}	131.1
1864	5	109	1.98×10^{-5}	131.1
1942	3	205	6.32×10^{-5}	131.9
1926	3	127	3.90×10^{-5}	132.7
1921	4	133	3.06×10^{-5}	133.3
1977	2	214	1.00×10^{-4}	132.5
1966	2	157	7.30×10^{-5}	133.0
1954	2.5	159	5.92×10^{-5}	133.0
1930	2.5	122	4.50×10^{-5}	132.4
1904	3	116	3.56×10^{-5}	131.6
1900	3	83	2.53×10^{-5}	132.6
1890	3	78	2.37×10^{-5}	132.2
1857	3	54	1.64×10^{-5}	131.3
1836	3	37	1.12×10^{-5}	131.2
1819	4	28	6.34×10^{-6}	132.1
1781	6	26	3.90×10^{-6}	131.1
1760	12	31	2.32×10^{-6}	131.4
1983	1	162	1.51×10^{-4}	131.2
2001	1	224	2.11×10^{-4}	131.1
1973	1	143	1.34×10^{-4}	131.1
2071	.5	155	2.95×10^{-4}	134.2
2065	1	307	2.92×10^{-4}	133.8
2041	1	242	2.29×10^{-4}	133.3
2075	1	383	3.65×10^{-4}	133.5
1971	2	155	7.21×10^{-5}	133.4
1927	2	71	3.26×10^{-5}	133.5
1871	3	43	1.32×10^{-5}	133.0
1800	5	24	4.28×10^{-6}	132.8
1736	20	22	9.80×10^{-7}	132.6
1794	9	27	2.69×10^{-6}	133.3
2012	1	147	1.38×10^{-4}	133.5
1997	1	114	1.07×10^{-4}	133.5
1886	3	69	2.11×10^{-5}	132.3
1910	3	98	2.99×10^{-5}	132.7
1875	4	65	1.48×10^{-5}	132.9
1709	100	40	3.48×10^{-7}	134.1
Mean ΔH_s° (298)				132.5
Standard deviation				1.0

Data are presented in experimental sequence.
*Rejected.
**Emissivity, ϵ_λ, assumed to be 0.242 at $\lambda = 0.667\mu$.

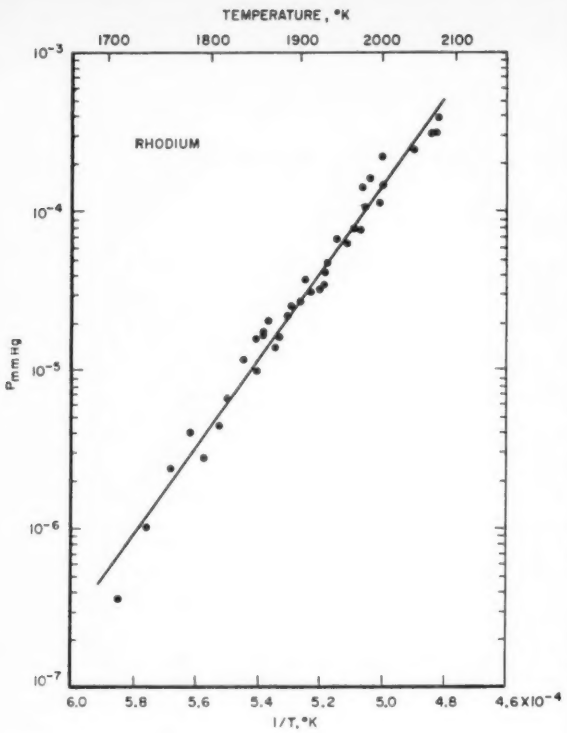

FIGURE 3. *Vapor pressure of rhodium versus reciprocal of absolute temperature.*

(Paper 65A4–113)

4. References

[1] W. R. Mott, Trans. Electrochem. Soc. **34,** 255 (1918).
[2] D. Richardson, Proc. fifth conference on spectroscopy and its applications, p. 64 (John Wiley & Sons, New York, N.Y., 1938).
[3] L. Brewer, The chemistry and metallurgy of miscellaneous materials: thermodynamics, L. L. Quill, ed., pp. 13 et seq. (McGraw-Hill Book Company, Inc., New York, N.Y., 1950).
[4] D. R. Stull and G. C. Sinke, Thermodynamic properties of the elements (Am. Chem. Soc., Washington, D.C. (1956)).
[5] I. Langmuir and G. M. J. Mackay, Phys. Rev. **4,** 377 (1914).
[6] H. A. Jones, I. Langmuir, and G. M. J. Mackay, Phys. Rev. **30,** 201 (1927).
[7a] L. H. Dreger and J. L. Margrave, Abstracts of papers, 137th meeting American Chemical Society, page 12R, Cleveland, Ohio, April 5–14, 1960.
[7b] Privately communicated preprints.
[8] A. A. Hasapis, M. B. Panish and C. Rosen, A study of the molecular species evaporating from condensed phases at high temperatures and the measurement of certain physical properties at high temperatures, Quarterly Summary Technical Report No. 2, Contract AF 33(616)–6840, Wright Air Development Division, Wright-Patterson Air Force Base, Ohio, May 18, 1960, ASTIA Document No. 23866.
[9] L. H. Dreger and J. L. Margrave, J. Phys. Chem. **64,** 1323 (1960).
[10] M. B. Panish and L. Reif, Private communication (to be published).
[11] R. F. Walker, J. Efimenko and N. L. Lofgren, Physical Chemistry in Aerodynamics and Space Flight, A. L. Myerson and A. C. Harrison, Eds (Pergamon Press Inc., N.Y., New York. 1961, pp. 24–30).
[12] R. F. Walker, Vacuum Microbalance Techniques, Vol. I, M. J. Katz, ed, (Plenum Press Inc., N.Y., New York, 1961, pp. 87–110).
[13] R. E. Stephens, J. Opt. Soc. Am. **29,** 158 (1939).
[14] A. G. Worthing, Phys. Rev. **28,** 174 (1926).
[15] D. L. Goldwater and W. E. Danforth, Phys. Rev. **103,** 871 (1956).
[16] L. V. Whitney, Phys. Rev. **41,** 458 (1935).

JOURNAL OF RESEARCH of the National Bureau of Standards—A. Physics and Chemistry
Vol. 65A, No. 4, July–August 1961

Crystallization of Bulk Polymers With Chain Folding: Theory of Growth of Lamellar Spherulites

John D. Hoffman and John I. Lauritzen, Jr.

(January 13, 1961)

A systematic study of the problem of spherulitic growth in linear polymers in bulk has been carried out. A calculation of the radial growth of polymer spherulites is given for four models. These concern growth where the surface nuclei that control the rate are (1) bundlelike and coherent, (2) chain folded and coherent, (3) chain folded and noncoherent, and (4) bundlelike and noncoherent. The required modifications of nucleation theory are given. Then the radial growth rate laws are derived for each model, and the type of "spherulite" that would be formed discussed.

The model with chain folded and coherent growth nuclei leads to a typical lamellar spherulite. The properties of the individual chain folded lamellae that form the spherulite are predicted, including the change of step height with growth temperature, melting behavior, and the behavior on recrystallization. (Chain folded lamellae may also occur in specimens that are not obviously spherulitic.) Under certain conditions, the noncoherent model with chain folds can lead to a modified lamellar spherulite. None of the bundlelike models will lead to a typical lamellar spherulite, though a spherical microcrystalline object might be formed. It is concluded that lamellar spherulites consist largely of chain folded structures.

The factors that could cause chain folded crystals to appear in profusion in bulk polymers are discussed. The case of homogeneous initiation is considered first. Homogeneous initiation of chain folded nuclei in bulk will prevail if the end surface free energy of the bundlelike nucleus exceeds that of the folded. It is shown that the end surface free energy of the bundlelike nucleus, as calculated with a density gradient model, will be larger than had been supposed previously. It is therefore considered to be theoretically possible that the end surface free energy of the bundlelike nucleus may in some cases exceed that of the folded nucleus. Attention is given to the possibility that folded structures appear in large numbers because cumulative strain or large chain ends prevent the growth of bundlelike nuclei to large size, even when the latter type of nucleus is energetically favored when small. Heterogeneous initiation of folded structures is then considered.

Other topics mentioned include: (1) Conditions that might lead to nonlamellar or nonspherulitic crystallization in bulk, (2) the origin of the twist that is frequently exhibited by the lamellae in spherulites, (3) the transitions that may sometimes occur in the radial growth rate law, and (4) interlamellar links.

Contents [1]

		Page
★ 1.	Introduction	297
★ 2.	Rate of homogeneous initiation in bulk for bundlelike and chain folded nuclei	299
★ 3.	Rate of radial growth of spherulites: preliminary considerations	308
4.	Polymer crystal growth by coherent bundlelike surface nucleation	311
★ 5.	Radial spherulitic growth by coherent surface nucleation with chain folds	313
★ 6.	Radial spherulitic growth by noncoherent surface nucleation with chain folds	321
7.	Polymer crystal growth by noncoherent bundlelike surface nucleation	324
★ 8.	Discussion	326
★ 9.	Summary and conclusions	331
10.	Appendix: Simplified density gradient model of the primary bundlelike nucleus	332
11.	References	335

★1. Introduction

In recent years there has been much interest in the growth of spherulites in bulk polymers. These objects are the principal site of the crystallization in a number of highly crystallizable linear polymers, at least under certain conditions. Further, the mechanical, optical, and dielectric properties of such polymers are known to be affected by the presence of spherulitic crystallinity. Hence the rate of spherulitic growth, and the type of crystals existing in the spherulites, are of prime importance in connection with any attempt to understand the physical properties of these systems. Except where specifically noted otherwise, this paper is confined to crystallization from the unoriented melt. Attention is directed mainly to polymers that may be represented as systems of flexible linear chains which can in time achieve a high degree of crystallinity.

[1] It is recommended that only the sections marked with a star (★) be considered in a first reading of the paper. These sections treat many of the main issues, and include the most important models of lamellar spherulitic growth (sections 5 and 6).

In introducing the subject of the nature of the crystals in polymer spherulites, it is essential to first mention the important studies of Keller and coworkers [1, 2] [2] on the nature of the platelike single crystals of linear polymers that may be deposited from supercooled dilute solutions. Polymer crystals formed in this manner consist of regularly shaped platelets that have a thinness or "step height" of roughly 50 to 250 A, depending on the degree of supercooling. (The step height is larger the lower the supercooling.) By electron diffraction experiments, Keller demonstrated that the long axes of the polymer molecules in such crystals are approximately perpendicular to the large and flat upper and lower surfaces. Since the polymer molecules were known to be much longer than the step height, the startling but nevertheless definite conclusion was reached that the upper and lower surfaces consist of *chain folds*. Stacks of thin platelets resembling a terraced pyramid are frequently formed in dilute solution preparations, often around what appears to be a spiral dislocation. In such cases, each terrace step corresponds to the thickness or step height of a single crystal. A theory describing the formation of single polymer crystals from dilute solution has been given by Lauritzen and Hoffman [3].

Spherulites in bulk polymers grow outward from a nucleation center that is frequently of a heterogeneous character. The radial growth of a spherulite is commonly the result of the formation of stacks of bladelike lamellae that grow outward from the nucleation center. As shown in electron micrographs of surface replicas of spherulites, these lamellae possess a thickness or "step height," corresponding to the thin dimensions of the blade, that is commonly between 50 and 250 A. The resemblance between the system of steps seen in a bulk polymer and the steps seen in the stacks of chain folded platelets in a dilute solution preparation of the same polymer is most striking. It is well known from optical studies that the polymer chains in the crystalline matter in spherulites are approximately normal to the spherulite radius. Since the lamellae lie mostly parallel to the radius of the spherulite, it is therefore reasonable to assume that the polymer chains are more or less normal to the large flat surfaces of the lamellae. (Evidence interpretable as proof that the chain axes are nearly normal to the flat lamellar surfaces in polyethylene has been obtained by microcamera X-ray diffraction studies by Fujiwara [42]. Other investigators [4] have shown by optical methods that a similar condition probably applies in certain other cases.) The lamellae often twist as they grow outward, so that a given sector of a spherulite somewhat resembles a stack of propeller blades (twisted lamellae) radiating from a central point. We refer to an object fitting this general description as a *lamellar spherulite*.[3]

In view of the above, it is certainly reasonable to give strong consideration to the possibility that a lamellar spherulite formed in bulk consists of chain folded crystals of the same general type known to arise in dilute solution, and to consider spherulite growth mechanisms based on the chain folded pattern. At the same time, one must attempt to construct a lamellar spherulite on the customary bundlelike pattern. By carrying out calculations on both models, it is possible to arrive at certain conclusions concerning the existence of chain folded crystals in bulk polymers. In the course of such an attack on the problem, it is natural to see if any of the models are capable of predicting the existence of a nonlamellar spherulite.

While no attempt will be made in this paper to effect a detailed comparison of theory and experiment, or to give a complete survey of the experimental situation with respect to the nature of spherulitic crystallization in bulk polymers, it is of interest to mention some of the studies on which the above remarks on spherulitic structure in bulk are based. Much of what is known about lamellae in spherulites has been learned from studying electron micrographs. An outstanding example of this approach is to be found in the recent work of Geil [5] on polyoxymethylene, where clear evidence of the lamellar structure of bulk crystallized material is presented. Geil, Symons, and Scott [6] have shown that chain folded crystals with a rather similar step height are formed from dilute solution by polyoxymethylene; the resemblance between the terraces formed by stacks of chain folded crystals in dilute solution and the terraces seen in material crystallized in bulk is especially striking in this polymer. Eppe, Fischer, and Stuart have presented clear evidence of lamellar structure in bulk polychlorotrifluoroethylene [40]. This and other examples that could be cited render it clear that lamellar structures are common in linear polymers crystallized in bulk. Information on the orientation of the lamellae and polymer chains in spherulites, and the twist of the lamellae, has been obtained by optical microscopy together with a detailed theory of the extinction patterns of such objects due to Keller [7], Keith and Padden [8, 9], and Price [10]. The beautiful rings seen in spherulites in a polarizing microscope are a result of the twist of the lamellae.

The body of the paper begins with a discussion of homogeneous initiation of bundle and loop type structures in bulk. It is concluded that if homogeneous nucleation is the cause of the prevalence of folded structures in bulk, the end surface free energy of the bundlelike nucleus, σ_e, must exceed that of the end surface free energy of the nucleus with chain folds, σ_e. (A simple bundlelike nucleus model that explicitly involves the density gradient at the bundle end is used to bring out certain factors that may contribute to σ_e.) Then the possibility that large chain ends or strain may tend to subdue growth of bundlelike nuclei to large size is considered. Finally, since it is by no means certain that spherulites are generally of homogeneous origin, heterogeneous initiation of chain folded lamellar structures is discussed.

[1] Figures in brackets indicate the literature references at the end of this paper.

[2] The schematic representation of the orientation of the lamellae and the polymer molecules in the lamellae, and the general nature of lamellar twist shown in figures 6 and 7 may prove useful in understanding the above general description of a lamellar spherulite. In real spherulites, the lamellae may be more fragmented and imperfect than shown in these figures.

With this background, attention is then directed toward the problem of calculating *the isothermal rate of radial growth of spherulites as a function of temperature* in supercooled bulk polymers. This property has been singled out for special emphasis because it can often be determined experimentally as a function of temperature, and does not depend on whether the spherulites are of heterogeneous or homogeneous origin.

Radial growth where the rate determining step is the formation of a two-dimensional *coherent* surface nucleus is treated first. (By the term "coherent" we mean to imply that the crystal structure and molecular orientation in the surface nucleus and in its polymer substrate are essentially the same.) Both *bundlelike* coherent surface nuclei and coherent surface nuclei with *chain folds* are considered.

Treatments of radial spherulitic growth by two-dimensional coherent surface nucleation have been given by Burnett and McDevit [11], Kahle and Stuart [12], Takayanagi [13], and Hirai [14]. We must now indicate why we shall add yet another.

First, it is considered desirable to give a detailed analysis of spherulitic growth for coherent nuclei with chain folds. Second, it is instructive to re-examine the theory of the radial growth rate for coherent bundlelike nuclei. It is evident that some problems connected with this model have not been emphasized previously, nor its full range of behavior elucidated. Third, it is necessary to treat the general problem of growth by monomolecular accretion, taking into account the fact that the activated state is in some instances reached in one step. This leads to an important revision of the nucleation and growth rate expressions, especially in the chain fold case. Fourth, it is important to consider the role of chain ends on the formation of polymer crystals. Finally, it is considered to be of special interest to examine closely the connection between a given model for the growth rate, and the physical structure and orientation of the crystalline bodies that this model actually implies in a spherulite. It will emerge that some of the models frequently cited in the literature and used for the analysis of radial growth rate data on spherulites will not lead to typical spherulitic structures.

It will be demonstrated that radial growth through the agency of coherent nucleation with chain folds can lead to a three-dimensional object recognizable as a lamellar spherulite. The existence of the lamellae, the orientation of these lamellae and the molecules in them with respect to the spherulite radius, the dependence of the step height on growth temperature, recrystallization behavior, and the twist exhibited by the lamellae, can be predicted. It is adduced that the coherent bundlelike model cannot lead to a lamellar spherulite.

The theory given here for the rate of radial spherulitic growth in bulk as controlled by coherent surface nuclei with chain folds is based mostly on an analysis by Lauritzen and Hoffman [3] on the appearance of polymer crystals with chain folds from dilute solution. Price [15] has independently treated some aspects of this problem.

The problem of calculating the rate of radial growth of a spherulite where the rate determining step is the formation of a three-dimensional *noncoherent* surface nucleus is treated next. (By the term "noncoherent" we mean to indicate that the orientation of the molecules in the surface nucleus is different from that in the polymer crystal to which it is attached, so that a definite interface exists between the substrate polymer crystal and the surface nucleus.) As before, *bundlelike* noncoherent surface nuclei, and noncoherent surface nuclei with *chain folds*, are treated. The concept of noncoherent surface nucleation in spherulites treated here is based largely on an interesting suggestion due to Price [16]. The radial growth rate laws are given, and the nature of the resultant physical structures is predicted.

The results obtained for the bundlelike noncoherent growth model resemble in general form those given previously by Flory and McIntyre [17], who proposed that the free energy of formation of the three-dimensional bundlelike surface nucleus is in some manner lowered in the vicinity of the growing boundary compared to the free energy of formation of the corresponding three-dimensional homogeneous nucleus. The present treatment is more explicit concerning the possible cause of the lowering of the free energy of formation of the surface nucleus. The noncoherent bundlelike model might possibly lead to a spherical and microcrystalline but nonlamellar object. The noncoherent chain folded model leads to a somewhat modified lamellar spherulite.

In all the calculations of the radial growth rate, an effort has been made not only to derive the rate laws near and somewhat below the melting point, but also to determine the type of behavior that might obtain at strong supercooling. Rather abrupt changes in the radial growth rate, and even the mode of crystallization, may occur with sufficient supercooling.

Toward the end of the paper, the radial growth rate equations are summarized in tabular form, and a discussion presented on various aspects of the initiation and growth of spherulites, and lamellar and nonlamellar crystallization in polymers.

★2. Rate of Homogeneous Initiation in Bulk for Bundlelike and Chain Folded Nuclei

2.1. Homogeneous Nucleation Theory

Turnbull and Fisher [18] give for the steady state rate of homogeneous nucleation in a condensed system the expression

$$I = K \frac{NkT}{h} \exp\left(\frac{\Delta S^*}{k}\right) \exp\left(-\frac{\Delta H^*}{kT}\right) \exp\left(-\frac{\Delta \phi^*}{kT}\right), \tag{1}$$

Here T is the absolute temperature, h Planck's constant, k Boltzmann's constant, ΔH^* the heat of activation of the elementary jump rate process at

the supercooled liquid—nucleus interface, ΔS^* the corresponding entropy of activation, and $\Delta\phi^*$ the free energy of formation of a nucleus of critical size, i.e., a nucleus at the saddle point in the appropriate free energy surface. The constant K has a numerical value within several orders of magnitude of unity for most nucleation problems of interest, and may be ignored for the present.[4] Equation (1) was derived on the basis that the nucleus contains a large number of segments or atoms, and is built up in a stepwise manner. The net nucleation rate was obtained by summation over all forward and backward reactions. The pre-exponential factor (NkT/h) exp $(\Delta S^*/k)$ nuclei sec^{-1} mole^{-1} may be converted to $I_0=(NkT/hm_0\overline{V}_a)$ exp $(\Delta S^*/k)$ nuclei sec^{-1} cm^{-3}, where m_0 is the molecular weight of the length of polymer segment that enters the nucleus in an elementary process, and $\overline{V}_a$ the specific volume of the supercooled liquid.

The main problem is the calculation of $\Delta\phi^*$ in terms of the surface free energies and other parameters associated with the model under consideration.

2.2. Primary Bundlelike Nuclei: The End Surface Free Energy Problem

We employ a bundlelike primary nucleus that is a rectangular parallelepiped as shown in figure 1a. The quantity σ is the lateral surface free energy, and σ_e is the end surface free energy. The surface free energies are defined as the work that is needed to isothermally form 1 cm^2 of the appropriate type of surface from the required number of segments in the normal (interior) crystalline phase.

The rectangular parallelepiped model is not proposed with the intention of conveying the meaning that the cross section of a nucleus or crystal is necessarily rectangular. The cross section could have other shapes, e.g., a parallelogram, hexagon, or other polygon. The lateral faces of the crystal will correspond to some single preferred crystallographic plane, and the lateral surface free energy σ will correspond to the work required to form 1 cm^2 of this surface. The particular geometrical model chosen is just the simplest that is sufficiently illustrative of the phenomena we wish to discuss. The slight modifications necessary to deal with other cross-sectional shapes have been outlined elsewhere [3].

Lateral Surface Free Energy (Bundles): The lateral surface free energy σ refers to a definite and well defined surface, and a reasonably good estimate of its numerical value can be obtained. We should expect σ to be fairly close to that for a typical molecular crystal of approximately the same chemical composition as the polymer, since the molecules on the lateral faces are not "connected" through covalent bonds to the surrounding supercooled liquid. Rough estimates of σ may be surmised from the results of Thomas and Stavely [19] on homogeneous crystallization in fogs of supercooled droplets of simple nonchain organic compounds. From this work we would anticipate that the lateral surface free energy σ would frequently be in the range of 5 to 25 erg cm^{-2}.

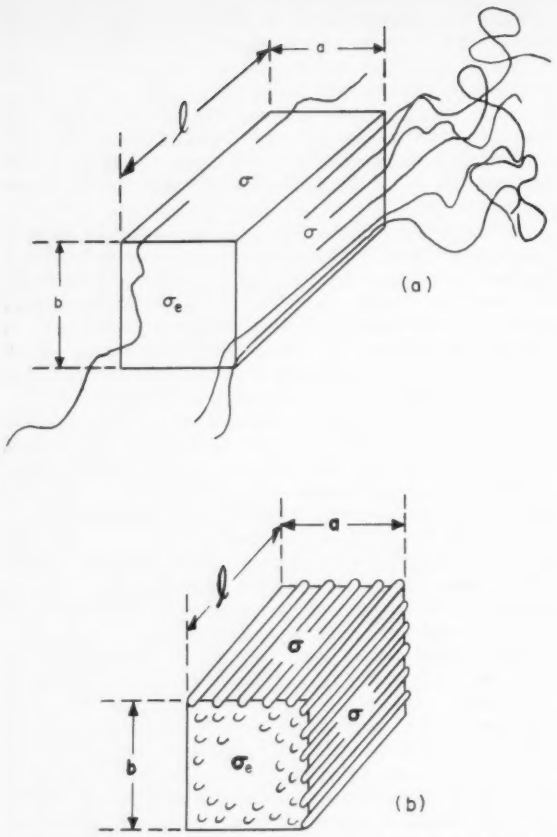

FIGURE 1. *Bundlelike and chain folded primary nuclei.*

(a) *Bundlelike nucleus:* ordinary symbols are used to denote the dimensions a, b, and l, and the lateral and end surface free energies σ and σ_e. A density gradient of considerable extent in the l direction will exist at the end surface.

(b) *Nucleus with chain folds:* bold face symbols are used for the dimensions **a**, **b**, and **l**, and the lateral and end surface free energies $\boldsymbol{\sigma}$ and $\boldsymbol{\sigma_e}$. Well defined surfaces exist on all faces.

It is useful to indicate a method of estimating the lateral surface free energy for a polymer that should generally give a value that is more accurate than would be guessed simply by perusing the results on nonchain type molecular crystals quoted by Thomas and Stavely. Several authors [19, 20] have suggested that for a specific class of compounds the ratio of the work required to form a certain amount of surface phase to the heat of fusion of the same amount of bulk phase is approximately a constant. This ratio may be written as

$$\frac{\sigma}{(\Delta h_f)d}=\alpha, \tag{2}$$

where (Δh_f) is the heat of fusion in erg cm^{-3}, d the lattice spacing in cm, and σ the surface free energy in erg cm^{-2}. The constant α is about 0.5 for many

[4] For many models treated in this paper, K varies as $(\Delta T)^{-2}$, neglecting less important temperature variations. Even such a dependence on temperature in the pre-exponential term is trivial in the analysis of data, the other terms being much more important.

metals [20], and about 0.3 for simple (non-chainlike) molecular crystals [19]. Using the values of σ obtained from carefully conducted homogeneous nucleation experiments with pure chain hydrocarbons dispersed in water recently quoted by Turnbull [21][5], we estimate that α is about 0.1 for the paraffin chain system. This value of α should hold quite well for the calculation of the *lateral* surface free energy σ of polyethylene ($\sigma \sim 10$ erg cm^{-2}). It is to be expected that a fairly similar value of α will hold for the estimation of the lateral surface free energies of other linear polymers. Turnbull's technique could be used to obtain more precise values of α appropriate to other types of chain structure.

End Surface Free Energy (Bundles): The value of σ_e appropriate to the bundlelike nucleus is difficult to assess. No reliable experimental values seem to be available. Flory [22] has treated the configurational contribution to the end surface free energy for a bundlelike crystal as a function of concentration. In this formulation, the end surface free energy at $v_2=1$ (bulk phase) is proportional to $RT \ln D$, where D is a parameter. No theoretical method of evaluating D was given. Also, Flory's treatment does not deal explicitly with the density gradient region at the bundle ends, where important contributions to σ_e will arise.

Insight into some of the factors that will contribute to the work required to build the end of a bundlelike nucleus with a flat end may be gained by noting the calculations in the appendix, section 10, for a cylindrical bundlelike nucleus with a density gradient at the bundle ends. This simplified treatment shows to the approximations indicated (see eq (A–20) of the appendix) that

$$\sigma_e=\frac{l_d(\Delta h_f)\rho_c}{6\rho_l}+\frac{l_d(\Delta\rho)^2\rho_0\Gamma}{6\rho_l^2\rho_c}. \qquad (3)$$

Here l_d is the length of one of the diffuse bundle ends in cm, (Δh_f) the heat of fusion in erg cm^{-3}, ρ_c and ρ_l the density in g cm^{-3} of the crystal and supercooled liquid, respectively, $(\Delta\rho)=\rho_c-\rho_l$, $\rho_0=(\rho_c+\rho_l)/2$, and Γ a constant in erg cm^{-3} that may reasonably be expected to exceed zero. The magnitude of Γ is related to the height of the maximum that will exist in the free energy somewhere in the bundle ends. This maximum must exist in order to cause phase separation, and may result from either repulsion or abnormal separation of the segments in the partly disordered region of the bundle ends. The derivation of eq (3) is valid only when the cross section of the nucleus contains a fairly large number of polymer molecules.

Equation (3) with $\Gamma=0$ may be used to obtain a reasonable lower limit on the value of σ_e for a bundlelike nucleus with a flat end, which we call $\sigma_{e(\min)}$. The minimum value of σ_e implied by eq (3) is surprisingly large. For example, with $(\Delta h_f)=3\times10^9$ erg cm^{-3}, $\rho_c/\rho_l=1.15$, parameters that apply approximately to polyethylene,[6] when taken together with the assumption that $l_d=10\times10^{-8}$ cm$=10$ A, lead to $\sigma_{e(\min)}\cong60$ erg cm^{-2}. Reflected in this result is the fact that a fairly large amount of work will be required to construct an interface between two phases that are connected together by chains containing covalent bonds.

The true value of σ_e for polyethylene is probably in excess of this, since Γ may be greater than zero. Also, certain cumulative strain contributions are neglected in the derivation of eq (3), and these would further increase σ_e. From the above we draw the conclusion that it is not necessary to consider the effect of small σ_e values, i.e., those substantially smaller than the lateral surface free energy σ, in calculating the properties of bundlelike nuclei.[7] It is entirely possible that σ_e for bundlelike nuclei may be at least several hundred erg cm^{-2} in some instances.

An analysis of the particular model used to arrive at eq (3) does not suggest a marked dependence of σ_e on temperature. Nevertheless, even the simplified treatment outlined in the appendix indicates that, under certain circumstances, σ_e could depend on temperature to a noticeable extent. In view of the above, *we must emphasize that the calculations to follow with σ_e treated as a constant are approximate.* Nevertheless, they are believed to be sufficient for the purpose of dealing with the question of how nuclei with chain folds might come to prevail over bundlelike nuclei in bulk. The symbol σ_e in the expressions to be derived for the bundlelike nucleus may be thought of as representing an effective value containing contributions analogous to those shown in eq (3).

2.3. Rate of Homogeneous Nucleation for Bundlelike Nuclei

Region A (steady state nucleation): In the temperature region near and somewhat below the melting point, which we designate region A, the primary nuclei are much larger than the unit cell, and the free energy of formation of a bundlelike crystal or embryo of the type shown in figure 1a may be written

$$\Delta\phi=2ab\sigma_e+2al\sigma+2bl\sigma-abl(\Delta f), \qquad (4)$$

where a, b, and l are treated as variables. (Δf) is the bulk free energy of fusion per unit volume of crystal. Both σ and σ_e are regarded as constants. The problem is to calculate $\Delta\phi^*$ by finding the saddle point in the free energy surface described by eq (4).

The saddle point in the free energy surface described by eq (4) is found by setting $\partial\Delta\phi/\partial a)_{bl}$, $\partial\Delta\phi/\partial b)_{al}$ and $\partial\Delta\phi/\partial l)_{ab}$ equal to zero to get $a^*=4\sigma/(\Delta f)$, $b^*=4\sigma/(\Delta f)$, and $l^*=4\sigma_e/\Delta f$. As plotted on the orthogonal coordinates $\Delta\phi$, l, $(ab)^{1/2}$, the saddle

[5] Turnbull finds $\sigma=9.6$ erg cm^{-2} for *n*-octadecane and $\sigma=7.2$ erg cm^{-2} for *n*-heptadecane. The high end surface free energy that may exist in large bundlelike nuclei or crystals in a high molecular weight polymer will not appear in such short chain materials.

[6] (Δh_f) is within a factor of 2 of 1.5×10^9 erg cm^{-3} for many linear polymers.

[7] This reverses an earlier opinion [3] that detailed consideration should be accorded the case where σ_e is substantially smaller than σ. Calculations based on the assumption $\sigma_e<<\sigma$ lead to a shift in the nucleation rate from the customary $(\Delta T)^{-2}$ to a $(\Delta T)^{-1}$ law at some moderate degree of supercooling [3]. It is improbable that this will commonly occur. Equation (3) indicates that it is highly unlikely that σ_e will be zero, as has sometimes been assumed for bundlelike nuclei.

point is at $l^*=4\sigma_e/\Delta f$, and $(a^*b^*)^{1/2}=4\sigma/(\Delta f)$. Inserting these values into eq (4) the value of the free energy of formation at the saddle point is found to be

$$\Delta\phi^*=\frac{32\sigma^2\sigma_e}{(\Delta f)^2}, \tag{5}$$

which may be compared with the value $8\pi\sigma^2\sigma_e/(\Delta f)^2$ for a bundlelike nucleus with a circular cross section. Then with eq (1), the steady-state nucleation rate is

$$I_A=I_0\exp\left(-\frac{\Delta H^*}{kT}\right)\exp\left(-\frac{32\sigma^2\sigma_e T_m^4}{T^2(\Delta h_f)^2(\Delta T)^2kT}\right), \tag{6}$$

$$[(\Delta T)^{-2}\text{ law}]$$

where we have set

$$\Delta f=\left(\frac{\Delta h_f(\Delta T)}{T_m}\right)\left(\frac{T}{T_m}\right). \tag{7}$$

Here Δh_f is the heat of fusion per unit volume of crystal at the equilibrium melting temperature, T_m, and (ΔT) the degree of supercooling, T_m-T, where T is the crystallization temperature. It has been shown in a previous study [23] that eq (7) is a good approximation in a glass-forming system.[8]

Region B (nonsteady state nucleation): Observe from the foregoing that $a^*=b^*=4\sigma/(\Delta f)$. From this expression and eq (7) it is clear that at some high degree of supercooling (large ΔT), the a and b dimensions of a nucleus of critical size will approach their minimal values, $a_{\min}$ and $b_{\min}$. This will occur at a temperature T_c corresponding to a degree of supercooling of approximately

$$\Delta T_c\cong 4\sigma T_m/(\Delta h_f)a_{\min}. \tag{8}$$

As a rough approximation the product $(a_{\min}b_{\min})$ may be taken as the area corresponding to a nucleus with a cross section containing roughly 5 to 7 polymer segments, i.e., a body with at least one central molecule in an ordered environment. This is the smallest object that may be considered as a typical nucleus. (Note that $a_{\min}$ will be somewhat larger than the corresponding dimensions of the unit cell.)

Because ΔT_c depends on the well-defined lateral surface free energy σ, for which numerical values can be estimated with reasonable accuracy, a fairly reliable conception of its magnitude can be obtained. Taking $\sigma=5$ erg cm^{-2}, $a_{\min}=b_{\min}=10\times10^{-8}$ cm, $T_m=400$ °K, and $(\Delta h_f)=10^9$ erg cm^{-3}, ΔT_c calculated from eq (12) comes to 80 °C. ΔT_c should rarely be less than 30 or 40 °C, and in many cases it may be so large that it falls near or below the glass transition, which would render it inherently unobservable.

It is clear that the nucleation rate will change its character near and below T_c. Attention is now directed to the interesting question of the nature of the nucleation process in the temperature region near and below T_c, region B.

At and below T_c, the free energy of formation may be written

$$\Delta\phi=2a_{\min}b_{\min}\sigma_e+l[2a_{\min}\sigma+2b_{\min}\sigma-a_{\min}b_{\min}(\Delta f)]. \tag{9}$$

The coefficient of l is zero at T_c, but becomes negative at lower temperatures. Thus, it is seen that the nucleus is formed by "increasing" its length l to its minimum possible dimension, which we call $l_{\min}$. Hence, in effect, we are calculating the steady-state nucleation rate for a nucleus of fixed dimensions $a_{\min}$, $b_{\min}$, $l_{\min}$. The modification of classical continuum free energy surface theory necessary to deal with this type of problem is mentioned in section 3.1. The appropriate free energy of formation is given by eq (9) with $l=l_{\min}$. The steady state nucleation rate in region B is

$$I_B=I_0\exp\left[-\frac{\Delta H^*+\Delta H^{**}}{kT}\right]\times\exp\left[\frac{a_{\min}b_{\min}l_{\min}(\Delta h_f)(\Delta T)}{T_mk}\right], \tag{10}$$

$$[(\Delta T)^{+1}\text{ law; will not be directly observable}]$$

where the constant term $2b_{\min}(a_{\min}\sigma_e+l_{\min}\sigma)$ is denoted as ΔH^{**}. (Ordinarily, ΔH^{**} will not exceed several kcal mole^{-1}.) This $(\Delta T)^{+1}$ steady state nucleation rate expression appears to be new in nucleation and growth theory. It must immediately be pointed out, however, that it is very unlikely that such a rate law would be observed over any substantial range of temperature because of the effect of nonsteady-state nucleation near and below T_c. In the case of such small nuclei forming by steady state nucleation in a strongly supercooled polymer, the additional effect of pre-existing embryos of minimal size must be taken into account.[9]

At any temperature T_1 above the melting point of the polymer, the free energy of formation of an embryo always increases as its size increases. This is in contrast to the case of embryos in the supercooled liquid state, where the free energy of formation goes through a maximum at a saddle point so that embryos can become nuclei, and eventually stable crystallites. Nevertheless, numerous small embryos will exist in the normal liquid above T_m, and the population of such embryos can be estimated by straightforward methods. (In the expression for $\Delta\phi$, ΔT simply changes sign above T_m.) Now when a polymer specimen is rapidly cooled from a temperature T_1 that is above T_m to a temperature T_2 in the strongly supercooled state, a number of these pre-existing embryos will be found to be of the critical size relevant to T_2. The number

[8] The usual expression $\Delta f=\Delta h_f(\Delta T)/T_m$ is less exact than eq (7) for glass-forming bulk systems. The extra factor T/T_m corrects for the fact that the entropy difference between the supercooled liquid and crystal falls below $\Delta h_f/T_m$ as the temperature falls below T_m.

[9] Even if the nonsteady state nucleation effect did not interfere at strong supercooling, the $(\Delta T)^{+1}$ law would not be closely obeyed near T_c because of disturbances in the nucleation rate related to the segmental character of the chain that will occur as l approaches $l_{\min}$.

of such pre-existing embryos that correspond to nuclei of critical size will be negligible if the stable nuclei are large, as will be the case at low or moderate supercooling, but near and below T_c, where the nuclei are of the minimal dimensions a_{min}, b_{min}, l_{min}, the number of pre-existing embryos that correspond to nuclei of critical size will be high. Thus, near and below T_c, this transport of bundlelike embryos from the normal melt to the strongly supercooled state will greatly *increase* the rate of injection of nuclei above that predicted by eq (10), or eq (6) as extrapolated into region B. Calculations show that this effect might become so pronounced somewhat below T_c as to cause a very rapid and fine-grained crystallization to occur that might aptly be described as a "nucleative collapse" of the supercooled liquid state. (This effect may deter glass formation as noted in section 8.2.)

At sufficiently low temperatures, the rate of injection will eventually fall because of the increasing importance of the interfacial jump rate term, $\exp(-\Delta H^*/kT)$. Depending on the values of ΔH^* and the various surface free energies involved, this could happen in regions A or B.

Summary: The overall picture of the homogeneous nucleation rate for bundlelike nuclei is shown in figure 2a. The interfacial jump rate term, $\exp(-\Delta H^*/kT)$, with its positive temperature coefficient, will commonly overcome the strongly negative temperature coefficient of the nucleation term, $\exp[-32\sigma^2\sigma_e T_m^4/T^2(\Delta h_f)^2(\Delta T)^2 kT]$, and cause a maximum to appear in the steady state nucleation rate in region A (see solid line). If the nucleation rate is still observable at all at and below T_c, the excess nucleation rate characteristic of nonsteady state nucleation in region B may be seen.

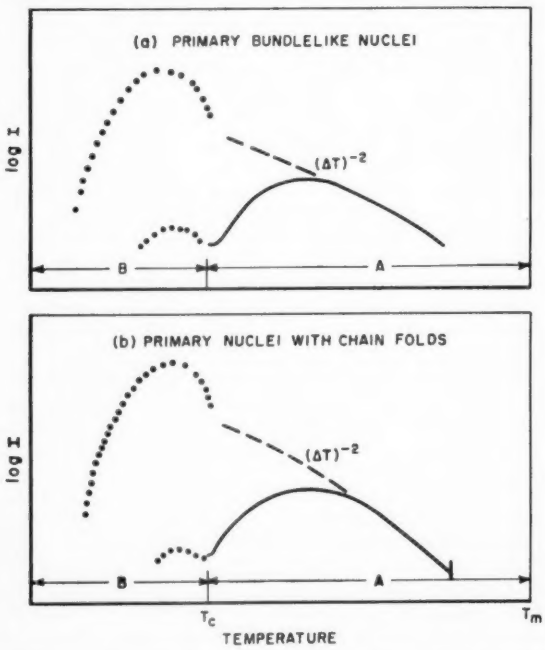

FIGURE 2. *Rate of injection of homogeneous nuclei as a function of temperature.*

I is the homogeneous nucleation rate in nuclei per second per unit volume. – – – – behavior of steady state value of log *I* if effect of jump rate is small; ——— customary behavior where jump rate lowers log *I*; . . . . . shows nucleation in excess of steady state value of log *I* in region B resulting from transport of nuclei of minimal size from above T_m.

2.4. Primary Nuclei With Chain Folds

Quantities that are closely related or specific to *chain folds* are denoted by *bold face* symbols. Note especially that

$$\text{folded nuclei or crystals} \begin{cases} \boldsymbol{\sigma}_e = \textit{end surface free energy} \\ \boldsymbol{\sigma} = \textit{lateral surface free energy} \end{cases}$$

The corresponding quantities for bundlelike systems are

$$\text{bundlelike nuclei or crystals} \begin{cases} \sigma_e = \textit{end surface free energy} \\ \sigma = \textit{lateral surface free energy} \end{cases}$$

The specific type of folded nucleus to be discussed is shown in figure 1b.

Lateral Surface Free Energy (Folded Crystals): The lateral surface free energy $\boldsymbol{\sigma}$ for the folded nucleus refers to an abrupt phase boundary, since no polymer molecules pass through this surface and connect the supercooled liquid and crystalline phases. The quantity $\boldsymbol{\sigma}$ is thus similar in general character to the quantity σ for the bundlelike system, i.e., $\sigma \cong \boldsymbol{\sigma}$, and eq (2) applies to its estimation. Thus, $\boldsymbol{\sigma}$ will usually fall between 5 and 25 erg cm^{-2}.

End Surface Free Energy (Folded Crystals): The end of the chain folded nucleus, unlike the end of the bundlelike nucleus, has a well defined phase boundary. Hence, *the folded nucleus has abrupt phase boundaries on all its faces.* As a consequence, the treatment of chain folded nuclei can be approached with more certainty than can bundlelike nuclei under like circumstances. Both $\boldsymbol{\sigma}$ and $\boldsymbol{\sigma}_e$ may to a good approximation be assumed to be independent of temperature and other variables.

The value of the surface free energy $\boldsymbol{\sigma}_e$ for a folded nucleus is related to the work required to form a fold [3]:

$$\boldsymbol{\sigma}_e = \boldsymbol{\sigma}_{e0} + \mathbf{q}/2A_0. \tag{11}$$

Here $\mathbf{q}$ is the work required to form a fold, and A_0 is the area of the cross section of the polymer molecule. An important contribution to $\mathbf{q}$ will arise from the internal rotational potential of atoms or groups of the loop itself, i.e., from the stiffness of the polymer chain. Then values of $\mathbf{q}$ in the range of roughly 1 to 10 kcal per mole of loops are to be expected. For molecules with the cross-sectional area ordinarily encountered, say 20×10^{-16} cm^2, this means that $\mathbf{q}/2A_0$ might be expected to run from roughly 15 to 150 erg cm^{-2}. (1 kcal/mole of folds$=6.95\times10^{-14}$ ergs/fold.) The quantity $\boldsymbol{\sigma}_{e0}$ is the contribution of $\boldsymbol{\sigma}_e$ due to factors other than folding, and is probably not in excess of $\boldsymbol{\sigma}$. Thus we might expect $\boldsymbol{\sigma}_e$ to be somewhere from 15 to 40 erg cm^{-2} to roughly 150

to 175 erg cm^{-2} for chains of normal flexibility and cross section. It is to be expected that σ_e will generally be larger than σ in any specific case.

2.5. Rate of Homogeneous Nucleation With Chain Folds

Region **A:** By simply replacing σ_e and σ in eq (4) with σ_e and σ, and proceeding as before, we get

$$\mathbf{I}_A=\mathbf{I}_0 \exp\left(-\frac{\Delta H^*}{kT}\right)\exp\left(-\frac{32\,\sigma^2\sigma_e T_m^4}{T^2(\Delta h_f)^2(\Delta T)^2 kT}\right) \quad (12)$$

$$[(\Delta T)^{-2}\ \text{law}]$$

for the steady state rate of injection of loop type nuclei in bulk.

The auxiliary equation

$$\mathbf{l}_p^*=4\sigma_e/(\Delta f)\cong 4\sigma_e T_m/(\Delta h_f)(\Delta T) \quad (13)$$

which defines the length or "step height" of the primary nucleus, is obtained in the derivation of eq (12). A numerical calculation using the estimated values of σ_e, and reasonable values of the other parameters in eq (13), reveals that the step height of the primary nucleus should frequently lie between 100 and 500 A for a degree of supercooling of 20° C. (As will be noted subsequently, the step height of chain folded lamellae growing by monomolecular accretion may initially be substantially less than that given by eq (13).) Observe from eq (13) that the step height of the primary nucleus increases as the degree of supercooling decreases.

The derivation of eqs (12) and (13) is based on the idea that the primary nucleus is large, i.e., the critical size is reached after many successive steps. Therefore, the free energy surface may be treated as a continuum. As will be seen in section 5.1, this assumption cannot be used for monomolecular growth with chain folds. For the latter, a different theory of the rate of nucleation and step height will be given.

Important restrictions exist on the path of nucleation on the free energy surface for loop type nuclei that are not evident in the simplified derivation indicated above. In particular, the step height of the primary nucleus, $\mathbf{l}_p^*$, may be regarded as essentially invariant as the nucleus is built up. The theory for the constancy of the step height of loop type primary nuclei has been given in detail elsewhere [3]. The step height of one primary nucleus as compared with another is restricted to a narrow range of values centering about $\mathbf{l}_p^*$ because of the steepness of the sides of the saddle point in the free energy surface, and the fact that the chain folds prevent (or seriously deter) an increase of length after a loop is laid down.[10] This type of restriction does *not* apply to bundlelike nuclei.

[10] In reference [3], it was shown in eqs (42-48) that the homogeneous nucleation rate for folded nuclei between the length $\mathbf{l}$ and $\mathbf{l}+d\mathbf{l}$ is proportional to $\exp(-\Delta H^*/kT)\exp(-\Delta\phi^*/kT)\exp\{-(\Delta\phi^*/kT)\,[(\mathbf{l}/\mathbf{l}_p^*-1)^2]/[1+2\,(\mathbf{l}/\mathbf{l}_p^*-1)]\}$, where $\Delta\phi^*$ is the free energy of formation at the saddle point, which is $32\sigma^2\sigma_e/(\Delta f)^2$ in the present geometry. This expression shows that the nucleation rate is a maximum at $\mathbf{l}=\mathbf{l}_p^*$. This was extended to show that primary nuclei with step heights much different than $\mathbf{l}_p^*$ are highly improbable.

Effect of Molecular Weight on Nucleation in Upper Part of Region **A:** The critical volume of the primary folded nucleus, $\mathbf{v}^*$, is $\mathbf{a}^*\mathbf{b}^*\mathbf{l}_p^*=64\ \sigma^2\sigma_e/(\Delta f)^3 \cong 64\sigma^2\sigma_e T_m^3/(\Delta h_f)^3(\Delta T)^3$. For the parameters $\sigma=5$ erg cm^{-2}, $\sigma_e=25$ erg cm^{-2}, $T_m=400$ °K, and $(\Delta h_f)=10^9$ erg cm^{-3}, this comes to $2.6\times10^{-16}/(\Delta T)^3$ cm^3. At relatively low supercooling, e.g., $(\Delta T)=10$ °C, this would give $\mathbf{v}^*=2.6\times10^{-19}$ cm^3. If it is now assumed that the average length of the polymer molecules, l_m, is 5000 A, and that the cross-sectional area is 20×10^{-16} cm, then the mean volume per molecule is calculated to be 10^{-19} cm^3 molecule^{-1}. In this case, the nucleus would have to be formed from more than one polymer molecule. If the polymer molecule has large chain ends that are excluded from the crystal, it follows that the folded nucleus will occasionally possess a chain that emanates bundle-fashion from the plane of the chain folds. This leads to no serious limitation on the theory of nucleation as presented above. At $\Delta T\geq 14$ °C, the primary nucleus could form from one molecule.

If the chain ends are so large as to be practically completely excluded from the crystal, a serious limitation on the ability of the polymer to form a primary nucleus with chain folds will occur as the step height approaches one half the length of the molecule. For the parameters cited above, $\mathbf{l}_p^*=4000\text{A}/(\Delta T)$ and $l_m=5000$ A. Then when $\Delta T\leq 1.6$ °C, chain folded primary nuclei cannot form if chain ends are excluded from the crystal. For materials with higher σ_e values or lower molecular weight, this limitation will appear further below T_m. For example, with $\sigma_e=50$ erg cm^{-2} and $l_m=2000$ A, this limitation would appear at $\Delta T\leq 8$ °C. This means that simple homogeneous nucleation with chain folds will not be possible very near the melting point if chain ends are strictly excluded from the crystal. (The same is of course true for bundlelike nucleation at some low supercooling if chain ends are excluded from the crystals.) For polymers of high molecular weight, this limitation on folding is not apt to be encountered in the region where the rate is commonly observed.

It will be possible to tolerate a certain concentration of small chain ends as defects in a polymer crystal. In this case, the degree of supercooling at which chain folds would have difficulty in forming because of chain end effects would be substantially smaller than indicated above. Also, a number of short chains may be included bundle fashion in the nucleus.

Region **B:** The expression given for $\mathbf{I}_A$ will hold from temperatures near T_m on down to considerably lower temperatures. Then there will be an increase in the rate of injection of loop type nuclei at a degree of supercooling $\Delta T_c=4\sigma T_m/(\Delta h_f)\mathbf{a}_{\min}$ resulting from the transport of pre-existing loop type embryos, resembling U shaped kinks, from the melt to the supercooled state. The argument for the existence of this nonsteady state nucleation effect is similar to that given previously for bundlelike nuclei, and need not be repeated here.

Note that the expressions for ΔT_c for the bundlelike nucleus and the loop type nucleus are similar,

and involve only the lateral surface free energy. The type of nucleus of minimal dimensions that will actually be deposited near and below T_c will be the one that has the lowest free energy of formation, and this will depend largely on which has the lowest end surface free energy. The same symbol is used to denote the transition temperature for both types of nuclei, since it is generally clear which kind is meant.

Summary: A schematic diagram of the rate of homogeneous injection of folded nuclei as a function of temperature is shown in figure 2b. The solid line indicates the manner in which the interfacial jump rate term exp $(-\Delta H^*/kT)$ will generally lower the nucleation rate at some degree of supercooling, causing a maximum to appear in $\mathbf{I_A}$. (This maximum would ordinarily appear between 0.8 to 0.9 T_m.) It is probable that the **A**→**B** transition will frequently be unobservable because the jump rate term lowers the nucleation rate so much that T_c falls near or below the glass transition. The pip mark just below T_m represents the temperature above which the molecular length is too small to accommodate chain folding if large chain ends are excluded from the crystal.

2.6. Bundlelike *Versus* Folded Nuclei in Bulk

As will be brought out subsequently, there are substantial reasons for believing that lamellar spherulites formed in bulk are composed of crystals with chain folds, each individual lamella having a thickness corresponding to the step height associated with the chain folds. The intriguing question of how folded structures could nucleate and then propagate in linear polymers crystallized in bulk will now be discussed in the light of what may be said about homogeneous nucleation in the bundlelike and folded patterns, the possibility that heterogeneous nucleation may be involved in the initiation act, and the fact that under certain conditions chain ends or strain may interfere with the formation of large bundle like objects, even under conditions where small bundlelike nuclei are formed easily.

Consider first the problem of how folded nuclei might predominate in bulk crystallization *on the assumption that the folded structures that are observed are of homogeneous origin*. (This assumption is by no means proved in any case of bulk crystallization known to the author, but serves as a convenient starting point for the discussion.) We will deal only with crystallization near the melting point.

There is no difficulty in explaining why crystals with chain folds are deposited from a sufficiently dilute solution of a linear polymer. Lauritzen and Hoffman [3] have discussed this in terms of the rate of injection of bundle and loop type nuclei in solution which are [11]

$$I_{\text{bundle}} = I_0 \exp\left(-\frac{\Delta H^*}{kT}\right) \exp\left(-\frac{32\ \sigma^2\sigma_e}{(\Delta f)^2 kT}\right) \times \exp\left(\frac{16\ \sigma^2 \log_e v_2}{A_0(\Delta f)^2}\right) \quad (14)$$

[11] The derivation of eq (14) is patterned after one given by Mandelkern [24] for a cylindrical bundlelike nucleus.

$$\mathbf{I}_{\text{loop}} = \mathbf{I}_0 \exp\left(-\frac{\Delta H^*}{kT}\right) \exp\left(-\frac{32\ \boldsymbol{\sigma}^2\boldsymbol{\sigma}_e}{(\Delta f)^2 kT}\right) \quad (15)$$

(dilute solution)

Equation (14) has been recast to accord with the particular notation and geometry used in the present paper. (The parameters σ, σ_e, I_0, ΔH^*, and (Δf) might have somewhat different values in dilute solution than in the bulk phase.) The quantity v_2 is the volume fraction of polymer. The lateral surface free energy for the bundlelike nucleus in solution will be essentially the same as the lateral surface free energy of the loop type nucleus in solution, i.e., $\sigma \simeq \boldsymbol{\sigma}$. The end surface free energies σ_e and $\boldsymbol{\sigma}_e$ will differ to a significant extent.

The important point to note in comparing these two expressions is that, *independent of the values of σ_e and $\boldsymbol{\sigma}_e$ that are chosen, I_{loop} will always exceed I_{bundle} if v_2 is taken to be sufficiently small, since the exponent in eq (14) containing* $\log_e v_2$ *will be a large negative number under these conditions.* Numerical estimates given in an earlier paper indicate that even if σ_e is taken to be considerably smaller than $\boldsymbol{\sigma}_e$, folded nuclei will predominate at concentrations of less than about 1 to 10 percent. The term in eq (14) involving $\log_e v_2$ results from the fact that a number of different polymer molecules must be gathered together to form a bundlelike nucleus, whereas only a few polymer molecules (and often a single one) can form a loop type primary nucleus. Therefore, there is a large configurational entropy contribution to the formation of a bundlelike nucleus in dilute solution that does not arise in the case of the loop nucleus.[12] In the case where σ_e is larger than $\boldsymbol{\sigma}_e$, folded nuclei will predominate across the entire concentration range (see below).

For this same basic reason, a folded crystal is more stable in sufficiently dilute solution than a bundlelike one *of the same size and shape* even if σ_e is smaller than $\boldsymbol{\sigma}_e$. Specifically, it can be shown [3] that the total end surface free energy per unit area for the two types of crystal may be written as [12]

$$\sigma_{\text{end bundle (tot.)}} = \sigma_e - (kT/2A_0)\log_e v_2 \quad (16)$$

and

$$\boldsymbol{\sigma}_{\text{end loop (tot.)}} = \boldsymbol{\sigma}_e. \quad (17)$$

The term in eq (16) containing $\log_e v_2$ arises from the configurational entropy effect mentioned earlier. Thus, even for the case $\sigma_e < \boldsymbol{\sigma}_e$, $\sigma_{\text{end bundle (tot.)}}$ will exceed $\boldsymbol{\sigma}_{\text{end loop (tot.)}}$ at some low concentration of polymer, and the folded crystal will be the most stable type in dilute solution because it has less total surface free energy. In the event $\sigma_e > \boldsymbol{\sigma}_e$, the folded crystal would be the most stable type across the entire concentration range when compared with a bundlelike crystal of the same size and shape.

We are thus led to a discussion of the relative homogeneous injection rates for bundle and loop type

[12] The expressions for I_{loop} and $\sigma_{\text{end loop (tot.)}}$ do in fact contain a small term in $\log_e v_2$, but this is entirely insignificant compared to the ones shown for I_{bundle} and $\sigma_{\text{end bundle (tot.)}}$ [3].

nuclei in bulk polymers. The appropriate comparison is given by eq (15) in the case of loop nuclei, and by eq (14) with $v_2 \to 1$ for bundlelike nuclei (*cf.* eqs (6) and (12)):

$$I_{\text{bundle}} = I_0 \exp\left(-\frac{\Delta H^*}{kT}\right) \exp\left(-\frac{32\sigma^2\sigma_e}{(\Delta f)^2 kT}\right) \quad (18)$$

$$\mathbf{I}_{\text{loop}} = \mathbf{I}_0 \exp\left(-\frac{\Delta H^*}{kT}\right) \exp\left(-\frac{32\boldsymbol{\sigma}^2\boldsymbol{\sigma}_e}{(\Delta f)^2 kT}\right). \quad (19)$$

(bulk phase)

Anywhere near the melting point, the exponents involving the surface free energies in these two expressions are by far the largest and most temperature dependent. Recall also that σ is essentially the same as $\boldsymbol{\sigma}$ for the two types of nuclei. It follows that *if homogeneous nucleation of folded nuclei is to prevail over any sensible temperature range in the bulk phase, the condition* $\sigma_e > \boldsymbol{\sigma}_e$ *must exist.*

While the condition $\sigma_e > \boldsymbol{\sigma}_e$ for homogeneous nuclei would lead to the dominance of folded nuclei (and the resultant chain folded lamellar structures) in bulk polymers, this is not necessarily the only condition that can lead to a significant number of such structures in bulk. Other factors must be taken into account. For example, chain ends may in some instances prevent the formation of large bundlelike objects, as Flory's theory [22] suggests. (Cumulative strain may have a similar effect.) Also, heterogeneous initiation, which is certainly a very common source of spherulite initiation, must be considered. However, before discussing these points it is worth commenting on the important case $\sigma_e > \boldsymbol{\sigma}_e$.

Conditions giving $\sigma_e > \boldsymbol{\sigma}_e$ (*chain folding the basic mode of nucleation and growth in bulk*): It has been shown for a bundlelike nucleus with a flat end and noncumulative strain that the minimum value of σ_e is given by $l_d(\Delta h_f)\rho_c/6\rho_l$, where l_d is the length of the part of the bundle end where the density falls from the crystal to the supercooled liquid value (see eq (A–20) in the appendix). Further, it was estimated in section 2.2 for the particular case of polyethylene that $\sigma_{e(\min)}$ was in the vicinity of 60 erg cm^{-2} on the basis of the assumption $l_d = 10$ A. An analysis of $\boldsymbol{\sigma}_e$ for folded polyethylene crystals based on data on single crystals formed in dilute solution due to Keller and O'Connor [1] suggests that $\boldsymbol{\sigma}_e$ is probably between 30 and 75 erg cm^{-2} [3]. More recently, a value in the vicinity of 100 erg cm^{-2} has been suggested [41]. (Although these figures apply to folded crystals formed in dilute solution, the $\boldsymbol{\sigma}_e$ value relevant to folded crystals formed in bulk should not differ greatly from that appropriate to dilute solution.) Thus, while it is not altogether certain that $\sigma_{e(\min)}$ is larger than $\boldsymbol{\sigma}_e$, it is clear for the particular model used that σ_e for the bundlelike nucleus can readily exceed $\sigma_{e(\min)} = 60$ erg cm^{-2}, since Γ will generally exceed zero. With this considered, σ_e could easily be as high as several hundred erg cm^{-2}. Therefore, the possibility that $\sigma_e > \boldsymbol{\sigma}_e$ for polyethylene would appear to exist.

Before drawing any conclusions from the above, several points must be made clear: (1) The value of $\sigma_{e(\min)} = 60$ erg cm^{-2} is admittedly based on the assumption $l_d = 10$ A. However, it is believed that this is if anything an underestimate, so $\sigma_{e(\min)}$ for the flat bundle end model without cumulative strain is probably even larger than the value cited. (2) The expression $\sigma_{e(\min)} = l_d(\Delta h_f)\rho_c/6\rho_l$ depends on the assumptions used in the simplified model for the heat content and entropy as a function of density in the bundle ends. For example, a narrower maximum in $\Delta H(\rho)$ would lead to a lower value of $\sigma_{e(\min)}$. Nevertheless, the estimate given for $\sigma_{e(\min)}$ is probably not significantly high on this account, and may be too low. (3) Cumulative strain at the flat bundle ends resulting from the density difference between the "connected" liquid and crystalline phases has been omitted from the calculations. However, this will in general lead σ_e to be underestimated. As will be seen subsequently in the discussion of the hypothetical bundlelike "lamellar" structure, cumulative strain will occur at flat bundle ends of large extent, especially in the case where the chain axes are perpendicular to the plane of the bundle ends. Crudely, one can think of such strain as greatly increasing Γ in eq (3), causing σ_e to attain values far in excess of $\sigma_{e(\min)}$. We regard that it is quite certain that $\sigma_e > \boldsymbol{\sigma}_e$ for large nuclei with polymer chains that are perpendicular to flat end surfaces on account of cumulative strain alone. (4) The cumulative strain in the flat bundle end model may be reduced by allowing the chains in the (still flat) surface phase to subtend a certain angle ζ with respect to those in the crystal itself (see section 4.3). (This is related to the fact that the end surface of a bundlelike crystal will tend to be curved in order to minimize the surface energy, as pointed out by Matsuoka and Maxwell [25], and Frank [26].) Estimates obtained using appropriate variations of the model treated in the appendix suggest that σ_e will be fairly large for the "tilted," model even if the cumulative strain is completely removed. The bending of the chains at a nontetrahedral angle, and the abnormal separation of the chains at the boundary nearest the crystal, produce the required contributions to the heat content in the surface phase.

With the above remarks in mind, it seems reasonable to suppose that it is entirely possible that $\sigma_e > \boldsymbol{\sigma}_e$ for polyethylene for the important case of flat end surfaces. This would lead in a natural way to a predominance chain folded nuclei in bulk in this polymer, as opposed to bundlelike nuclei with flat ends. From this illustrative example, we consider that it is at least not nonsense to propose that σ_e may exceed $\boldsymbol{\sigma}_e$ in some linear polymers.

The free energy of formation of a bundlelike nucleus with curved ends ("ellipsoidal" model) has not been explicitly considered here. This would probably require the use of considerations akin to those proposed by Cahn and Hilliard [27] for homogeneous nucleation in systems with density gradients. This model is not considered revelant to the problem of the nucleation and growth of bundlelike "lamellae" with large flat end surfaces. Thus, while it seems

reasonable on the basis of our calculations to suppose that in some cases $\sigma_e > \sigma_e$ for nuclei with flat ends, no such simple calculations will provide as much information on whether or not the free energy of formation in bulk of a folded nucleus (which of course has flat ends) is less than that of an ellipsoidal bundlelike nucleus under similar conditions. Nevertheless, our surmise would be that the necessity of having the chain molecules go through a density gradient in the ellipsoidal bundlelike case might well be able to increase its free energy of formation to the point that folded primary nuclei are still the favored type in the bulk phase. This is not certain, however, and the possibility therefore exists that ellipsoidal bundlelike nuclei may form more readily at a specified supercooling than folded nuclei, even when folded nuclei are preferred to bundlelike nuclei with flat end faces. However, if strain or chain ends limited bundlelike growth, the macroscopically observable crystals would still be of the folded type even though coexisting with a number of bundlelike microcrystals or embryos (see below).

Possibility of chain folds in case $\sigma_e < \sigma_e$: We now mention certain conditions that might lead to the appearance of a considerable amount of chain folded material in a bulk polymer even in the case where $\sigma_e < \sigma_e$ for primary nuclei.

Consider the effect of chain ends on the formation of the two types of nuclei (or crystals) under discussion, namely the bundlelike and the folded. We deal principally with the case where the chain ends are assumed to be sufficiently large so that the majority cannot enter the crystal.

It is reasonable to ignore the effect of even large chain ends in constructing the expression for the free energy of formation of relatively small bundlelike *nuclei* of a polymer of high molecular weight. However, this is not the case for bundlelike *crystallites* where large chain ends are excluded. Flory has clearly indicated for this case that there are restrictions of an equilibrium character on the size of the bundlelike polymer crystals [22]. The restriction discussed explicitly in Flory's paper refers to a limitation on the mean length of the crystallites. Flory's theory of bundlelike crystallization also implies a limitation on the mean radius of the crystallites. The net result is that a large number of bundlelike microcrystals of varying sizes is predicted to exist in a polymer with a distribution of molecular weight. The restriction on the ultimate (equilibrium) size of bundlelike crystallites must be given consideration in dealing with the formation of large nuclei, and the growth of crystallites, in the bundlelike pattern. The description of bundlelike microcrystallinity just mentioned does not appear to suggest the existence of large numbers of lamellae of uniform thickness and extended "radial" dimensions of the type seen in lamellar spherulites.

Even the assumption that chain ends are totally excluded from the crystal will not cause folded nuclei or thin folded crystals to fail to grow to large dimensions in the "radial" direction, i.e., in the direction normal to the polymer chain axes. (Once formed, a folded crystal will grow slowly, if at all, in the chain axis direction because of the existence of the folds, and the slowness of the requisite internal "lengthwise" diffusion mechanism.) A chain end can readily be "denucleated" the short distance to the plane of the chain folds when it finds itself on the lateral (growing) surface, thus being rapidly and efficiently excluded from the interior of the folded crystal. Such chain ends would protrude outward from the fold plane on a short section of polymer chain.

Thus, thin chain folded crystals, once nucleated, should be able to grow to large "radial" dimensions, corresponding to a certain fraction or even the entire radius of a spherulite. The main limitation would arise with low molecular weight material where the molecular length was less than twice the step height, but all molecules that were significantly longer than this would be potentially crystallizable in a basically chain folded manner. Some of the chains (including rather short ones) may be included bundle fashion in the otherwise folded crystal.

The concept that chain ends are excluded from polymer crystals must not be pressed too far, especially in the case of small chain ends. A substantial number of sufficiently small chain ends may enter chain type crystals. (This evidently applies in the case of the $—CH_3$ end groups in the solid solutions formed by the *n*-paraffins of different lengths.) In the case where a certain number per unit volume of such ends can be assimilated by the polymer crystal, the restrictions noted in Flory's theory on the size of bundlelike crystals would be relaxed, i.e., larger crystallites would form. Similarly, any restrictions on the ultimate size of the step height due to finite molecular length would be minimized, as noted earlier in section 2.5.

The radial growth of bundlelike nuclei may be significantly reduced or even stopped by cumulative strain at the bundle ends resulting from the density difference of the liquid and crystalline phases. As mentioned earlier, this will certainly be the case for bundlelike nuclei with flat ends where the chain axes are perpendicular to the end face. This may possibly even occur for ellipsoidal bundlelike nuclei, or bundlelike nuclei with flat ends where the chain axes are inclined at an angle to the end surface. In such situations, the condition $\sigma_e < \sigma_e$ might exist for small nuclei or very small crystals, while cumulative strain leads to $\sigma_e > \sigma_e$ for large nuclei or crystals. Homogeneous nucleation of tiny bundlelike nuclei would then prevail over the folded type, but the crystals apparent on a large scale in the system would be formed on a basically chain folded pattern.

Even in the case where $\sigma_e < \sigma_e$ for small nuclei, and $\sigma_e > \sigma_e$ for large nuclei, the rate of homogeneous nucleation of lamellar spherulites with chain folds will be given approximately by eq (19), especially at moderate to low supercooling where the nuclei will be rather large. The nucleus, though starting on the bundlelike pattern, would begin folding as it grew and exhibit the overall energetics characteristic of a folded nucleus. At high supercooling, stable bundlelike nuclei would appear in profusion, though

592653—61——3

folding would occur as these grew to large size. In this region, the apparent homogeneous injection rate of folded objects would increase above that given by eq (19). This effect may strongly resemble the onset of region B.

The above remarks form the basis of the conception that even if $\sigma_e < \boldsymbol{\sigma}_e$ for *small* nuclei, chain folded structures may under certain circumstances be the most prevalent and physically obvious form of bulk crystallization in linear polymers. Specifically, cumulative strain or sufficiently large chain ends may poison the coherent growth of bundlelike crystals to large dimensions, causing any strictly bundlelike crystals that were initiated to be of limited size: then any folded structures that were introduced into the system through the agency of either homogeneous or heterogeneous nucleation might be able to grow to very large size in the two dimensions normal to the chain axes in the same general sense that folded single crystals do in dilute solution. In this case, it is important to distinguish between the prevalence and ease of observation of a certain type of crystal on the one hand, and the rate of homogeneous initiation of small nuclei of limited growth potential on the other. For the case where $\sigma_e > \boldsymbol{\sigma}_e$ for nuclei, the formation of folded structures will dominate the bulk crystallization process.

The remaining point concerning the origin of nuclei deals with the possibility of heterogeneous nucleation. In real polymer systems, the initiation of spherulites is for the most part of pseudohomogeneous or heterogeneous origin. (Pseudohomogeneous initiation, which refers to the essentially sporadic initiation events that may take place on the flat surfaces of weakly wettable heterogeneities, can imitate the truly sporadic initiation characteristic of homogeneous initiation.) As a result of special interactions, heterogeneities might conceivably have a strong predilection for producing structures containing loops on their surfaces, even if $\sigma_e < \boldsymbol{\sigma}_e$ for the homogeneous process. This might cause chain folded structures to be prevalent in linear polymers crystallized in bulk. In the case where $\sigma_e > \boldsymbol{\sigma}_e$, chain folded structures of heterogeneous or pseudohomogeneous origin would arise in numbers far in excess of that characteristic of homogeneous nucleation if suitable heterogeneities were present, and these structures would certainly be the dominant form present. Certain questions relating to homogeneous, pseudohomogeneous, and heterogeneous nucleation will be discussed subsequently in section 8.

Summary: The following conclusions may be drawn. If folded nuclei are to predominate in the supercooled bulk phase of a polymer on a *homogeneous* basis over any important range of temperature, the end surface free energy of the bundlelike nucleus must for some reason exceed that of a folded nucleus ($\sigma_e > \boldsymbol{\sigma}_e$). (This statement refers specifically to nuclei with flat end surfaces.) Because of a certain flexibility in the parameters that define σ_e and $\boldsymbol{\sigma}_e$, it is not possible to say *a priori* that homogeneous formation of folded nuclei should dominate the bulk nucleation mechanism. However, a plausible case can be made for supposing that σ_e might well exceed $\boldsymbol{\sigma}_e$ under certain circumstances. In any event, the quantity σ_e is evidently considerably larger than has been assumed in the past. (A compelling theoretical case can be made for the dominance of folded nuclei of homogeneous origin in sufficiently dilute solution.) In the case of heterogeneous nucleation under the condition $\sigma_e > \boldsymbol{\sigma}_e$ folded structures are to be expected. It is probably not absolutely necessary that σ_e always be greater than $\boldsymbol{\sigma}_e$ to have a significant amount of folded structures appear in bulk. Sufficiently large chain ends may poison the formation of large bundlelike crystallites, but at the same time not seriously affect the formation of large chain folded objects. Similarly, cumulative strain may abort the growth of bundlelike crystals; this corresponds to $\sigma_e < \boldsymbol{\sigma}_e$ for small bundlelike nuclei, and $\sigma_e > \boldsymbol{\sigma}_e$ for large bundlelike nuclei or crystals. Further, heterogeneities, a common source of spherulite initiation, might induce folded surface nuclei by specialized interactions.

Attention is now directed to the main problem of the rate of radial growth of spherulites, and the connection between the proposed mechanisms and spherulite structure.

★3. Rate of Radial Growth of Spherulites: Preliminary Considerations

3.1. The Two Types of Nucleation Problem in Spherulitic Growth

We will repeatedly encounter two types of nucleation problem in connection with the rate of radial growth of a spherulite. The first of these is quite similar to that already treated for primary nuclei in the previous sections, in that it deals with a nucleus that is built up, step by step, until a critical size is finally reached. Nucleation of this type has already been treated by Turnbull and Fisher [18], and is readily adapted to deal with surface nuclei that are gradually built up to critical size in a stepwise manner. The second type of nucleation problem commonly encountered is that where the maximum in the free energy barrier is reached in a single step, rather than in a large number of steps. This problem often arises when nucleation of a monomolecular layer is considered. The problem of monomolecular layer growth has been considered by Lauritzen and Hoffman [3].

If the surface nucleus is built up by successive addition of a large number of elements until a nucleus of critical size is reached, the free energy of formation may be represented as in figure 3a. Each elementary forward reaction has a reaction rate of the form $(kT/h)\exp(-w_f/kT)$, and each backward reaction a rate of the form $(kT/h)\exp(-w_b/kT)$. Then by summing over all the forward and backward reactions in the manner described by Turnbull and Fisher, it is found that the overall rate of nucleation per unit area of substrate is

$$I_s = I_{s(0)} \exp\left(-\frac{\Delta F^*}{kT}\right) \exp\left(-\frac{\Delta\phi_s^*}{kT}\right), \qquad (20)$$

where ΔF^* is the free energy of activation of the interfacial jump rate, $\Delta\phi_s^*$ the work required to build a nucleus of critical size, and $I_{s(0)}$ a factor that does not depend strongly on temperature. As before, the term in ΔF^* may be broken up to give $\Delta H^* - T\Delta S^*$. The quantity $\Delta\phi_s^*$ is, in general, calculated in a manner similar to that used previously for primary nuclei, i.e., the free energy surface is treated as a continuum. Each nucleus then rapidly grows across the substrate crystal and produces a new layer, or substantial fraction thereof. A new surface nucleus will then form on this new layer. Accordingly, the rate of growth on this crystal face depends on the rate of nucleation on the face. When the crystal face in question corresponds to that leading to radial growth of the spherulite the steady state rate of radial growth may be written

$$G = dr/dt = G_0 \exp\left(-\frac{\Delta H^*}{kT}\right) \exp\left(-\frac{\Delta\phi_s^*}{kT}\right) \quad (21)$$

(large surface nuclei built up step by step: $\Delta\phi_s^*$ calculated from continuum model of free energy surface)

Here G_0 is a constant with the dimensions $/t^{-1}$, r the radius of the spherulite at time t. The quantity G_0 contains the factor exp $(\Delta S^*/k)$, and certain relatively unimportant geometrical factors. The principal problem connected with calculating the radial growth rate for a model is the evaluation of $\Delta\phi_s^*$. As in the case of homogeneous nucleation, $\Delta\phi_s^*$ is the free energy at the saddle point described by the appropriate free energy function.

At low to moderate supercooling, the main temperature dependence in eq (21) is due to the $\Delta\phi_s^*$ term, the term in ΔH^* being next in importance. The temperature dependence of G_0 is negligible in comparison.[13] For steady state surface nucleation, the term in $\Delta\phi_s^*$ always has a negative temperature coefficient. The term in ΔH^* has the usual positive temperature coefficient.

The problem takes on a somewhat different character in cases where the activated state is reached in one step (fig. 3b). Although from a formal standpoint the free energy surface in question may have a saddle point, it is not correct to treat the free energy of formation $\Delta\phi$ as a continuous function of the width a of the nucleus when the activated state is reached at $a = a_0$. Then $\Delta\phi$ is defined only for discrete values of a. The net rate is maximized when the length of the step element has a critical length l^*, the nucleus being formed by passage over part of the barrier ridge which is not necessarily at the saddle point in the free energy surface treated as a continuum. For this problem, a summing of all the forward and backward reactions leads to a nucleation rate per unit area of surface of the form [3]:

[13] The pre-exponential is sometimes written as $G_0 T$, apparently in the belief that the main temperature dependence of the pre-exponential arises from the factor (kT/h) that applies to the elementary jump rate processes for each individual forward and backward reaction. Actually $I_{s(0)}$ contains a factor analogous to K in eq (1) that varies as $(\Delta T)^{-2}$ for a number of models. Even this dependence on temperature is negligible in the problems of interest here, and G_0 may be considered to be independent of temperature to a sufficient approximation.

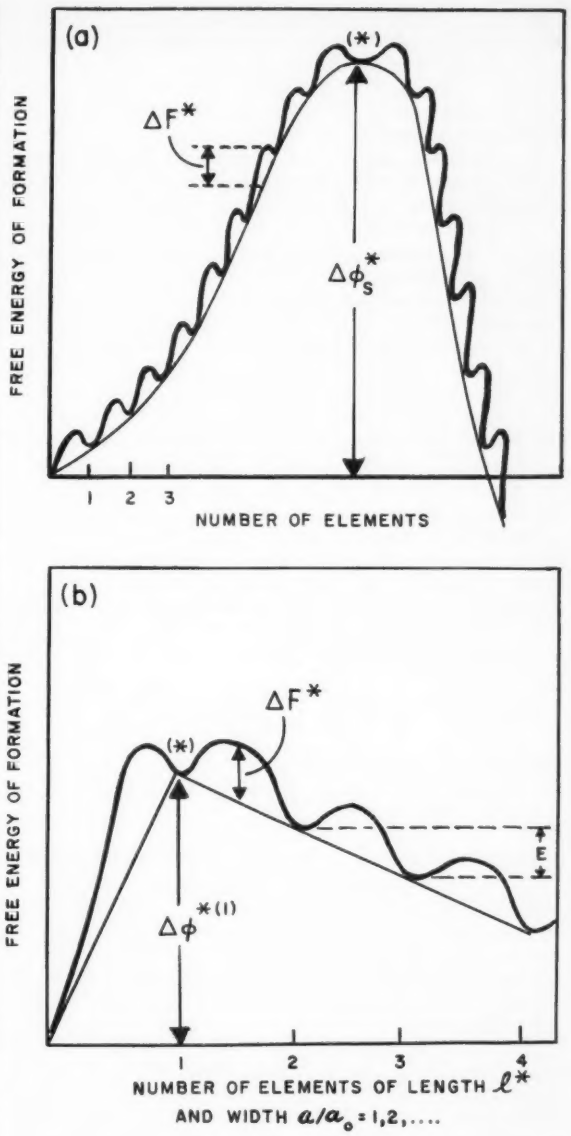

FIGURE 3. *The two types of nucleation problem encountered in calculating the rate of radial growth of polymer spherulites.*

(a) Activated state (*) reached by successive addition of a large number of elements (Turnbull and Fisher, continuum free energy surface model).
(b) Activated state (*) reached in single step, i.e., by the accretion of one element of length l^*, as in certain cases of monomolecular layer growth (Lauritzen and Hoffman, discrete free energy surface model).

$$I_s = I_{s(1)} \left[\frac{\sinh(E/2kT)}{1+\exp(-\Delta\phi_s^{*(1)}/2kT)\sinh(E/2kT)}\right] \times \exp\left[-\frac{\Delta H^*}{kT}\right] \exp\left[-\frac{\Delta\phi_s^{*(1)}}{kT}\right]. \quad (22)$$

Here $\Delta\phi_s^{*(1)}$ is the free energy function $\Delta\phi_s$ evaluated for the case $\nu=1$, where ν is the number of elements (i.e., the number of chains of critical length l^*) laid side by side on the crystal substrate, and E the incremental increase of stability on adding each new element (see fig. 3b).

In the case under consideration, the activated state is reached when one such element of length l^* attaches to the surface. This is what is meant by the statement that the activated state is reached in "one step"; the term "one step" does not refer here to the elementary process where a single polymer segment is laid down during the process of building up the length l^*. The value of ΔF^* and ΔH^* relevant to the interfacial jump rate characteristic of the laying down of an entire step element of length l^* may be larger than ΔF^*_{seg} and ΔH^*_{seg}, which refer to the jump rate at the interface for the elementary segmental processes. The principal contribution to ΔF^* and ΔH^* probably comes from jump rate processes at the end of the nucleus, especially in the case of folded systems.

In most cases of practical interest, the term in brackets involving sinh $(E/2kT)$ will be sufficiently independent of temperature to be taken into the pre-exponential. Then by applying the same arguments used earlier, I_s may be transformed into an expression for the radial growth rate of a spherulite:

$$G=dr/dt=G_{0(1)}\exp\left(-\frac{\Delta H^*}{kT}\right)\exp\left(-\frac{\Delta\phi_s^{*(1)}}{kT}\right). \quad (23)$$

(small surface nuclei where activated state is reached in single step; $\Delta\phi^{*(1)}$ calculated from discrete free energy surface model)

It is emphasized that eq (23) frequently applies in the important case of growth by addition of monomolecular layers. If eq (21) is inadvertently applied in such instances, misleading or even erroneous results may be obtained; it is important not to confuse $\Delta\phi_s^*$ (continuum model) with $\Delta\phi_s^{*(1)}$ (discrete model) in calculating the work required to form the nucleus of critical size.

The calculations of the radial growth rate of spherulites to be given in this paper refers to experiments where an unoriented polymer is *first* heated well above T_m and *then* rapidly cooled to the growth temperature. The less readily interpretable experiments where specimens are first quenched from the melt and then rewarmed to the growth temperature are discussed briefly in section 8.2.

3.2. The Jump Rate Term in Supercooled Liquids

Another point of interest is that the interfacial jump rate term may require modification, particularly if it depends strongly on segmental motions in the supercooled liquid polymer. If such motions dominate the interfacial jump rate process, it can be shown that the term $\exp[-\Delta H^*/kT]$ in the various equations that have been given may be replaced by the empirical expression based on the work of Williams, Landel, and Ferry [28]

$$\exp[4.12\times10^3T^2/RT(51.6+T-T_g)^2] \quad (24)$$

that is valid between T_g and $T_g+100°$. Here T_g is the glass transformation temperature. This is equivalent to the statement that ΔH^* depends on temperature, and has the value $4.12\times10^3T^2/(51.6+T-T_g)^2$. For the sake of simplicity, and for the reason that crystallization temperatures of interest often lie above $T_g+100°$, we have not employed this empirical expression in the body of the paper. Near the melting point, the constant value $\Delta H^*=20{,}000$ cal mole^{-1} may be employed for trial purposes.

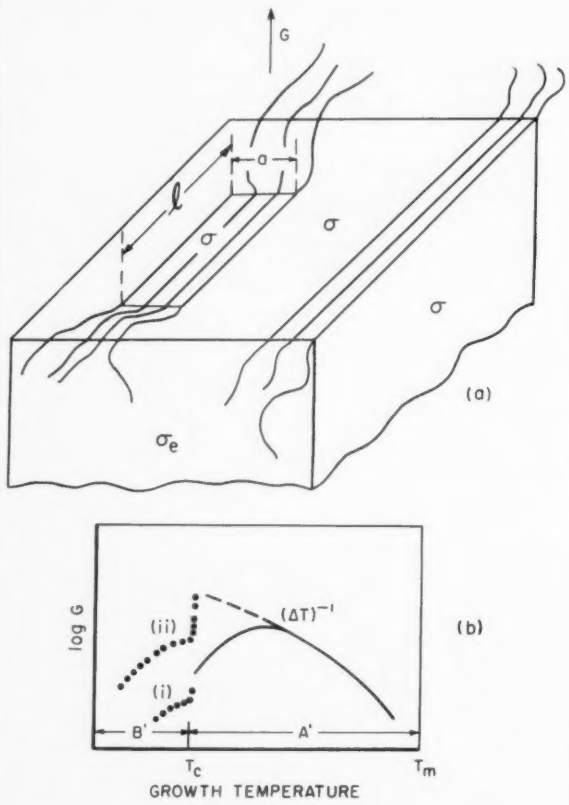

FIGURE 4. *The coherent bundlelike surface nucleus model and its crystal growth rate behavior.*

(a) Coherent nucleus of length l, width a, and monomolecular layer thickness b_0 on substrate crystal. Heavy arrow marked G indicates direction of crystal growth.

(b) The logarithm of growth rate versus temperature, – – – – log G versus T if effect of jump rate is small; —— behavior where jump rate lowers log G causing maximum to appear in log G versus T; . . . . possible effect of interference with growth by excess nucleation in surrounding medium (cf. fig. 1(a)).

4. Polymer Crystal Growth by Coherent Bundlelike Surface Nucleation

4.1. Model

The model used is shown in figure 4a. The polymer molecules in the nucleus are colinear with those in the substrate, i.e., the surface nucleus is of the *coherent* type. The thickness of the surface nucleus is b_0, corresponding to one molecular layer.[14] Once formed, this nucleus, which has a length l and width a, leads to the rapid completion of a layer of thickness b_0 on some large area of the growing face. Note that the molecules are oriented at a right angle to the direction of growth, which is marked "G". The lateral surface free energy is σ, and the end surface free energy is σ_e.

The coherent bundlelike surface nucleus model (or one of several simple modifications of it) has been presented at various places in the literature as a pattern for typical spherulitic growth. However, calculations on this model should be approached with full recognition of the fact that it is very improbable that it will lead to a typical lamellar spherulite. The relationship of this model to the structure of spherulites will be discussed shortly. Meanwhile, we shall treat the model as if it did produce a large crystal for which one could define a radial growth rate G.

4.2. Growth Rate for Bundlelike Coherent Nucleus Model

A prime will be used to distinguish the quantities connected with coherent surface nuclei from those belonging to primary nuclei. Later, a double prime will be used to denote quantities related to noncoherent nuclei.

Region A′: In region A', i.e., from temperatures near T_m on down to those corresponding to rather high supercooling, a and l may be regarded as not having reached their minimal values, and the free energy of formation may be written as

$$\Delta\phi = 2ab_0\sigma_e + 2b_0l\sigma - ab_0l(\Delta f). \tag{25}$$

Notice that no term involving al appears in this expression: for a strictly coherent nucleus, only the work required to build the sides enters. By setting $(\partial\Delta\phi/\partial a)_l$ and $(\partial\Delta\phi/\partial l)_a$ equal to zero, it is determined that $a^* = 2\sigma/(\Delta f)$ and $l^* = 2\sigma_e(\Delta f)$. Then it is found that

$$\Delta\phi^* = \frac{4b_0\sigma\sigma_e}{(\Delta f)}. \tag{26}$$

Since a and l are variables, so that the surface nucleus is not formed in one step, G is to be calculated with eq (21):

$$G_{A'} = G_0 \exp\left(-\frac{\Delta H^*}{kT}\right) \exp\left(-\frac{4b_0\sigma\sigma_e T_m^2}{T(\Delta h_f)(\Delta T)kT}\right). \tag{27}$$

[$(\Delta T)^{-1}$ law]

Region B′: The question must now be raised as to what behavior must be expected of the radial growth rate at high degrees of supercooling, provided that the jump rate term has not already caused G to fall to a low value.

Suppose that the crystals whose radial growth rate we have discussed were of heterogeneous origin, so that in region A' they were born near $t=0$. Then at the T_c transition in the supercooled bulk phase, a vast number of tiny bundlelike nuclei would be injected by the nonsteady state nucleation mechanism described in section 2.3 into the matrix in which the crystal was attempting to grow. Thus, at or near the T_c transition characteristic of the pure bulk phase, which will take place at $\Delta T_c \cong 4\sigma T_m/(\Delta h_f)a_{\min}$, the radial growth of the older and larger crystals would be rather abruptly slowed down because of depletion of crystallizable material, and impingements.

If it is assumed that the crystallites are of entirely homogeneous origin, a rather similar phenomenon can take place. Here I_A, as calculated for a bundlelike nucleus in section 2 may be regarded as being proportional to the rate of injection. Barring interference from the jump rate term, the injection rate would rather abruptly attain a value considerably in excess of the extrapolated value of I_A. Such a high injection rate at and below T_c due to nonsteady state nucleation would lead to a massive number of impingements. Any crystallites formed in these circumstances would tend to be small, and have a significantly reduced growth rate.

Summary: A schematic diagram of the variation with temperature of the radial growth rate of a body that is governed by a coherent bundlelike surface nucleus is shown in figure 4b. Curves (i) and (ii) in region B' are intended to represent different degrees of interference with the growth resulting from the incursion of a vast number of competing microcrystals resulting from nonsteady state nucleation. The solid line in region A', which exhibits a maximum in G because of the effect of the jump rate term, shows the type of behavior that is most probable if the model is valid.

It is considered that the treatment of the secondary (coherent) bundlelike surface nucleus outlined in section 4.2 is more fully illustrative than that given previously using the customary pillbox surface nucleus (cf. reference [11]). The pillbox nucleus requires only a single surface free energy that corresponds to our σ, and leads to a nucleation term involving σ^2. For a surface nucleus consisting of chain molecules lying on a flat surface, it seems better to distinguish between the lateral surfaces, and the end surface, giving a nucleation term involving the product $\sigma\sigma_e$. If the growth nucleus were assumed to form on the end of the bundle, so that the direction of growth was parallel to the polymer chains, then the pillbox nucleus with its single lateral surface free

[14] Note that a_0 has a different meaning than $a_{\min}$. The quantities a_0 and b_0 refer to the appropriate lateral lattice spacings in the polymer crystal, while $a_{\min}$ and $b_{\min}$ refer to the minimum values that a and b may take on in a homogeneous nucleus. In general, $a_{\min}$ and $b_{\min}$ will be larger than a_0 and b_0.

energy would be justified. However, this model would not lead to a "spherulite" where the polymer chains were normal to the radius.

4.3. Coherent Bundlelike Growth and Spherulite Structure

Though much attention has been given here and elsewhere to various coherent bundlelike growth nucleus models, it remains to be seen whether or not such a growth mechanism would lead to a roughly spherical object that would be recognized as a spherulite. When this is done, it will emerge that one must have strong reservations about the ability of the model to reproduce anything resembling a typical lamellar spherulite.

Suppose that we attempt to construct a single "lamella" on the strictly bundlelike pattern of the type shown in figure 5(a) where the polymer chain axes are perpendicular to the σ_e plane. It is simply not possible to create a large flat surface of the type commonly seen in lamellar spherulites in this manner because of the density difference between the supercooled liquid and crystalline phases, and the fact that polymer molecules with covalent bonds connect these two phases in the bundlelike system of crystallization. Growth in the "radial" direction, G_r, for such a hypothetical "lamella" would clearly result in cumulative strain at the bundle ends. As pointed out by Matsuoka and Maxwell [25], and Frank [26], the crystal would actually tend to become ellipsoidal (see dotted lines in figure 5(a)) in order to minimize the total surface free energy. If the bundle end were assumed to remain flat, the effective value of σ_e would increase enormously as the crystal grew in the G_r direction, thus aborting its growth.

This effect should become distinctly apparent for nuclei where the radius corresponds to a mismatch between the supercooled liquid and crystal of one molecular diameter. A conservative estimate would place this radius at less than 50 A under normal circumstances. The coherent bundlelike growth model where the polymer chains in the crystal are perpendicular to the hypothetical σ_e plane is clearly defective in its ability to predict anything resembling a typical lamella.

It might be suggested that the cumulative strain problem discussed above for the perpendicular case can be minimized by allowing the chains on the faces of a flat bundlelike lamella to exit from the crystal at an angle ζ. In such a "lamella", the chain axes would thus be tilted with respect to the presumably flat surface of the end, as shown schematically in figure 5(b). The idea is that the chains in the surface region open up to spacings $a_0+\Delta a_0$ and $b_0+\Delta b_0$ that closely corresponds to the mean molecular spacing in the supercooled liquid polymer. It is not entirely clear that this would relieve the cumulative strain of the type that exists in the perpendicular case if the σ_e surface must be kept flat. It must be remembered that the "lamella" will be three dimensional, i.e., both the a and b spacings in the surface phase must be larger than a_0 and b_0. It seems likely that the end surface would tend to become curved. Even ignoring these effects, it is clear that the work required to bend the polymer bonds at the required angle, and to increase the spacings in the surface phase, will lead to at least a fairly large σ_e value from noncumulative strain as noted in section 2.6. As will be demonstrated below, a lamella with a sensible end surface free energy that is not subject to cumulative strain will not maintain its "step height" or "lamellar" thickness.

Consider now the relative growth rates in the radial (r) and lengthwise (l) directions for a bundlelike crystal of the type illustrated in figures 5(a) and 5(b) on the assumption that cumulative strain is absent. The growth in the radial direction has already been calculated:

$$G_r=G_0 \exp\left(-\frac{\Delta H^*}{kT}\right) \exp\left(-\frac{4b_0\sigma\sigma_e T_m^2}{T(\Delta h_f)(\Delta T)kT}\right). \tag{28}$$

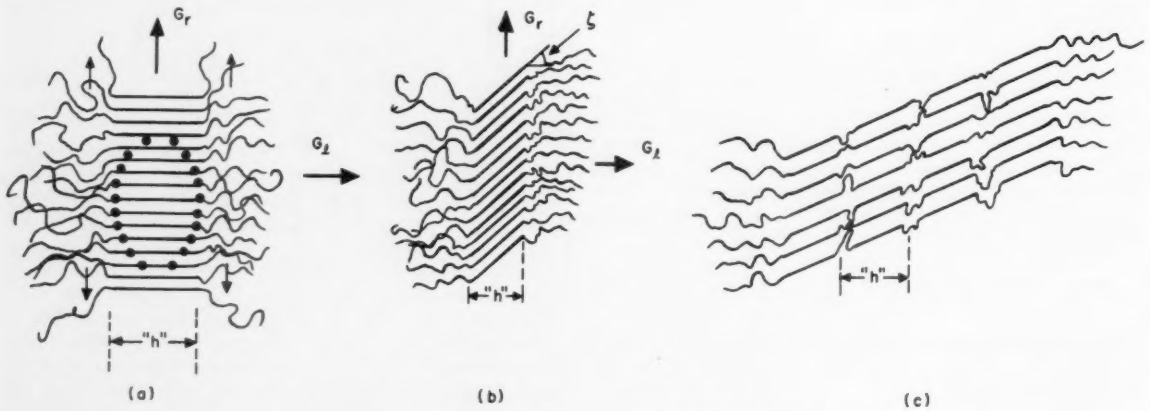

FIGURE 5. *Hypothetical structure of bundlelike lamellae.*

(a) Isolated lamella with chains perpendicular to flat bundle ends. Light arrows show site of cumulative strain. "h" represents hypothetical step height. Dotted lines illustrate how crystal would round off end to reduce strain and total surface free energy.
(b) Isolated lamella with chains tilted with respect to flat bundle end. Cumulative strain is reduced, but "lamella" will grow in both G_l and G_r directions.
(c) Stacks of interconnected bundlelike "lamellae" with tilted chains.

The corresponding growth rate on the σ_e faces of the "lamella" is

$$G_l = G_0 \exp\left(-\frac{\Delta H^*}{kT}\right) \exp\left(-\frac{4l_{\min}\sigma^2 T_m^2}{T(\Delta h_f)(\Delta T)kT}\right), \tag{29}$$

where $l_{\min}$ is the length of the coherent surface nucleus that forms on the bundle end. (If cumulative strain occurred in the bundle ends, both σ and σ_e would increase rapidly with coherent growth in the r and l directions, and the crystal would not grow to form a large crystal like a lamella, but would form instead an ellipsoidal bundlelike microcrystal of limited size as noted in section 7.)

The quantity $l_{\min}$ may be taken as the minimum length of polymer chain that is crystallizable. It is impossible to escape the fact that the bundlelike crystal will grow at a sensible rate on the σ_e face if growth on the other surfaces is rapid at the same supercooling. Even if $l_{\min}$ is assumed to be several times larger than b_0, it must be remembered that σ_e will probably be substantially larger than σ. Thus we must expect G_l to be roughly comparable to G_r, or possibly even considerably larger. In such a case the bundlelike "lamella" would not maintain its hypothetical step height "h" as radial growth progressed. The above calculation accords with the concept that a high energy surface will grow more rapidly than a low energy one.[15] It may be concluded that an isolated "lamella" that maintained its thickness or "step height" cannot be predicted with either of the bundlelike models depicted in figure 5(a) and 5(b).[16]

We consider it preferable to consider only theories of polymer crystal growth capable of predicting the existence of an isolated lamella in a straight forward manner. It is then a simple manner to generalize to the case where the lamellae occur in stacks. However, there is one rather arbitrary model involving stacks of bundlelike "lamellae" that deserves comment. This is shown in figure 5(c). Here one polymer molecule participates in more than one sheet, with entangled and "amorphous" polymer between. By drawing the model as shown, i.e., with chains tilted with respect to the σ_e plane, the question of cumulative strain is supposedly minimized. Also the point that bundlelike lamellae will grow on the σ_e face is temporarily evaded, except at the outer edges. This model of "lamellar" structure suffers from some drawbacks. First, there would appear to be no simple way to predict the formation of such a structure on theoretical grounds. Second, it is difficult to discern how such a structure could lead to the fracture or surface replica patterns, with many easily distinguishable steps, that characterize lamellar spherulites. To do this, it would apparently be necessary to assume that covalent bonds broke only in the amorphous regions. It seems much more likely that relatively few covalent bonds are broken, and that the lamellar separation is opposed mainly by van der Waals forces, for example those at two chain folded surfaces. Finally, the tipping of crystals at low draw ratios is difficult to explain with the model.

The bundlelike models for "lamellae" criticized above are all in the category where the flat "lamellar" surfaces are assumed to be of the σ_e type, i.e., where polymer chains protrude from the surface. We now consider briefly the possibility that the flat faces of the lamellae might correspond to polymer chains that lie bundle fashion parallel to the large flat faces, but where the chains still subtend a right angle to the radius of the spherulite. Entirely apart from the fact that there is already some evidence that the polymer chains are essentially normal to the large flat lamellar faces (see [4] and [42]), this is an unlikely model for a stable lamella of uniform step height. The flat faces would be σ type, and would therefore grow normal to the spherulite radius at a rate comparable to the radial growth rate, as implied by eq (28), if cumulative strain did not occur. If cumulative strain did occur, large lamellae with large flat σ-type faces would not be formed since the crystallites would be of limited size, and tend to be ellipsoidal in shape.

Our conclusion is that the coherent bundlelike surface nucleus model does not lead to a tenable representation of a typical lamellar spherulite, where large stacks of more or less separable lamellae comprising the major fraction of the crystallization present exist, and where at a fixed growth temperature each lamella has a relatively uniform step height even with extended growth.

The remaining question concerns whether the coherent bundlelike model of polymer crystal growth can lead to a spherical object that is not lamellar. For the case of large chain ends that are excluded from the crystal, this theory appears to lead to microcrystals scattered here and there throughout the medium, the equilibrium dimensions of these microcrystals being determined by the distribution of molecular weight (see sec. 2.5). Similarly, cumulative strain would lead to ellipsoidal microcrystals of limited size. For the strictly coherent case, there is no reason to suppose that these microcrystals would be arranged into a spherical array. With the additional assumption of noncoherent nucleation on the surfaces, a spherical array of bundlelike but nonlamellar microcrystals can be predicted (sec. 7).

★5. Radial Spherulitic Growth by Coherent Surface Nucleation With Chain Folds

5.1. Details of the Model and Derivation of the Radial Growth Rate Law

Here it is assumed that the rate determining step is the formation of a coherent surface nucleus of monomolecular thickness $\mathbf{b}_0$, length $\mathbf{l}$, and width a on

[15] An exception to this occurs in the case of a high energy surface comprised of chain folds, which for obvious reasons cannot grow in the same sense as a bundlelike crystal in the chain direction.

[16] It is extremely improbable that chain entanglements would cause all bundlelike nuclei to abruptly stop growing in the G_l direction in such a manner as to produce a uniform length comparable to the thickness of a lamella.

the substrate crystal (fig. 6a). The end surface free energy of this nucleus is σ_e, and the two lateral surface free energies are each taken as σ. The quantity σ_e is defined as in eq (1), and σ has the same meaning as in section 2.4. Both of these surface free energies refer to abrupt phase boundaries, and are well defined quantities.

The objective is to calculate the rate of nucleation on the growing face of the lamella, since this establishes the radial growth rate of the spherulite (the direction of radial growth is denoted by the heavy arrow marked "G"). The growing face may actually be wedge-shaped, the face on either side of the peak having a surface free energy σ. The assumption of such a geometry would not materially alter the calculations to be given, and it is sufficient for the purpose of calculating the radial growth rate to consider the simpler model with one growing face. Note that the polymer chains are normal to the spherulite radius.

The value of $\mathbf{l}$ for the initial substrate could be assumed to be that of a primary nucleus, $\mathbf{l}_p^*=4\sigma_e/(\Delta f)$, but this is not necessary for the treatment: one could equally well assume heterogeneous initiation. The model leads in a natural way to many features of lamellar spherulites. The connection between this model and spherulite structure will be discussed in section 5.4.

Region **A′**: The free energy of formation of the surface nucleus is

$$\Delta\phi=2\mathbf{a}\mathbf{b}_0\sigma_e+2\mathbf{b}_0\mathbf{l}\sigma+2\mathbf{a}\epsilon-\mathbf{a}\mathbf{b}_0\mathbf{l}(\Delta f). \qquad (30)$$

The edge free energy ϵ is included to take account of the possibility that a loop in a surface nucleus where $\mathbf{l}\leq\mathbf{l}^*$ may be more difficult to form than one where $\mathbf{l}>\mathbf{l}^*$.[17] The inclusion of the edge free energy leads to only a slight complication of the results, and is useful in discussing the step height and melting behavior of the crystal lamellae that will be observed (see sec. 5.2).

The treatment for the coherent surface nucleus with chain folds differs significantly from that given for the corresponding bundlelike nucleus. The quantity $\mathbf{l}$ will not change rapidly with growth, and is to be regarded as fixed for a given nucleus as it traverses the nucleation path. (Other folded nuclei may of course have different values of $\mathbf{l}$, but in each case $\mathbf{l}$ is constant for a given nucleus.) In this situation, the barrier ridge that must be overcome to form a stable surface nucleus is at $\mathbf{a}=\mathbf{a}_0$. Thus, during the formation process for a given nucleus, two of its dimensions, namely, $\mathbf{b}=\mathbf{b}_0$ and $\mathbf{l}=\mathbf{l}^*$, are fixed. It remains to be determined what value of $\mathbf{l}$ leads to the maximum rate of steady state nucleation. This value of $\mathbf{l}$ is denoted $\mathbf{l}^*$.

From eq (30) it is readily determined that a growable nucleus can be formed only when $\mathbf{l}$ is slightly in excess of

$$\mathbf{l}=\frac{2\sigma_e}{(\Delta f)}+\frac{2\epsilon}{\mathbf{b}_0(\Delta f)}. \qquad (31)$$

If $\mathbf{l}$ has a value less than this, the embryo becomes increasingly less stable as the width $\mathbf{a}$ is increased, as shown in figure 6b. Similarly, if $\mathbf{l}$ has exactly the value given by eq (31), no stable nucleus will be formed, since the free energy of formation is a constant and cannot ever become negative with any increase of $\mathbf{a}$ (fig. 6b). Hence $\mathbf{l}^*$ must be slightly in excess of that given by the above expression.

The competition between two effects determines the conditions under which the maximum rate of nucleation will be observed. Notice from the schematic diagram in figure 6b that at $\mathbf{a}=\mathbf{a}_0$ the activated state with the *highest* free energy is associated with a value of $\mathbf{l}$ that leads to the formation of

[17] The edge free energy is taken as ϵ for $\mathbf{l}\leq\mathbf{l}^*$, and zero for $\mathbf{l}>\mathbf{l}^*$. In a more detailed analysis, the edge free energy might be taken as ϵ_1 for $\mathbf{l}<\mathbf{l}^*$, ϵ_2 for $\mathbf{l}=\mathbf{l}^*$, and zero for $\mathbf{l}>\mathbf{l}^*$.

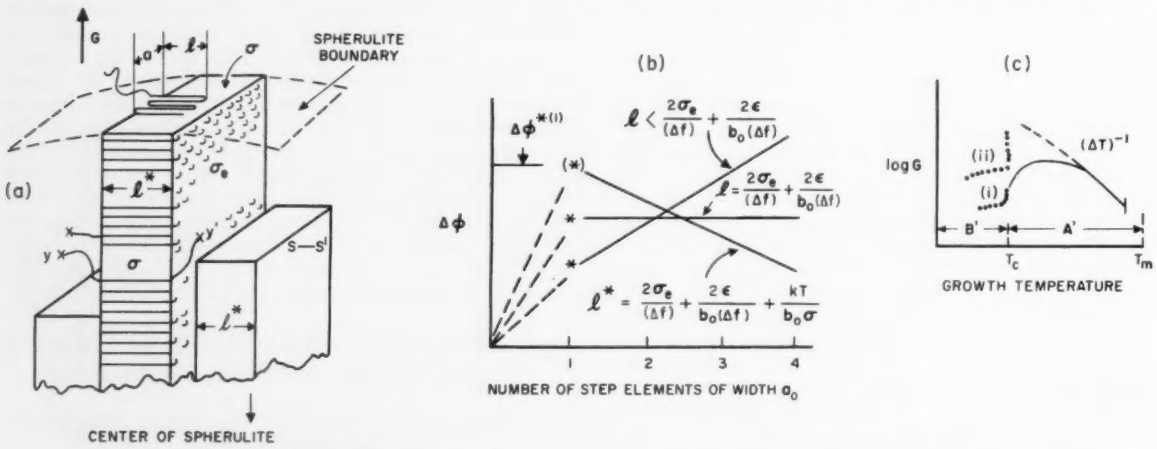

FIGURE 6. *The coherent chain folded surface nucleus model of spherulitic growth and its rate behavior.*

(a) Lamella with folded coherent nucleus of length $\mathbf{l}$, width $\mathbf{a}$, and monomolecular layer thickness $\mathbf{b}_0$ on its surface. Heavy arrow marked **G**, indicates direction of radial growth of lamellar spherulite. Arrow s–s′ indicates axis of spiral dislocation. Chain y–y′ indicates molecule incorporated bundle fashion into lamella.
(b) Schematic diagram illustrating cause of a certain value of the step height, $\mathbf{l}^*$, giving maximum surface nucleation rate.
(c) Logarithm of radial growth rate of spherulite as function of temperature. — — — log **G** versus T if jump rate effect is small; —— most representative case where jump rate lowers log **G** causing maximum to appear near $(T_m+T_c)/2$; . . . . exhibits effect of excess nucleation rate in medium surrounding spherulite.

a stable nucleus on further addition of step elements, and conversely, the activated state with the *lowest* free energy is associated only with the formation of a metastable embryo. (The free energy of activation at $\mathbf{a}=\mathbf{a}_0$ is marked "*" in each instance.) Thus there is some length slightly greater than that given by eq (31) which will lead to a maximum steady state rate of nucleation.

It has been shown in detail elsewhere (see eqs (59) to (66) and appendix 5.2 of reference [3]) that

$$\mathbf{l}^*=\frac{2\boldsymbol{\sigma}_e}{(\Delta f)}+\frac{2\boldsymbol{\epsilon}}{\mathbf{b}_0(\Delta f)}+\frac{kT}{\mathbf{b}_0\boldsymbol{\sigma}} \tag{32}$$

is the value of the length of the growth nucleus that leads to the maximum rate of steady state nucleation. This is, of course, the step height of the crystal that will actually be formed by the coherent nucleation process.

On inserting eq (32) into (30) with $\mathbf{a}=\mathbf{a}_0$, the free energy of formation is found to be

$$\boldsymbol{\Delta\phi}^{*(1)}=\frac{4(\mathbf{b}_0\boldsymbol{\sigma}\boldsymbol{\sigma}_e+\boldsymbol{\sigma}\boldsymbol{\epsilon})}{(\Delta f)}-\frac{\mathbf{a}_0(\Delta f)kT}{\boldsymbol{\sigma}}+2kT. \tag{33}$$

The second two terms in eq (33) arise from the term $kT/\mathbf{b}_0\boldsymbol{\sigma}$ in eq (32). On inserting $\boldsymbol{\Delta\phi}^{*(1)}$ into eq (23), there is obtained

$$\mathbf{G}_{\mathbf{A}'}=\mathbf{G}_{0(1)}\exp\left(-\frac{\Delta H^*}{kT}\right)\exp\left(-\frac{4\mathbf{b}_0\boldsymbol{\sigma}\,[\boldsymbol{\sigma}_e+(\boldsymbol{\epsilon}/\mathbf{b}_0)]T_m^2}{T(\Delta h_f)(\Delta T)kT}+\frac{\mathbf{a}_0(\Delta h_f)(\Delta T)T}{T_m^2\boldsymbol{\sigma}}\right), \tag{34a}$$

if the unimportant factor e^2 arising from $2kT$ in eq (33) is ignored. An evaluation of the term $\exp[\mathbf{a}_0(\Delta h_f)(\Delta T)T/T_m^2\boldsymbol{\sigma}]$ shows that it comes to approximately $\exp[(\Delta T)/100]$ for normal values of the parameters. This dependence on temperature is completely negligible compared to the other two exponential terms in eq (34a), and the term may safely be taken into the pre-exponential factor $\mathbf{G}_{0(1)}$. Then we have as a good approximation the expression

$$\mathbf{G}_{\mathbf{A}'}=G_{0(1)}\exp\left(-\frac{\Delta H^*}{kT}\right)\exp\left(-\frac{4\mathbf{b}_0\boldsymbol{\sigma}[\boldsymbol{\sigma}_e+(\boldsymbol{\epsilon}/\mathbf{b}_0)]T_m^2}{T(\Delta h_f)(\Delta T)kT}\right) \tag{34b}$$

$[(\Delta T)^{-1}\text{ law}]$

for the rate of growth of chain folded systems in region $\mathbf{A}'$, which extends from near T_m down to T_c (see below). The term $\boldsymbol{\epsilon}/\mathbf{b}_0$ will not exceed $\boldsymbol{\sigma}_e$ in magnitude, and may be considerably smaller.

It is somewhat misleading to derive eq (34b) by differentiating eq (30) with respect to $\mathbf{a}$ and $\mathbf{l}$, setting the results equal to zero to get $\mathbf{l}^*=2\boldsymbol{\sigma}_e/(\Delta f)+2\boldsymbol{\epsilon}/\mathbf{b}_0(\Delta f)$ and $\mathbf{a}^*=2\boldsymbol{\sigma}/(\Delta f)$, inserting these into (30) to get $\Delta\boldsymbol{\phi}^*=4(\mathbf{b}_0\boldsymbol{\sigma}\boldsymbol{\sigma}_e+\boldsymbol{\sigma}\boldsymbol{\epsilon})/(\Delta f)$, and thence to eq (34b) by way of eq (21). Calculations involving this method have been proposed in the literature in connection with chain fold growth for the case $\boldsymbol{\epsilon}=0$ [15]. The free energy surface is not a continuum in the region of interest as implied by the differentiation, and the value of $\mathbf{l}^*$ obtained does not permit growth at all, as is seen in figure 6b.

At very low supercooling, the step height will become large enough so that a considerable number of the molecules cannot fold if large chain ends are excluded from the crystal, as mentioned in section 2.5.

Region $\mathbf{B}'$: The rate law cited above will be valid from near T_m on down to a temperature $\mathbf{T}_c$ corresponding to a degree of supercooling of approximately $\Delta T_c=4\boldsymbol{\sigma}T_m/(\Delta h_f)\mathbf{a}_{\min}$. At this temperature and below, folded nuclei of minimal size of the type described in section 2.5 will appear in profusion in the supercooled medium due to nonsteady state nucleation, and slow up or even stop the radial growth of any fairly well developed spherulites that are already present. The region below T_c is called region $\mathbf{B}'$. If it were not for the nonsteady state nucleation effect, Region $\mathbf{B}'$ would exhibit a $(\Delta T)^{+1}$ radial growth rate law analogous to eq (10). Alternatively, bundlelike nuclei of nonsteady state origin may appear at T_c if σ_e is sufficiently small for embryos of minimal size.

Summary: A schematic diagram of the growth rate behavior of this model is shown in figure 6c. Curves (i) and (ii) in region $\mathbf{B}'$ represent different degrees of interference with the radial growth rate of the spherulite caused by the rapid incursion of crystallites of nonsteady state origin into the surrounding medium. The vertical mark near T_m indicates the restriction that will occur on chain folding when the step height approaches one half the molecular length if large chain ends are excluded from the crystal. In the case of small chain ends that can be accepted as defects in the crystal, this restriction will be relaxed, and chain folding can then occur nearer to T_m.

In these plots, the negative temperature coefficient part of the curves near the melting point is due to the nucleation term, and the positive temperature part occurring at lower temperatures is due to the effect of the jump rate term.

Using normal values of the parameters in the nucleation term in eq (34b), and setting $\Delta H^*=20{,}000$ cal mole^{-1} (or alternatively, using eq (24) in its range of validity), the maximum in log $\mathbf{G}_{\mathbf{A}'}$ is found to appear somewhere between 0.8 and 0.9 T_m. Since the glass transition temperature T_g for many polymers obeys the empirical relation $T_g=0.66\ T_m$, it is seen that the maximum in log $\mathbf{G}_{\mathbf{A}'}$ falls about midway between T_m and T_g. T_c will often occur well below the maximum in log $\mathbf{G}_{\mathbf{A}'}$, say at 0.75 T_m. It follows that the T_c transition will frequently be obscured by the lowering of log $\mathbf{G}_{\mathbf{A}'}$ by the jump rate term. Thus it is to be expected that only a simple maximum of log $\mathbf{G}_{\mathbf{A}'}$ versus T will appear in many instances, as denoted by the solid line in figure 6c. The T_c transition would be most easily found in a polymer with low $\boldsymbol{\sigma}$ and high $\mathbf{a}_{\min}$, the transition being closest to T_m in this case.

It can be shown for a number of systems that an excellent fit of the radial growth rate of the spherulites as a function of temperature can be obtained with an expression of the form of eq (34b), i.e.,

$\log_e(G/G_0) = -\Delta H^*/RT - K_1/T^2(\Delta T)$, where K_1 is a constant. The value of K_1 can be used to determine the product $\sigma\sigma_e$, or more precisely $\sigma(\sigma_e + \epsilon/\mathbf{b}_0)$, for a chain folded lamellar spherulite. This product should frequently lie in the range 100 to 1,000 erg^2 cm^{-4}. Such values are obtained, but it is not certain that they all refer to distinctly lamellar spherulites.

5.2. Behavior of the Step Height

The step height of a growing lamella, $\mathbf{l}^*$, is given by eq (32). This expression holds no matter whether the lamella was originally heterogeneously or homogeneously nucleated. The term $2\sigma_e/(\Delta f)$ will contribute at least one half of the full value of $\mathbf{l}^*$, and possibly almost all of it. The contribution from the $kT/\mathbf{b}_0\sigma$ term is rather small, and nearly constant, as indicated previously. The other term, $2\epsilon/\mathbf{b}_0(\Delta f)$, will now be considered, especially in relation to how it affects the step height of the growth nucleus compared to the primary one.

The step height of a homogeneous nucleus with folds is $4\sigma_e/(\Delta f)$.[18] If ϵ is negligible, the step height of the coherently grown lamella will be only slightly over one half of this value, namely, $2\sigma_e/(\Delta f) + kT/\mathbf{b}_0\sigma$. As the effect of ϵ increases, the step height of the growing lamella will eventually approach the value $4\sigma_e/(\Delta f)$. The step height of the growth nucleus will not exceed that of the primary nucleus because ϵ is a function of position, and will fall to a low or zero value outside the edge of the primary nucleus. (It will be recalled that ϵ is a measure of any extra work that might be required to cause a loop to lie on a flat substrate in from the edge or at the edge; it is therefore either zero or quite small for a loop protruding over the edge.)

The main point here is that it is not always to be expected that a growing lamella will have the same step height as the primary nucleus with folds.

Temperature Dependence of Step Height: The temperature dependence of the step height is of considerable interest. It is seen from eqs (7) and (32) that the step height of a growing lamella is

$$\mathbf{l}^* = \frac{(2\sigma_e + 2\epsilon/\mathbf{b}_0)T_m^2}{(\Delta h_f)(\Delta T)T} + \frac{kT}{\mathbf{b}_0\sigma}. \tag{35}$$

Ignoring relatively unimportant variations with temperature, this may be written in the approximate form

$$\mathbf{l}^* = \frac{\mathbf{Y}}{(\Delta T)} + \mathbf{Z}. \tag{36}$$

Thus, $\mathbf{l}^*$ will increase with rising temperature, reaching large values near T_m. In most experiments, the quantity $\mathbf{Z} = kT/\mathbf{b}_0\sigma$ will be negligible compared to $\mathbf{Y}/(\Delta T)$. (The value of $\mathbf{Z}$ will commonly be roughly 20 A.)

It should prove possible in some cases to verify the temperature dependence of the step height predicted by eq (36) by careful low-angle X-ray studies on unoriented bulk polymer specimens crystallized at various temperatures. If the X-ray spacings indicate such a dependence of step height with degree of supercooling, this may be regarded as a confirmation of the kinetic nucleation viewpoint of chain folded growth proposed in this paper. This confirmation would be especially convincing in the case of a polymer that was known from electron microscope studies to have a lamellar texture, since this in itself strongly implies the existence of substantially chain folded crystals. It is very doubtful that strictly bundlelike crystallization could lead to eq (36), because such crystals would either grow in the $\mathbf{l}$ direction (noncumulative strain) or abort (cumulative strain). However, a demonstration that eq (36) is obeyed may still only mean that a substantial fraction of the crystallization present is in the chain folded configuration, rather than all of it; some bundlelike character is to be expected in the otherwise chain folded lamellae, and numerous small bundlelike embryos may be present. (See also remarks in section 8.3 concerning crystallization from the highly oriented melt.)

An interesting point that arises in connection with the above is that the theory predicts that the characteristic step height of the lamellae in a spherulite can be alternated between different values by successively crystallizing at different temperatures. In this way it should be possible to make lamellae that are alternately thick and thin as the radial growth of a spherulite proceeds.

It is emphasized that the results quoted above refer to *isothermal* crystallization. For slowly growing spherulites, sufficiently isothermal conditions will be maintained, but at strong supercooling where the rate of crystallization becomes high, the heat of crystallization may raise the local temperature and tend to artificially flatten out the $\mathbf{l}^*$ *versus* T curve predicted by eq (35) or (36).

Melting Behavior: Consider now the melting point of the chain folded lamellae. It is readily deduced from eq (30) that the temperature of melting of a lamella that is large in the $\mathbf{a}$ and $\mathbf{b}$ dimensions is given by

$$T_m'(\mathbf{l}) = T_m\left[1 - \frac{2\sigma_e}{(\Delta h_f)\mathbf{l}}\right] \tag{37a}$$

where $\mathbf{l}$ is the step height of the crystal [3]. It is seen that the equilibrium melting temperature, T_m, is the melting point of a lamella of infinite step height. From this expression and eq (32) with $\epsilon = 0$, it is readily found that a lamellae of step height $\mathbf{l}^*$ formed at a crystallization temperature T_x will melt only slightly above T_x on rewarming if the edge free energy is unimportant. If on the other hand ϵ is large, so that the step height of the lamellae is the same as that of a primary nucleus, $4\sigma_e/(\Delta f)$, then its melting point T_m' will be just midway between T_x and T_m, i.e., $T_m' = (T_m + T_x)/2$.

The melting point of a polymer is commonly understood to refer to the temperature where the last detectible trace of crystallinity disappears. Lamellae will ordinarily exhibit a certain distribution of step heights, and the "observed" melting

[18] The primary nucleus may have a characteristic value of the edge free energy ϵ_p, which will cause $\mathbf{l}_p^*$ to slightly exceed $4\sigma_e/(\Delta f)$ [3], but this may be ignored.

point, T'_m (obs.), will thus refer to the larger of these. We must expect the step height at the observed melting point to reflect the mean step height of the growth or primary nucleus, whose $\mathbf{l}$ value varies as $1/(\Delta T)$. Suppose that the observed melting point corresponds to a step height $\boldsymbol{\beta}$ times larger (or smaller) than the mean step height of a primary nucleus. Then $\mathbf{l}=\boldsymbol{\beta}\mathbf{l}^*_p\cong 4\boldsymbol{\sigma}_e\boldsymbol{\beta}T_m/(\Delta h_f)(\Delta T)$, where $\boldsymbol{\beta}$ is to a first approximation assumed to be constant. For this simple illustrative example one finds

$$T'_m\,(\text{obs.})=T_m\left(1-\frac{1}{2\boldsymbol{\beta}}\right)-\frac{T_x}{2\boldsymbol{\beta}}. \qquad (37b)$$

This expression indicates that a plot of the observed melting point (as obtained on warming without recrystallization) as a function of crystallization temperature will be a straight line that intersects the line $T_x=T'_m$ (obs.) at T_m. This may prove useful in determining the equilibrium melting temperature. However, the main points here are that the observed melting point will tend to increase as the crystallization temperature is increased, and that it is entirely possible that such melting points may either all be above the line T'_m (obs.)$=(T_m+T_x)/2$, as for $\boldsymbol{\beta}>1$, or all below as for $\boldsymbol{\beta}<1$. If the edge free energy is large, and the distribution fairly broad, $\boldsymbol{\beta}$ may be in the vicinity of 1.5 or slightly more. On the other hand, if the edge free energy is negligible and the distribution narrow, $\boldsymbol{\beta}$ will tend to fall in the range 0.6 to perhaps 1.0. Experiments showing that $\boldsymbol{\beta}$ was in the range 0.6 to say 1.5 or 2.0 would provide strong evidence for the retention of the step height of the crystal near that of the nucleus length.

The above results apply to the case where the lamellae maintain their original step heights as they are rewarmed. Small lamellae will melt out well below T_m, and any subsequent recrystallization at this higher temperature would form higher-melting lamellae (see below). Also, a certain increase in step height may sometimes arise from lengthwise diffusion effects in the chain folded crystal. Either way, $\boldsymbol{\beta}$ will increase, and T''_m (obs.) will be correspondingly closer to T_m. Values of $\boldsymbol{\beta}$ as high as 5 or so may still be regarded as being consistent with chain folded growth, but the most clear cut case is that where $\boldsymbol{\beta}$ lies in the range of about 0.6 to roughly 1.5 or 2.0.

Some recent experiments indicate that a satisfactory explanation of the melting of certain bulk polymers of the lamellar type is given by eq (37b) with reasonable $\boldsymbol{\beta}$ values [44].

Combination of eqs (37a) and (38) shows that the melting process will be sharper for an assembly of thick lamellae formed near T_m than the thinner ones produced at lower temperatures. To this approximation, the breadth of the melting process is proportional to (ΔT). This result will be modified somewhat when the distribution of step heights within a given lamella is considered.

Recrystallization on Warming: Recrystallization may occur on rewarming. The thinner lamellae formed in the original crystallization at $T_{x(1)}$ will melt out at the T'_m value characteristic of their step height as described above. Then lamellar crystals with the larger step height characteristic of the crystallization temperature $T_{x(2)}=T'_m$ will tend to form from the melted material. Thus, on warming from $T_{x(1)}$ to $T_{x(2)}$, *a small step height will tend to be replaced by a larger one*. This effect should not be confused with the slow and monotonic increase of step height due to lengthwise diffusion of the chains in the crystal that may sometimes take place. The latter process, if it occurs, should be identifiable, since it will lead to a slow and isothermal increase of step height at the original crystallization temperature.[19]

Since the step height increases on recrystallization, the new lamellae formed in this process will be smaller in the **a** and **b** directions than the patch originally melted out. The recrystallization process may be promoted by the presence of loop type crystals in the immediate vicinity. Something rather like what has been described may occur for a lamella on a heterogeneous surface, but here the problem is more complicated because of the interaction with the foreign substrate.

Growth of the step height to increasingly higher values by recrystallizing at successively higher temperatures through slow warming cannot be carried out indefinitely, since kinetic considerations will at some temperature near the melting point prevent such recrystallization from taking place at a sensible rate. The large step height achieved by recrystallization at the highest practical temperature is *not* to be regarded as a "limiting" step height from a theoretical point of view.

Distribution of Step Heights: We turn now to the question of what the model implies about the distribution of step heights of various lamellae. To a good approximation, it has been shown that the mean square deviation of the step heights of different lamellae about the mean value $\bar{\mathbf{l}}$ is given by [3]

$$\left\langle(\mathbf{l}-\bar{\mathbf{l}})\right\rangle^2=\frac{1}{2}\left(\frac{kT}{\mathbf{b}_0\boldsymbol{\sigma}}\right)^2. \qquad (38)$$

For $\boldsymbol{\sigma}=10$ erg cm^{-2}, $T=400$ °K, and $\mathbf{b}_0=5\times10^{-8}$ cm, the quantity $\langle(\mathbf{l}-\bar{\mathbf{l}})\rangle^2$ comes to 60 A, corresponding to a mean deviation about $\bar{\mathbf{l}}$ of only 7.8 A. Thus the mean step height of a given lamella formed in the coherent growth process is apt to be quite close to the average for the entire assembly of lamellae.

If the edge free energy is greater than zero on the face of the crystal, and falls to a lower value at the edge, then the distribution of step heights of different lamellae will be even less than that given by eq (38). The case described amounts to the physical situation where a loop is a little easier to form at the edge rather than upon the flat face of the lamella.

The treatment leading to eq (38) for surface nucleation with chain folds is quite different from the one that establishes the distribution of step heights for primary folded nuclei. The difference is that the distribution of step heights for various

[19] If the step height does not increase to any marked extent on storage under isothermal conditions at T_x, and if on rewarming in the manner indicated, a small step height is replaced by a larger one, melting followed by recrystallization is reasonable as the mechanism of the increase l.

folded primary nuclei about l_p^* may be properly treated in terms of a continuum model of the free energy surface (see p. 83 and appendix 5.1 of reference [3]),[10] while in the case of the folded surface nucleus of monomolecular thickness the discrete character of the free energy surface must be recognized in the calculation of the distribution of step heights about l^* (see pp. 86–87 and appendix 5.2 of reference [3]). However, the narrow range of values of the step height at a certain growth temperature is in both cases a result of the fact that the rate of formation of the appropriate nucleus is at a sharp maximum for some value of the step height, i.e., at l^* or l_p^*.

The question of the constancy of the step height within a given coherently growing lamella subsequent to the initial surface nucleation act has been treated in some detail by Lauritzen [29].[20] Allowing the height of each step element to fluctuate occasionally about l^*, and assuming that the polymer chain (because of its segmental character) can take on only discrete values of l, it was shown that the step height would maintain itself slightly above the value $l=2\sigma_e/(\Delta f)$ for the case $\epsilon=0$ from near T_m down to temperatures corresponding to a rather high degree of supercooling. Though some minor differences exist, the more rudimentary theory given in this paper, where l^* is assumed to remain constant after the initial surface nucleation act, is verified on the main points.[20] Physically, the constancy of the step height of a given lamella during growth is a result of the fact that the step height cannot become smaller than $2\sigma_e/(\Delta f)$ without becoming unstable, and does not tend to become substantially larger than this value because it is expensive from an energetic standpoint to allow a loop to protrude much out of the fold plane. This causes the lamella to have the maximum steady-state growth rate when its step height is l^* (cf. sec. 5.1).

Insofar as the disorder of a folded crystal is a result of the distribution of step heights, i.e., irregularities in the fold plane, Lauritzen's calculations indicate that crystals formed at low supercooling should be more ordered than those produced at high supercooling, where fluctuations are more pronounced.

5.3. Coherent Loop Type Growth and Spherulite Structure: Lamellar Twist

Growth by coherent nucleation of folded nuclei can lead to the formation of a spherical object that in most important respects strongly resembles a lamellar spherulite.

[20] The authors are deeply indebted to Prof. F. C. Frank and Dr. M. P. Tosi for sending them a manuscript [41] of their work on fluctuations of step height prior to publication. The paper of Lauritzen's referred to above, also unpublished, borrows heavily from the methods outlined by Frank and Tosi. However, they do not treat a polymer chain that is explicitly made up of discrete units. As a result of this and possibly other differences, Frank and Tosi predict that chain folded growth will not occur above a certain temperature because $l^* \to 2\sigma_e/(\Delta f)$. Lauritzen's calculations indicate that this upper limit is removed by the assumption of discrete chain segments.

Both of the treatments with fluctuations suggest that l^*, after falling initially with increasing supercooling more or less according to eq (36), will begin to rise again at strong supercooling. However, Lauritzen's analysis suggests that this would probably be seen experimentally as a certain flattening out of the l^* versus T curve; the sharp rise in l^* occurs at such strong supercooling that it will frequently not be in the experimentally accessible range, and may be below T_c. Hence eq (36) applies as a good approximation from moderate to very low supercooling.

Consider first the case of a heterogeneously initiated spherulite. Here stacks of lamellae of the general type shown in figure 6a will grow outward from various sites on the nucleation center. (The reader is reminded again that the growing surface may actually be wedged-shaped.) The σ_e planes of the lamellae (loop containing surfaces) will be more or less parallel to the spherulite radius, and the polymer chains will be essentially normal to the radius.

The spherulite will tend to fill out and become a three-dimensional object by virtue of one or more of several processes. First, new lamellae will tend to form and grow along the σ_e faces of those already in existence. Second, spiral dislocations can occur. The axis of these dislocations, $s—s'$, will be at a right angle to the σ_e plane, i.e., normal to the spherulite radius, and "radial" growth will occur from the edges of such dislocations. Certain types of branching are also possible as secondary nucleation events. For example, noncoherent nucleation may occur on the faces or edges of a lamella.

It is evident from the above that this model leads in a natural way to the lamellar and polymer chain orientation common in spherulites, and it is also clear that a three-dimensional spherical object can be formed. If the number of active heterogeneous nuclei is very large, easily recognizable spherulitse may not form because of early impingement, but the polymer texture will still be basically lamellar. This effect may be greatly reduced by ridding the system of the heterogeneities, which is difficult, or somewhat reduced by destroying some of the embryos in the fissures on the surface of the heterogeneities by heating the sample further above T_m prior to crystallization (see sec. 8.4.).

Homogeneous nucleation can also lead to a lamellar spherulite. Here the nucleus will first grow a small platelet. Then by the mechanisms mentioned above, a three-dimensional object can form from it. Early in its life, the spherulite may be fan or sheaflike. (The same would be true of a heterogeneously nucleated spherulite if only a few nucleation sites on each heterogeneity were active.) The spiral dislocation mechanism is probably important in creating a three-dimensional spherulite, but the radial growth itself is not due to the formation of such spiral ramps. At sufficient supercooling, the number of homogeneous nuclei will become very large even early in the crystallization process, so that obvious spherulites may not appear despite the fact that the texture is actually lamellar.

An essential point to bear in mind in the case of ideal coherent growth with chain folds is that a number of the lamellae should extend outward from the nucleation center without interruption a substantial fraction of the way to the boundary of the spherulite. It should be possible to obtain information on this point by examining electron micrographs of a cross section of a spherulite. Evidence that a single lamella without any obvious disruption extended over a substantial fraction of the spherulite radius would be consistent with the coherent growth with chain folds mechanism, and at the same time give reason for anticipating a $(\Delta T)^{-1}$ radial growth rate law.

Geil [5] has shown that individual lamellae extend over the entire radius in the spherulitic structures of bulk polyoxymethylene.

In the coherent growth process, chain ends will appear from time to time on the growing surface as the loops are laid down. Continuation of growth of the surface layer involved may be accomplished by allowing the incomplete step element to come off the crystal face and protrude like a cilia from the σ_e face. This is certainly what will happen in high molecular weight material if the chain ends are sufficiently large. Renucleation with a new molecule at the sites where the other molecule terminated would be more rapid than the formation of a new coherent surface nucleus, so such a process would not materially alter the rate equations given. Small ends that can enter the crystal in sufficient numbers will allow relatively normal chain folding even for material of moderate molecular weight. Chain ends may play a role in initiating dislocations.

It has already been noted that the perfection of the folded surface will increase with increasing crystallization temperature. This will tend to cause more perfect crystals of higher density to be formed at higher temperatures. It might be thought that the inclusion of chain ends in the folded crystal might have a strong effect in the opposite direction. Actually, a simple calculation shows that over a wide range of step height, the number of chain ends included in the crystal per unit volume will not depend strongly on the step height, so increasing density with increasing crystallization temperature is commonly to be expected.[21] The inclusion of a certain number of chain ends in the folded crystals of a high molecular weight polymer must be expected to slightly lower the melting point. Nevertheless, for polymer crystallized in the usual range of supercooling, the finite step height must be expected to be the main cause of the lowering of the melting point below T_m, as described by eqs (37).

Some homopolymers may be practically completely lamellar when crystallized, but in other cases a considerate amount of amorphous matter may exist between the lamellae, especially if the lamellae are strongly twisted. The amorphous material between lamellae may be oriented, and abnormal in other respects.

The chain fold model of spherulitic growth leads in a straightforward way to the existence of terraces corresponding to the lamellar step height in surface replicas of fractured spherulites. In the case where the number of interlamellar links is low (see below), van der Waals interactions comprise the main forces that must be overcome to separate the lamellae. Steps of the type illustrated in figure 6(a), as viewed from a direction essentially normal to the σ_e plane, are to be expected. This appears to correspond closely to what is often observed in electron micrographs of material crystallized from the unoriented melt. If the number of interlamellar links is high, cleavage of the lamellae may be quite difficult, and result in considerable damage to the step structure.

[21] Other manifestations of increased perfection, such as a sharpening of certain X-ray lines, are also to be expected as the crystallization temperature is increased.

Interlamellar Links: A fairly large number of molecules may be incorporated bundle-fashion into a chain folded lamella growing in the bulk supercooled liquid, as illustrated in figure 6a by the molecule marked $y-y'$. This may be done to a certain extent without seriously affecting the step height of the folds or the rate expressions. Even the fairly frequent inclusion of such chains will not tend to incur the cumulative strain effects that may be associated with the formation of purely bundlelike structures. Also, groups of lamellae will tend to grow outward from the nucleation center together. The situation should resemble that shown in figure 6a, except that the growing faces of the lamellae will frequently be closer together. Under these circumstances, it is inevitable that one polymer molecule will occasionally become involved in two or perhaps even three different lamellae, creating interlamellar links. These links should affect the mechanical properties of spherulitic bulk polymers, since the lamellae will be more difficult to separate than would be the case if such links were absent.

Polymer molecules emanating bundle-fashion from the fold plane may sometimes return to the same crystal at a position well removed from the original point of exit. This type of "folding" may be denoted as "nonadjacent re-entry", as opposed to the usual type of chain folding, which exhibits adjacent re-entry. However, it seems quite unlikely that the basic structure of a well-defined lamellar polymer crystal formed at low to moderate supercooling consists of folds that largely or entirely exhibit nonadjacent re-entry.

In unoriented bulk polymers crystallized under conditions where the number of interlamellar links is low, elongation of the specimens by cold stretching in one direction should cause the lamellae to tend to aline in the direction of stretch; in such a case, the polymer molecules in the crystals would tend to be oriented more or less *perpendicular* to the direction of stress. Such a result would provide strong support for the existence of lamellae with chain folds. The existence of too many interlamellar links, local melting caused by rapid stress, or excessive elongation, could easily lead to the opposite result. (It should be understood that the above refers to polymer crystallized from the unoriented and relatively unstrained supercooled liquid state; experiments carried out on crystallization of highly oriented liquids, e.g., cooling of hot-drawn filaments, are specifically exempted.) Examples where the tipping of crystals at low draw ratios has been observed may be found in the literature [30, 31, 32, 33]. At least some of these studies appear to refer to the required type of experiment. Results of this kind led Storks [34] to originally suggest the existence of chain folds.

The existence of interlamellar links in polymer crystallized in bulk may cause such material to differ from masses of chain folded polymer platelets filtered from dilute solution preparations. In the latter case, interlamellar links should be virtually absent. If numerous, the interlamellar links in the bulk crystallized polymer might cause disturb-

ances in the solubility, mechanical properties, and melting behavior.

Lamellar Twist: The remaining question is that of the origin of twist of the lamellae. The optical studies noted earlier indicate that the lamellae (or more correctly stacks of lamellae) in many real spherulites are twisted, and it remains to be seen if coherently grown lamellae with chain folds could exhibit such an effect. The type of twist under consideration here is shown schematically in figure 7a. The bladelike lamellae have a definite pitch, and revert from time to time to their original orientation at a repeat distance $\mathbf{d}_\theta$ as one proceeds along the radius of the spherulite. The heavy arrow marked "G" indicates the direction of radial growth. The leading face of the lamella has been drawn wedge-shaped to correspond to growth in a preferred crystallographic plane (see also fig. 7b).

The twist of the lamellae can arise from stress in the plane of the chain folds. One way in which the required type of stress can arise will now be outlined.

Let the polymer chains in the interior of a lamella be arranged in some definite pattern, say the hexagonal array shown as small heavy black dots in figure 7b. It is assumed that this internal packing arrangement does not lead to twist. Now consider the "lattice" of the chain folds that is consistent with this internal structure. If we consider the chain folds as occupying a roughly spherical volume element, the situation shown in figure 7b results. If the chain folds occupy more than a certain volume (denoted by large open circles) repulsive forces will act between the folds as indicated by the overlap (shaded). The main point to notice is that the "lattice" created by the chain folds on the two σ_e surfaces is not the same as that characteristic of the interior of the crystal, and that if the folds are larger than a certain size, an anisotropic surface stress is certain to result. (A different packing of the chain folds can be introduced by alternating the chain folds in the layers of molecules in figure 7b, but this simply leads to straight rows of folds that lie at an angle of 60° to those shown.) The surface stress increases the free energy of the crystal, and the system will tend to undergo slight rearrangements that will minimize the total free energy.

There are two basic ways in which the lamella can reduce the repulsion of the chain folds. First, the lamella can twist slightly to create better surface packing (see below). This will, of course, tend to be balanced by forces due to the internal packing arrangement. Second, the chain folds may tend to become staggered, causing the folded surface to resemble a terra cotta roof. The staggered configuration corresponds to that where the polymer chain axes are no longer perpendicular to the plane of the chain folds.[22] Specific forces in the interior of the lamella, related to the particular way in which the X-X-X groups that comprise the chain achieve best packing, may tend to resist such staggering. It is possible that the minimum in free energy will be achieved if both effects occur.

Now consider the problem of the origin of the twist in a body with surface stress of the type that may occur in polymer lamellae. The particular type of surface stress arising from the model shown in figure 7b may be illustrated schematically as in figure 7c. Here the solid body of dimensions **x**, **y**, and **l*** possesses a surface stress f in dynes cm^{-2} that is distributed over a surface layer of thickness

[22] The individual chain folded crystals formed from dilute solution may either be flat, or resemble hollow pyramids. In the latter case the folds are staggered, and the chains are not perpendicular to the σ_e plane. (See for example ref. [43].)

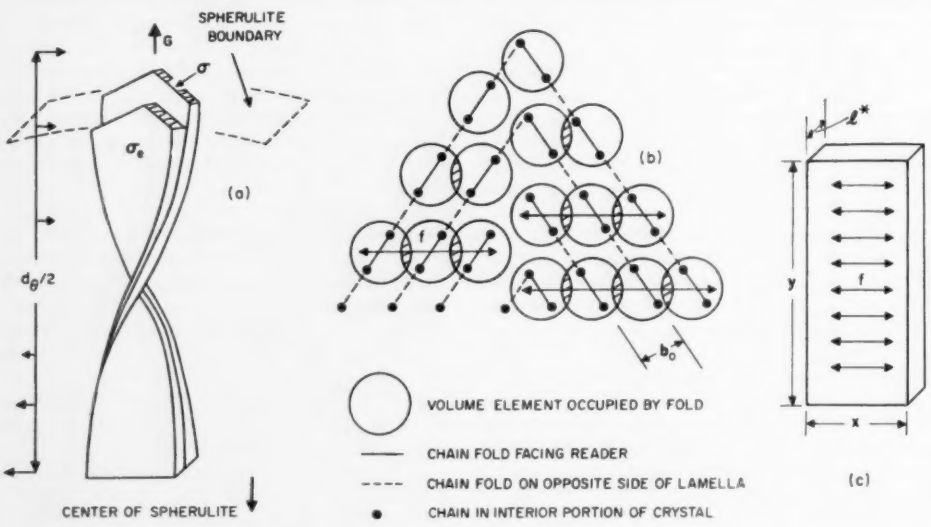

FIGURE 7. *Origin of lamellar twist in spherulites.*

(a) Schematic representation of lamellar twist.
(b) Schematic view normal to fold plane of lamellar crystal showing repulsion (shaded areas) leading to surface stress f.
(c) Macroscopic model of surface stress. A similar stress pattern exists on the opposite side of the body.

$\gamma \mathbf{l}^*$, where γ is a small fraction. The situation on the opposite side of the parallelepiped is identical to that just described.

From the theory of the buckling of plates,[23] it can be shown that such an object will develop twist or warp when f exceeds a certain value which is

$$f_c = \frac{S}{2\gamma}\left(\frac{\mathbf{l}^*}{\mathbf{x}}\right)^2. \tag{39}$$

Here S is the shear modulus. Numerical estimates for the extremely thin lamellae characteristic of spherulitic crystallization indicate that twist can arise for surprisingly low values of f_c/S if $\mathbf{l}^*$ is in the usual range for such crystals. It is therefore considered entirely reasonable to propose that surface repulsions of the type described can lead to the twist of the lamellae. Surface stress arising from other causes could also lead to a similar effect.

If for some value of $\mathbf{l}^*$ the crystal is already twisted, the twist will tend to become more prominent if $\mathbf{l}^*$ is reduced further. This assumes, of course, that $\mathbf{x}$ does not fall off as rapidly as $\mathbf{l}^*$. The variation of γ with $\mathbf{l}^*$ is unimportant in most applications.

Perhaps the most important prediction that arises from the present conception of the origin of twist in coherently grown lamellae is that $\mathbf{d}_\theta$ will tend to increase rapidly as the growth temperature is increased and at some temperature become extremely large. In practical terms this means that the concentric bands observed in many spherulites when viewed with crossed nicol prisms will become separated more and more as the growth temperature is increased, finally disappearing altogether. The lattice forces in the interior of a lamella tend to keep it in the untwisted state, while the surface stress promotes twist. Hence, if the step height $\mathbf{l}^*$ increases as it does with an increase of growth temperature, the twist will rapidly become less pronounced at the same time.

When a certain value of $\mathbf{l}^*$ is reached (or more precisely, a certain value of $\mathbf{l}^*/\mathbf{x}$), the twist will disappear completely. Examples where the twist diminishes rapidly with increasing growth temperature are well known in lamellar spherulites. It is conceivable that the situation described above could be reversed in some cases because $\mathbf{x}$ increases more rapidly than $\mathbf{l}^*$ with rising growth temperature.

Considering the proposed mechanism leading to twist, it would not be surprising to find that lamellae with a marked warp or twist were also characterized by the polymer chains being not exactly perpendicular to the plane of the chain folds.

A heterogeneously nucleated spherulite may have sectors with both right and left handed twist. At any given nucleation site on a heterogeneity, lamellae with a given sense of twist will be generated, and the sector that grows out from this site will tend to preserve this particular twist (see below). The quantity $\mathbf{d}_\theta$ will be the same for both right and left handed sectors. If the polymer is heated above T_m, embryos preserving the sense of twist may be retained in cracks or pores in a heterogeneity, with the result that a spherulite similar to the original one will frequently be regenerated at the same place on subcooling. A boundary will exist between right and left handed sectors. Since the probability of polymer chain connections between these sectors is small, spherulites should frequently fracture under shear at such boundaries.

If the lamellae growing out from a nucleation center are either densely packed, or grow out together as a stack, the sense of the twist in the sector under consideration will be preserved. (This is the "cooperative effect" of Keith and Padden [9].) However, if the individual lamellae are fibril-like and loosely packed, a spherulite where right- and left-handed lamellae are intertwined may appear. Such a spherulite would not exhibit distinct bands when viewed under crossed nicol prisms, despite the fact that the individual lamellae, or groups of lamellae, were actually twisted. Only the maltese cross effect would then be seen.

Summary: The foregoing development indicates that the coherent growth mechanism with chain folds can reproduce many of the structural features of lamellar spherulites. The existence of the lamellae themselves, and the behavior of the step height that characterizes them is explained. The orientation of the lamellae, and the orientation of the polymer chains in the lamellae, is in the correct relation with respect to the radius of the spherulite. Moreover, the twist frequently exhibited by stacks of the lamellae can be accommodated by the theory, thus removing one of the objections that had heretofore been leveled at coherent growth mechanism generally.

Our conclusion is that the coherent growth mechanisms with chain folds, with its $(\Delta T)^{-1}$ radial growth rate law, is worthy of serious consideration in the analysis of the behavior of lamellar spherulites.

Consideration will now be given to the problem of spherulitic growth by noncoherent surface nucleation with chain folds.

★6. Radial Spherulitic Growth by Noncoherent Surface Nucleation With Chain Folds

6.1. Basis of Model

It is conceivable that coherent growth of the kind described in the previous section will be hampered by certain effects so that such growth practically ceases after a time. For example, continued coherent growth may in some cases lead to *cumulative* surface strain on the σ_e faces because of the existence of chain folds that are slightly too large. Then after coherent growth has proceeded for a time, the end surface free energy will take on a value $\sigma_{e(s)}$ that is larger than σ_e, which is sufficient to practically completely arrest coherent growth. The value of σ on the coherently growing face will probably

[23] The author is indebted to J. N. Frankland of NBS for deriving this result, and for several helpful discussions of the problem of twist in lamellar systems.

also take on a higher value which may be denoted $\sigma_{(s)}$. The subscript (s) denotes strain.

The problem that will be studied in this section is whether or not it is possible that radial growth can be reactivated in such a case by the formation of a *noncoherent* surface nucleus on the presumably still wettable face of the stunted lamella. The rate laws for such growth will be derived, and the conditions under which the formation of a noncoherent surface nucleus will be the rate determining step in the radial growth of a spherulite determined. The effect of such nucleation on spherulitic structure will be mentioned.

The concept that noncoherent surface nucleation may be involved in spherulitic growth is due to Price [16]. He suggested that the cessation of coherent growth might result from chain entanglements. The assumption used here that the cessation of coherent growth results from cumulative strain seems justified, if only as an initial hypothesis, by the structural considerations mentioned above. The rate laws to be derived below should hold at least approximately for noncoherent surface nucleation that follows upon the cessation of coherent growth due to any cause.

The model shown in figure 8a is used. A noncoherent surface nucleus with chain folds in the form of a parallelepiped of dimensions **a, b,** and **l** is assumed to form the face of the stunted lamella The noncoherent nucleus has normal "unstrained" values of σ, σ_e, and Δh_f. The substrate lamella bears the strained values of the surface free energies $\sigma_{(s)}$ and $\sigma_{e(s)}$, but the volume contribution, Δh_f, has its normal value. The noncoherent surface nucleus attaches to the substrate lamellar face at an angle, ψ or $2\pi - \psi$, that is consistent with minimizing strain. Thus, there is a true interface between the surface nucleus and the strained substrate crystal. This means that the noncoherent surface nucleus will behave in a three-dimensional manner, provided that neither **a, b,** nor **l** falls to minimal dimensions. Observe that the term "noncoherent" does *not* mean that the surface nucleus is not attached to the substrate.

Once a noncoherent surface nucleus of stable size is attained, coherent growth begins again, and the spherulite radius at first grows rapidly in the direction indicated by the heavy arrow marked "**G**". Then the surface strain gradually accumulates, and the lamella is stunted after growing a distance λ. After a time, a noncoherent surface nucleus forms, and the process is repeated. Under appropriate circumstances, the formation of the three-dimensional noncoherent surface nucleus may be the rate determining step in the radial growth process.

6.2. Rate of Radial Growth With Chain Folded Noncoherent Surface Nuclei

Region **A''** (upper): Assuming that **a**, **b**, and **l** may be regarded as variables in the sense that they have not reached minimal values, the free energy of formation of the unstrained noncoherent surface nucleus illustrated in figure 8a may be written

$$\Delta\phi = 2\mathbf{ab}\sigma_e + 2\mathbf{bl}\sigma + (2\sigma - \delta)\mathbf{al} - \mathbf{abl}\Delta f \qquad (40)$$

where δ is defined by the relation

$$\sigma_{\text{interface}} = \sigma_{(s)} - \delta + \sigma. \qquad (41)$$

Here $\sigma_{\text{interface}}$ is the total interfacial free energy between the surface nucleus and the lamella to which it is attached; $\sigma_{(s)}$ is the surface free energy on the face of the strained lamella. The other quantities have the same significance as in section 5. The edge free energy is omitted for simplicity.

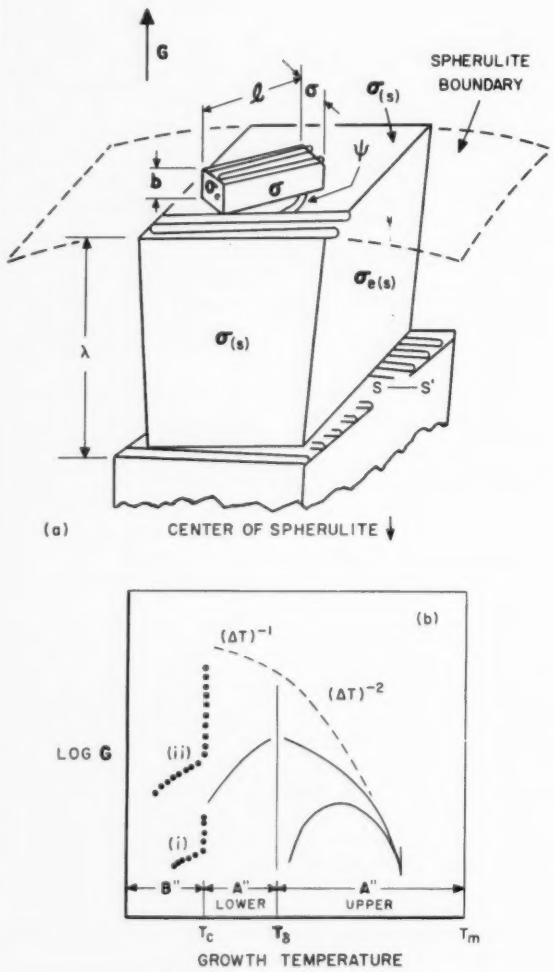

FIGURE 8. *The noncoherent chain folded surface nucleus model of spherulitic growth and its rate behavior.*

(a) Noncoherent surface nucleus of dimensions **a**, **b**, and **l** on strained substrate lamella. Heavy arrow marked **G** shows direction of radial growth of modified lamellar spherulite.

(b) Logarithm of radial growth rate of spherulite as a function of temperature. — — — — log **G** versus T, if jump rate effect is small; ——— most representative cases where jump rate causes maximum to appear in log **G**; . . . . exhibits effect of excess nucleation in medium surrounding spherulite.

The quantity $\boldsymbol{\delta}$ is a measure of the interaction of the noncoherent surface nucleus with the strained substrate lamella. It takes on a value of zero if there is no interaction between the two objects. In this case $\boldsymbol{\Delta\phi}$ is identical to that for a primary nucleus with chain folds. On the other hand, if $\boldsymbol{\sigma}_{(s)} \rightarrow \boldsymbol{\sigma}$ and $\boldsymbol{\delta} \rightarrow 2\boldsymbol{\sigma}$, eq (40) becomes identical to the expression for strictly coherent surface nucleation (*cf.* eq (30) with $\boldsymbol{\epsilon} \rightarrow 0$). Thus $\boldsymbol{\delta}$ will in general have a value between zero and $2\boldsymbol{\sigma}$.

A large value of $\boldsymbol{\delta}$ thus indicates strong interaction of the noncoherent surface nucleus with the substrate (high degree of wettability), and a small value of $\boldsymbol{\delta}$ indicates weak interaction (low wettability).

Near the melting point, $\mathbf{a}$, $\mathbf{b}$, and $\mathbf{l}$ may be regarded as variables, and it is therefore proper to calculate $\boldsymbol{\Delta\phi}^*$ on the basis that the nucleus is formed from many step elements. Using procedures of the type outlined in sections 2.3 and 2.5, it is found that

$$\mathbf{l}^* = 4\boldsymbol{\sigma}_e/\Delta f, \tag{42a}$$

$$\mathbf{a}^* = 4\boldsymbol{\sigma}/\Delta f, \tag{42b}$$

and

$$\mathbf{b}^* = (4\boldsymbol{\sigma} - 2\boldsymbol{\delta})/\Delta f, \tag{42c}$$

so the free energy of formation at the saddle point in the free energy surface described by eq (40) is at

$$\boldsymbol{\Delta\phi}^* = \frac{32\boldsymbol{\sigma}(\boldsymbol{\sigma} - \boldsymbol{\delta}/2)\boldsymbol{\sigma}_e}{(\Delta f)^2}. \tag{43}$$

Thus from eq (21) the radial growth rate would be [24]

$$\mathbf{G}_{\mathbf{A}''(\text{upper})} = G_0 \exp\left(-\frac{\Delta H^*}{kT}\right) \exp\left(-\frac{32\boldsymbol{\sigma}(\boldsymbol{\sigma} - \boldsymbol{\delta}/2)\boldsymbol{\sigma}_e T_m^4}{T^2(\Delta h_f)^2(\Delta T)^2 kT}\right) \tag{44}$$

$$[(\Delta T)^{-2} \text{ law}]$$

provided that (1) the quantity $\mathbf{b}^*$ had not fallen to $\mathbf{b}_0$ because of too large supercooling and (2) noncoherent surface nucleation was actually the rate determining step.

Let us now consider the range of validity of eq (44). First, it is readily found from eq (42c) that the nucleus will maintain its three-dimensional character only if the degree of supercooling is less than

$$\Delta\mathbf{T}_\delta \cong \frac{4(\boldsymbol{\sigma} - \boldsymbol{\delta}/2)T_m}{(\Delta h_f)\mathbf{b}_0}. \tag{45}$$

At temperatures lower than $\mathbf{T}_\delta$, the nucleus is monomolecular, i.e., $\mathbf{b} = \mathbf{b}_0$, and the $(\Delta T)^{-2}$ law does not apply. Further, the condition

$$\exp\left(-\frac{4b_0\boldsymbol{\sigma}\boldsymbol{\sigma}_e}{(\Delta f)kT}\right) >> \exp\left(\frac{-32\boldsymbol{\sigma}(\boldsymbol{\sigma} - \boldsymbol{\delta}/2)\boldsymbol{\sigma}_e}{(\Delta f)^2 kT}\right) >> \exp\left(-\frac{4\mathbf{b}_0\boldsymbol{\sigma}_{(s)}\boldsymbol{\sigma}_{e(s)}}{(\Delta f)kT}\right) \tag{46}$$

must hold. The left hand inequality simply states that "unstrained" coherent nucleation must be more rapid than noncoherent nucleation. This will always be true when the degree of supercooling does not exceed $\Delta\mathbf{T}_\delta$, and need not be considered further. The right hand inequality states that noncoherent nucleation must be more rapid than "strained" coherent growth, so that noncoherent nucleation will be the rate determining step in the radial growth process.[25] This will be true when

$$\frac{\boldsymbol{\sigma}_{(s)}\boldsymbol{\sigma}_{e(s)}}{\boldsymbol{\sigma}\boldsymbol{\sigma}_e} > \frac{2(\Delta\mathbf{T}_\delta)}{(\Delta T)}, \tag{47}$$

a condition that will hold according to the assumptions used in the model.

Region $\mathbf{A}''$ (lower): At a degree of supercooling equal to or exceeding that given in eq (45), the noncoherent nucleus becomes monomolecular. Here the free energy of formation at $\mathbf{a} = \mathbf{a}_0$ is

$$\boldsymbol{\Delta\phi}^{*(1)} = \frac{4\mathbf{b}_0^2\boldsymbol{\sigma}(\boldsymbol{\sigma}_e + \boldsymbol{\epsilon}/\mathbf{b}_0)}{\mathbf{b}_0(\Delta f) - (2\boldsymbol{\sigma} - \boldsymbol{\delta})} \tag{48}$$

when the edge free energy is included. Somewhat below $\mathbf{T}_\delta$, $\mathbf{b}_0(\Delta f)$ will be considerably larger than $(2\boldsymbol{\sigma} - \boldsymbol{\delta})$, and the radial growth rate may be approximated as

$$\mathbf{G}_{\mathbf{A}''(\text{lower})} \cong \mathbf{G}_{0\,(1)} \exp\left(-\frac{\Delta H^*}{kT}\right) \exp\left(-\frac{4\mathbf{b}_0\boldsymbol{\sigma}(\boldsymbol{\sigma}_e + \boldsymbol{\epsilon}/\mathbf{b}_0)T_m^2}{T(\Delta h_f)(\Delta T)kT}\right), \tag{49}$$

$$[(\Delta T)^{-1} \text{ law}]$$

which is identical to the radial growth rate for coherent loop type growth in region $\mathbf{A}'$.

Region $\mathbf{B}''$: The rate law described by eq (49) will hold down to temperatures corresponding to a supercooling $\Delta T_c \cong 4\boldsymbol{\sigma}T_m/(\Delta h_f)\mathbf{a}_{\min}$. There and below, the rate of injection of nuclei in the surrounding medium will increase as described under Region $\mathbf{B}'$ of section 5.2.

Summary: A schematic diagram of the growth rate behavior of this model is shown in figure 8b. Even a fairly large value of $\boldsymbol{\delta}$, say in the vicinity of $3\boldsymbol{\sigma}/2$, will still give a $(\Delta T)^{-2}$ radial growth rate region that extends from near the melting point on down to growth temperatures corresponding to a rather high degree of supercooling. For such values of $\boldsymbol{\delta}$, $\boldsymbol{\sigma}_{(s)}\boldsymbol{\sigma}_{e(s)}$ need be only several times larger than $\boldsymbol{\sigma}\boldsymbol{\sigma}_e$ at ordinary supercooling to satisfy eq (47). However, the possibility exists that a rate transition from a $(\Delta T)^{-2}$ to a $(\Delta T)^{-1}$ law may occur at $\mathbf{T}_\delta$, as noted in figure 8b. This transition will not be particularly abrupt, and in the case where $\Delta\mathbf{T}_\delta$ is large, the rate laws will be mixed to the point that they cannot be clearly differentiated.

[24] If an edge free energy $2a\epsilon$ had been included in eq (40), $\mathbf{l}^*$ would have been $4\boldsymbol{\sigma}_e/\Delta f + 2\boldsymbol{\epsilon}/(2\boldsymbol{\sigma} - \boldsymbol{\delta})$, and eq (44) would have an additional term $\exp[-8\boldsymbol{\sigma}\boldsymbol{\epsilon}T_m^2/T(\Delta h_f)(\Delta T)kT]$. This will not seriously alter the $(\Delta T)^{-2}$ law predicted by eq (44) in its range of validity.

[25] The right hand term in eq (46) will be even smaller than indicated when the growth is strongly arrested by cumulative strain.

6.3. Noncoherent Loop Type Growth and Spherulite Structure

In broad aspect, a spherulite built up with chain folds by the process (rapid coherent growth→arrested "strained" coherent growth→noncoherent nucleation) will resemble one built on the coherent loop pattern. The spherulite will be basically lamellar, the chain axes will be normal to the radius, and the plane of the chain folds will tend to lie along the spherulite radius. Also, the coherently grown part of the lamellae will behave in a manner similar to that described in the previous section. However, there will be certain differences that may distinguish coherently grown from noncoherently grown loop type spherulites.

During the growth process, the lamellae will be disoriented with respect to the substrate at an angle of ψ or 2π-ψ at intervals of λ. For a completely isolated lamella, the noncoherent nucleus will attach to the substrate with equal probability at ψ or 2π-ψ, so that such a lamella might show disturbances in its sense of twist at intervals of λ. Also, a distribution of ψ values may exist.

Perhaps the most unusual feature of spherulitic growth on this pattern that may become observable in an optical microscope is that if λ becomes sufficiently large, spasmodic radial growth may be observed. Each rapid increase in radial growth would correspond to the coherent growth that follows upon the formation of a noncoherent nucleus. The distance traveled in each pulse would correspond to λ. If sufficiently small, the repeat distance λ may lead to characteristic X-ray spacings, but these would probably be very difficult to identify or observe.

Since σ_e increases because of cumulative strain as coherent growth proceeds, the characteristic step height l^* will tend to increase somewhat as the coherent growth step takes place. This is shown schematically in figure 8a. This effect would probably be observed only with difficulty.

The extension of the interface between the strained crystallites should provide possible sites for the initiation of spiral dislocations (see s—s' in figure 8a).

Another interesting point is that the accumulated strain will tend to cause the lamellae to melt out on rewarming just a little above the crystallization temperature. As noted earlier, coherently grown lamellae with chain folds will generally melt out well above the crystallization temperature (eq 37b). The predicted low melting of the lamellae with cumulative strain may prove useful in eliminating the possibility of noncoherent growth in specific cases where such behavior is known not to occur.

Noncoherent nucleation may contribute to the formation of dendritic structures even in the case where the rate determining step is strictly coherent. Thus, noncoherent nucleation on the σ-type faces of a coherently formed lamella (such as that facing the reader in figure 6a) could lead to fern- or treelike structures. Such effects probably assist spiral dislocations in forming three-dimensional semicrystalline spherulites in some instances.

The noncoherent loop type growth model is realistic enough to at least warrant testing spherulite growth rate data to see if they accord with a $(\Delta T)^{-2}$ law. This rate law is to be anticipated in lamellar spherulites that grow in a spasmodic manner near the melting point, since the coherent model with chain folds will not lead to such an effect.[26]

7. Polymer Crystal Growth by Noncoherent Bundlelike Surface Nucleation

7.1. Basis of Model

Suppose that large chain ends limit coherent bundlelike growth as described in section 4, so that only tiny crystallites can develop by this mechanism. We will now examine the possibility that noncoherent surface nucleation will enter and reinitiate growth, and thereby produce a large microcrystalline and spherical object.

The model employed is shown schematically in figure 9a. The inhibition to continued coherent growth of the substrate crystal is a result of the physical obstruction presented by the chain ends—x. We assume that the presence of the chain ends also causes the surface free energies of the substrate crystal to have the "strained" values $\sigma_{(s)}$ and $\sigma_{e(s)}$ which are larger than the normal values σ and σ_e. The latter refer to the surface free energies of relatively small bundlelike structures as yet unaffected by chain ends.

Alternatively, it could be assumed that cumulative strain resulting from growth in the a and b directions caused σ and especially σ_e to increase.

It is considered that if a large spherical object is to be built at all on the bundlelike pattern, the present model is, at least in the beginning, a more reasonable one than the strictly coherent bundlelike model discussed in section 4, where the possible restrictions imposed on crystallite size by large chain ends or strain were arbitrarily neglected.

We will assume that a noncoherent surface nucleus in the form of a parallelepiped with the dimensions a, b, and l forms on the strained substrate crystal. This noncoherent bundlelike surface nucleus has normal values of σ_e and σ. The noncoherent surface nucleus is assumed to form by virtue of the wettability of some portion of the substrate crystal by a normal crystal. Once it reaches critical size, this noncoherent surface nucleus will lead to coherent growth of a new crystallite of limited size. Then the process will be repeated. It is emphasized that the noncoherent surface nucleus is actually attached to the substrate, and that there is a true interface between the two objects.

7.2. Rate of Radial Growth With Noncoherent Bundlelike Surface Nuclei

Region A'' (*upper*): Sufficiently near the melting point, a, b, and l may be regarded as unrestricted

[26] In making this comment, it is assumed that other possible causes of spasmodic growth, such as fluctuating temperature at the spherulite boundary due to experimental conditions (e.g., rise and fall of bath temperature) or heat dissipation effects, have been eliminated.

by any minimal molecular dimensions. The free energy of formation of the noncoherent bundlelike surface nucleus shown in figure 9a is

$$\Delta\phi = 2ab\sigma_e + 2bl\sigma + (2\sigma - \delta)al - abl(\Delta f) \qquad (50)$$

where δ is defined in a manner analogous to eq (41). It is readily determined that

$$l^* = 4\sigma_e/(\Delta f) \qquad (51a)$$

$$a^* = 4\sigma/(\Delta f) \qquad (51b)$$

$$b^* = (4\sigma - 2\delta)/(\Delta f) \qquad (51c)$$

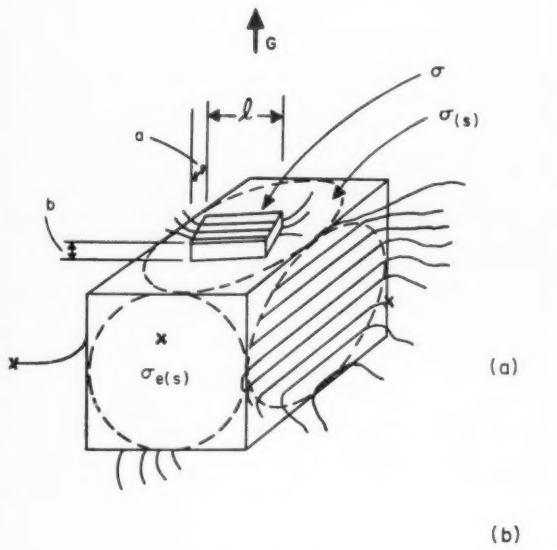

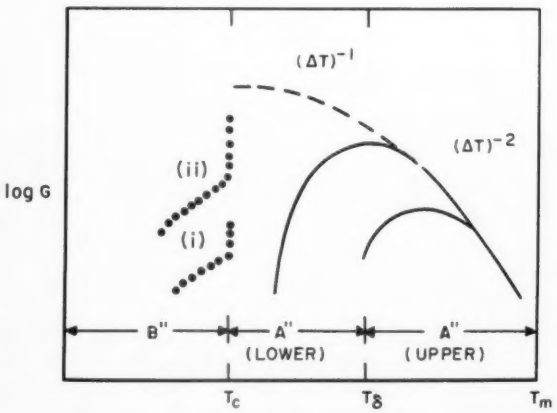

FIGURE 9. *The noncoherent bundlelike surface nucleus model and its growth rate behavior.*

(a) Noncoherent surface nucleus of length l, width a, and thickness b on strained substrate crystal. Chain ends denoted ——×.
(b) Logarithm of radial growth rate as a function of temperature. The solid, dashed, and dotted lines have the same significance as in previous diagrams. (See text for assumptions required to obtain spherical object from this model.)

which on insertion in eq (50) leads to

$$\Delta\phi^* = \frac{32\sigma(\sigma - \delta/2)\sigma_e}{(\Delta f)^2}. \qquad (52)$$

Then with eq (21) we have

$$G_{A''\,(\text{upper})} = G_0 \exp\left(-\frac{\Delta H^*}{kT}\right) \exp\left(-\frac{32\sigma(\sigma - \delta/2)\sigma_e T_m^4}{T^2(\Delta h_f)^2(\Delta T)^2 kT}\right) \qquad (53)$$

$$[(\Delta T)^{-2}\ \text{law}]$$

if the formation of the noncoherent surface nucleus is indeed the rate determining step in the radial growth process. The quantity l^* is *not* a step height in the case of a bundlelike nucleus, since the nucleus will grow to at least a certain extent in the l direction.

By comparison of eq (53) with the corresponding expression for homogeneous nucleation of bundlelike nuclei, eq (6) or (18), it is seen that the noncoherent surface nucleus model can provide a simple physical explanation for the reduction in the free energy of formation of a three-dimensional growth nucleus below that of the corresponding three-dimensional primary nucleus proposed by Flory and McIntyre [17]. The reduction factor is $1-(\delta/2\sigma)$, and this results from the assumption that an unstrained surface nucleus can wet a strained crystallite of the same polymer to some extent.

Region A'' (lower): Equation (53) will hold on down to a temperature where b approaches b_0. This will occur at a degree of supercooling

$$\Delta T_\delta \cong \frac{(4\sigma - 2\delta)T_m}{(\Delta h_f)b_0}. \qquad (54)$$

Below T_δ, the rate law may be approximated as

$$G_{A''(\text{lower})} = G_0 \exp\left(-\frac{\Delta H^*}{kT}\right) \exp\left(-\frac{4b_0\sigma\sigma_e T_m^2}{T(\Delta h_f)(\Delta T)kT}\right). \qquad (55)$$

$$[(\Delta T)^{-1}\ \text{law}]$$

Region B'': At a growth temperature corresponding to a degree of supercooling of $\Delta T_c = 4\sigma T_m/(\Delta h_f)a_{\min}$, bundlelike embryos of small size will be transported from the superheated state above T_m into the supercooled state by nonsteady state nucleation where they will become nuclei of stable size. As in previous cases, this will lower the radial growth rate of any spherulites born at or near $t=0$.

Summary: A diagram of the radial growth rate behavior possible with this model is shown in figure 9b. A $(\Delta T)^{-2}$ law will appear near and somewhat below the melting point because of the three-dimensional character of the noncoherent surface nucleus in that region. A transition to a $(\Delta T)^{-1}$ rate law may occur if the δ is fairly large. This transition will not be abrupt.

7.3. Noncoherent Bundlelike Growth and Spherulite Structure

There is nothing in the present model that suggests the existence of lamellae of large extent that have a uniform step height.

If large chain ends that cannot be assimilated into the crystal are taken to be the cause of the limitation on lengthwise growth of each of the individual crystallites in the coherent growth process, a large distribution of lengths, i.e., "lamellar thicknesses" would result. The mean length of the individual crystallites would depend on the molecular weight and its distribution, rather than on the degree of supercooling. With small chain ends that can occasionally enter the crystal, there is still no reason to suspect anything but a large distribution of such lengths, though the mean length would be larger and in any event not be of the correct magnitude to correspond to the thickness of a lamella. It is in our view extremely improbable that a collection of bodies of varying radii and length would aggregate in such a manner as to form slabs of uniform thickness with flat faces. We therefore conclude that the asumption that chain ends limit lengthwise growth is not consistent with the prediction of typical lamellae. Even if one considers bundlelike crystals before such a mean "equilibrium" length is attained, one must contend with the fact that large bundlelike crystals will tend to be ellipsoidal in order to minimize the total surface free energy and strain [25, 26], and the fact they will continue to grow in the l direction.

If cumulative strain at the bundle ends is taken as the cause of the cessation of coherent growth, the "length" of the crystals might be quite uniform. However, the existence of such strain would clearly tend to force the individual bundlelike crystallites to have curved end surfaces, which is inconsistent with lamellar structure. Here again the mean length of the ellipsoidal crystallites would not depend strongly on the degree of supercooling.

In both of the cases mentioned above, the introduction of the noncoherent nucleation step allows the continuation of radial growth, but in no way suggests that true lamellae could be produced from the decidedly irregular or ellipsoidal microcrystals produced in the coherent step.

No contradiction to the concept that bundlelike crystallization will not lead to typical lamellar structures arises when the noncoherent variations of the special models depicted in figures 5b or 5c are considered. If the model illustrated in 5b were actually capable of eliminating cumulative strain (which is by no means certain), such strain could not be the cause of the cessation of coherent growth. The "lamella" would grow in the l direction as noted in section 4.2 until chain ends stopped them, but then they would possess a distribution of lengths as noted previously. Alternatively, if cumulative strain were not relieved by the tilting, each crystallite would have curved ends, and therefore not be able to form a lamella. The latter objection also holds for the model shown in figure 5c if cumulative strain is not relieved by tilting. If such strain is eliminated by the tilt for 5c, one is forced to the assumption that unassimilable chain ends must be the ultimate limitation on coherent growth, but this has already been seen to be inconsistent with the existence of typical lamellae. Also, the other objections to 5c noted in section 4.3 still hold.

The bundlelike microcrystals will tend to melt close to the crystallization temperature because of the accumulated strain.

The bundlelike noncoherent growth model might lead to a more or less spherical and semicrystalline aggregate composed of a vast number of small crystallites of nonuniform size. (The introduction of the noncoherent step involves the assumption that suitable surfaces for such nucleation are formed by the individual coherently grown crystals.) If such an object is identified in some bulk polymer by electron microscopy or other methods, it would be reasonable to attempt to treat its radial growth with this model. However, it would seem more appropriate to treat a typical lamellar spherulite in terms of the coherent or noncoherent chain fold models.

If noncoherent nucleation is impossible because no suitable surface is presented by the coherently grown crystal (e.g., because of excessive curvature), small bundlelike crystallites may appear more or less at random in the system. These aborted structures might coexist with folded structures that were meanwhile growing to large size.

★8. Discussion

8.1. Synopsis of Radial Growth Rate Laws

The most important laws describing the rate of radial growth of spherulites derived in this paper may be summarized in the general form:

$$\log_e (G/G_0) = -(\Delta H^*/RT) - K_1/T^2(\Delta T) \quad (56)$$

$$[(\Delta T)^{-1} \text{ law}]$$

and

$$\log_e (G/G_0) = -(\Delta H^*/RT) - K_2/T^3(\Delta T)^2. \quad (57)$$

$$[(\Delta T)^{-2} \text{ law}]$$

Another law was mentioned, but it is probably of little importance and is included mainly for the sake of completeness:

$$\log_e (G/G_0) = [-(\Delta H^{**} + \Delta H^*)/RT] + K_3(\Delta T). \quad (58)$$

$$[(\Delta T)^{+1} \text{ law}]$$

A convenient summary of the rate laws as they arise in the various models is given in table 1 for coherent and noncoherent surface nuclei for both the bundlelike and chain folded classes. Given also is the best estimate of the type of "spherulite" that each model implies, and the sequence of rate transitions.

General Interpretation of Rate Laws: The $(\Delta T)^{+1}$ radial growth rate law holds when the rate determining surface nucleus has no dimensions that may

be regarded as variables in the expression for the free energy of formation of the nucleus. The nucleus associated with this model, which is of the size a_{min}, b_{min}, l_{min}, may therefore be described as *zero-dimensional*.

The $(\Delta T)^{-1}$ radial growth rate law bears the general meaning that the rate determining step involves a surface nucleus that has one fixed and two variable dimensions. (Such a body is commonly called a *two-dimensional* surface nucleus.) This meaning holds true for both the $(\Delta T)^{-1}$ law that appears beginning at the melting point in the coherent growth models, and the $(\Delta T)^{-1}$ law that arises at moderate or strong supercooling for the noncoherent growth models.

The $(\Delta T)^{-2}$ radial growth rate law arises when the rate determining step is the formation of a surface nucleus that has three dimensions that are to be regarded as variables in the expression that describes the free energy of formation; such a body is commonly referred to as a *three-dimensional* surface nucleus. In the present conception, such a nucleus could be formed if the polymer molecules were deposited on the polymer substrate in such a manner that they were no longer colinear with those in the substrate, thus forming an interface between the two bodies. In this event, the surface nucleus takes on the three-dimensional character of a primary nucleus as regards temperature dependence, but is energetically preferred to the corresponding primary nucleus by virtue of the wettability of the substrate by the noncoherent surface nucleus. In our view, then, the observation of a $(\Delta T)^{-2}$ radial growth rate law would not only mean that the rate determining step was the formation of a three-dimensional surface nucleus, but would also imply that a noncoherent surface nucleus was involved.

Experimental Expectations: It is of interest to indicate what the theory implies concerning the probability that the various rate laws will be observed experimentally, together with a number of related points that may prove useful in attempting to apply the theory.

It is considered highly improbable that the $(\Delta T)^{+1}$ rate law will be frequently encountered in experimental studies. This rate law will generally be obscured or distorted by nonsteady state nucleation effects. If it did appear, it would do so at moderate to strong supercooling where the jump rate term would make it difficult to identify.

The $(\Delta T)^{-1}$ radial growth rate law would appear to deserve strong consideration in the analysis of data, especially in the case of obviously lamellar spherulites. We refer here specifically to the $(\Delta T)^{-1}$ law arising from the *coherent model with chain folds*. This model is capable of predicting many of the details of a lamellar spherulite, and coherent growth must be regarded as a probable mechanism, particularly if there is any reason to believe that a small and efficiently packed chain fold that is consistent with the interior lattice structure can be formed. On the grounds that studies on solution-grown single crystals appear to indicate that such folds can be formed in a number of cases, and the fact that lamellae of considerable extension have been observed in spherulitic bulk polymer samples, we believe that it is reasonable to suppose that a $(\Delta T)^{-1}$ radial growth rate law arising from coherent growth with chain folds should be found experimentally. Linear polymers with no bulky side groups or effective atactic sections are doubtless promising systems for such studies.[27] The melting behavior of a number of spherulitic polymers seems more consistent with coherent growth than noncoherent growth.

The coherent bundlelike model also leads to a $(\Delta T)^{-1}$ growth rate law, but we do not consider this a likely source of such a rate law. It cannot produce a lamellar spherulite at all. Under a variety of conditions, the model does not even lead in a straightforward way to any kind of spherical object.

The $(\Delta T)^{-2}$ radial growth rate law deserves consideration in the analysis of data, most particularly in connection with the noncoherent chain fold model. It seems conceivable that in some polymers the chain folds may be too bulky to allow continued coherent growth, and in such cases it is possible that noncoherent three-dimensional surface nuclei may form, and constitute the rate determining step in the radial growth mechanism. (It is to be expected that such bulky chain folds would first induce a tilting of the polymer chain axes with respect to the σ_e plane, lamellar twist, or even a change of crystal structure to a more open form.) If spasmodic growth of the spherulite radius is observed near the melting point, a $(\Delta T)^{-2}$ law becomes a good possibility.

The $(\Delta T)^{-2}$ law arising from the noncoherent bundlelike model need only be considered for nonlamellar spherulites.

It is evident that a combination of knowledge obtained from electron and optical microscopy and other appropriate physical methods concerning the texture of a spherulite, together with a knowledge of its radial growth rate law, would be very useful in deciding in detail how these objects were formed.[28]

8.2. Transitions in the Radial Growth Rate

The objective of this section is to bring out some points connected with the rate transitions that may occur in the radial growth rate of spherulites when the growth rate is considered as a function of temperature.

Two different types of rate transition have been postulated. In the first, the transition is due to some dimension of the surface nucleus approaching a minimal value, causing a different radial growth rate law to exist at lower temperatures (*transition in surface nuclei*). The second type of transition postulated in the radial growth rate is not due to any change in the surface growth nucleus itself; bundle or loop type nuclei where all three dimensions are of

[27] Even when present in low concentration, noncrystallizable units in a copolymer must be expected to disrupt the formation of regularly folded crystals.

[28] It is actually quite difficult to distinguish experimentally between the $(\Delta T)^{-1}$ and $(\Delta T)^{-2}$ laws in many cases, largely because of the uncertainty in T_m. The value of ΔH^* must not either implicitly or explicitly be set equal to zero in attempting to determine the ΔT law. This strongly and incorrectly favors the $(\Delta T)^{-2}$ law over the $(\Delta T)^{-1}$ law. Methods of determining the radial growth rate law from data on spherulites will be discussed in detail in a forthcoming publication [35].

minimal size appear in large numbers as a result of nonsteady state nucleation in the surrounding medium, and interfere with the growth of well developed spherulites (*transition in surrounding medium*).

Transitions in Surface Nuclei: In the text, these are denoted **A''** (upper)→**A''** (lower) and A'' (upper) →A'' (lower). Such transitions occur only for noncoherent surface nuclei (see table 1). The transition is a result of the b dimension of the growth nucleus falling to its minimal value.

If it occurs, this type of transition will not be particularly abrupt. The theory for G in the transition region can be worked out for some simple models. The result is that G is actually continuous across the transition, provided that G_0 and ΔH^* are either constant with growth temperature, or smooth and continuous functions of temperature. It could happen that ΔH^* or G_0 was different in the two regions, so that the plot of log G against T near the transition resembled a branch point, or even exhibited a small discontinuity. In any event, it is emphasized that the rate laws cited in this paper hold at growth temperatures somewhat removed from the transition region.

The coherent folded nucleus model does not exhibit this type of transition, but the noncoherent folded nucleus model does. Therefore, if a rate transition involving a $(\Delta T)^{-2}$ law near the melting point and a $(\Delta T)^{-1}$ law beginning somewhat below it is found in a lamellar spherulite, the noncoherent model with chain folds would be indicated. A similar situation in a nonlamellar spherulite would point to the noncoherent bundlelike model.

In general, the appearance of transitions due to a dimension of a surface nucleus approaching a minimal value is not considered very likely, with the possible exception of the one associated with the noncoherent folded model. If found, such transitions would provide valuable insight into the spherulitic growth process.

Transition in Surrounding Medium (*nonsteady state nucleation*): Consideration will now be given to the transition at T_c resulting from the rapid

TABLE 1. *Spherulitic growth*

Model	$\log_e(G/G_0)$	Temperature range	Rate law	Remarks
Coherent surface nucleus models [a]				
Coherent folded nuclei [b]	$-\frac{\Delta H^*}{kT}-\frac{4\mathbf{b}_0\boldsymbol{\sigma}\boldsymbol{\sigma}_e}{(\Delta f)kT}$ (two-dimensional nucleus)	Region **A'**, T_m to T_c.	$(\Delta T)^{-1}$	Predicts a typical lamellar spherulite.
Coherent bundlelike nuclei	$-\frac{\Delta H^*}{kT}-\frac{4b_0\sigma\sigma_e}{(\Delta f)kT}$ (two-dimensional nucleus)	Region A', T_m to T_c.	$(\Delta T)^{-1}$	Does not lead to lamellar spherulite. Will give microcrystals scattered throughout medium; formation of spherical object of macroscopic size doubtful.
Noncoherent surface nucleus models [a]				
Noncoherent folded nuclei [b]	$-\frac{\Delta H^*}{kT}-\frac{32\boldsymbol{\sigma}(\boldsymbol{\sigma}-\boldsymbol{\delta}/2)\boldsymbol{\sigma}_e}{(\Delta f)^2kT}$ (three-dimensional nucleus)	Region **A''** (upper), T_m to $\mathbf{T}''_\delta$.	$(\Delta T)^{-2}$	Produces a modified lamellar spherulite. Radius will increase spasmodically in Region **A''** (upper).
	$-\frac{\Delta H^*}{kT}-\frac{4\mathbf{b}_0\boldsymbol{\sigma}\boldsymbol{\sigma}_e}{(\Delta f)kT}$ (two-dimensional nucleus)	Region **A''** (lower), $\mathbf{T}''_\delta$ to T_c.	$(\Delta T)^{-1}$	
Noncoherent bundlelike nuclei.	$-\frac{\Delta H^*}{kT}-\frac{32\sigma(\sigma-\delta/2)\sigma_e}{(\Delta f)^2kT}$ (three-dimensional nucleus)	Region A'' (upper), T_m to T''_δ.	$(\Delta T)^{-2}$	May lead to a microcrystalline nonlamellar spherulite.
	$-\frac{\Delta H^*}{kT}-\frac{4b_0\sigma\sigma_e}{(\Delta f)kT}$ (two-dimensional nucleus)	Region A'' (lower), T''_δ to T_c.	$(\Delta T)^{-1}$	

[a] $\boldsymbol{\sigma}$ and $\boldsymbol{\sigma}_e$ are the lateral and end surface free energies, respectively, for folded nuclei; σ and σ_e are the corresponding quantities for bundlelike nuclei. The quantity (Δf) is given by $[(\Delta h_f)(\Delta T)/T_m][T/T_m]$.

[b] In the expressions for $\log_e(G/G_0)$ for the folded nuclei, the edge free energy $\boldsymbol{\epsilon}$ has been set equal to zero to simplify them (see text for complete expressions).

ingress of loop (or bundlelike) nuclei in the medium surrounding a spherulite that may interfere with its growth.

It is to be expected that the T_c transition can be relatively abrupt, occurring over a temperature range as little as several degrees. It will be accompanied by a noticeable fall in G. A transition fitting this general description has been found by Takayanagi [13] in poly(ethylene adipate) as may be seen by noting the lower transition in his figure 7. An even more remarkable drop in the radial growth rate of spherulites in poly(chlorotrifluoroethylene) at 156 °C, which is about 65 °C below T_m, has been found by Hoffman and Weeks [35]. Another point of interest is that the rate of bulk crystallization, as measured dilatometrically, should increase at T_c, even though G falls. This effect is particularly striking in the case of poly(chlorotrifluoroethylene).

The T_c transition as such is certainly not to be expected in radial growth rate studies in all polymers. For many polymeric substances, σ will be around 10 erg cm^{-2}, and $\mathbf{a}_{\min}$ will be perhaps 10 A. Then the T_c transition would appear only at a degree of supercooling of about 150 °C or more if (Δh_f) lies in the usual range. This will usually be below T_g, where the radial growth rate has already been greatly lowered by the jump rate effect. Even if T_c is nearer to the melting point than this, it is rather likely to be obscured by experimental difficulties arising from extremely rapid growth. The T_c transition is most apt to be observed in materials where it is nearest to the melting point, i.e., those with a low lateral surface free energy and a large molecular diameter.

On the basis of the above remarks, the situation where the radial growth rate is low near T_m, rises to a maximum below T_m, and then falls again without any obvious discontinuities anywhere is the one to be most commonly expected. However, it is important to bear in mind the possibility that rate transitions can occur when analyzing radial growth rate data for polymeric systems.

Glass formation might be practically impossible, even with the most rapid quenching, if T_c falls well above the glass transition temperature. Then the supercooled liquid (which would otherwise form a glass on cooling below T_g) would tend to nucleate and crystallize rapidly at or somewhat below T_c. At the very least, such a "glass" would contain a large number of "frozen in" embryos, nuclei, or crystallites in addition to any truly amorphous glassy material. The ordinary homogeneous mechanism (or a heterogeneous one) could, of course, cause crystallization to become very rapid above T_c. In any event, the failure of many linear polymers to easily form truly amorphous glasses may involve the "nucleative collapse" effect beginning at T_c.

The basic effect that causes the T_c transition, namely, transport of a large number of nuclei of minimal size from the melt to the supercooled state, can be employed to explain certain effects associated with prequenching on spherulitic growth. In the case of the theory discussed so far, it has been assumed that we were dealing with specimens that were cooled directly from well above T_m to the growth temperature, and the rate of radial growth observed under these conditions. Suppose, however, that experiments were carried out by first *quenching* the polymer to some low temperature, and then observing radial growth after the specimen is *rewarmed* to a certain growth temperature. Then at this growth temperature, G will often be lower than if the value of G had been obtained in the normal way at the same growth temperature. Results of this type are known, and may be ascribed to the incursion of small nuclei during the quenching process. The difference might be negligible if T_c is near or below T_g. Growth rate data obtained on prequenched and reheated specimens should be regarded with caution from an interpretive standpoint, since the retardations to radial growth will involve factors that have not been considered in deriving the expressions for G.[29]

8.3. Crystallization Without Chain Folds or Spherulites

The objective of this section is to emphasize the possibility that (1) crystallization without chain folds may occur, and (2) that crystallization with chain folds but without any obvious spherulites may exist.

Normal Bundlelike Crystallization: In the event that $\sigma_e < \sigma_e$ for both nuclei and crystals, and assuming that loop type structures are not initiated at heterogeneities, bundlelike crystallites might occur on a considerable scale. If noncoherent surface nucleation did not take place, the (probably ellipsoidal) crystallites formed would be scattered throughout the medium, i.e., no spherulites would form, but if noncoherent nucleation did take place, a spherical and microcrystalline but distinctly nonlamellar "spherulite" might form (see sections 4 and 7). The condition $\sigma_e > \sigma_e$ will lead to chain folded structures, but under certain conditions these may not be in a readily identifiable spherulite (see below).

Crystallization of Oriented Polymers: Suppose it is known for a certain polymer that when it is crystallized by cooling the unoriented melt to a temperature slightly below T_m that lamellar spherulites are formed, and that the principal site of the crystallization is in the spherulites. Typical lamellar spherulitic crystallization frequently occurs under these conditions. We now ask what might change this state of affairs.

Assume now that the polymer liquid is in some manner caused to be in a highly oriented state above T_m, and that this system is then supercooled. The possibility then exists that bundlelike rather than loop type crystals will form. In this event, the sample would contain neither lamellae or lamellar spherulites. A distinct long X-ray spacing may arise from such bundlelike crystallites if they have a fairly uniform size in the l direction due to strain or other factors. This spacing will almost certainly not vary as $1/(\Delta T)$ as will the spacings from chain folded crystals formed from the unoriented melt, and care

[29] Abnormally large ΔH^* values can result for spherulitic growth taking place in a medium that contains competing nuclei or crystallites.

should be taken not to confuse the spacings obtained on strongly oriented and unoriented specimens. In moderately oriented systems, chain folded and bundlelike crystals may coexist.

Crystallization in Region B: Another possible source of nonspherulitic crystallization in a polymer whose macroscopically observable growth form at low to moderate supercooling is of the lamellar spherulitic type is rapid crystallization well below T_c, i.e., in region B. This will often lead to a hierarchy of very tiny crystallites, most so small they scatter but little visible light. (A similar failure of well developed spherulites to appear may be caused by the presence of large numbers of active heterogeneous nuclei, or a very high rate of homogeneous nucleation.) It is reasonable to suppose that $\sigma_e < \boldsymbol{\sigma}_e$ might hold for nuclei of minimal size even when $\sigma_e > \boldsymbol{\sigma}_e$ for larger nuclei and crystals. This is implied by the concept that cumulative strain may exist at the bundle ends. In such a case, chain folded lamellar spherulites or other lamellar structures would form above T_c, while many of the small crystals and embryos formed below T_c would be bundlelike. The fine-grained crystallization produced below T_c will tend to be mixed with spherulites formed above T_c during the subcooling process.

In summary, the presence (or absence) of typical lamellar spherulites could depend on the previous orientation of the melt, the temperature of crystallization, the number of heterogeneities present, and the ratio $\sigma_e/\boldsymbol{\sigma}_e$. Conditions may exist where bundlelike and chain folded structures occur together.

8.4. The Initiation of Spherulites in Real Systems: Heterogeneous, Pseudohomogeneous, and Homogeneous Nucleation

One important reason for attempting to obtain the homogeneous injection rate of spherulites as a function of temperature lies in the fact that the temperature dependence of this quantity determines certain products involving the surface free energies that are different from those obtained from the radial growth rate. Thus, for a lamellar spherulite near T_m, a knowledge of $\mathbf{I}_A$ as a function of temperature would allow the product $\boldsymbol{\sigma}^2\boldsymbol{\sigma}_e$ to be determined by eq (6) or (18). However, certain phenomena stemming from the presence of heterogeneities can closely imitate homogeneous injection, and lead to "$\boldsymbol{\sigma}^2\boldsymbol{\sigma}_e$" values that are significantly low. These effects are discussed below, partly with the objective of indicating why the radial growth rate of spherulites, rather than their "homogeneous" injection rate, was stressed in the paper.

Consider first *heterogeneous* nucleation of spherulites. Turnbull [36] has shown that if a substance contains thermally stable (and wettable) heterogeneities containing pores or cavities on their surfaces, crystalline embryos can persist in these on an equilibrium basis well above the melting point. Such a body will act as a center of growth at or near $t=0$ after the material is supercooled. The number of such active embryos is strongly dependent on the temperature T_1 above T_m to which the system is initially heated if a crack-size distribution exists. By sufficient superheating, the embryos in the pores or cavities can be melted out, thus rendering them inactive as nucleation centers in a subsequent crystallization. Turnbull's theory shows that, other things being equal, the embryos in the larger pores are melted out first as T_1 is increased. In cases where the cavities are small, and where the heterogeneity is rather strongly wetted by the crystalline phase, the embryos may persist hundreds of degrees above the bulk melting point.

Spherulites in many cases are well known to follow this pattern of heterogeneous initiation. In such a case they are all born at or near $t=0$, and their number per unit volume is markedly dependent on T_1—increasing T_1 substantially reduces this number. (In cases where they are born later than $t=0$, they tend to be born in a narrow range of times about an induction time, τ_i.) It is therefore clear that spherulite producing structures can be, and frequently are, maintained in cracks or fissures in heterogeneities.

We turn now to *pseudohomogeneous* nucleation of spherulites. Heterogeneities may contain flat but wettable regions in addition to pores or cracks. No embryos will persist on these flat surfaces above the bulk melting point. However, when a system containing such heterogeneities is supercooled, nuclei will preferentially appear on these flat surfaces by virtue of the wettability of these surfaces by the polymer crystal. If the number of heterogeneities with flat surfaces is large, the resulting crystals can appear in the supercooled system essentially sporadically in time instead of at $t=0$ or $t=\tau_i$. Under these conditions the crystals will appear not only sporadically in time, but also (on a macroscopic scale) randomly in space. For convenience we have denoted this as "pseudohomogeneous" nucleation. (This is the case of "heterogeneous" nucleation discussed by Avrami [37, 38].) Sporadic birth is, of course, also a property of crystallization in a truly homogeneous bulk phase.

Spherulites are sometimes seen to appear nearly sporadically in time and space in polymers. Pseudohomogeneous initiation should be suspected in any sample where the number of spherulites formed per unit volume in unit time for a given growth temperature depends on T_1, or where a hierarchy of spherulites born at $t=0$ also appears together with those born sporadically. Such effects indicate the presence of numerous wettable heterogeneities. Some of the studies reported in the literature, where the polymer spherulites were believed to be of truly homogeneous origin for the reason that they appeared more or less sporadically in time and randomly in space, may actually refer to the pseudohomogeneous category.

Homogeneous nucleation refers to the process where crystallization centers are spontaneously formed at random positions in the pure (homophase) mother phase by thermal fluctuations. Such a process is characterized by a rate of production of nuclei per unit volume of mother phase that is, after the establishment of the steady state, truly constant

in time. In short, the nuclei appear sporadically in time and randomly in space in the supercooled liquid. This process will be independent of T_1 for a wide range of T_1 values. True homogeneous nucleation of a bulk phase is an ideal situation not easily achieved experimentally in any bulk system, heterogeneous or pseudohomogeneous nucleation undoubtedly being much more common.

Spherulites of strictly homogeneous origin may appear in polymers, but a proof that this is true would be quite difficult. The following conditions are consistent with homogeneous initiation: (a) The spherulites appear sporadically in time with no excess population at or near $t=0$; (b) the spherulites appear at random positions in space, and show no memory of previous position in space in successive experiments;[30] (c) further steps to rid the system of heterogeneities (e.g., filtration, centrifugation, or partial precipitation of solutions) do not alter the results; and (d) the rate of injection of spherulites is not dependent on T_1.

It should be realized that true homogeneous nucleation has rarely been achieved or proved even with very carefully prepared specimens of ordinary size of *any* bulk material. One would hardly expect polymers to be an exception. Only work with fogs [19] or dispersions [21], where the heterogeneous nuclei are greatly outnumbered by the number of particles with no adventitious centers, has heretofore been found effective in producing conditions where homogeneous nucleation predominated and could be identified. Accordingly, rate of spherulite injection data on bulk samples should not be treated using homogeneous nucleation theory unless there is substantial reason to believe that the injection mechanism was principally homogeneous. It seems probable that a number of the "$\sigma^2\sigma_e$" values quoted in the literature on the basis of the assumption of homogeneous nucleation in the bulk phase are too low.

It would be of great interest to obtain reliable $\sigma^2\sigma_e$ values using dispersions of polymers in a manner analogous to that used by Turnbull for the *n*-paraffins [21].

8.5. Comment on Alternative Theory of Step Height

An alternative theory for the existence of a "step height" in polymer crystals has been advanced by Peterlin and Fischer [39]. They propose that the length ("step height") of a polymer crystal is limited because the longitudinal lattice vibrations become incoherent, and raise the free energy of the crystal if its gets too long. The "step height" of lamellae is thus believed by these authors to exist because of equilibrium considerations. They predict that the step height decreases with lowering temperature.

Entirely apart from the question of whether or not such a concept is correct in principle, the following comments are relevant: (1) The Peterlin-Fischer theory does not predict, or even in the mode analysis take account of, the existence of chain folds in bulk or in dilute solution. (2) To the extent that their work may be interpreted as referring to the bundlelike system with chains normal to the bundle ends, the objection illustrated in figure 5a applies to the prediction of bundlelike "lamellae" of large dimensions. (3) Since the "step height" is a phenomenon based on equilibrium considerations in the Peterlin-Fischer theory, it should depend on the *ambient* temperature rather than the *growth* temperature, the latter being the case for the theory presented in this paper. There is no evidence suggesting, for example, that the lamellae in bulk become thinner with lowering ambient temperature.[31] It is our conclusion that if the limitation on length proposed by Peterlin and Fischer exists, it evidently refers to a much larger dimension than the step height of a lamella.

The theory presented here and in an earlier paper shows how chain folded crystals can come into being, and provides a reasonably detailed picture of the properties of systems crystallizing in this pattern.

★9. Summary and Conclusions

We now give a brief summary of some major points that have been brought out concerning spherulitic crystallization in bulk polymers.

It was demonstrated that if one assumes that the end surface free energy of a bundlelike nucleus is larger than the corresponding quantity for a folded nucleus, i.e., $\sigma_e > \boldsymbol{\sigma}_e$, then homogeneous nucleation of chain folded structures will prevail in bulk. It was noted that heterogeneous nucleation is much more probable in real polymer systems, but that if $\sigma_e > \boldsymbol{\sigma}_e$, this type of nucleation will in all likelihood still initiate chain folded structures in bulk. It was then shown that coherent surface nucleation with chain folds will lead to structures possessing a considerable number of physical features commonly associated with lamellar spherulites. (The chain folded mode of crystal growth is highly probable if $\sigma_e > \boldsymbol{\sigma}_e$, and coherent nucleation is feasible if the folds are such that they do not lead to cumulative strain in the fold plane.) It was also indicated that the assumption of noncoherent nucleation with chain folds could produce a modified lamellar spherulite. In each case, emphasis was placed on predicting the radial growth rate of the spherulite as a function of the crystallization temperature. This property follows a different law for coherent and noncoherent growth, and a differentiation of the two is amenable to careful

[30] In polymers, retained orientation might create memory effects, but it should be possible to eliminate these by storing the samples above T_m for a time.

[31] Experiments aimed at differentiating between the "equilibrium" theory of Peterlin and Fischer, where the step height is a function of ambient temperature, and the "kinetic" theory presented in this paper, where the step height is a function of the growth temperature, must be carried out and interpreted with caution. For example, if a lamella with a certain step height in bulk is warmed, it will melt, and if kinetics permit, recrystallize at a new and larger step height (sec. 5.2). This must not be mistaken for an "equilibrium" increase in step height. Experiments conducted by lowering the temperature after crystallization are free of this objection provided no additional crystallization of supercooled liquid polymer take place at the lower temperatures, thus introducing thinner lamellae. Studies of the changes of step height of chain folded lamellae in dilute solution are of problematical value in this connection. They may show an increase of step height on warming due to melting followed by recrystallization. If the solubility is finite, thin lamellae will form from thicker ones in dilute solution on lowering the temperature. Neither of these effects in dilute solution may be interpreted as supporting the "equilibrium" theory. In some polymers, a slow increase of step height due to internal diffusion mechanisms in the crystal may take place, and further complicate matters. However, as noted in section 5.2, such a diffusion mechanism is distinguished by the fact it can take place isothermally at the original crystallization temperature.

experiment. Also, the behavior of the step height of a chain folded lamella in bulk was discussed. This included the step height as a function of growth temperature, the behavior on rewarming (melting, recrystallization), and the uniformity of the step height. The predictions given are mostly subject to experimental verification, and some are known to be at least qualitatively correct. It is highly significant that a kinetic theory of crystal growth, wherein a nucleus length maintains itself during growth because of chain folds, can reproduce so many of the known features of spherulitic crystallization in bulk.

Given the basic lamellar structure produced by the kinetic crystal growth theory with chain folds, it was shown how surface stress could cause the lamellae to warp or twist. A slight and noncumulative repulsion of the chain folds in the σ_e plane is sufficient to create the required type of surface stress. Others have previously shown that such twist can explain many aspects of the optical extinction patterns of spherulites, most particularly the complex rings that are often seen with a polarizing microscope.

An effort was made to indicate the nature of the reasons that σ_e might exceed σ_e. It was concluded that the value of σ_e will be considerably larger than had been supposed heretofore, because of the fact that a bundlelike nucleus clearly must possess a density gradient of considerable size at the bundle ends: calculations with a simple model were given showing that even the minimal value of σ_e would be quite large because of the work required to construct this density gradient region. When considered together with the theoretical and experimental estimates for σ_e, the result is that it is certainly not implausible to suppose that $\sigma_e > \sigma_e$, at least in some situations. In the one specific case that was considered (polyethylene), it was clear enough that this condition might indeed apply. If $\sigma_e > \sigma_e$ for a polymer, chain folded growth is to be regarded as an intrinsic mode of crystallization in the bulk phase.

Certain circumstances were mentioned whereby chain folded structures might be prevalent, though in competition with numerous small bundlelike crystallites, in a bulk polymer even if $\sigma_e < \sigma_e$ (poisoning of growth of extended bundlelike structures by cumulative strain or large chain ends; heterogeneous nucleation with special interactions). In sufficiently dilute solution, chain folded platelets will form, no matter whether $\sigma_e > \sigma_e$ or $\sigma_e < \sigma_e$, because of entropy considerations.

Assuming that the condition $\sigma_e > \sigma_e$ does exist, at least for fairly large crystals, we regard the most probable cause of this condition to be cumulative or noncumulative strain at the ends of the bundlelike nucleus or crystal. Such strain arises ultimately from the fact that for a bundlelike system, the crystal and liquid phases are "connected" through covalent bonds, a situation that does not occur to a significant extent in the folded system. Again we emphasize the fact that the condition $\sigma_e > \sigma_e$ virtually assures the predominance of the chain folded growth mechanism, whatever the type of initiation.

Considerable attention was directed toward a critical examination of whether the classical bundlelike model of polymer crystal growth, or certain variations of it, could lead to a lamellar spherulite. It was concluded that this was highly improbable.

In general, the bundlelike models suffered one or more of the following drawbacks: (1) The bundlelike nucleus with noncumulative strain is found to grow in the polymer chain direction, thus destroying any semblance of the stability or uniformity of the step height as observed experimentally in spherulites. (2) Bundlelike crystallites will have a tendency to exhibit rounded ends because of considerations based on strain or minimization of total surface free energy, or both, and this is not consistent with the existence of lamellae with large and flat σ_e-type faces. The bundlelike nucleus with cumulative strain will not grow to large size, and will definitely have rounded ends. (3) The assumption that the exclusion of large chain ends from the crystal ultimately causes the cessation of lengthwise growth of the bundles (on an equilibrium basis) leads to a wide distribution of crystallite lengths that is not consistent with either the uniform thickness, or the surface smoothness of a typical lamella. (4) The tipping of polymer crystals at low draw ratios is not readily understood in terms of bundlelike crystals. (5) It seems improbable that assemblies of strictly bundlelike "lamellae" would cleave along the required planes.

The deficiencies of the bundlelike models, as contrasted with the ability of the chain fold models to reproduce many of the significant structural feaures of lamellar spherulites, leads to the conclusion that it is highly probable that lamellar spherulites formed in bulk consist of structures that are built on a basically chain folded pattern.

To this it must be added that some bundlelike character, in the form of interlamellar links, or chains protruding from the fold plane, must be expected in lamellar spherulites. Further, the existence of a microcrystalline but nonlamellar spherulite built on the bundlelike pattern by noncoherent nucleation is by no means excluded. Therefore, the possiblilty exists that there is more than one basic scheme for the construction of spherulites in bulk despite the evidence that a number that have been carefully studied are lamellar.

Finally, some limitations that may exist on spherulitic growth with chain folds were noted. Exclusion of chain ends from the crystal for reasons of large size may hinder fold formation at low supercooling where the step height is large. At high supercooling, nonsteady state nucleation may occur in the medium surrounding a spherulite, and seriously hinder its growth.

10. Appendix: Simplified Density Gradient Model of the Primary Bundlelike Nucleus

Density Gradient Model: The treatment given below is not represented as a rigorous or complete solution of the problem of the bundlelike nucleus with a density gradient at the bundle ends. Our

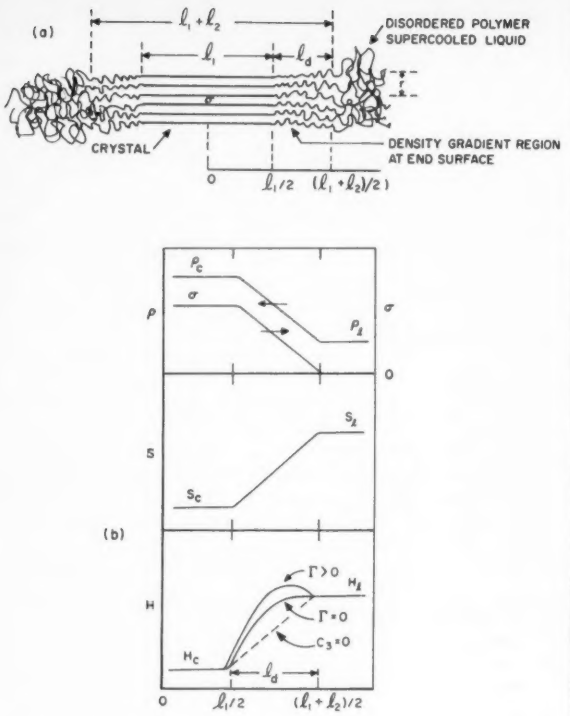

FIGURE 10. *Density gradient model of the primary bundlelike nucleus.*

(a) Schematic diagram of model showing dimensions and coordinates.
(b) Density, lateral surface free energy, entropy, and heat content as a function of length in the density gradient region at a bundle end.

intention in presenting the treatment below is to illuminate with a simple example some of the factors that might contribute to σ_e.

Consider a bundlelike nucleus with a middle section of normal crystal density ρ_c and lateral surface free energy σ, which has length l_1 and radius r. In addition, the nucleus has two diffuse bundle ends where the density gradually falls off from ρ_c to ρ_l, the latter being the density of the supercooled liquid. Call the radius of the diffuse end r, and let the total length of the nucleus be l_1+l_2. Let the l coordinate be zero at the center of the nucleus. Then the normal crystalline section of density ρ_c extends from zero to $l_1/2$, and the diffuse section, where the density falls to ρ_l, extends from $l_1/2$ to $(l_1+l_2)/2$. (See fig. 10a.)

For this model, the free energy of formation may be approximated as

$$\Delta\phi=2\pi r l_1\sigma+4\pi r W_s+2\pi r^2 W_e-\pi r^2 l_1(\Delta f), \quad \text{(A–1)}$$

where

$$W_s=\int_{\frac{1}{2}l_1}^{\frac{1}{2}(l_1+l_2)}\sigma(\rho)\,dl \quad \text{(A–2)}$$

and

$$W_e=\int_{\frac{1}{2}l_1}^{\frac{1}{2}(l_1+l_2)}\Delta F(\rho)\,dl. \quad \text{(A–3)}$$

Here $\sigma(\rho)$ is the lateral surface free energy as a function of density in the diffuse end region, and $\Delta F(\rho)$ the free energy of formation as a function of density in the same region.

$2\pi r l_1$ is the work required to form the lateral surface of the normal crystalline section of length l_1, and $4\pi r W_s$ is the work required to form the lateral surface of both diffuse ends. The quantity $\sigma(\rho)$ will be equal to σ at $l_1/2$, and zero at $(l_1+l_2)/2$. W_s will have a positive value, and not depend strongly on temperature.

$2\pi r^2 W_e$ represents the free energy of formation of the two diffuse bundle ends. This will contain some negative contributions, since $\Delta F(\rho)$ is equal to $-(\Delta f)$ at $l_1/2$, and zero at $(l_1+l_2)/2$. However, $\Delta F(\rho)$ will be positive for a certain range of l values between these limits, causing the net value of W_e to be positive. W_e may depend on temperature to some extent.

The model does not explicitly treat cumulative strain caused by radial growth. To do so would greatly complicate the model.

By the usual methods one finds $r^*=2\sigma/(\Delta f)$ and $l_1^*=2W_s/\sigma+4W_e/\Delta f$. On substitution of these in eq (A–1), there is obtained.

$$\Delta\phi^*=\frac{8\pi W_s\sigma}{(\Delta f)}+\frac{8\pi\sigma^2 W_e}{(\Delta f)^2}. \quad \text{(A–4)}$$

Hence, the homogeneous nucleation rate is,

$$I=I_0\exp\left(-\frac{\Delta H^*}{kT}\right)\exp\left(-\frac{8\pi W_s\sigma}{(\Delta f)kT}\right)\exp\left(-\frac{8\pi\sigma^2 W_e}{(\Delta f)^2 kT}\right). \quad \text{(A–5)}$$

The $(\Delta T)^{-1}$ term involving W_s will in some cases be nearly cancelled by components of opposite sign arising from W_e (see below). In any event, eq (A–5) will lead to a $(\Delta T)^{-2}$ nucleation rate behavior sufficiently near T_m.

Comparison With Sharp Boundary Model: The corresponding cylindrical bundlelike model with σ_e treated as a single constant representing the surface free energy as if it were concentrated at an abrupt phase boundary has the free energy of formation

$$\Delta\phi=2\pi r l_1\sigma+2\pi r^2\sigma_e-\pi r^2 l_1(\Delta f), \quad \text{(A–6)}$$

which leads to

$$\Delta\phi^*=\frac{8\pi\sigma^2\sigma_e}{(\Delta f)^2} \quad \text{(A–7)}$$

and

$$I=I_0\exp\left(-\frac{\Delta H^*}{kT}\right)\exp\left(-\frac{8\pi\sigma^2\sigma_e}{(\Delta f)^2}\right). \quad \text{(A–8)}$$

Except for unimportant differences in geometry, eqs (A–6) and (A–8) are analogous to eqs (4) and (6) or (18) of the text.

Comparison of eqs (A–4) and (A–7) show that

$$\sigma_e = W_e + \frac{(\Delta f) W_s}{\sigma}. \qquad \text{(A–9)}$$

A similar result is obtained if the parallelepiped geometry is used to treat the bundlelike density gradient model. Therefore, to the approximations inherent in eq (A–1), the above expression may be regarded as showing some of the factors that contribute to the effective value of σ_e for the bundlelike nucleus treated as if it had a sharp phase boundary at the bundle ends.

Application: A highly approximate but nevertheless instructive application of the density gradient model will now be given. The objective is to calculate σ_e as given by eq (A–9) in terms of the appropriate quantities. This requires that W_s and W_e be evaluated.

In order to calculate W_e, some assumptions must be made concerning $\Delta F(\rho)$. A crude model will suffice for the purpose of illustrating what contributes to W_e.

Begin by assuming that, at constant temperature, the entropy as a function of density in the diffuse bundle end has the form $C_1(\rho_0/\rho)$, where C_1 is a positive constant in the units erg deg^{-1} cm^{-3}, ρ_0 a reference density $(\rho_l+\rho_c)/2$, and ρ the density characteristic of some value l in the bundle end. No claim is made that this is exactly the relationship between entropy and density. However, the proposed expression does lead to an increase in entropy with a decrease in density, corresponding to the increase of entropy that must occur as a path is traversed from $\rho=\rho_c$ at $l_1/2$ at the normal crystal, out through the increasingly disordered bundle end to $\rho=\rho_l$ at $(l_1+l_2)/2$. From the proposed empirical function we see that

$$S - S_l = \Delta S(\rho) = C_1\rho_0\left(\frac{1}{\rho} - \frac{1}{\rho_l}\right). \qquad \text{(A–10)}$$

Assume further that the heat content as a function of density in the bundle ends is of the form $C_2(\rho/\rho_0) + C_3(\rho_0/\rho)$. Then

$$H - H_l = \Delta H(\rho) = \frac{C_2(\rho_l-\rho)}{\rho_0} + C_3\rho_0\left(\frac{1}{\rho_l} - \frac{1}{\rho}\right). \qquad \text{(A–11)}$$

The constants C_2 and C_3 are in erg cm^{-3}. This function is proposed with the express intent of causing a maximum to exist in $\Delta H(\rho)$ as one goes from $l_1/2$, where $\rho=\rho_c$ and $H=H_c$, out through the bundle end to $(l_1+l_2)/2$, where $\rho=\rho_l$ and $H=H_l$. (Both C_2 and C_3 must have positive values to give this maximum.) This maximum, whose magnitude is related to C_3 and Γ (see below), may be considered to result from noncumulative volume strain (repulsions or abnormal separations, of the chain segments) in the bundle end. The maximum in $\Delta H(\rho)$ in turn contributes to a maximum in $\Delta F(\rho)$ whose height depends on C_3 (or Γ). *This maximum in the free energy must exist in the surface region in order to cause phase separation.* (There is a small maximum in $\Delta F(\rho)$ even if $C_3=0$.) No assertion is made that eq (A–11) is an accurate representation of the heat content as a function of density in the bundle end; it is merely an empirical function meeting certain boundary conditions and other physical requirements of the problem at hand.

Accordingly, the free energy $F-F_l$ in the boundary region is

$$F - F_l = \Delta F(\rho) = \frac{C_2(\rho_l-\rho)}{\rho_0} + C_3\rho_0\left(\frac{1}{\rho_l} - \frac{1}{\rho}\right) - TC_1\rho_0\left(\frac{1}{\rho} - \frac{1}{\rho_l}\right). \qquad \text{(A–12)}$$

Applying the conditions $F_l - F_c = \Delta h_f(T_m - T)/T_m$, and $F_l - F_c = 0$ at T_m, one finds $C_1 = (\Delta h_f/\rho_0 T_m)(\rho_c\rho_l/\Delta\rho_l)$ and $C_2 = \rho_0^2(C_3 + T_m C_1)/\rho_c\rho_l$, where $\Delta\rho = \rho_c - \rho_l$. This gives

$$F - F_l = \rho_0 C_3\left[\frac{1}{\rho_c} + \frac{1}{\rho_l} - \frac{\rho}{\rho_c\rho_l} - \frac{1}{\rho}\right] + \frac{\Delta h_f \rho_c \rho_l}{T_m(\Delta\rho)}\left[\frac{T_m}{\rho_c} + \frac{T}{\rho_l} - \frac{T}{\rho} - \frac{T_m\rho}{\rho_c\rho_l}\right]. \qquad \text{(A–13)}$$

The expression for W_e may be written

$$W_e = \int_{\rho_c}^{\rho_l} (F - F_l)\frac{dl}{d\rho}\, d\rho. \qquad \text{(A–14)}$$

Assuming that the density falls off linearly with l in the density gradient region, $dl/d\rho = -l_d/(\Delta\rho)$, where l_d is the length of the gradient region at one of the bundle ends. Carrying out the integration and expanding $\ln(\rho_c/\rho_l)$ as $(\Delta\rho/\rho_l) - \frac{1}{2}(\Delta\rho/\rho_l)^2 + \frac{1}{3}(\Delta\rho/\rho_l)^3 - \ldots$, the result is

$$W_e = \frac{l_d(\Delta\rho)^2}{6\rho_l^2\rho_c}\left[\rho_0 C_3 + \frac{\Delta h_f \rho_l \rho_c}{(\Delta\rho)}\right] - \frac{l_d(\rho_c/\rho_l)(\Delta f)}{2}. \qquad \text{(A–15)}$$

Both of the terms in the brackets make positive contributions to W_e, since C_3 is positive. In arriving at (A–15) it was assumed that terms involving $(\Delta\rho/\rho)^4$ could be neglected.

The behavior of W_s may now be examined. Assuming that $\sigma(\rho)$ falls off linearly from σ at ρ_c to zero at ρ_l as

$$\sigma(\rho) = \sigma\left(\frac{\rho - \rho_l}{\Delta\rho}\right), \qquad \text{(A–16)}$$

one gets

$$W_s = \frac{l_d\sigma}{2}. \qquad \text{(A–17)}$$

Combining (A–15) and (A–17) according to (A–9) we get

$$\sigma_e=\frac{l_d(\Delta\rho)^2}{6\rho_l^2\rho_c}\left[\rho_0 C_3+\frac{(\Delta h_f)\rho_l\rho_c}{(\Delta\rho)}\right]. \qquad \text{(A–18)}$$

A term $[l_d(\Delta f)/2](1-\rho_c/\rho_l)$ has been omitted from eq (A–18) since it is too small to be of any consequence in this case. In other instances, however, the term involving (Δf) could be larger.

The nature of the various thermodynamic functions in the end surface region are shown schematically in figure 10b as a function of the distance traversed out through the bundle end. These were converted from $\sigma(\rho)$, $\Delta H(\rho)$ and $\Delta S(\rho)$ by assuming ρ is a linear function of l.

For $C_3=0$, which corresponds to a monotonic increase of heat content in the bundle ends, it is seen that $\sigma_e=l_d(\Delta h_f)(\Delta\rho)/6\rho_l$. This comes to roughly 9 erg cm^{-2} for the particular example relating to polyethylene cited in section 2.2. However, it is clear on physical grounds that the heat content must possess at least a flat maximum in the boundary region corresponding to a nonzero value of C_3. Consideration of this leads to a larger and more realistic minimum value of σ_e.

In a system where each molecule is forced to participate in the crystal and liquid (or supercooled liquid) phases, as is the case at the end of a bundle-like nucleus or crystal in a polymer, we consider it highly probable that the heat content at some point in the surface phase must be even higher than it is in the liquid. This effect may be taken to be a result of the volume strain that must occur in such situations. (The above remarks refer to nuclei of substantial size, say with a radius of 50 A or more, where density differences between the liquid and crystal will become effective. The volume strain effect would tend to be unimportant if only three or four chains were involved. The model is in any case not valid for such small radii.)

Consider now the value of C_3 that will lead to a maximum in $\Delta H(\rho)$ between $l_1/2$ and $(l_1+l_2)/2$. It is easily shown that C_3 must be larger than $(\Delta h_f)\rho_l^2\rho_c/\rho_0(\Delta\rho)^2$ in order that this maximum exist.[32] Therefore we may write

$$C_3=\frac{(\Delta h_f)\rho_l^2\rho_c}{\rho_0(\Delta\rho)^2}+\Gamma \qquad \text{(A–19)}$$

where $\Gamma\geqq 0$. Hence, from (A–18) and (A–19), one gets

$$\sigma_e=\frac{l_d(\Delta h_f)\rho_c}{6\rho_l}+\frac{l_d(\Delta\rho)^2\rho_0\Gamma}{6\rho_l^2\rho_c}. \qquad \text{(A–20)}$$

The quantity Γ is in erg cm^{-3}. The case $\Gamma=0$ corresponds to that where there is no maximum in $\Delta H(\rho)$. This in turn corresponds to the smallest maximum in $\Delta F(\rho)$, and therefore the smallest value of σ_e, that is physically realistic according to the model. Actual values of σ_e would almost certainly involve $\Gamma>0$.

[32] The maximum in $\Delta H(\rho)$ occurs at $\rho^2_{max}=\rho_l\rho_c/[1+(\Delta h_f)\rho_c\rho_c/\rho_0 C_3(\Delta\rho)]$. Since $\rho^2_{max}\geqq\rho_l^2$, the condition noted follows.

The particular model treated above does not lead to a large temperature dependence of σ_e, though the term $(\Delta\rho)^2$ will fall with lowering temperature. However, there are a number of reasons for expecting σ_e to depend somewhat more on temperature in the more general case. For example, the residual term involving (Δf) that practically cancelled in eq (A–18) may be larger if other assumptions concerning $\Delta F(\rho)$, $\sigma(\rho)$, and $dl/d\rho$ are used.

Special thanks are due Dr. A. Keller for his criticism of an early version of the manuscript, and for many helpful discussions in which he imparted much useful information to the authors, some as yet unpublished. Thanks are also due Drs. F. P. Price, D. Turnbull, H. D. Keith, H. Wyckoff, W. M. D. Bryant, P. H. Geil, W. O. Statton, D. W. McCall, and A. Posner for commenting on the manuscript and bringing important points of view and information to the attention of the authors. Also, the calculation concerning lamellar twist by Dr. J. N. Frankland noted in this paper is gratefully acknowledged. Finally, we reiterate our earlier acknowledgement to Prof. F. C. Frank and Dr. M. P. Tosi, who generously made their unpublished work on fluctuations of step height in chain folded lamellae available to us.

11. References

[1] A. Keller and A. O'Connor, Discussions, Faraday Soc. **25** 114 (1958).
[2] A. Keller, Phil. Mag. **2** 1171 (1957).
[3] J. I. Lauritzen and J. D. Hoffman, J. Research NBS **64A** 73 (1960).
[4] H. D. Keith and F. J. Padden, Jr., N. Walter, and H. Wyckoff, J. Appl. Phys. **30** 1485 (1955).
[5] P. H. Geil, J. Polymer Sci. (*in press*).
[6] P. H. Geil, N.K.J. Symons, R.G. Scott, J. Appl. Phys., **30** 1516 (1959).
[7] A. Keller, J. Polymer Sci. **39** 151 (1959).
[8] H. D. Keith and F. J. Padden, Jr., J. Polymer Sci. **39** 101 (1959).
[9] H. D. Keith and F. J. Padden, Jr., J. Polymer Sci. **39** 123 (1959).
[10] F. P. Price, J. Polymer Sci. **39** 139 (1959).
[11] B. B. Burnett and W. F. McDevit, J. Appl. Phys. **28** 1101 (1957).
[12] B. Kahle and H. A. Stuart, J. Polymer Sci. **25** 485 (1957).
[13] M. Takayanagi, Memoirs Fac. Kyushu Univ. **16** 111 (1957).
[14] N. Hirai, J. Polymer Sci. **42** 213 (1960).
[15] F. P. Price, J. Polymer Sci., **42** 49 (1960).
[16] F. P. Price, Ann. New York Acad. Sci. **83** 20 (1959).
[17] A. D. McIntyre, PhD. thesis (Cornell University, Ithaca, N.Y., 1956); P. J. Flory and A. D. McIntyre, J. Polymer Sci. **18** 592 (1955).
[18] D. Turnbull and J. C. Fisher, J. Chem. Phys. **17** 71 (1949).
[19] D. G. Thomas and L. A. K. Stavely, J. Chem. Soc. 4569 (1952).
[20] Thermodynamics in physical metallurgy (American Society for Metals, Cleveland, Ohio, 1950) See chapter entitled "Principles of Solidification," by D. Turnbull.
[21] D. Turnbull, private communication (to be published in J. Chem. Phys.).
[22] P. J. Flory, J. Chem. Phys. **17** 223 (1949).
[23] J. D. Hoffman, J. Chem. Phys. **28** 1192 (1958).
[24] L. Mandelkern, SPE Journal **15** (1959).
[25] S. Matsuoka and B. Maxwell, Plastics Lab. Tech. Rept. 53E (Princeton University, 1959).

[26] F. C. Frank, remarks in "Growth and perfection of crystals" edited by R. H. Doremus, B. W. Roberts, and D. Turnbull (John Wiley & Sons, New York, (1958).
[27] J. W. Cahn and J. E. Hilliard, J. Chem. Phys. **31** 688 (1959).
[28] M. L. Williams, R. F. Landel, and J. D. Ferry, J. Am. Chem. Soc. **77** 3701 (1955).
[29] J. I. Lauritzen (manuscript in preparation).
[30] A. Keller, J. Polymer Sci. **17** 351 (1955).
[31] A. Keller, J. Polymer Sci. **21** 363 (1956).
[32] W. J. Dulmage and A. L. Geddes, J. Polymer Sci. **31** 199 (1958).
[33] R. S. Stein and F. H. Norris, J. Polymer Sci. **25** 381 (1956).
[34] K. H. Storks, J. Am. Chem. Soc. **60** 1753 (1938).
[35] J. D. Hoffman and J. J. Weeks (manuscript in preparation).
[36] D. Turnbull, J. Chem. Phys. **18** 198 (1950).
[37] M. Avrami, J. Chem. Phys. **7** 1103 (1939).
[38] M. Avrami, J. Chem. Phys. **8** 212 (1940).
[39] A. Peterlin and E. W. Fischer, Z. Physik **159** 272 (1960).
[40] Eppe, Fischer, and Stuart, J. Polymer Sci. **34** 721 (1959).
[41] F. C. Frank and M. P. Tosi (to be published).
[42] Fujiwara, J. Appl. Polymer Sci. **4** 10 (1960).
[43] D. H. Reneker and P. H. Geil, J. Appl. Phys. **31** 1916 (1960).
[44] J. D. Hoffman and J. J. Weeks (manuscript in preparation).

(Paper 65A4-114)

JOURNAL OF RESEARCH of the National Bureau of Standards—A. Physics and Chemistry
Vol. 65A, No. 4, July–August 1961

Phase Equilibrium Relations in the Binary System Barium Oxide-Niobium Pentoxide

R. S. Roth and J. L. Waring

(April 11, 1961)

A large portion of the phase equilibrium diagram for the binary system barium oxide-niobium pentoxide has been constructed from observations of fusion characteristics and X-ray diffraction data. In the system five binary compounds were observed with BaO : Nb_2O_5 ratios of 5:2, 1:1, 6:7, 3:5, and 1:3 and a 6:1 compound was postulated. The 1:1 compound was found to melt congruently at 1,455 °C and have only one stable polymorph, although a second metastable polymorph can also be prepared. The 5:2 compound melts congruently at 1,542 °C; the 6:7, 3:5, and 1:3 phases melt incongruently at 1,330, 1,290, and 1,315 °C, respectively. The phase relations of the 6:1 compound could not be determined due to the reaction between this phase and platinum metal. No 2:1 compound was observed in this system.

1. Introduction

A study of phase relationships in the binary system BaO-Nb_2O_5 has been conducted as part of a program of fundamental phase equilibria studies of ceramic materials. The compound $BaO \cdot Nb_2O_5$ has been previously reported by several workers [1,2][1], and one report exists in the literature of a compound having the formula $2BaO \cdot Nb_2O_5$ [3]. However, no systematic attempt to study the phase equilibrium relations in the entire binary system has been previously published.

X-ray diffraction data, together with the determination of the melting points of the compounds and of the solidus and liquidus temperatures at various compositions across the system have supplied data from which an equilibrium diagram has been constructed.

Owing to the reaction of BaO with Pt metal the high BaO portion of the system could not be studied by the present methods. This portion of the phase diagram, therefore, is necessarily left unknown, as is the case with all previously published phase diagrams involving BaO.

2. Sample Preparations and Test Methods

The following starting materials were employed for the preparation of specimens:

Nb_2O_5—high purity grade niobium pentoxide, manufacturer's designation over 99.7 percent. Spectrographic analysis indicated less than about: 0.1 percent Si, 0.01 percent Fe, Sn, and Ti, 0.001 percent Ca and Mg. Cu was not determined because of Nb interference.

$BaCO_3$—Reagent grade barium carbonate, manufacturer's designation 99.3 percent purity.

For the preparation of batches the weight percent calculations were computed to within ± 0.01 percent, with no corrections made for percentage purity of the raw materials except for loss on ignition. The starting materials were weighed to the nearest ± 0.1 mg, in sufficient quantities to yield 3 g batches. Each batch was mixed in a mechanical shaker, and the bulk specimens were then ground in a mechanical agate mortar for 1 hr. At the termination of grinding a few drops of distilled water were added to facilitate pressing. The ground material was pressed into a disk in a $\frac{5}{8}$ in. diameter mold at 10^4 lb/in.^{2} The disks were placed on platinum foil and then calcined in air between 700 and 900 °C using an electrically heated furnace. No analyses were made after firing.

Following this preliminary heat treatment the disks were ground, reformed in a $\frac{5}{8}$ in. mold at 1.5×10^4 lb/in.^{2}, and reheated to 1,100 °C for 8 hr.

Subsolidus as well as melting point data were obtained by the quenching technique on samples sealed in platinum tubes. An electrically heated, vertical tube furnace wound with 80 percent Pt-20 percent Rh wire was used. Temperatures were measured with a Pt versus Pt 10 percent Rh thermocouple which had been calibrated against the melting points of gold (1,063 °C) and barium disilicate (1,420 °C). The thermocouple was recalibrated several times during the course of the work. The first sign of adherence of the specimen to the platinum tube was interpreted as the first experimental evidence for the solidus temperature. This technique seemed justified for this particular system because of the marked fluidity of the liquid. The formation of a concave meniscus indicated the liquidus temperature.

[1] Figures in brackets indicate the literature references at the end of this paper.

Equilibrium was considered to have been obtained when the X-ray patterns of successively heated specimens showed no change. X-ray powder patterns were made using a high angle recording Geiger counter diffractometer and nickel-filtered copper radiation, with the Geiger counter traversing the specimen at 1/4°/min and the radiation being recorded on the chart at 1° 2θ/in.

3. Compounds in the BaO-Nb_2O_5 System

3.1. Nb_2O_5

The stability relations of the various reported polymorphs of Nb_2O_5 have been summarized by several workers [4, 5, 6, 7]. Here it is only necessary to note that the so-called high temperature form of Nb_2O_5 was the only modification encountered in the present work. The indexed X-ray diffraction powder pattern and the unit cell dimensions of this monoclinic phase were listed in a previous publication on the PbO-Nb_2O_5 binary system [8].

3.2. Compounds $3BaO{\cdot}5Nb_2O_5$ and $BaO{\cdot}3Nb_2O_5$

These two compositions have been observed to be essentially the end members of an "interrupted" solid solution series (a series involving a morphotropic phase transformation) having a distorted tungsten bronze type structure. The structure of the tungsten bronze type compounds will be discussed in section 5. It is only an academic question as to whether these compositions are true compounds or merely end members of the solid solution series. They were always observed to be single phase below the solidus and the compositions 5:8, on the high BaO side of 3:5, and 24:76, on the high Nb_2O_5 side of 1:3, show two phases. For these reasons the two end members are referred to as compounds for the sake of convenience. The X-ray patterns of the two compounds are very similar (tables 1 and 2), but have slightly different "superstructure" peaks indicating slightly different symmetries.

The diffraction peaks cannot be completely indexed on either the tetragonal or the orthorhombic modifications of the tungsten bronze structure observed for $PbO{\cdot}Nb_2O_5$ [9]. The $3BaO{\cdot}5Nb_2O_5$ solid solution (including $BaO{:}2Nb_2O_5$) appears to be isostructural with $PbO{\cdot}2Nb_2O_5$ [8]. The change in the position of the diffraction peaks in this solid solution region corresponds to an increase in the c/a ratio of the pseudotetragonal cell with decreasing BaO content, caused mostly by a decrease in a (with only a slight, if any, increase in c). The 1:3 solid solution on the other hand has a decrease in c/a ratio with decreasing BaO content, caused mostly by a decrease in c.

3.3. Compound $6BaO{\cdot}7Nb_2O_5$

A new compound has been observed at approximately this composition in the present study. This compound is very difficult to form as a single phase even at temperatures very near the solidus and may possibly be only metastable. However, the compound $BaO{\cdot}Nb_2O_5$ is never observed in specimens heated below the solidus for compositions richer in Nb_2O_5 than the 6:7 mole ratio; therefore this new compound is concluded to be a true equilibrium phase. Its X-ray diffraction powder pattern is listed in table 3.

TABLE 1. *X-ray diffraction powder data for the composition* $BaO : 3Nb_2O_5$ (CuKα *radiation*)

d	I/I_0	$1/d^2_{obs}$	$1/d^2_{calc}$	hkl [a]	d	I/I_0	$1/d^2_{obs}$	$1/d^2_{calc}$	hkl [a]
8.82	13	0.0129	0.0129	110	2.384	6	0.1760		
6.25	10	.0256	.0257	020	2.318	7	.1862	0.1863	250
5.58	2	.0321	.0321	120	2.283	7	.1919	.1920	241
4.41	12	.0514	.0514	220	2.1386	28	.2186	.2185	350
3.966	95	.0636	.0635	001	2.1105	4	.2245	.2241	431
3.943	65	.0643	.0643	130	2.0804	5	.2310	.2313	060
3.767	6	.0705			1.9840	55	.2541	.2541	002
3.709	15	.0727			1.9721	19	.2571	.2570	260
3.654	9	.0749			1.8595	25	.2892	.2891	360
3.461	65	.0835	.0835	230	1.7644	66	.3213	.3212	170/550
3.350	16	.0891	.0892	021	1.7486	18	.3270	.3269	451
3.234	50	.0956	.0956	121	1.7211	10	.3376	.3376	232
3.151	6	.1007			1.7154	9	.3398	.3405	270
3.117	8	.1029	.1028	040	1.6834	21	.3530	.3526	361
3.024	100	.1093	.1092	140	1.6592	32	.3632	.3633	142
2.941	72	.1157	.1149	221	1.6445	15	.3698	.3697	332
			.1157	330	1.6163	14	.3828	.3826	242
2.857	7	.1225			1.6119	26	.3849	.3848	171/551
2.835	6	.1244			1.5584	7	.4117	.4112	080
2.796	90	.1279	.1278	131	1.5469	9	.4180	.4176	470/180
2.791	72	.1284	.1285	240	1.5120	8	.4374	.4369	280
2.723	9	.1348			1.4809	6	.4560	.4554	561
2.681	7	.1391			1.4598	8	.4692	.4690	380
2.608	50	.1471	.1470	231	1.4553	9	.4721	.4725	352
2.453	18	.1663	.1663	041	1.4511	8	.4749	.4747	081
2.448	17	.1669	.1671	150					
2.405	12	.1729	.1727	141					

[a] These hkl values are given by analogy to the tetragonal "bronze" structure. This is only a pseudocell, as there are many peaks which cannot be indexed on this basis. The pseudotetragonal cell has unit cell parameters of $a=12.48$ A, $c=3.97$ A.

TABLE 2. *X-ray diffraction powder data for the composition* $3BaO : 5Nb_2O_5$ (CuKα *radiation*)

d	I/I_0	$1/d^2_{obs}$	$1/d^2_{calc}$	hkl[a]	d	I/I_0	$1/d^2_{obs}$	$1/d^2_{calc}$	hkl[a]
8.81	10	0.0129	0.0128	110	2.453	15	0.1662	0.1661	041
6.25	14	.0256	.0256	020				.1666	150
5.60	6	.0319	.0320	120	2.365	5	.1788	.1789	331
3.964	51	.0637	.0635	001	2.317	5	.1862	.1858	250
			.0641	130	2.140	20	.2180	.2178	350
3.860	5	.0671			2.0814	6	.2308	.2301	151
								.2306	060
3.778	4	.0701			2.0001	7	.2499	.2493	521
3.619	10	.0764	.0764	111	1.9835	40	.2542	.2542	002
3.545	9	.0796			1.8624	16	.2883	.2883	360
3.463	35	.0834	.0833	230	1.8461	6	.2934	.2942	061
3.350	25	.0891	.0892	021					
					1.7678	60	.3200	.3198	261
3.233	80	.0957	.0956	121				.3203	170/550
3.091	5	.1047			1.7518	17	.3259	.3262	451
3.026	100	.1092	.1089	140	1.7196	7	.3382	.3375	232
2.945	52	.1153	.1148	221				.3396	270
			.1153	330	1.6860	13	.3518	.3518	361
2.872	6	.1212			1.6598	27	.3630	.3631	142
2.796	90	.1279	.1276	131	1.6450	12	.3696	.3695	332
			.1281	240	1.6135	19	.3841	.3839	171/551
2.636	6	.1439							
2.601	35	.1471	.1468	231					

[a] These *hkl* values are given by analogy to the tetragonal "bronze" structure. This is only a pseudocell, as there are many peaks which cannot be indexed on this basis. The pseudotetragonal cell has unit cell parameters of $a=12.49$ A, $c=3.97$ A.

TABLE 3. *X-ray diffraction powder data for the compound* $6BaO{\cdot}7Nb_2O_5$(CuKα *radiation*)

d	I/I_0	d	I/I_0
3.973	18	1.8599	8
3.506	15	1.8500	8
3.466	17	1.8219	16
3.270	23	1.7787	15
3.231	17	1.7650	8
3.170	100	1.7527	16
3.124	17	1.7299	9
3.034	100	1.7217	37
2.995	60	1.6992	10
2.947	12	1.6636	18
2.880	13	1.6568	25
2.797	25	1.6166	12
2.779	12	1.6044	11
2.686	28	1.5798	10
2.627	8	1.5511	5
2.605	26	1.5473	7
2.597	9	1.5290	5
2.392	5	1.5027	8
2.279	4	1.4988	8
2.2265	15	1.4830	8
2.1938	12	1.4545	8
2.1776	8	1.4020	6
2.1372	5	1.3542	7
2.0891	9	1.3150	13
1.9873	50	1.2854	6
1.9418	10	1.2370	9
1.9106	7	1.1809	9

3.4. Compound $B\sim O{\cdot}Nb_2O_5$

A compound of this composition was apparently first recorded by Krylov and Alekseev [10] as cubic with $a=9.02$ A; however, the X-ray diffraction pattern which they listed for this phase does not correspond to cubic symmetry. This reported phase had been formed by decomposition of a hydrate and was never encountered in the present work.

a. Metastable Hexagonal Modification

Francombe [11] first reported a hexagonal modification of $BaO{\cdot}Nb_2O_5$ as "stable over a narrow temperature range below the melting point". In the present work this hexagonal modification was not found at temperatures near the melting point. However, the hexagonal phase was encountered only under nonequilibrium conditions in the 1:1 BaO–Nb_2O_5 composition which was held for long periods of time at the relatively low temperatures of 900° to 1,100 °C. This modification is apparently not stable throughout the whole temperature range. The hexagonal phase is apparently a metastable intermediary structure between the orthorhombic $BaO{\cdot}Nb_2O_5$ and the tungsten-bronze type structures. The X-ray diffraction powder pattern is given in table 4, with indices based on unit cell dimensions $a=12.07$ A, $c=3.95$ A.

TABLE 4. *X-ray diffraction powder data for the metastable hexagonal form of* $BaO{\cdot}Nb_2O_5$(CuKα *radiation*)

d[a]	I/I_0	hkl[b]
5.22	12	200
3.95	38	001/210
3.15	100	201
3.02	100	220
2.904	10	310
2.791	8	211
2.613	7	301/400
2.393	11	221/320
2.180	75	401
2.043	5	321
1.974	50	002
1.881	15	510/112
1.846	9	501
1.769	50	212
1.765	40	421
1.745	45	600
1.716	14	430
1.697	13	511
1.653	33	222

[a] As this phase was found only in mixtures containing orthorhombic $BaO{\cdot}Nb_2O_5$ the d values due to the later compound have been ignored for this table.
[b] The parameters upon which these *hkl* values are based are: $a=12.07$ A, $c=3.95$ A.

b. Stable Orthorhombic Modification

Apparently the only truly stable form of $BaO \cdot Nb_2O_5$ is the orthorhombic modification. This phase was reported previously by others and a comparison of unit cell dimensions is given below.

	a	b	c
	A	*A*	*A*
1957 Goodman [1]	12.24	10.29	7.90
1958 Coates and Kay [2]	12.16	10.27	7.78
1959 Francombe [12]	12.17	10.25	7.88
1960 Roth and Waring	12.194	10.268	7.856

The indexed X-ray diffraction powder pattern for orthorhombic $BaO \cdot Nb_2O_5$ is listed in table 5.

TABLE 5. *X-ray diffraction powder data for the stable orthorhombic form of* $BaO \cdot Nb_2O_5$ *(*CuK_α *radiation)*

d	I/I_0	$1/d^2_{obs}$	$1/d^2_{calc}$ [a]	hkl
5.53	4	0.0327	0.0324	111
3.924	15	.0649	.0648	002
			.0648	220
3.607	5	.0769	.0767	301
3.297	11	.0920	.0917	202
			.0921	130
3.142	100	.1013	.1012	212
3.118	80	.1028	.1028	022
3.046	50	.1078	.1076	400
2.984	100	.1123	.1123	230
2.949	6	.1149	.1147	321
2.921	7	.1172	.1171	410
2.565	4	.1520	.1518	040
2.479	5	.1627	.1621	331
			.1633	322
2.365	13	.1788	.1787	240
2.343	17	.1821	.1822	213
2.271	18	.1940	.1938	511
2.1801	29	.2104	.2104	422
2.1488	27	.2166	.2166	042
2.0924	10	.2284	.2285	341
2.0714	8	.2331	.2330	502
1.9689	18	.2580	.2578	432
1.9644	32	.2591	.2593	004
1.9262	9	.2695	.2697	531
1.8900	11	.2800	.2801	620
1.8398	12	.2954	.2956	214
1.8050	11	.3069	.3069	602
1.7775	12	.3164	.3164	612
1.7574	22	.3238	.3235	513
			.3241	224
1.7446	47	.3286	.3289	252
1.7125	15	.3410	.3415	060
1.7025	7	.3450	.3449	622
1.6521	17	.3664	.3669	404
1.6415	32	.3711	.3715	234

[a] These values are based on the unit cell parameters: $a=12.194$ A, $b=10.268$ A, $c=7.856$ A.

3.5. Compound $5BaO \cdot 2Nb_2O_5$

The compound $5BaO \cdot 2Nb_2O_5$ is previously unreported. The X-ray diffraction powder pattern (table 6) can be completely indexed on the basis of a hexagonal unit cell with the dimensions $a=5.794$ A, $c=11.784$ A. The powder pattern was indexed on the basis of its similarity to the metastable hexagonal modification of $BaO \cdot Nb_2O_5$ and the low temperature stable rhombohedral form of $PbO \cdot Nb_2O_5$. However, this compound has many diffraction lines not allowed by the rhombohedral cell found in $PbO \cdot Nb_2O_5$, and there are no lines in the powder pattern indicating the true cell has the larger $(a\sqrt{3})$ dimension of the hexagonal counterpart of this rhombohedral cell.

TABLE 6. *X-ray diffraction powder data for the compound* $5BaO \cdot 2Nb_2O_5$ *(*$CuK\alpha$ *radiation)*

d	I/I_0	$1/d^2_{obs}$	$1/d^2_{calc}$ [a]	Hexagonal hkl
4.61	5	0.0471	0.0469	101
3.827	9	.0683	.0685	102
3.063	100	.1045	.1045	103
2.897	100	.1192	.1192	110
2.540	8	.1550	.1549	104
2.453	7	.1663	.1661	201
2.358	12	.1799	.1800	005
2.308	25	.1877	.1877	202
2.1324	14	.2199	.2198	105
2.1143	100	.2237	.2237	203
1.9106	9	.2739	.2741	204
1.8298	49	.2987	.2990	106
1.7080	62	.3428	.3429	213
1.6726	33	.3575	.3575	300
1.5963	7	.3924	.3926	107
1.5468	21	.4180	.4181	206
1.4487	27	.4765	.4767	220
1.3977	8	.5119	.5117	207
1.3644	22	.5372	.5373	216
			.5375	305
1.3120	21	.5809	.5812	313
1.2583	3	.6316	.6316	314
1.1940	15	.7003	.7004	403
1.1933	14	.7022	.7025	119
1.1363	9	.7744	.7756	316
1.1050	10	.8189	.8195	323
1.0953	11	.8335	.8342	410
1.0925	9	.8378	.8393	1·1·10
1.0577	5	.8939	.8948	406
1.0311	5	.9405	.9408	309

[a] These values are based on the hexagonal unit cell parameters: $a=5.794$ A, $c=11.784$ A.

3.6. Compound $6BaO \cdot Nb_2O_5$

A compound of this formula type has been previously reported by Brixner [13] for the BaO-Ta_2O_5 and SrO-Ta_2O_5 systems as having a cryolite type structure. The specimens were prepared by Brixner by heating in sealed evacuated silica tubes. The compound $6BaO \cdot Nb_2O_5$ was also observed by Francombe [12]. This phase has not been observed in the present study due to the reaction of BaO with Pt which occurs in compositions higher in BaO than the 5:2 ratio. However, certain compositions in the BaO-Nb_2O_5-Gd_2O_3 system [14] have been observed to show a single phase cubic solid solution of the cryolite type which is apparently based on the 6:1 compound and confirms its existence as a true binary phase. The high BaO portion of the binary system can probably only be studied in vacuum or inert atmosphere; however, the composition of the specimen holder for high temperatures is still a problem.

4. Discussion of Phase Equilibria

The phase-equilibrium diagram of the binary system BaO-Nb_2O_5 is shown in figure 1. The data from which the diagram has been constructed are given in table 7. Most of the data was obtained from quenched specimens except where noted in the table. The designation Tet-ss in table 7 stands for the tetragonal tungsten bronze type structure, and signifies that the material which crystallized as "Tet-ss" must have been in the liquid state at the temperature from which the specimen was quenched (see discussion in section 5). The system contains two compounds which melt congruently, $5BaO{\cdot}2Nb_2O_5$ and $BaO{\cdot}Nb_2O_5$; and three compounds which melt incongruently, $6BaO{\cdot}7Nb_2O_5$, $3BaO{\cdot}5Nb_2O_5$, and $BaO{\cdot}3Nb_2O_5$. The melting point data for the compound $6BaO{\cdot}Nb_2O_5$ have not been determined.

The compound $5BaO{\cdot}2Nb_2O_5$ was found to melt congruently at about 1,542 °C. No phase transformations were observed in this composition. Compositions between $5BaO{\cdot}2Nb_2O_5$ and $BaO{\cdot}Nb_2O_5$ when heated in air were found to contain only these two phases.[1] A eutectic exists in the binary system between the two congruently melting compounds at 1,320 °C and is interpreted as occurring at about 62 mole percent BaO.

A compound of the ratio $2BaO{\cdot}Nb_2O_5$ was reported by Ismailzade [3] as tetragonal with $a=10.928$ A and $c=11.167$ A. No justification can be found in the present work for a compound at this ratio. From the unit cell dimensions listed, this phase would apparently be a tetragonally distorted pyrochlore structure. It can be deduced from the work of Isupov [15] that a pyrochlore type compound would not be expected to form in the BaO–Nb_2O_5 system.

The compound $BaO{\cdot}Nb_2O_5$ was found to melt congruently at 1,455 °C. The hexagonal polymorph of this composition was not found above about 1,100 °C and was never found as a single phase (see table 7). The orthorhombic polymorph was present in nonequilibrium mixtures as low as 900 °C. As the hexagonal polymorph has never been shown to exist stably, it is concluded that this phase is merely metastable in the binary system.

A small amount of solid solution has been observed on the high niobia side of the $BaO{\cdot}Nb_2O_5$ composition. This solid solution has not been entirely "quenched in" by the method employed and some nonequilibrium $3BaO{\cdot}5Nb_2O_5$ is always found in the X-ray patterns (see $48BaO{:}52Nb_2O_5$, table 7). The solid solution apparently extends beyond 48:52 as the compound $6BaO{\cdot}7Nb_2O_5$ is never observed in long heat treatments of this composition. A two phase

[1] When heated in a helium atmosphere, however, the composition $6BaO{\cdot}5Nb_2O_5$ contained essentially a single phase bronze type structure which would probably correspond to the ternary compound $Ba_6^{+2}(Nb_5^{+5}Nb_2^{+4})O_{30}$.

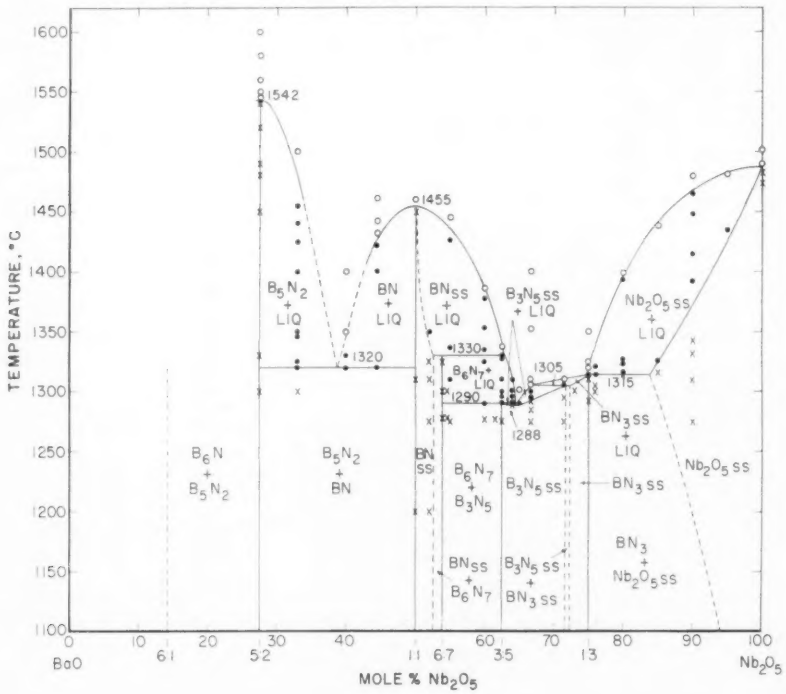

FIGURE 1. *Postulated phase equilibrium diagram for the system BaO–Nb_2O_5.*

x—not melted.
●—partially melted.
o—completely melted.

TABLE 7. *Experimental data for compositions in the binary system* $BaO–Nb_2O_5$

Composition [a]		Heat treatment [b]		Results	
BaO	Nb_2O_5	Temperature	Time	Physical observation	X-ray diffraction analyses [c]
mole %	*mole %*	*°C*	*hr*		
71.43 (5:2)	28.57	1300	16	No melting	$5BaO·2Nb_2O_5$.
		1330	0.167	do	Do.
		1450	.5	do	Do.
		1480	.5	do	
		1490	17	do	
		1520	0.5	do	
		1540	.5	do	$5BaO·2Nb_2O_5$.
		1545	.333	Completely melted.	
		1550	.333	do	
		1560	.5	do	
		1580	.333	do	
		1600	.167	do	
		1650	.5	do	$5BaO·2Nb_2O_5$.
66.67	33.33	[d] 1100	60	No melting	$5BaO·2Nb_2O_5$+ Or−$BaO·Nb_2O_5$.
		1300	0.5	do	Do.
		1300	16	do	Do.
		1320	0.25	Just began to melt.	
		1325	.25	Some melting.	
		1346	.25	Partially melted.	
		1350	1.0	do	$5BaO·2Nb_2O_5$+ Or−$BaO·Nb_2O_5$.
		1400	0.5	Considerably melted.	Do.
		1425	.25	do	Do.
		1440	.25	do	Do.
		1455	.25	do	Do.
		1500	.5	Completely melted.	Do.
60	40	1320	0.25	Just began to melt.	
		1330	.167	Considerably melted.	
		1350	.25	Completely melted.	
		1400	.25	do	
54.55	45.45	1320	0.167	Just began to melt.	
		1400	.25	Partially melted.	Or−$BaO·Nb_2O_5$+ $5BaO·2Nb_2O_5$.
		1422	.25	do	
		1432	.25	Completely melted.	
		1442	.25	do	
		1461	.25	do	
50	50	[d] 900	136	No melting	$5BaO·2Nb_2O_5$+ Or−$BaO·Nb_2O_5$. +H−$BaO·Nb_2O_5$+$3BaO·5Nb_2O_5$.
		1050	64	do	Or−$BaO·Nb_2O_5$+ H−$BaO·Nb_2O_5$. +$5BaO·2Nb_2O_5$+$3BaO·5Nb_2O_5$.
		1100	64	do	H−$BaO·Nb_2O_5$+ Or−$BaO·Nb_2O_5$.
		[d] 1200	1	do	Or−$BaO·Nb_2O_5$.
		[d] 1310	1	do	Do.
		1450	0.33	do	Do.
		1460	0.33	Completely melted.	Do.
48	52	1100	64	No melting	H−$BaO·Nb_2O_5$+ Or−$BaO·Nb_2O_5$+$3BaO·5Nb_2O_5$.
		1200	64	do	Or−$BaO·Nb_{2.5}O_{5.5}$+$3BaO·5Nb_2O_5$.
		1275	1	do	Or−$BaO·Nb_{2.5}O_{5.5}$+$6BaO·7Nb_2O_5$+$3BaO·5Nb_2O_5$.
		1310	16	do	Or−$BaO·Nb_{2.5}O_{5.5}$+$3BaO·5Nb_2O_5$ (trace).
		1325	0.33	do	Do.
		1350	.33	Just began to melt.	Do.

TABLE 7. *Experimental data for compositions in the binary system* $BaO–Nb_2O_5$—Continued

Composition [a]		Heat treatment [b]		Results	
BaO	Nb_2O_5	Temperature	Time	Physical observation	X-ray diffraction analyses [c]
mole %	*mole %*	*°C*	*hr*		
46.15 (6:7)	53.85	1278	2	No melting	$6BaO·7Nb_2O_5$+ Or−$BaO·Nb_{2.5}O_{5.5}$+$3BaO·5Nb_2O_5$.
		1300	160.5	do	$6BaO·7Nb_2O_5$.
		1325	23	do	$6BaO·7Nb_2O_5$+ Or−$BaO·Nb_{2.5}O_{5.5}$+$3BaO·5Nb_2O_5$.
45.45	54.55	1278	64	No melting	$6BaO·7Nb_2O_5$+ $3BaO·5Nb_2O_5$.
		1300	0.833	do	Do.
		1300	160.5	do	Do.
45	55	1275	0.583	No melting	$6BaO·7Nb_2O_5$+ $3BaO·5Nb_2O_5$.
		1310	1.0	Partially melted.	$6BaO·7Nb_2O_5$+ Tet−ss.
		1337	0.167	do	Or−$BaO·Nb_2O_5$+ Tet−ss.
		1426	0.167	Considerably melted.	
		1445	0.167	Completely melted.	
40	60	1277	15	No melting	$3BaO·5Nb_2O_5$+ $6BaO·7Nb_2O_5$.
		1290	0.167	Just began to melt.	
		1292	1.0	do	Tet−ss+$6BaO·7Nb_2O_5$.
		1325	0.167	Considerably melted.	Do.
		1335	.167	do	Tet−ss+or−$BaO·Nb_2O_5$.
		1353	.167	do	Do.
		1378	.167	do	
		1386	.167	Completely melted.	
38.46	61.54	1277	15	No melting	$3BaO·5Nb_2O_5$+ $6BaO·7Nb_2O_5$.
37.5 (3:5)	62.5	1275	0.583	No melting	$3BaO·5Nb_2O_5$.
		1275	1.0	do	Do.
		1291	0.167	Just began to melt.	
		1296	.167	Considerable melting.	
		1300	.5	do	Tet−ss+$6BaO·7Nb_2O_5$.
		1310	.75	do	
		1327	1.0	do	
		1330	0.167	do	
		1337	.167	Completely melted.	Do.
36	64	1291	0.167	Just began to melt.	
		1296	.167	Considerably melted.	
		1301	1.0	do	Tet−ss+$6BaO·7Nb_2O_5$ (trace).
		1310	0.167	do	
35	65	1290	0.167	Just began to melt.	
		1301	.167	Completely melted.	
33.33	66.67	1277	.5	No melting	
		1285	.167	do	
		1292	.333	do	$3BaO·5Nb_2O_5$ss.
		1295	.033	Just began to melt.	
		1300	1.0	Partially melted.	$3BaO·5Nb_2O_5$ss (+Tet−ss?).
		1306	0.167	Completely melted.	
		1310	.083	do	
		1352	.25	do	
		1400	.167	do	Tet−ss.
28.57	71.43	1275	.583	No melting	$3BaO·5Nb_2O_5$ss.
		1295	.033	do	
		1306	.167	Partially melted.	
		1310	.5	Completely melted.	Tet−ss.

See footnotes at end of table.

TABLE 7. *Experimental data for compositions in the binary system* BaO–Nb_2O_5—Continued

Composition [a]		Heat treatment [b]		Results	
BaO	Nb_2O_5	Temperature	Time	Physical observation	X-ray diffraction analyses [c]
mole %	*mole %*	*°C*	*hr*		
27	73	1301	16	No melting	$BaO{\cdot}3Nb_2O_5$ss.
25 (1:3)	75	1292	1.0	No melting	
		1310	0.333	do	$BaO{\cdot}3Nb_2O_5$.
		1311	.167	do	
		1314	.083	Partially melted.	$BaO{\cdot}3Nb_2O_5$ (+Tet−ss?).
		1315	.167	do	
		1320		Completely melted.	
		1325	.25	do	Tet−ss.
		1350	.083	do	Do.
24	76	1300	.167	No melting	$BaO{\cdot}3Nb_2O_5$+ Nb_2O_5 (trace).
		1305	.167	do	
		1315	.167	Just began to melt.	
		1321	.167	Partially melted.	
20	80	1314	.167	No melting	
		1316	.167	Just began to melt.	
		1323	.167	Partially melted.	
		1327	.167	do	
		1394	.167	Considerably melted.	
		1399	.167	Completely melted.	
15	85	1316	.167	No melting	
		1326	.167	Just began to melt.	
		1438	.167	Completely melted.	
10	90	1275	.583	No melting	Nb_2O_5+$BaO{\cdot}3Nb_2O_5$.
		1310	.75	do	Do.
		1332	.25	do	
		1343	.25	do	
		1392	.333	Just began to melt.	
		1415	.167	Partially melted.	
		1448	.25	Considerably melted.	
		1465	.333	do	
		1480	.167	Completely melted.	
5	95	1439	.167	Just began to melt.	
		1482	.167	Completely melted.	
0	100	1474	.333	No melting	
		1483	.5	do	
		1490	.167	Completely melted.	
		1502	.167	do	

[a] All specimens containing more than 71.43 mole percent BaO reacted with the Pt containers.
[b] Unless otherwise indicated all specimens were quenched in sealed Pt tubes.
[c] The phases identified are given in the order of the amount present at room temperature. The phases are not necessarily those present at the temperature to which the specimen was heated. H—hexagonal, Or—orthorhombic, Tet—tetragonal, ss—solid solution.
[d] These specimens were heated in air on Pt foil, and slow cooled.

region of $BaO{\cdot}Nb_2O_5$ solid solution and $6BaO{\cdot}7Nb_2O_5$ is postulated as extending from about 47.5 mole percent BaO to the 6:7 composition. As explained below, specimens in this composition range would always show three phases when quenched from below the solidus ($BaO{\cdot}Nb_2O_5$+$6BaO{\cdot}7Nb_2O_5$+$3BaO{\cdot}5Nb_2O_5$).

The presence of the $3BaO{\cdot}5Nb_2O_5$ phase in the X-ray patterns of compositions between 1:1 and 6:7 has two possible explanations: (1) The $BaO{\cdot}Nb_2O_5$ compound takes up excess Nb_2O_5 in soldid solution. This Nb_2O_5 cannot be retained on quenching and is exsolved. The $3BaO{\cdot}5Nb_2O_5$ forms instead of the $6BaO{\cdot}7Nb_2O_5$ because the former crystallizes very readily and the latter only with great difficulty. (2) The $3BaO{\cdot}5Nb_2O_5$ phase is formed as a nonequilibrium phase on heating and has not been transformed to the equilibrium $6BaO{\cdot}7Nb_2O_5$ even in 64 hr. Both explanations depend on the great ease of formation of the 3:5 bronze-type structure and the great difficulty of formation of the $6BaO{\cdot}7Nb_2O_5$ phase.

The compound $6BaO{\cdot}7Nb_2O_5$ was interpreted as melting incongruently to $BaO{\cdot}Nb_2O_5$ solid solution plus liquid at 1,330 °C. Compositions between $6BaO{\cdot}7Nb_2O_5$ and $3BaO{\cdot}5Nb_2O_5$ were found to contain only these two phases below the solidus. The solidus corresponds to the incongruent melting temperature of the 3:5 composition. A solid of 3:5 composition was observed to melt incongruently to $6BaO{\cdot}7Nb_2O_5$ plus liquid at 1,290 °C. When quenched from any temperature above 1,330 °C, compositions between 6:7 and 3:5 showed the $BaO{\cdot}Nb_2O_5$ solid solution instead of the $6BaO{\cdot}7Nb_2O_5$ compound.

From 37.5 mole percent BaO to 25 mole percent BaO a single phase solid solution area was observed. However, the end members of this solid solution series have slightly different "superstructure" peaks in their X-ray patterns (tables 1 and 2). A two phase area is therefore required somewhere in the solid solution series, at least at lower temperatures. This two phase area has not been observed experimentally but must exist between 28.57 mole percent BaO and 27 mole percent BaO or at about 72 mole percent Nb_2O_5. The existence of this two phase area is further indicated by the suggestion of a break in slope of the liquidus values occurring at 1,305 °C. This temperature corresponds to the solidus value projected for the 72 mole percent Nb_2O_5 composition. If the slope of the liquidus on the solid solution side is of opposite sign at the two ends of a solid solution area, a minimum is required. Experimentally, the difference between the 1,290 °C solidus of the $3BaO{:}5Nb_2O_5$ composition and the required minimum in the solidus could not be definitely proved. However, the minimum in the liquidus definitely occurs between 35 and 36 mole percent BaO and is shown in figure 1 as about 1,288 °C.

The compound $BaO{\cdot}3Nb_2O_5$ was also interpreted as melting incongruently at about 1,315 °C to Nb_2O_5 solid solution plus liquid. However, this composition is just slightly incongruent. The nature of the melting was inferred from the observation that compositions slightly higher in Nb_2O_5, which contain two phases, began melting at experimentally the same temperature as was found for the 1:3 composition.

Compositions containing 85 mole percent, or more, Nb_2O_5 were found to begin melting at increasingly higher temperatures, indicating solid solution of BaO in Nb_2O_5. This solid solution is shown in figure 1 as extending to about 16 mole percent BaO at the

solidus temperature. The solid solution could not be "quenched-in" at room temperature and specimens in this compositional range indicate two phases with little or no parameter change in the Nb_2O_5 phase. As indicated in table 7, the melting point of Nb_2O_5 was found to be about 1,487 °C, in reasonably good agreement with the value of 1,491 °C found by Holtzberg et al. [16].

5. Bronze-Type Solid Solution

From the location of the minimum in the liquidus at 35 to 36 mole percent BaO to the 1:3 composition (25 mole percent BaO), the liquid, when quenched, crystallizes as a metastable tetragonal bronze-type phase (table 7). This phase apparently also occurs in compositions on either side of this solid solution range, together with the other equilibrium phase, when quenched from above the solidus. However, any specimens quenched from below the solidus always exhibit a superstructure in the X-ray pattern of the bronze-type phase. The unit cell dimensions of the pseudotetragonal cell of the solid solution series are essentially the same as the unit cell dimensions of the true, metastable, tetragonal cell of the same composition. Apparently, the specimens quenched from the liquid exhibit "frozen-in" disorder, which gives rise to a higher symmetry.

The structure of the bronze-type phase is based on the structure of tetragonal potassium tungsten bronze described by Magneli [17]. This structure type has the general chemical formula $A_6B_{10}O_{30}$, but often exhibits a deficiency of the *A*-type ions. It can be described as being made up of "octahedra coupled together in a rather intricate way forming rings or polygons of three, four, or five octahedra" [17]. The crystallographical formula can be written as $[A_2A'_4][B_2B'_8]O_{30}$. Thus there are two different A positions in the unit cell. The first position has two A ions surrounded by four octahedra and the second position has four A ions surrounded by five octahedra. The rings of three octahedra leave a vacancy in the lattice.

The superstructures occurring in the present bronze solid solutions might very likely be related to an ordering of Ba^{+2} ions in the A position which contains two ions surrounded by four octahedra. Thus the change in superstructure would be expected to occur at or near a composition which contains two Ba^{+2} ions per unit cell. As the exact ionic distribution in the 3:5 to 1:3 BaO-Nb_2O_5 bronze solid solutions is not yet known, the chemical formulas can be written in several different forms. However, without the use of single crystal data nothing can be said about the exact nature of the various order-disorder phases.

6. Summary

The system BaO-Nb_2O_5 was studied by means of solid state reactions, fusion characteristics, and X-ray diffraction data. The existence of six compounds in the system was postulated. They are $6BaO{\cdot}Nb_2O_5$, $5BaO{\cdot}2Nb_2O_5$ which melts congruently at about 1,542 °C, $BaO{\cdot}Nb_2O_5$ which melts congruently at 1,455 °C, $6BaO{\cdot}7Nb_2O_5$ which melts incongruently at about 1,330 °C, $3BaO{\cdot}5Nb_2O_5$ which melts incongruently at about 1,290 °C, and $BaO{\cdot}3Nb_2O_5$ which melts incongruently at about 1,315 °C. A eutectic occurs at about 62 mole percent BaO and 1,320 °C, and a minimum in a solid solution series occurs at about 35 to 36 mole percent BaO and 1,288 °C.

Complete solid solution was found between $3BaO{\cdot}5Nb_2O_5$ and $BaO{\cdot}3Nb_2O_5$ although a change in superstructure symmetry occurred at about 28 mole percent BaO. A small amount of solid solution was noted on the high Nb_2O_5 side of $BaO{\cdot}Nb_2O_5$, and Nb_2O_5 was found to accept about 16 mole percent BaO in solid solution at the solidus temperature. Neither of the partial solid solutions was quenchable, resulting in two phases at room temperature.

7. References

[1] G. Goodman, private communication (Nov. 12, 1957).
[2] R. V. Coates and H. F. Kay, Phil. Mag. **3,** 1449–1459 (1958).
[3] I. G. Ismailzade, Izvest. Akad. Nauk. S.S.S.R. Ser. fiz. **22** [12] 1485–1487 (1958).
[4] F. Holtzberg, A. Reisman, M. Berry, and M. Berkenblit. Jr. Am. Chem. Soc. **79,** 2039–2043 (1957).
[5] M. W. Shafer and R. Roy, Zeit. für Krist. **110** [3], 241–248 (1958).
[6] H. J. Goldschmidt, Jr. of the Institute of Metals **87,** 235–239 (1958–59).
[7] A. Reisman and F. Holtzberg, Jr. Am. Chem. Soc. **81,** 3182–3184 (1959).
[8] R. S. Roth, J. Research NBS **62** [1], 27–38 (1959).
[9] R. S. Roth, Acta Cryst. **10,** 437 (1957).
[10] E. I. Krylov and Y. I. Alekseev, Jr. Gen. Chem. U.S.S.R. **25** [6], 1013–1016 (1955).
[11] M. H. Francombe, Bull. Am. Phys. Soc. Series II **4** [5] June 18 (1959).
[12] M. H. Francombe, private communication (Sept. 2, 1959).
[13] L. H. Brixner, Jr. Am. Chem. Soc. **80** [13], 3214–3215 (1958).
[14] R. S. Roth to be published.
[15] V. A. Isupov, Kristallograffija, S.S.S.R. **3** [1], 99–100 (1958).
[16] F. Holtzberg, A. Reisman, M. Berry, and M. Berkenblit, Jr. Am. Chem. Soc. **79,** 2039–2043 (1957).
[17] A. Magneli, Arkiv. für Kemi **1** [24], 213–221 (1949).

(Paper 65A4-115)

JOURNAL of RESEARCH of the National Bureau of Standards—A. Physics and Chemistry
Vol. 65A, No. 4, July–August 1961

Solid State Reactions Involving Oxides of Trivalent Cations

S. J. Schneider, R. S. Roth, and J. L. Waring

(April 11, 1961)

Selected mixtures in 69 binary systems involving Al_2O_3, Ga_2O_3, Cr_2O_3, Fe_2O_3, Sc_2O_3, In_2O_3, Y_2O_3, and the rare earth oxides were studied by X-ray diffraction techniques after heat treatment at various temperatures. A plot of the radii of the A^{+3} cations versus the radii of B^{+3} cations shows the regions of stability for the different structure types found for the double oxides of the trivalent cations. The following structure types were encountered: A, B, and C-type rare earth oxide; corundum, beta gallia; kappa alumina; garnet; perovskite; and several types which could not be definitely related to known structures. The majority of $A^{+3}B^{+3}O_3$ compounds have the perovskite structure. Several phases, including $(1\text{-}x)Fe_2O_3 \cdot xAl_2O_3$ ss and $(1\text{-}x)Fe_2O_3 \cdot xGa_2O_3$ ss, appear to have structures similar to kappa alumina. Solid solution definitely occurs in many of the garnet type compounds which contain gallia. Based on the data collected in this survey, the subsolidus phase equilibria relationships of 79 binary systems were drawn.

1. Introduction

In the field of phase equilibria research it is often beneficial to first survey a series of related systems before commencing on a detailed analysis of specific systems. A survey was recently conducted by the authors [1][1] on the various solid state reactions that occur in mixtures of the trivalent rare earth oxides. It was found in the work that ionic size was the primary controlling factor in determining the various subsolidus phase relationships. This study has since been extended to include the oxides of the smaller trivalent cations, In^{+3}, Sc^{+3}, Fe^{+3}, Cr^{+3}, Ga^{+3}, and Al^{+3}. These cations, together with the lanthanide series comprise almost the entire group of ions which are commonly trivalent.

To date, only a limited number of binary oxide systems involving only trivalent cations have been completely studied. With the exception of the previously mentioned paper by Schneider and Roth [1], most of the research has been concerned with studies of $A^{+3}B^{+3}O_3$ and to a lesser extent $A_3^{+3}B_5^{+3}O_{12}$ type compounds. The $A^{+3}B^{+3}O_3$ and $A_3^{+3}B_5^{+3}O_{12}$ compounds have the perovskite and garnet structures respectively. It is noteworth that the oxides of the trivalent cations, $A_2^{+3}O_3$, may be considered in a general way as $A^{+3}B^{+3}O_3$ ($A^{+3}A^{+3}O_3$) type compounds. None of these $A_2^{+3}O_3$ oxides, however, are known to have a perovskite structure. Goldschmidt and his coworkers [2] were perhaps the first to investigate $A^{+3}B^{+3}O_3$ compounds in detail. Many other investigators, including Keith and Roy [3], Roth [4], and Geller and his coworkers [5, 6, 7] have substantially contributed to the data available on this formula-type compound.

The purpose of the present investigation was to survey the various structure types that occur under equilibrium conditions for different binary mixtures of the oxides of the trivalent cations and to establish the subsolidus phase equilibria relationships for various systems. Special emphasis was given to a classification of the structure types found for equimolar mixtures according to the ionic radii of the constituent cations.

2. Sample Preparation and Test Methods

With the exception of Cr_2O_3 and Fe_2O_3 which were reagent grade, the materials used in this investigation had a purity of about 99.9 percent. Specimens were prepared from either 0.5 or 1.0 gram batches of various binary combinations of different oxides. Calculated amounts of each end member, corrected for ignition loss, were weighed to the nearest milligram. Each batch was mixed, formed into a ⅜ in.-diam pellet by pressing at 10,000 lb/in.^{2} and fired at some relatively low temperature (at least 800 °C) for varying lengths of time. Most of the specimens were then ground, remixed, again pressed into pellets and fired at successively higher temperatures until equilibrium was obtained.

All specimens containing In_2O_3 or Cr_2O_3, were ground, mixed, and then sealed in platinum tubes for the higher temperature heat treatments. The duration and temperature of each heat treatment generally varied with the particular system under consideration. In general, the specimens were slow cooled at approximately 4 °C/min. However, a few of the mixtures were quenched from elevated temperatures.

All heatings were performed in an air atmosphere using a conventional muffle furnace for the low temperature heats and a program-controlled tube furnace or a manually operated quench furnace for the heat treatment between 1000 and 1650 °C. An induction furnace, having as the susceptor a small iridium crucible, was used for heat treatments above 1650 °C. Temperatures were controlled to at least ±10 °C.

Equilibrium was considered to have been attained when the X-ray patterns of a specimen showed no change with successive heat treatment of the speci-

[1] Figures in brackets indicate the literature references at the end of this paper.

men or when the X-ray powder data was consistent with the results predicted from a previous set of experiments. All specimens were examined at room temperature by X-ray diffraction with a Geiger-counter diffractometer employing nickel-filtered copper radiation.

3. Results

The data obtained in this investigation are given in table 1. The table lists six groups of binary systems, each having either Al_2O_3, Ga_2O_3, Cr_2O_3, Fe_2O_3, Sc_2O_3, or In_2O_3 as one component. Each of these groups in turn is arranged according to decreasing cation size of the second component. Selected literature references are included for compositions not studied experimentally in the present work. No attempt was made to incorporate into the table any data pertaining solely to mixtures involving only oxides of the trivalent rare earth cations. These data were reported in a recent publication by Schneider and Roth [1]. The table was designed primarily to present sufficient data to estimate the subsolidus phase relationships of a majority of the listed binary systems.

Figure 1 gives a classification of the various structure types found for equimolar mixtures of the oxides of the trivalent cations. The coordinates of the figure are the radii of the A^{+3} and B^{+3} cations. For convenience the larger cation in any mixture is taken as the A^{+3} cation (ordinate) and the smaller as B^{+3} (abscissa). The radii of the different cations are indicated on the figure by open triangles.[2] The solid triangles on the diagonal line represent the

[2] Radii values are according to Ahrens [8] with the exception of Y^{+3}, In^{+3} and Sc^{+3} which were taken from Roth and Schneider [9]. The following radii values were used throughout this report: La^{+3}–1.14 A, Ce^{+3}–1.07 A, Pr^{+3}–1.06 A, Nd^{+3}–1.04 A, Sm^{+3}–1.00 A, Eu^{+3}–.98 A, Gd^{+3}–.97 A, Tb^{+3}–.93 A, Dy^{+3}–.92 A, Ho^{+3}–.91 A, Y^{+3}–.91 A, Er^{+3}–.89 A, Tm^{+3}–.87 A, Yb^{+3}–.86 A, Lu^{+3}–.85 A, In^{+3}–.77 A, Sc^{+3}–.68 A, Fe^{+3}–.64 A, Cr^{+3}–.63 A, Ga^{+3}–.62 A, and Al^{+3}–.51 A.

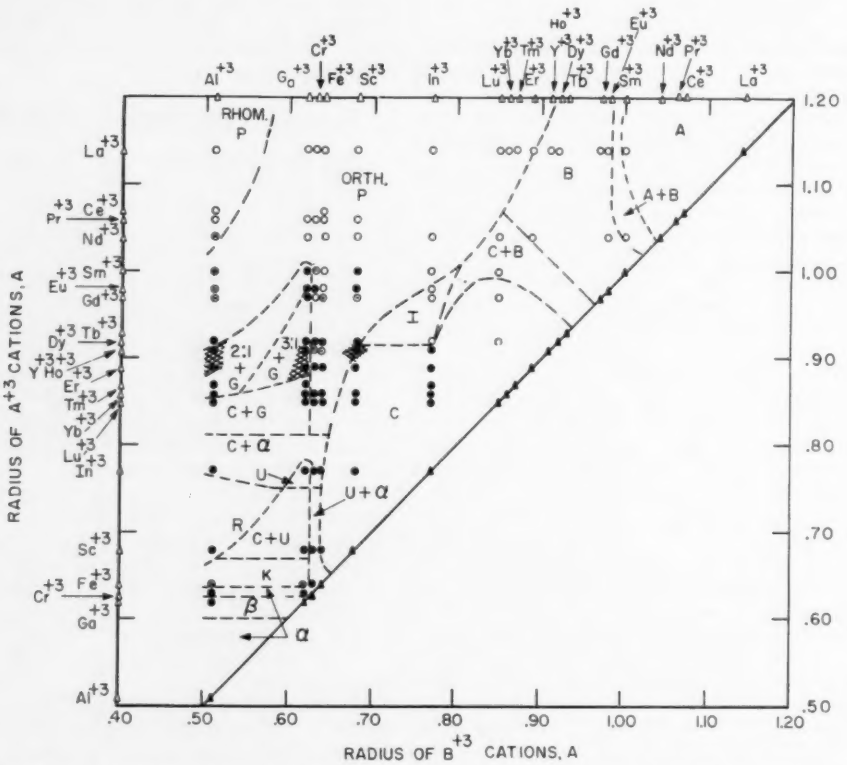

FIGURE 1. *Classification of structure types for equimolar mixtures of trivalent cations.*

△—radii of cations
▲—pure oxide
●—compositions studied in present work
○—data taken from literature

A—A-type rare earth oxide
B—B-type rare earth oxide
C—C-type rare earth oxide
G—garnet
I—unknown type
α—corundum
β—beta gallia
K—kappa alumina
U—unknown type similar to kappa alumina
P—perovskite
R—unknown type
2:1—unknown type
3:1—unknown type

individual oxides. Each circle represents an equimolar composition containing either one or two phases which have the indicated structures at room temperature. In most instances, these same types also exist stably at elevated temperatures. The one known exception to this is the listed structure of the 1:1 mixture of Fe_2O_3 and Al_2O_3 which is metastable at room temperature [10]. The diagram does not indicate any reversible phase transformations or decompositions that occur at elevated temperatures. It should be emphasized that the boundaries outlining each field were arbitrarily drawn. They do not indicate the division of different structure types for solid solutions which may exist between adjacent equimolar mixtures.

The occurrence of metastable phases was prevalent in a number of the double oxides which are near the boundary lines of figure 1. It was extremely difficult at times to establish the equilibrium phases. For this reason certain areas in the diagram are shaded to indicate that the position of certain portions of the boundary lines are somewhat in doubt. Several of these borderline systems are now being investigated in detail by the authors in order that the equilibrium phases can be definitely ascertained.

The majority of $A^{+3}B^{+3}O_3$ type compounds formed from double oxides of the trivalent cations are those having the perovskite structure. This field of perovskite types encompasses the largest single phase area of the diagram. The other single phase areas generally represent solid solutions and not true compounds. The two-phase areas, of course, contain compounds (3:1, 2:1, and 3:5) but not of the $A^{+3}B^{+3}O_3$ type.

Figure 1 not only designates the structure types for equimolar mixtures but also, with two exceptions, is applicable for all molar ratios of binary combinations of oxides of the listed cations. The two exceptions are the beta alumina (La_2O_3-Al_2O_3 and La_2O_3-Fe_2O_3 systems) and the spinel (Fe_2O_3-R_2O_3 systems) structures. The spinel structure, of course, occurs only when FeO is present as a third component. The various structure types are discussed in succeeding sections.

4. Discussion

4.1. A, B, C, Beta Gallia, and Corundum Structure Types

The structure type of the stable forms of the oxides of the trivalent cations (fig. 1, solid triangles) can be generally grouped in the following manner according to the ionic radius of the constituent cations: 1.14 A to 1.04 A-hexagonal A-type rare earth oxide structure; 1.00 A to 0.97 A-monoclinic B-type rare earth oxide structure; 0.93 A to 0.68 A-cubic C-type rare earth oxide structure; 0.64 A to 0.63A-rhombohedral corundum structure; 0.62 A-monoclinic beta gallia structure; and 0.51 A-rhombohedral corundum structure. In the above listing the structure types are seemingly out of order with respect to radii in that the beta gallia type is intermediate between two corundum types. This inconsistency emphasizes that other factors besides radii must be considered in generalizations such as given above.

Generally the effects of partial covalent bonding in essentially ionic type materials are neglected. Mooser and Pearson [11] related the structures of certain simple compounds to average quantum numbers and electronegativity values. From their work and others [11, 12] it is apparent that the covalent character (directional properties of the bonds) of a compound is directly related to the difference in the electronegativities of the cation and anion. Generally the greater the difference, the less the covalent type bonding. Using the electronegativity values given by Gordy and Thomas [13] to calculate relative covalent character, the aforementioned grouping of structure types can be rearranged according to increasing covalent character: A, B, or C types (Ln_2O_3)[3] $<$C-type (Sc_2O_3)$<$C-type (In_2O_3)$<$beta gallia type (Ga_2O_3)$<$corundum type (Al_2O_3)$<$corundum type (Cr_2O_3)$<$corundum type (Fe_2O_3). This method of arrangement, although on a very relative scale, does group like structure types together. It would be increasingly more difficult to apply this type of classification to compounds containing ions of different valence as well as those containing multiple ions of the same valence.

A number of the trivalent oxides have metastable polymorphs which have structures different from the stable modifications. A B-type structure has been reported for Nd_2O_3 [14], while Sm_2O_3, Eu_2O_3, and Gd_2O_3 are known to form the C-type [9]. Gallia (Ga_2O_3) and Al_2O_3 are similar in many respects in that they both have polymorphs of the same structure type. Gamma Al_2O_3 and gamma Ga_2O_3 are isostructural, as are alpha Al_2O_3 and alpha Ga_2O_3 [15]. This is also true for epsilon Ga_2O_3 and kappa Al_2O_3 and for beta Ga_2O_3 and theta Al_2O_3 [15]. A metastable polymorph of a pure oxide may appear as a stable phase in solid solutions. Examples of this occur in solid solutions between the oxides of the trivalent rare earth ions. For instance, the B-type structure in solid solutions is stable over a far greater range of average radii values than the pure oxides [1].

4.2. Perovskite Structure Type

The various combinations of double oxides that form 1:1 compounds which have the perovskite structure are indicated in figure 1. Each of these compounds has modifications which are distorted from the ideal cubic structure assuming either rhombohedral or orthorhombic symmetry at room temperature. At elevated temperatures other symmetries may occur. It has been suggested that the order of transformation with temperature is probably orthorhombic to rhombohedral to cubic [7].

Goldschmidt and coworkers [2] derived a tolerance factor (t) for the perovskite structure which is

[3] The symbol "Ln" represents the lanthanide series, lanthanum through lutecium.

given by the following formula:

$$t=\frac{R_A+R_O}{\sqrt{2}(R_B+R_O)}$$

where

t=tolerance factor
R_A=radius of larger cation
R_B=radius of smaller cation
R_O=radius of oxygen (1.40 A).

As t approaches unity, the tendency for the formation of a perovskite structure becomes greater. The lower limit or minimum value of t for a given series can only be determined experimentally. For the Ln_2O_3·Ga_2O_3 and Ln_2O_3·Al_2O_3 series of perovskite type compounds, the minimum values of t were found to be 0.85 and 0.84 respectively. In comparison, the lower limit of t for the other perovskite type series, La_2O_3·Ln_2O_3 [1], Ln_2O_3·In_2O_3, Ln_2O_3·Sc_2O_3, Ln_2O_3·Fe_2O_3 and Ln_2O_3·Cr_2O_3, are all equal to about 0.78.

Dalziel [16], considering only the Fe_2O_3, Ga_2O_3, and Al_2O_3 perovskite series, attempted to explain the differences in minimum t values on the basis of partial covalent character of the non rare earth cation-oxygen bond. To test the relative covalent character of the different series, Dalziel presented a graph similar to that given in figure 2. Expanding Dalziel's graph to include all appropriate data in table 1, figure 2 shows the relationship between the volumes of the Ln^{+3} cations in 12-fold coordination and the volumes of one formula weight of Ln_2O_3·M_2O_3 perovskite type compounds, as both determined experimentally (solid lines) and as predicted from the lanthanide contraction (dashed lines). For a given series, the volumes should decrease in a regular manner with the lanthanide contraction. The decrease, however, will be modified somewhat from that predicted, due to: (1) the deviation from close packing caused by increased distortion of the lattice and (2) the influence of covalent character of the cation-oxygen bonds [16]. The former would result in larger volumes than those predicted while the latter would produce an opposite effect.

In general, it can be concluded from figure 2 that for a given series, the covalent character significantly increases as the size of the Ln^{+3} cation decreases. It is difficult to compare the different series with regard to which group is more covalent because of

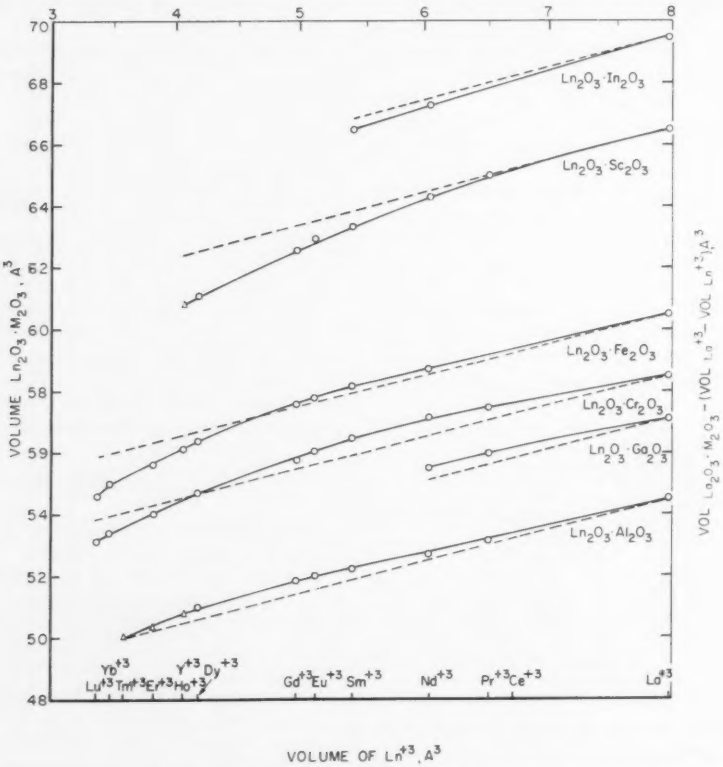

FIGURE 2. *Relationship between volumes of one formula weight of Ln_2O_3·M_2O_3 perovskites and volumes of cations in 12-fold coordination.*

Solid Curve—Determined experimentally
Dashed Curve—Predicted from lanthanide contraction, [$V_{La_2O_3 \cdot M_2O_3}$—(V_{La}—V_{Ln})]
⊙—Stable compound
△—Possibly metastable compound

masking effects of the various factors. It does appear, however, that the effect of partial covalent bonding is less pronounced in the Al_2O_3 and perhaps the Ga_2O_3 series than in the other groups. This would account for the larger minimum tolerance factors of the Al_2O_3 and Ga_2O_3 series.

4.3. Garnet Structure Type

The garnet structure occurs at the ideal 3:5 molar ratio in a number of binary systems involving oxides of the trivalent cations. Specifically, these include systems containing either Fe_2O_3, Ga_2O_3, or Al_2O_3 as one end member and a rare earth oxide (Y_2O_3) as the other. The chemical formula of a garnet type compound can be written as $[A_3^{+3}][B_2^{+3}][C_3^{+3}]O_{12}$, where $[A^{+3}]$, $[B^{+3}]$, and $[C^{+3}]$ indicate cations which occur in 8-fold, 6-fold, and 4-fold coordination, respectively [17]. In binary systems the rare earth cations or Y^{+3} can be usually thought of as occupying the $[A^{+3}]$ sites with the smaller cations, Fe^{+3}, Ga^{+3}, or Al^{+3} filling the $[B^{+3}]$ and $[C^{+3}]$ positions.

Compounds having the garnet structure do not occur in binary systems containing Cr_2O_3. This agrees with the observation [17] that Cr^{+3} prefers only octahedral type of coordination ($[B^{+3}]$ sites) in the garnet structure. Apparently the Cr^{+3} cations will never appreciably occupy tetrahedral sites in the garnet structure, even when it is the most likely cation to be tetrahedrally coordinated.

Solid solution of the garnet type compounds which occurs in binary systems containing Ga_2O_3 has been generally overlooked because of the simultaneous report of solid solution between the perovskite and garnet structures in the Y_2O_3-Al_2O_3 system [3]. Solid solution definitely occurs in many binary gallia garnets. Figure 3 shows plots of the radii of the rare earth cations against both the compositional range of solid solution of the various garnet compounds (no. 1) and the corresponding change in unit cell dimensions (no. 2). In these garnet solid solutions, the rare earth cation apparently subsitutes for Ga^{+3} in the octahedral ($[B^{+3}]$) positions.[4]

The amount of solid solution as well as the amount of change in unit cell dimensions increases to a maximum at about Tm^{+3} as the size of the constituent rare earth cation decreases. The reason for this behavior is unknown. In addition, the values determined for the garnet solid solution in the Y_2O_3-Ga_2O_3 system were excessively larger than expected and do not fit the general curves of figure 3.

It is interesting to observe that solid solution of the garnet type compound for the gallia series occurs only in binary systems in which a perovskite-type compound does not exist as a stable phase. On this premise it was considered likely and experimentally verified that solid solution does occur in the smaller alumina garnets, $3Yb_2O_3{\cdot}5Al_2O_3$ and $3Lu_2O_3{\cdot}5Al_2O_3$. Although not determined exactly, the extent of garnet solid solution is fairly small, probably about

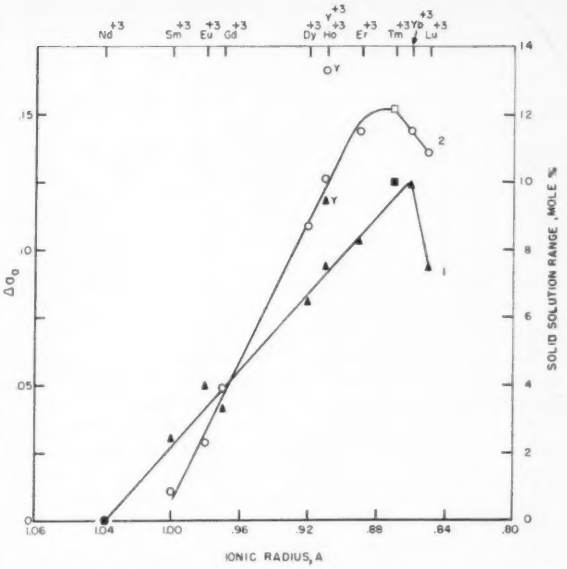

FIGURE 3. *Relationship between ionic radii and both compositional range of solid solution and corresponding parameter change in several gallia garnets at 1500 °C.*

Curve 1—Solid solution range
Curve 2—Change in unit cell dimension
$\triangle a_0 = a_0$ 1:1—a_0 3:5
□ =estimated

two mole percent. Substitutional type solid solution of the Fe_2O_3 garnets probably does not occur. However, as illustrated by the Y_2O_3-Fe_2O_3 system [18], partial reduction of Fe_2O_3 in these garnets may produce solid solution to a limited extent.

4.4. Kappa Alumina Structure Type

Considerable confusion exists in the literature with regard to the various low temperature, metastable polymorphs of Al_2O_3 and Ga_2O_3. These polytypes are ill-defined primarily because of the inability to obtain clear, interpretable X-ray diffraction data. Of particular interest in the present investigation are the kappa alumina and epsilon gallia polymorphs and their characteristic structures. Roy et al. [15] have clearly demonstrated through a series of solid solution studies that kappa alumina and epsilon gallia in reality have the same structure. The alumina polymorph having the kappa alumina structure has been reported [19] to be orthorhombic with a=8.49 A, b=12.73 A, and c=13.39 A. The reported d-spacings were not given with sufficient accuracy to verify the cell dimensions.

Richardson et al. [20] described the phase which occurs at the equimolar mixture of Fe_2O_3 and Al_2O_3 as having a structure similar to that of kappa alumina. The X-ray pattern for the $50Fe_2O_3$:$50Al_2O_3$ phase was indexed by Richardson et al. [20] on the basis of an orthorhombic cell with a=7.03 A, b=6.33 A, and c=7.41 A.[5] However, the calculated

[4] It has been suggested by S. Geller in a private communication that the solid solution may be of the interstitual and/or vacancy types instead of substitutional and thus result in a defect structure.

[5] Unit cell dimensions converted from kX units.

and observed d-spacings do not appear to be in close enough agreement to justify the reported indexing. In the present investigation three Fe_2O_3-Al_2O_3 mixtures, 47:53, 50:50, and 53:47 were prepared. Each specimen contained the same single phase as that reported by Richardson et al. [20]. The X-ray pattern of the $53Fe_2O_3$:$47Al_2O_3$ specimen was successfully indexed on the basis of an orthorhombic cell with a=8.59 A, b=9.23 A, and c=4.98 A as given in table 2. The indexing was accomplished only after comparison with the X-ray pattern of the $50Fe_2O_3$:$50Ga_2O_3$ specimen, a phase described by Wood [21]. The orthorhombic phases which occur in the Fe_2O_3-Al_2O_3 and Fe_2O_3-Ga_2O_3 systems are apparently isostructural and represent solid solutions rather than compounds. The similarity in structures is important because of the reported magnetic and piezoelectric properties of the $(1-x)Fe_2O_3 \cdot xGa_2O_3$ ss phase. These properties in $(1-x)Fe_2O_3 \cdot xAl_2O_3$ ss will be reported on in a future publication. Muan and Somiya [10] reported the complete phase relations for the Fe_2O_3-Al_2O_3 system and showed that the orthorhombic phase has both a minimum and maximum decomposition temperature.

There is not yet sufficient evidence to classify the orthorhombic phases of the Fe_2O_3-Al_2O_3 and Fe_2O_3-Ga_2O_3 systems as having a kappa alumina structure although there is a definite similarity. The X-ray patterns given in the literature for the kappa alumina and epsilon gallia polymorphs could not be indexed on the same basis as that given for $53Fe_2O_3$:$47Al_2O_3$ in table 2. The failure to index these patterns may be due to the inaccurate X-ray data available rather than dissimilar structures.

TABLE 2. *X-ray powder diffraction data for* $(1-x)Fe_2O_3 \cdot xAl_2O_3$ ss

($53Fe_2O_3$: $47Al_2O_3$ mixture)

hkl[1]	d[2]	I[3]	$\frac{1}{d^2}$	
			obs	cal
	A		A^{-2}	A^{-2}
100	6.03	25	0.0253	0.0253
020	4.64	23	.0464	.0470
111	3.90	18	.0657	.0656
121	3.144	38	.1012	.1008
220				.1012
130	2.899	38	.1190	.1193
221	2.658	100	.1415	.1415
131	2.497	29	.1604	.1596
002				.1610
012	2.407	18	.1726	.1728
102	2.393	34	.1747	.1746
311				.1741
040	2.306	14	.1881	.1881
022	2.193	23	.2080	.2080
321	2.186	38	.2093	.2093
400	2.146	13	.2171	.2171
122	2.125	21	.2214	.2216
331	1.9000	29	.2679	.2681
042	1.6920	20	.3493	.3491
123	1.5377	16	.4226	.4229

[1] Based on orthorhombic cell with a=8.59 A, b=9.23 A, and c=4.98 A.
[2] Interplanar spacing.
[3] Relative intensity.

Figure 4, as well as table 3, presents X-ray powder data for all the phases encountered in this investigation which may have structures similar to kappa alumina. It is apparent, from figure 4, that the patterns for kappa alumina, epsilon gallia, $50Fe_2O_3$:$50Al_2O_3$ and $50Fe_2O_3$:$50Ga_2O_3$ are related. Each of the X-ray patterns of the other phases, $50In_2O_3$:

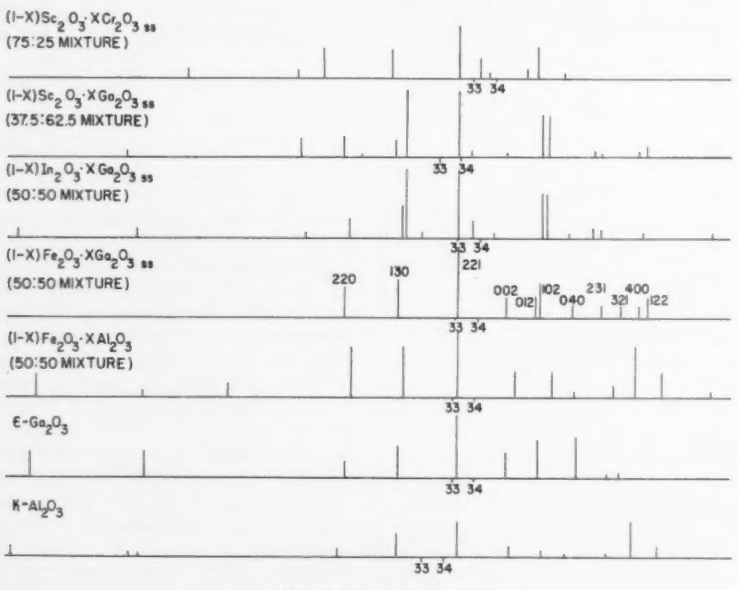

FIGURE 4. *Diagrammatic X-ray powder diffraction patterns for kappa alumina [25], epsilon gallia [15], $50Fe_2O_3$:$50Al_2O_3$ $50Fe_2O_3$:$50Ga_2O_3$, $50In_2O_3$:$50Ga_2O_3$, $37.5Sc_2O_3$:$62.5Ga_2O_3$ and $75Sc_2O_3$:$25Cr_2O_3$.*

For the kappa alumina pattern, d-values apparently due to extraneous phases were deleted, as was done by Roy et al. [15].

TABLE 3. *X-ray powder diffraction data for* $(1\text{-}x)In_2O_3 \cdot xGa_2O_3$ *, ,* $(1\text{-}x)Sc_2O_3 \cdot xGa_2O_3$ *, , and* $(1\text{-}x)Sc_2O_3 \cdot xCr_2O_3$ *, ,*

$50In_2O_3:50Ga_2O_3$ mixture		$37.5Sc_2O_3:62.5Ga_2O_3$ mixture		$75Sc_2O_3:25Cr_2O_3$ mixture	
d [1]	I [2]	d [1]	I [2]	d [1]	I [2]
A		*A*		*A*	
9.72	13	4.73	12	4.44	18
6.83	18	3.404	36	3.559	21
4.88	9	3.110	39	3.400	59
4.84	17	3.034	8	3.046	57
3.423	11	2.889	29	2.763	100
3.183	37	2.878	100	2.687	45
2.279	57	2.852	100	2.653	12
2.917	100	2.653	88	2.531	15
2.851	11	2.598	16	2.501	52
2.710	100	2.486	11	2.417	9
2.661	57	2.385	88	1.9713	13
2.590	9	2.365	90	1.9465	49
2.437	80	2.247	13	1.9072	80
2.426	80	2.231	8	1.7984	11
2.363	11	2.144	14	1.7172	16
2.298	15	2.131	24	1.6573	49
2.279	8	1.830	6	1.6247	15
2.177	13	1.7905	52	1.6861	27
2.031	13	1.7836	39	1.4903	11
1.9434	8	1.7077	46	1.4666	15
1.9155	9	1.6800	100	1.4395	10
1.8273	33	1.6017	52	1.4221	10
1.8200	34	1.5858	10	1.4127	10
1.7190	100	1.5793	28	1.3902	10
1.6709	8			1.3824	10
1.6345	25	1.5167	24	1.3442	10
1.6148	23			1.3180	11
1.6055	8	1.4933	10	1.2514	11
1.5494	31	1.4890	10		
1.5253	11	1.4839	49		
		1.4447	54		
1.5217	11				
1.5176	24	1.4328	11		
1.5158	32				
1.4784	26	1.4281	24		
1.4756	39	1.4158	42		
		1.3966	48		
1.4592	14	1.3640	9		
1.4551	15				
1.4491	30	1.3496	11		
1.4265	42				
1.3937	14	1.3466	11		
		1.3267	13		
1.3816	9	1.3048	18		
1.3558	14				
1.3310	8				

[1] Interplanar spacing.
[2] Relative intensity.

$50Ga_2O_3$, $37.5Sc_2O_3:62.5Ga_2O_3$, and $75Sc_2O_3:25Cr_2O_3$, could not be indexed although they, too, appear similar to the pattern of kappa alumina. It would seem, strictly by the comparison of X-ray patterns, that In_2O_3-Ga_2O_3 and Sc_2O_3-Ga_2O_3 phases are isostructural with each other, but not necessarily with kappa alumina. The phase most dissimilar with kappa alumina in this entire group is that of $75Sc_2O_3:25Cr_2O_3$.

4.5. Other Structure Types

Keith and Roy [3] reported that an unknown phase occurs in a melted 50:50 mixture of In_2O_3 and Al_2O_3. They designated this phase as a high form of In_2O_3:Al_2O_3 and listed several of its X-ray reflections. In an effort to obtain this phase, the experiment of Keith and Roy was repeated. The melted specimen of 50:50 In_2O_3-Al_2O_3 contained two phases, In_2O_3 and apparently the same phase as reported by Keith and Roy. Other experiments with the $50In_2O_3$:$50Al_2O_3$ mixture indicated that the unknown phase is probably metastable in the In_2O_3-Al_2O_3 system and occurs only on quenching the melt.

TABLE 4. *X-ray powder diffraction data for* $(1\text{-}x)Sc_2O_3 \cdot xAl_2O_3$ *, ,*

($50Sc_2O_3$: $50Al_2O_3$ mixture)

Rhom. hkl [1]	d [2]	I [3]	$\frac{1}{d^2}$obs	$\frac{1}{d^2}$cal
	A		A^{-2}	A^{-2}
222	2.842	29	0.1238	0.1238
$2\bar{2}2$	2.687	100	.1385	.1385
$0\bar{4}0$	2.359	21	.1797	.1798
$0\bar{4}1/2\bar{3}2$	2.265	5	.1940	.1948
$22\bar{3}$	2.241	5	.1991	.1984
240	2.138	7	.2185	.2174
332	2.004	9	.2491	.2500
043	1.8496	5	.2923	.2920
$15\bar{2}$	1.7051	21	.3440	.3436
$04\bar{4}$	1.6350	28	.3741	.3741
$26\bar{2}$	1.4180	12	.4973	.4979
$\bar{2}62$	1.3990	5	.5123	.5130

[1] Rhombohedral cell, a=9.45 A, α=87.4°.
Hexagonal cell, a=13.07 A, c=17.05 A.
[2] Interplanar spacing.
[3] Relative intensity.

In the Sc_2O_3-Al_2O_3 system a stable phase occurs which, according to X-ray powder data, appears to be isostructural with the metastable phase of the In_2O_3-Al_2O_3 system. This phase occurs over a region of Sc_2O_3-Al_2O_3 compositions and represents a solid solution and not a true compound. The X-ray pattern of the $50Sc_2O_3:50Al_2O_3$ mixture is given in table 4. The pattern was indexed on the basis of a rhombohedral cell by comparison with the pattern of $2PbO \cdot Nb_2O_5$, a rhombohedral distortion of the pyrochlore structure. The X-ray pattern for the Sc_2O_3-Al_2O_3 phase was diffuse regardless of heat treatment of the specimen, and therefore the agreement between observed and calculated values, given in table 4, is only fair for the less intense reflections. Single crystal data is needed to ascertain the correct structure type. Superstructure peaks, necessary to differentiate a body centered C-type structure or a face centered pyrochlore structure from the fluorite or Sb_2O_3-type structures, could not be found in the X-ray pattern. The fluorite structure would require that all the oxygen vacancies be disordered. For the Sc_2O_3-Al_2O_3 phase to have a C-type or a Sb_2O_3-type structure a complete ordering of the vacant oxygen sites would be required while the pyrochlore structure would necessitate only partial ordering.

A number of different phases encountered in this investigation have not been identified or even related with a specific known structure type. These phases, apparently all compounds, exist in various systems at either the 3:1, 2:1 or 1:1 molar compositions.

The 3:1 compounds occur exclusively in galliate systems; specifically, Ga_2O_3 with either Sm_2O_3, Eu_2O_3, Gd_2O_3, Dy_2O_3, Ho_2O_3, Y_2O_3, or Er_2O_3. These compounds, all apparently isostructural, have not been previously reported. The X-ray data of $3Gd_2O_3 \cdot Ga_2O_3$, which is given in table 5, is typical of all the patterns of these isostructural 3:1 compounds. The only

difference between the various patterns is the appropriate shift in the *d*-spacings of the X-ray reflections due to cation size differences. It is noteworthy that the 3:1 compound does not occur in systems in which a perovskite type compound forms as a stable phase.

A series of apparently isostructural 2:1 compounds exist in both aluminate and galliate systems. The first 2:1 compound of this type studied extensively was the $2Y_2O_3 \cdot Al_2O_3$ phase [22]. In binary aluminate systems, Gd^{+3}, Dy^{+3}, Ho^{+3}, Er^{+3}, Tm^{+3}, and Yb^{+3} can be substituted for Y^{+3}. In galliate systems, however, only the oxides of the larger cations La^{+3}, Nd^{+3}, Sm^{+3}, and Eu^{+3} form 2:1 compounds with Ga_2O_3. Evidently this structure type is dependent on radius ratios and will only occur within specific ranges of cation radii values. An example of this occurs in the Yb_2O_3-Al_2O_3 and Lu_2O_3-Al_2O_3 systems. The 2:1 compound forms in the Yb_2O_3-Al_2O_3 system but not in the Lu_2O_3-Al_2O_3 system, even though the radius of Lu^{+3} is only 0.01 A smaller than that of Yb^{+3}. However, the X-ray pattern of the 3:5 mixture in the Lu_2O_3-Al_2O_3 system showed, in addition to the garnet peaks, a few minor reflections which may represent a 2:1 phase. At present, it would appear that the occurrence of a 2:1 compound in the Lu_2O_3-Al_2O_3 system is strictly a metastable phenomenon.

Table 6 compares the X-ray pattern for $2Y_2O_3 \cdot Al_2O_3$ obtained in this investigation with that reported by Warshaw and Roy [22]. They described this 2:1 phase as being distorted cubic with a primitive lattice. Because of certain line splitting in the X-ray pattern, they infer that the material may actually have rhombohedral symmetry. The two patterns given in table 6 are very similar and obviously represent the same phase; neither pattern could be indexed in the present work. It is evident, from the present X-ray data, that $2Y_2O_3 \cdot Al_2O_3$ has low symmetry and cannot be designated as cubic or rhombohedral.

TABLE 5. *X-ray powder diffraction data for* 3 $Gd_2O_3 \cdot Ga_2O$

d [1]	I [2]	d [1]	I [2]
4.53	20	2.005	30
4.11	13	1.9918	15
3.204	14		
3.054	100	1.9027	15
3.025	57	1.8349	32
		1.8097	14
2.990	27	1.7672	17
2.908	22	1.7184	17
2.824	29		
2.630	17	1.6808	17
2.301	15	1.6450	24
		1.5788	24
2.241	17	1.5456	17
2.199	13	1.5276	25
2.032	39		

[1] Interplanar spacing.
[2] Relative intensity.

The only $A^{+3}B^{+3}O_3$ type compounds found in the present investigation which do not have the perovskite structure are those which occur in the Eu_2O_3-In_2O_3, Gd_2O_3-In_2O_3, and Dy_2O_3-In_2O_3 systems (designated as I in fig. 1). These 1:1 compounds will be reported on more extensively in a following publication [23]. The $Eu_2O_3 \cdot In_2O_3$, $Gd_2O_3 \cdot In_2O_3$, and $Dy_2O_3 \cdot In_2O_3$ compounds appear to be isostructural, having pseudohexagonal symmetry. The $Dy_2O_3 \cdot In_2O_3$ compound apparently decomposes between 1600 °C and 1650 °C to a mixture of B- and C-rare earth oxide structure types.

4.6. Subsolidus Phase Equilibria Relationships

Figure 5 gives the subsolidus phase equilibria relationships for various binary combinations of oxides of the trivalent cations. The figure is divided into

TABLE 6. *X-ray powder diffraction data for* $2Y_2O_3 \cdot Al_2O_3$

hkl [1]	Warshaw and Roy [22]		Present work		hkl [1]	Warshaw and Roy [22]		Present work	
	d [2]	I [3]	d [2]	I [3]		d [2]	I [3]	d [2]	I [3]
110	7.46	10	7.41	63				1.9811	16
200	5.28	3	5.26	16				1.9449	15
210	4.71	22	4.69	100				1.9163	12
			4.54	16				1.9027	16
220	3.71	7	3.705	19	440	1.843	18	1.8426	80
310	3.33	33	3.326	100	522/441 [4]	1.828	20	1.8298	85
301	3.01	100	3.011	100+	522/441 [4]	1.816	19	1.8164	81
320	2.91	94	2.908	100	530/433	1.793	7	1.7921	32
			2.884	47	600/442	1.732	10	1.7317	32
400	2.62	17	2.615	48	610 [4]	1.722	13	1.7235	61
410/322 [4]	2.56	10	2.559	64	610 [4]	1.716	13		
410/322 [4]	2.53	10	2.538	29	611/532	1.711	8		
			2.523	61				1.6279	27
			2.486	21				1.6236	20
			2.470	39				1.6126	23
330/411	2.46	9	2.454	37	622	1.575	9	1.5759	41
421 [4]	2.29	7	2.291	43				1.5661	45
421 [4]	2.27	7	2.274	28	630/542	1.561	12	1.5621	60
			2.129	12	631	1.551	7	1.5504	44
500/430	2.07	22	2.090	13				1.5065	32
510/431	2.06	12	2.063	87	543/710/550	1.484	4	1.4847	27
			2.046	41				1.4809	24
								1.4541	15
					720/641	1.436	4	1.4379	23
								1.3850	15

[1] Based on cubic cell with $a=10.40$ A [22].
[2] Interplanar spacing.
[3] Relative intensity.
[4] "Splitting may represent a possible rhombohedral distortion of the cubic lattice" [22].

six groups of diagrams, each having either Al_2O_3, Ga_2O_3, Cr_2O_3, Fe_2O_3, Sc_2O_3, or In_2O_3 as one component. Previously published diagrams pertinent to a given series are not reproduced here but are included as literature references in the legend of the figure.

All the diagrams were drawn primarily from the data contained in table 1. Data points are indicated by circles on the diagrams. In some instances entire diagrams, or portions thereof, were estimated from the phase relations of similar known systems. The boundaries of the garnet solid solutions were determined by the parametric method while the solid solution areas of A-, B-, or C-type phases were established by a variation of this method as previously described [1]. The boundaries of most of the other type solid solution areas were approximated from X-ray patterns on the basis of the relative amounts of each phase present in a specimen containing two phases. Possible variations of solid solubility with temperature have been ignored in this work. In general, the diagrams must be considered as approximate and minor shifts in solid solution boundary limits may be expected.

The subsolidus phase diagram for the Y_2O_3-Al_2O_3 system has been included in figure 5a although the diagram has been previously published by Warshaw and Roy [22]. The present diagram differs from the previous one in that a 1:1 perovskite type compound is shown to have a region of stability at elevated temperatures. At lower temperatures, the compound apparently decomposes to a mixture of $2Y_2O_3 \cdot Al_2O_3$ and $3Y_2O_3 \cdot 5Al_2O_3$. The present work does not contradict the published data, but merely extends to temperature ranges not previously reported. A complete reinvestigation of this system is now being undertaken. Because the stability of the 1:1 compound in the Y_2O_3-Al_2O_3 system is still unknown, the stability of the perovskite phase in the related systems of Ho_2O_3-Al_2O_3 and Er_2O_3-Al_2O_3 is also in doubt.

Perhaps one of the more interesting systems investigated is that of Dy_2O_3-In_2O_3, figure 5f. The phase diagram of this system indicates a solid solution area of B-type rare earth oxide. Since Dy_2O_3 and In_2O_3 both have the C-type structure, it is unusual for a B-type structure to occur. The largest average cation radius of the B-type solid solution in the Dy_2O_3-In_2O_3 system is about 0.87 A. This value is appreciably smaller than the radius of Gd^{+3} (0.97 A) which is the smallest rare earth ion to form a pure B-type oxide. Goldschmidt et al. [24] reported that Dy_2O_3 formed a B-type structure at elevated temperatures but his work has not yet been confirmed [9]. The formation of the solid solution area of B-type in the Dy_2O_3–In_2O_3 system might actually indicate that Dy_2O_3 does transform from C- to B-type in the pure state. Specimens of Dy_2O_3 heated above the melting point of platinum shattered in a manner indicative of a possible reversible phase transformation.

5. Summary

A survey was made of the subsolidus reactions that occur in various binary systems involving oxides of the trivalent cations. Incorporated into the study were Al_2O_3, Ga_2O_3, Cr_2O_3, Fe_2O_3, Sc_2O_3, In_2O_3, Y_2O_3, and most of the trivalent rare earth oxides. Mixtures in 69 different binary systems were investigated. Specimens were heated at various temperatures until equilibrium was attained and then examined at room temperature by X-ray powder diffraction techniques.

According to the radii of constituent cations, a classification was made of the structure types of the various phases found for equimolar mixtures. The classification consists of a plot of the radii of A^{+3} cations versus the radii of B^{+3} cations and shows specific regions of stability for the different structure types. The graph is divided into regions of one and two phase areas and represents, in addition to several unknown types, the following structures: A-, B-, and C-type rare earth oxide; corundum; beta gallia; kappa alumina; garnet; and perovskite. The classification essentially summarizes the structure types found in all possible binary mixtures of oxides of the trivalent cations studied.

With one exception, all the $A^{+3}B^{+3}O_3$ type compounds which occur have the perovskite structure. The minimum tolerance factors of the alumina and gallia series of perovskite compounds are significantly larger than the Cr_2O_3, Fe_2O_3, Sc_2O_3, and In_2O_3 series. The appreciable difference in minimum tolerance factor apparently can be related to the effect of partial covalent bonding.

Appreciable solid solution of the garnet type compounds occurs in binary systems containing Ga_2O_3. The range of solid solution generally increases to a maximum at about Tm^{+3} as the radii of the rare earth cation decreases. Solid solution of the garnet compound does not occur in binary systems containing a stable perovskite phase.

Based on the similarity of X-ray patterns, the structure of kappa alumina appears to be related to the structures of $(1-x)Fe_2O_3 \cdot xAl_2O_3$ ss and $(1-x)Fe_2O_3 \cdot xGa_2O_3$ ss. There is also a similarity between these phases and other solid solution phases which occur in the In_2O_3-Ga_2O_3, Sc_2O_3-Ga_2O_3, and Sc_2O_3-Cr_2O_3 systems.

A 2:1 compound occurs in a number of those systems containing either Al_2O_3 or Ga_2O_3 as one component. A 3:1 compound occurs exclusively in systems containing Ga_2O_3. The structures of the 2:1 and 3:1 compounds were not related to any known structure type. A rhombohedral phase which occurs stably in the Sc_2O_3-Al_2O_3 system and metastably in the In_2O_3-Al_2O_3 system may have either a fluorite, Sb_2O_3, pyrochlore, or C-type structure.

The subsolidus phase assemblages for 79 binary systems were predicted from the data compiled in this investigation.

TABLE 1.—*Binary oxide mixtures of the trivalent cations*

Al^{+3} and larger cations

System	Composition	Heat [1] treatment		Phases identified by X-ray diffraction	Structure type	Symmetry	Unit cell dimensions				Remarks	References [2]
		Temp.	Time				a	b	c	α		
	Mole %	*°C*	*hr*				*A*	*A*	*A*	*deg*		
La_2O_3–Al_2O_3	50:50			$La_2O_3 \cdot Al_2O_3$	Perovskite	Rhombohedral	5.357			60.1	Rhombohedral to cubic transformation occurs at 435±25 °C [7].	Geller and Bala [7].
	8.3:91.7	1800	1	$La_2O_3 \cdot 11Al_2O_3$	Beta alumina	Hexagonal	5.556		22.030			Roth and Hasko [31].
Ce_2O_3–Al_2O_3	50:50	1600	1	$Ce_2O_3 \cdot Al_2O_3$	Perovskite	Rhombohedral	3.766			90.2	Unit cell dimensions based on face-centered pseudo cell.	Roth [4].
Pr_2O_3–Al_2O_3	50:50			$Pr_2O_3 \cdot Al_2O_3$	Perovskite	Rhombohedral	5.307			60.33		Geller and Bala [7].
Nd_2O_3–Al_2O_3	66.7:33.3	1350	6									
		1500	6									
		1650	6	$Nd_2O_3 + Nd_2O_3 \cdot Al_2O_3$	A-type + perovskite	Hexagonal + rhombohedral.						
	50:50			$Nd_2O_3 \cdot Al_2O_3$	Perovskite	Rhombohedral	5.286			60.42		Geller and Bala [7].
	37.5:62.5	1350	6									
		1500	6									
		1650	6	$Nd_2O_3 \cdot Al_2O_3$	Perovskite	Rhombohedral					Al_2O_3 not detected; equilibrium phases probably $Nd_2O_3 \cdot Al_2O_3 + Al_2O_3$.	
Sm_2O_3–Al_2O_3	66.7:33.3	1350	6									
		1500	6									
		1650	6	$Sm_2O_3 + Sm_2O_3 \cdot Al_2O_3$	B-type + perovskite	Monoclinic + orthorhombic.						
	50:50			$Sm_2O_3 \cdot Al_2O_3$	Perovskite	Orthorhombic	5.285	5.290	7.473		Results confirmed in present work for specimen heat treated at 1650 °C. Orthorhombic to rhombohedral transformation occurs at 800 °C [6].	Geller and Bala [7]. Geller [6].
	37.5:62.5	1350	6									
		1650	6	$Sm_2O_3 \cdot Al_2O_3$	Perovskite	Orthorhombic					Al_2O_3 not detected; equilibrium phases probably $Sm_2O_3 \cdot Al_2O_3 + Al_2O_3$.	
Eu_2O_3–Al_2O_3	50:50			$Eu_2O_3 \cdot Al_2O_3$	Perovskite	Orthorhombic	5.271	5.292	7.458		Results confirmed in present work for specimen heat treated at 1650 °C.	Geller and Bala [7].
Gd_2O_3–Al_2O_3	66.7:33.3			$2Gd_2O_3 \cdot Al_2O_3$	Unknown	Unknown					The 2:1 phase also forms in the following systems: Dy_2O_3–Al_2O_3, Ho_2O_3–Al_2O_3, Y_2O_3–Al_2O_3, Er_2O_3–Al_2O_3, Tm_2O_3–Al_2O_3 and Yb_2O_3–Al_2O_3 [32].	Warshaw and Roy [32].
	50:50			$Gd_2O_3 \cdot Al_2O_3$	Perovskite	Orthorhombic	5.247	5.304	7.417		Results confirmed in present work for specimen heat treated at 1650 °C.	Geller and Bala [7].
	37.5:62.5	1350	6									
		1650	6	$Gd_2O_3 \cdot Al_2O_3 + Al_2O_3$	Perovskite + corundum.	Orthorhombic + rhombohedral.						
Dy_2O_3–Al_2O_3	50:50	1350	6									
		1650	6	$Dy_2O_3 \cdot Al_2O_3 + 3Dy_2O_3 \cdot 5Al_2O_3$	Perovskite + garnet	Orthorhombic + cubic.					Nonequilibrium	
		1850	.17	$Dy_2O_3 \cdot Al_2O_3$	Perovskite	Orthorhombic	5.21	7.38	5.31			
	37.5:62.5			$3Dy_2O_3 \cdot 5Al_2O_3$	Garnet	Cubic					Garnet phase (3:5) also forms in the following systems: Tb_2O_3–Al_2O_3, Ho_2O_3–Al_2O_3, Y_2O_3–Al_2O_3, Er_2O_3–Al_2O_3, Tm_2O_3–Al_2O_3, Yb_2O_3–Al_2O_3 and Lu_2O_3–Al_2O_3 [32].	Warshaw and Roy [32].
Ho_2O_3–Al_2O_3	50:50	1350	6									
		1650	6	$2Ho_2O_3 \cdot Al_2O_3 + Ho_2O_3 \cdot Al_2O_3 + 3Ho_2O_3 \cdot 5Al_2O_3$	Unknown + perovskite + garnet.	Unknown + orthorhombic + cubic.					Nonequilibrium	
		1850	.17	do	do	do					Nonequilibrium; $2Ho_2O_3 \cdot Al_2O_3$ and $3Ho_2O_3 \cdot 5Al_2O_3$ decreased in amounts relative to previous heat.	
		1910	.5	$Ho_2O_3 \cdot Al_2O_3$	Perovskite	Orthorhombic	5.18	7.36	5.33			

Y_2O_3–Al_2O_3 [3a]	66.7:33.3	1100	16									
		1650	6	$2Y_2O_3 \cdot Al_2O_3$	Unknown	Unknown						Geller and Bala [7].
	50:50			$Y_2O_3 \cdot Al_2O_3$	Perovskite	Orthorhombic	5.179	5.329	7.370			
		1350	6									
		1500	6	$Y_2O_3 + 2Y_2O_3 \cdot Al_2O_3 + 3Y_2O_3 \cdot 5Al_2O_3 + Y_2O_3 \cdot Al_2O_3$	C-type+unknown+garnet+perovskite.	Cubic+unknown+cubic+orthorhombic.					Nonequilibrium	
		1850	.5	$Y_2O_3 \cdot Al_2O_3$	Perovskite	Orthorhombic						
		1705	.5	$Y_2O_3 \cdot Al_2O_3 + 2Y_2O_3 \cdot Al_2O_3 + 3Y_2O_3 \cdot 5Al_2O_3$	Perovskite+unknown+garnet.	Orthorhombic+unknown+cubic.					Perovskite apparently decomposing; nonequilibrium.	
		1645	1	do	do	do					Garnet and 2:1 phases increased in amount relative to previous heat; nonequilibrium.	
	37.5:62.5	1650	2	$3Y_2O_3 \cdot 5Al_2O_3$	Garnet	Cubic	12.01					Yoder and Keith 33].
		1730	1	do	do	do						
Er_2O_3–Al_2O_3	75:25	1350	6									
		1500	6									
		1650	6	$Er_2O_3 + 2Er_2O_3 \cdot Al_2O_3$	C-type+unknown	Cubic+unknown						
	50:50	1350	6									
		1650	6	$Er_2O_3 + 2Er_2O_3 \cdot Al_2O_3 + Er_2O_3 \cdot Al_2O_3 + 3Er_2O_3 \cdot 5Al_2O_3$.	C-type+unknown+perovskite+garnet.	Cubic+unknown+orthorhombic+cubic.	11.983				Nonequilibrium; listed dimension for garnet phase in mixture.	
		1800	.5	do	do	do					Nonequilibrium; no apparent change in relative amounts from previous heat.	
		1350	6									
		1650	6									
		1850	6	do	do	do					Nonequilibrium; C-type, 2:1 and garnet phases reduced in amount relative to 1650 °C heat.	
		1350	6									
		1650	6									
		1900	.75	$Er_2O_3 \cdot Al_2O_3$	Perovskite	Orthorhombic					Specimen melted	
		1350	6									
		1650	6									
		1910	.08									
		1840	.75	$Er_2O_3 \cdot Al_2O_3$	Perovskite	Orthorhombic	5.16	7.33	5.32		Specimen melted; then annealed	
	37.5:62.5	1350	6									
		1600	6									
		1650	12	$Er_2O_3 \cdot Al_2O_3 + 3Er_2O_3 \cdot 5Al_2O_3$	Perovskite+garnet	Orthorhombic+cubic	11.983				Nonequilibrium; listed dimension for garnet phase in mixture.	
Tm_2O_3–Al_2O_3	50:50	1350	6									
		1650	6	$2Tm_2O_3 \cdot Al_2O_3 + Tm_2O_3 \cdot Al_2O_3 + 3Tm_2O_3 \cdot 5Al_2O_3$.	Unknown+perovskite+garnet.	Unknown+orthorhombic+cubic.	5.15 11.96	7.29	5.33		Nonequilibrium; listed dimensions for perovskite and garnet phases in mixture.	
		1850	.7	do	do	do					Nonequilibrium; no apparent change in relative amounts from previous heats.	
		1350	6									
		1650	6									
		1870	.08									
		1845	.25	$2Tm_2O_3 \cdot Al_2O_3 + Tm_2O_3 \cdot Al_2O_3 + 3Tm_2O_3 \cdot 5Al_2O_3$.	Unknown+perovskite+garnet.	Unknown+orthorhombic+cubic.					Specimen melted; then annealed. Nonequilibrium; perovskite considerably reduced in amount compared to 1850 °C specimen.	
	37.5:62.5	1350	6									
		1600	6									
		1650	12	$3Tm_2O_3 \cdot 5Al_2O_3$	garnet	Cubic	11.96					
Yb_2O_3–Al_2O_3	50:50	1350	6									
		1650	6	$Yb_2O_3 + 2Yb_2O_3 \cdot Al_2O_3 + 3Yb_2O_3 \cdot 5Al_2O_3$ ss.	C-type+unknown+garnet.	Cubic+unknown+cubic.	11.946				Nonequilibrium; listed dimension for garnet phase in mixture.	
		1770	0.33	do	do	do					Nonequilibrium C-type phase reduced in amount relative to previous heat.	
		1850	.33	do	do	do					Nonequilibrium; C-type phase reduced in amount relative to previous heat.	
	37.5:62.5	1350	6									
		1600	6									
		1650	12	$3Yb_2O_3 \cdot 5Al_2O_3$	Garnet	Cubic	11.931					
Lu_2O_3–Al_2O_3	50:50	1350	6									
		1650	6	$Lu_2O_3 + 3Lu_2O_3 \cdot 5Al_2O_3$ ss.	C-type+garnet	Cubic+cubic	11.927				Listed dimension for garnet phase in mixture.	
		1800	0.17	do	do	do						

See footnotes at end of table.

TABLE 1.—*Binary oxide mixtures of the trivalent cations*—Continued

Al^{+3} and larger cations—Continued

System	Composition	Heat[1] treatment		Phases identified by X-ray diffraction	Structure type	Symmetry	Unit cell dimensions				Remarks	References[2]
		Temp.	Time				a	b	c	α		
	Mole %	*°C*	*hr*				*A*	*A*	*A*	*deg*		
	37.5:62.7	1350	6									
		1600	6									
		1650	6	$3Lu_2O_3$-$5Al_2O_3$	Garnet	Cubic	11.912				May be some 2:1 phase present	
In_2O_3–Al_2O_3	50:50	800	20									
		1350	6									
		1500	‹6	In_2O_3 ss+Al_2O_3	C-type+corundum	Cubic+rhombohedral						
		1650	‹2	do	do	do						
		800	20									
		1350	6									
		1700	0.0	In_2O_3 ss+unknown	C-type+unknown	Cubic+unknown					Specimen melted, unidentified phase appears to be isostructural with rhombohedral phase of Sc_2O_3–Al_2O_3 system. This phase similar to unknown phase previously reported by Keith and Roy [3].	
Sc_2O_3–Al_2O_3	66.7:33.3	1350	6									
		1650	6	Sc_2O_3 ss+$(1-x)Sc_2O_3$·xAl_2O_3 ss	C-type+unknown	Cubic+rhombohedral						
	50:50	1350	6									
		1650	9.5	$(1-x)Sc_2O_3$·xAl_2O_3 ss	Unknown	Rhombohedral	9.45			87.4	Structure type appears to be rhombohedral distortion of fluorite type; see text.	
		1790	0.08	do	do	do						
		1960	.08	do	do	do					Specimen melted	
Fe_2O_3–Al_2O_3[3b]	53:47	800	20									
		1000	65									
		1375	‹9	$(1-x)Fe_2O_3$·xAl_2O_3 ss	Kappa alumina	Orthorhombic						
	50:50	800	20									
		1000	65									
		1350	‹6	$(1-x)Fe_2O_3$·xAl_2O_3 ss	Kappa alumina	Orthorhombic						
		1450		$(1-x)Fe_2O_3$·xAl_2O_3 ss	Kappa alumina	Orthorhombic	7.03	6.33	7.411		This cell apparently not correct; see text.	Richardson, Ball and Rigby [20].
	47:53	800	20									
		1000	65									
		1350	‹6	$(1-x)Fe_2O_3$·xAl_2O_3 ss	Kappa alumina	Orthorhombic	8.59	9.23	4.98			
Cr_2O_3–Al_2O_3[3c]	50:50	1000	6									
		1600	6	$(1-x)Cr_2O_3$·xAl_2O_3 ss	Corundum	Rhombohedral						
Ga_2O_3–Al_2O_3[4d]	50:50	1350	6									
		1650	6	Ga_2O_3 ss	Beta gallia	Monoclinic						
	30:70	1350	6									
		1650	6	Ga_2O_3 ss+Al_2O_3 ss	Beta gallia+Corundum.	Monoclinic+rhombohedral.						

Ga^{+3} and larger cations

La_2O_3–Ga_2O_3	66.7:33.3	1350	6									
		1500	‹2	$2La_2O_3$·Ga_2O_3	Unknown	Unknown					May be small amount of perovskite type compound present.	
	50:50			La_2O_3·Ga_2O_3	Perovskite	Orthorhombic	5.496	5.524	7.787		Orthorhombic to rhombohedral transformation occurs at 875 °C [6].	Geller [6].
	8.2:91.8	1000	20									
		1350	6	La_2O_3·Ga_2O_3+Ga_2O_3	Perovskite+beta gallia	Orthorhombic+monoclinic.						
Pr_2O_3–Ga_2O_3	50:50			Pr_2O_3·Ga_2O_3	Perovskite	Orthorhombic	5.465	5.495	7.729			Geller [6].
Nd_2O_3–Ga_2O_3	75:25	1350	6									
		1500	6	Nd_2O_3+$2Nd_2O_3$·Ga_2O_3	A-type+unknown	Hexagonal+unknown						
	66.7:33.3	1350	6								Specimen partially melted	
		1500	6	Nd_2O_3+$2Nd_2O_3$·Ga_2O_3+Nd_2O_3·Ga_2O_3.	A-Type+unknown+perovskite.	Hexagonal+unknown+orthorhombic.					Nonequilibrium	
	50:50	1575	6	$2Nd_2O_3$·Ga_2O_3	Unknown	Unknown						
				Nd_2O_3·Ga_2O_3	Perovskite	Orthorhombic	5.496	5.502	7.706			Geller [6].

				Ga_2O_3+Nd_2O_3-Ga_2O_3.	perovskite.	known+orthorhombic.					Nonequilibrium	
		1575	6	$2Nd_2O_3$-Ga_2O_3	Unknown	Unknown						
	50:50			Nd_2O_3-Ga_2O_3	Perovskite	Orthorhombic	5.426	5.502	7.706			Geller [6].
	40:60	1000	6									
		1350	4 6	Nd_2O_3-Ga_2O_3+ $3Nd_2O_3$-$5Ga_2O_3$	Perovskite+garnet	Orthorhombic+cubic	12.505				Listed dimension for garnet phase in mixture.	
	37.5:62.5	1000	6									
		1350	6									
		1500	4 6	$3Nd_2O_3$-$5Ga_2O_3$	Garnet	Cubic	12.505					
Sm_2O_3-Ga_2O_3	75:25	1350	6									
		1500	6	$3Sm_2O_3$-Ga_2O_3+ $2Sm_2O_3$-Ga_2O_3	Unknown+unknown	Unknown+unknown					Nonequilibrium	
		1575	6	$3Sm_2O_3$-Ga_2O_3	Unknown	Unknown						
	50:50	1350	6									
		1500	6	$2Sm_2O_3$-Ga_2O_3+ $3Sm_2O_3$-$5Ga_2O_3$ „	Unknown+garnet	Unknown+cubic	12.448				Listed dimension for garnet phase in mixture.	
	40:60	1000	20									
		1350	6									
		1500	4 4	$2Sm_2O_3$-Ga_2O_3+ $3Sm_2O_3$-$5Ga_2O_3$ „	Unknown+garnet	Unknown+cubic	12.448				Listed dimension for garnet phase in mixture.	
	37.5:62.5	1000	6									
		1350	6									
		1500	4 6	$3Sm_2O_3$-$5Ga_2O_3$	Garnet	Cubic	12.434					
Eu_2O_3-Ga_2O_3	75:25	1350	6									
		1500	6	$3Eu_2O_3$-Ga_2O_3+ $2Eu_2O_3$-Ga_2O_3	Unknown+unknown	Unknown+unknown						
		1575	6	$3Eu_2O_3$-Ga_2O_3	Unknown	Unknown						
	50:50	1350	6									
		1500	6	$2Eu_2O_3$-Ga_2O_3+ $3Eu_2O_3$-$5Ga_2O_3$ „	Unknown +garnet	Unknown+Cubic	12.431				Listed dimension for garnet phase in mixture.	
	40:60	1000	6									
		1350	6									
		1500	4 4	$3Eu_2O_3$-$5Ga_2O_3$ „	Garnet	Cubic	12.422					
	37.5:62.5	1000	6									
		1350	6									
		1500	4 6	$3Eu_2O_3$-$5Ga_2O_3$	Garnet	Cubic	12.403					
Gd_2O_3-Ga_2O_3	75:25	1350	6									
		1500	6	$3Gd_2O_3$-Ga_2O_3	Unknown	Unknown						
		1600	6	$3Gd_2O_3$-Ga_2O_3	Unknown	Unknown						
	50:50	1350	6									
		1500	6	$3Gd_2O_3$-Ga_2O_3+ $3Gd_2O_3$-$5Ga_2O_3$ „	Unknown+garnet	Unknown+cubic	12.426				Listed dimension for garnet phase in mixture.	
	40:60	1000	6									
		1350	6									
		1500	4 4	$3Gd_2O_3$-$5Ga_2O_3$ „	Garnet	Cubic	12.416					
	37.5:62.5	1000	6									
		1350	6									
		1500	4 6	$3Gd_2O_3$-$5Ga_2O_3$	Garnet	Cubic	12.377					
Dy_2O_3-Ga_2O_3	75:25	1350	6									
		1500	6	$3Dy_2O_3$-Ga_2O_3	Unknown	Unknown						
		1600	6	Dy_2O_3+$3Dy_2O_3$-Ga_2O_3	C-type+unknown	Cubic+unknown					Nonequilibrium; the 3:1 phase apparently is decomposing.	
		1650	6	do	do	do					do	
	66.7:33.3	1350	6									
		1500	6	$3Dy_2O_3$-Ga_2O_3+ $3Dy_2O_3$-$5Ga_2O_3$	Unknown+garnet	Unknown+cubic						
	50:50	1350	6									
		1500	6	$3Dy_2O_3$-Ga_2O_3+ $3Dy_2O_3$-$5Ga_2O_3$ „	Unknown+garnet	Unknown+cubic	12.417				Listed dimension for garnet phase in mixture	
	40:60	1000	6									
		1350	6									
		1500	4 4	$3Dy_2O_3$-$5Ga_2O_3$ „	Garnet	Cubic	12.349					
	37.5:62.5	1000	6									
		1350	6									
		1500	4 6	$3Dy_2O_3$-$5Ga_2O_3$	Garnet	Cubic	12.308					
Ho_2O_3-Ga_2O_3	75:25	1350	6									
		1500	6	Ho_2O_3+$3Ho_2O_3$-Ga_2O_3	C-type+unknown	Cubic+unknown					Nonequilibrium	
		1600	6	do	do	do					do	
		1650	6	do	do	do					do	
	66.7:33.3	1350	6									
		1500	6	$3Ho_2O_3$-Ga_2O_3+ $3Ho_2O_3$-$5Ga_2O_3$ „	Unknown+garnet	Unknown+cubic						
	50:50	1350	6									
		1500	6	$3Ho_2O_3$-Ga_2O_3+ $3Ho_2O_3$-$5Ga_2O_3$ „	Unknown+garnet	Unknown+cubic	12.408				Listed dimension for garnet phase in mixture.	
	40:60	1000	6									
		1350	6									
		1500	4 4	$3Ho_2O_3$-$5Ga_2O_3$ „	Garnet	Cubic	12.324					

See footnotes at end of table.

TABLE 1.—*Binary oxide mixtures of the trivalent cations*—Continued

Ga^{+3} and larger cations—Continued

System	Composition	Heat[1] treatment		Phases identified by X-ray diffraction	Structure type	Symmetry	Unit cell dimensions				Remarks	References[2]
		Temp.	Time				a	b	c	α		
	Mole %	*°C*	*hr*				*A*	*A*	*A*	*deg*		
	37.5:62.5	1000	6									
		1350	6									
		1500	[3] 6	$3Ho_2O_3 \cdot 5Ga_2O_3$	Garnet	Cubic	12.282					
Y_2O_3–Ga_2O_3	75:25	1350	6									
		1500	6	$Y_2O_3 + 3Y_2O_3 \cdot Ga_2O_3 + 3Y_2O_3 \cdot 5Ga_2O_3$ ss	C-type+unknown+garnet.	Cubic+unknown+cubic					Nonequilibrium.	
		1600	6	do	do	do					do.	
		1650	6	do	do	do					do.	
	66.7:33.3	1350	6									
		1500	6	$3Y_2O_3 \cdot Ga_2O_3 + 3Y_2O_3 \cdot 5Ga_2O_3$ ss	Unknown+garnet	Unknown+cubic						
	50:50	1350	6									
		1500	6	$3Y_2O_3 \cdot Ga_2O_3 + 3Y_2O_3 \cdot 5Ga_2O_3$ ss	Unknown+garnet	Unknown+cubic	12.441				Listed dimension for garnet phase in mixture.	
		1600	6	do	do	do						
	40:60	1000	6									
		1350	6									
		1500	[3] 4	$3Y_2O_3 \cdot 5Ga_2O_3$ ss	Garnet	Cubic	12.318					
	37.5:62.5	1000	6									
		1350	6									
		1500	[3] 6	$3Y_2O_3 \cdot 5Ga_2O_3$	Garnet	Cubic	12.275					
Er_2O_3–Ga_2O_3	90:10	1350	6									
		1500	6	$Er_2O_3 + 3Er_2O_3 \cdot Ga_2O_3$	C-type+unknown	Cubic+unknown						
	80:20	1350	6									
		1500	6	$Er_2O_3 + 3Er_2O_3 \cdot Ga_2O_3$	C-type+unknown	Cubic+unknown						
		1620	1.3	do	do	do						
		1350	6									
		1500	6									
		1750	.08									
		1625	.25	$Er_2O_3 + 3Er_2O_3 \cdot 5Ga_2O_3$ ss	C-type+garnet	Cubic+cubic					Specimen melted; then annealed.	
	75:25	1350	6									
		1500	6	$Er_2O_3 + Er_2O_3 \cdot Ga_2O_3 + 3Er_2O_3 \cdot 5Ga_2O_3$	C-type+unknown+garnet	Cubic+unknown+cubic					Nonequilibrium.	
		1700	6	$Er_2O_3 + 3Er_2O_3 \cdot Ga_2O_3$	C-type+unknown	Cubic+unknown					Nonequilibrium; C-type phase considerably reduced in amount relative to previous heat.	
		1750	6	do	do	do					Nonequilibrium; C-type phase increased in amount relative to previous heat.	
		1350	6									
		1500	6									
		1745	.08									
		1700	.5	$Er_2O_3 + 3Er_2O_3 \cdot 5Ga_2O_3$ ss	C-type+garnet	Cubic+cubic					Specimen melted; then annealed.	
	50:50	1350	6									
		1500	6	$3Er_2O_3 \cdot Ga_2O_3 + 3Er_2O_3 \cdot 5Ga_2O_3$ ss	Unknown+garnet	Unknown+cubic	12.400				Listed dimension for garnet phase in mixture.	
		1645	.5	do	do	do						
		1350	6									
		1500	6									
		1745	.08									
		1735	.25	$Er_2O_3 + 3Er_2O_3 \cdot 5Ga_2O_3$ ss	C-type+garnet	Cubic+cubic					Specimen melted; then annealed.	
	40:60	1000	6									
		1350	6									
		1500	[3] 4	$3Er_2O_3 \cdot 5Ga_2O_3$ ss	Garnet	Cubic	12.300					
	37.5:62.5	1000	6									
		1350	6									
		1500	[3] 6	$3Er_2O_3 \cdot 5Ga_2O_3$	Garnet	Cubic	12.254					
Tm_2O_3–Ga_2O_3	50:50	1350	6									
		1500	6	$Tm_2O_3 + 3Tm_2O_3 \cdot 5Ga_2O_3$ ss	C-type+garnet	Cubic+cubic	12.369				Listed dimension for garnet phase in mixture.	
Yb_2O_3–Ga_2O_3	50:50	1350	6									
		1500	6	$3Yb_2O_3 \cdot Ga_2O_3 + 3Yb_2O_3 \cdot 5Ga_2O_3$ ss	Unknown+garnet	Unknown+cubic	12.344				Listed dimension for garnet phase in mixture.	

Tm_2O_3–Ga_2O_3	50:50	1350	6									
		1500	6	Tm_2O_3+3Tm_2O_3·5Ga_2O_3 ss	C-type+garnet	Cubic+cubic	12.369				Listed dimension for garnet phase in mixture.	
Yb_2O_3–Ga_2O_3	50:50	1350	6									
		1500	6	Yb_2O_3+3Yb_2O_3·5Ga_2O_3 ss	C-type+garnet	Cubic+cubic	12.344				Listed dimension for garnet phase in mixture.	
	40:60	1000	6									
		1350	6									
		1500	[4] 4	3Yb_2O_3·5Ga_2O_3 ss	Garnet	Cubic	12.232					
	37.5:62.5	1000	6									
		1350	6									
		1500	[4] 6	3Yb_2O_3·5Ga_2O_3	Garnet	Cubic	12.200					
Lu_2O_3–Ga_2O_3	50:50	1350	6									
		1500	6	Lu_2O_3+3Lu_2O_3·5Ga_2O_3 ss	C-type+garnet	Cubic+cubic	12.320				Listed dimension for garnet phase in mixture.	
	40:60	1000	6									
		1350	6									
		1500	[4] 4	3Lu_2O_3·5Ga_2O_3 ss	Garnet	Cubic	12.231					
	37.5:62.5	1000	6									
		1350	6									
		1500	[4] 6	3Lu_2O_3·5Ga_2O_3	Garnet	Cubic	12.183					
In_2O_3–Ga_2O_3[3c]	50:50	800	20									
		1400	[4] 6									
		1450	[4] 6	(1−x)In_2O_3·xGa_2O_3 ss	Unknown	Unknown					Similar to kappa alumina type phases.	
Sc_2O_3–Ga_2O_3	66.7:33.3	1350	6									
		1500	6	Sc_2O_3 ss+(1−x)Sc_2O_3·xGa_2O_3 ss	C-type+unknown	Cubic+unknown						
	50:50	1350	6									
		1500	6									
		1650	6	Sc_2O_3 ss+(1−x)Sc_2O_3·xGa_2O_3 ss	C-type+unknown	Cubic+unknown						
	37.5:62.5	1350	6									
		1500	6									
		1650	6	(1−x)Sc_2O_3·xGa_2O_3 ss	Unknown	Unknown					Unknown phase similar to kappa alumina type phases. It also appears to be isostructural with (1−x)In_2O_3·xGa_2O_3 ss	
	33.3:66.7	1350	6									
		1500	6									
		1650	6	(1−x)Sc_2O_3·xGa_2O_3 ss	Unknown	Unknown						
Fe_2O_3–Ga_2O_3	~50:50			(1−x)Fe_2O_3·xGa_2O_3 ss (x~.5)	Unknown	Orthorhombic	8.75	9.40	5.07			Wood [21].
	50:50	800	20									
		1000	65									
		1300	6	(1−x)Fe_2O_3·xGa_2O_3 ss	Kappa alumina	Orthorhombic	8.73	9.38	5.08		Same phase as reported by Wood [2].	
		1500	6	Fe_2O_4 ss+Ga_2O_3 ss	Spinel+beta gallia	Cubic+monoclinic						
Cr_2O_3–Ga_2O_3	50:50	800	6									
		1000	6									
		1600	6	Cr_2O_3 ss+Ga_2O_3 ss	Corundum+beta gallia.	Rhombohedral+monoclinic.						
	33.3:66.7	800	20									
		1350	6									
		1500	6	Cr_2O_3 ss+Ga_2O_3 ss	Corundum+beta gallia.	Rhombohedral+monoclinic.						
	20:80	800	20									
		1350	6									
		1500	6	Ga_2O_3 ss	Beta gallia	Monoclinic						

Cr^{+3} and larger cations

La_2O_3–Cr_2O_3	50:50			La_2O_3·Cr_2O_3	Perovskite	Orthorhombic	5.477	5.514	7.755			Geller [6].
Pr_2O_3–Cr_2O_3	50:50			Pr_2O_3·Cr_2O_3	Perovskite	Orthorhombic	5.444	5.484	7.710			Geller [6].
Nd_2O_3–Cr_2O_3	50:50			Nd_2O_3·Cr_2O_3	Perovskite	Orthorhombic	5.412	5.494	7.695			Geller [6].
Sm_2O_3–Cr_2O_3	66.7:33.3	800	20									
		1350	6									
		1500	6	Sm_2O_3+Sm_2O_3·Cr_2O_3	B-type+perovskite	Monoclinic+orthorhombic.						
	50:50			Sm_2O_3·Cr_2O_3	Perovskite	Orthorhombic	5.372	5.502	7.650		Results confirmed in present work for specimen heat treated at 1600 °C.	Geller [6].
	37.5:62.5	800	20									
		1350	6									
		1500	6	Sm_2O_3·Cr_2O_3+Cr_2O_3	Perovskite+corundum	Orthorhombic+rhombohedral						
Eu_2O_3–Cr_2O_3	50:50	1000	6									
		1600	6	Eu_2O_3·Cr_2O_3	Perovskite	Orthorhombic	5.33	7.61	5.50			

See footnotes at end of table.

TABLE 1.—*Binary oxide mixtures of the trivalent cations*—Continued

Cr^{+3} and larger cations—Continued

System	Composition	Heat [1] treatment		Phases identified by X-ray diffraction	Structure type	Symmetry	Unit cell dimensions				Remarks	References [2]
		Temp.	Time				a	b	c	α		
	Mole %	*°C*	*hr*				*A*	*A*	*A*	*deg*		
Gd_2O_3–Cr_2O_3	66.7:33.3	800	20									
		1350	6									
		1500	6	Gd_2O_3+Gd_2O_3·Cr_2O_3	B-type+perovskite	Monoclinic+orthorhombic						
	50:50			Gd_2O_3·Cr_2O_3	Perovskite	Orthorhombic	5.312	5.514	7.611		Results confirmed in present work for specimen heat treated at 1600 °C.	Geller [6].
	37.5:62.5	800	20									
		1350	6									
		1500	6	Gd_2O_3·Cr_2O_3+Cr_2O_3	Perovskite+corundum	Orthorhombic+rhombohedral						
Dy_2O_3–$C_{12}O_3$	50:50	1000	6									
		1600	6	Dy_2O_3·Cr_2O_3	Perovskite	Orthorhombic	5.26	7.50	5.51			
Y_2O_3–Cr_2O_3	50:50			Y_2O_3·Cr_2O_3	Perovskite	Orthorhombic	5.247	5.518	7.540			Geller [6].
Er_2O_3–Cr_2O_3	50:50	1000	6									
		1600	6	Er_2O_3·Cr_2O_3	Perovskite	Orthorhombic	5.22	7.51	5.51			
Yb_2O_3–Cr_2O_3	66.7:33.3	800	20									
		1350	6									
		1500	6	Yb_2O_3+Yb_2O_3·Cr_2O_3	C-type+perovskite	Cubic+orthorhombic						
	50:50	1000	6									
		1600	6	Yb_2O_3·Cr_2O_3	Perovskite	Orthorhombic	5.18	7.51	5.49			
	37.5:62.5	800	20									
		1350	6									
		1500	6	Yb_2O_3·Cr_2O_3+Cr_2O_3	Perovskite+corundum	Orthorhombic+rhombohedral						
Lu_2O_3–Cr_2O_3	50:50	1000	6									
		1600	6	Lu_2O_3·Cr_2O_3	Perovskite	Orthorhombic	5.17	7.46	5.49			
In_2O_3–Cr_2O_3	50:50	1000	6									
		1600	[4] 6	$In_2O_{3\,ss}$+$Cr_2O_{3\,ss}$	C-type+corundum	Cubic+rhombohedral						
Sc_2O_3–Cr_2O_3	80:20	800	20									
		1350	6									
		1500	6	$Sc_2O_{3\,ss}$+$(1-x)Sc_2O_3$·$xCr_2O_{3\,ss}$	C-type+unknown	Cubic+unknown						
	75:25	800	6									
		1350	6									
		1500	6	$(1-x)Sc_2O_3$·$xCr_2O_{3\,ss}$	Unknown	Unknown					Unknown phase similar to kappa alumina type phase.	
	66.7:33.3	800	20									
		1600	6	$(1-x)Sc_2O_3$·$xCr_2O_{3\,ss}$ +$Cr_2O_{3\,ss}$	Unknown+corundum	Unknown+rhombohedral						
Sc_2O_3–Cr_2O_3	50:50	1000	20									
		1600	6	$(1-x)Sc_2O_3$·$xCr_2O_{3\,ss}$ +$Cr_2O_{3\,ss}$	Unknown+corundum.	Unknown+rhombohedral.						
Fe_2O_3–Cr_2O_3 [3f]	50:50	1000	6									
		1350	6	$(1-x)Fe_2O_3$·$xCr_2O_{3\,ss}$	Corundum	Rhombohedral						

Fe^{+3} and larger cations

La_2O_3–Fe_2O_3 [3g]	50:50	1500	1	La_2O_3·Fe_2O_3	Perovskite	Orthorhombic	5.545	7.851	5.562			Roth [4].
Pr_2O_3–Fe_2O_3	50:50			Pr_2O_3·Fe_2O_3	Perovskite	Orthorhombic	5.495	5.578	7.810			Geller and Wood [5].
Nd_2O_3–Fe_2O_3	50:50			Nd_2O_3·Fe_2O_3	Perovskite	Orthorhombic	5.441	5.573	7.753			Geller and Wood [5].
Sm_2O_3–Fe_2O_3	50:50			Sm_2O_3·Fe_2O_3	Perovskite	Orthorhombic	5.394	5.592	7.711			Geller and Wood [5].
	37.5:62.5			$3Sm_2O_3$·$5Fe_2O_3$	Garnet	Cubic	12.524				Garnet phase does not form stably in binary mixtures containing Fe_2O_3 and trivalent cations larger than Sm^{+3} [34].	Bertaut and Forrat [34].
$_2O_3$–Fe_2O_3	50:50			Eu_2O_3·Fe_2O_3	Perovskite	Orthorhombic	5.371	5.611	7.686			Geller and Wood [5]. Bertaut and

$_2O_3$–Fe_2O_3	50:50			$Eu_2O_3 \cdot Fe_2O_3$	Perovskite	Orthorhombic	5.371	5.611	7.686		Geller and Wood [5].
	37.5:62.5			$3Eu_2O_3 \cdot 5Fe_2O_3$	Garnet	Cubic	12.518				Bertaut and Forrat [34].
Gd_2O_3–Fe_2O_3[3h]	50:50			$Gd_2O_3 \cdot Fe_2O_3$	Perovskite	Orthorhombic	5.346	5.616	7.668	Results confirmed in present work for specimen heat treated at 1300 °C.	Geller and Wood [5].
	37.5:62.5			$3Gd_2O_3 \cdot 5Fe_2O_3$	Garnet	Cubic	12.479				Bertaut and Forrat [34].
Dy_2O_3–Fe_2O_3	66.7:33.3	800	20								
		1000	20								
		1350	6	$Dy_2O_3 + Dy_2O_3 \cdot Fe_2O_3$	C-type+perovskite	Cubic+orthorhombic					
	50:50	800	20								
		1000	65								
		1300	6	$Dy_2O_3 \cdot Fe_2O_3 + 3Dy_2O_3 \cdot 5Fe_2O_3$	Perovskite+garnet	Orthorhombic+cubic				Nonequilibrium	
		1500	6	$Dy_2O_3 \cdot Fe_2O_3$	Perovskite	Orthorhombic	5.30	7.62	5.59		
	37.5:62.5			$3Dy_2O_3 \cdot 5Fe_2O_3$	Garnet	Cubic	12.414				Bertaut and Forrat [34].
Ho_2O_3–Fe_2O_3	50:50	800	20								
		1000	65								
		1350	6	$Ho_2O_3 \cdot Fe_2O_3 + 3Ho_2O_3 \cdot 5Fe_2O_3$	Perovskite+garnet	Orthorhombic+cubic				Nonequilibrium	
		1500	6	$Ho_2O_3 \cdot Fe_2O_3$	Perovskite	Orthorhombic	5.30	7.58	5.59		
	37.5:62.5			$3Ho_2O_3 \cdot 5Fe_2O_3$	Garnet	Cubic	12.380				Bertaut and Forrat [34].
Y_2O_3–Fe_2O_3[3i]	50:50	1500	1	$Y_2O_3 \cdot Fe_2O_3$	Perovskite	Orthorhombic	5.279	7.609	5.590		Roth [4].
	37.5:62.5			$3Y_2O_3 \cdot 5Fe_2O_3$	Garnet	Cubic	12.376				Bertaut and Forrat [34].
Er_2O_3–Fe_2O_3	50:50	800	20								
		1000	65								
		1300	6								
		1500	6	$Er_2O_3 \cdot Fe_2O_3$	Perovskite	Orthorhombic	5.26	7.58	5.58		
	37.5:62.5			$3Er_2O_3 \cdot 5Fe_2O_3$	Garnet	Cubic	12.349				Bertaut and Forrat [34].
Tm_2O_3–Fe_2O_3	37.5:62.5			$3Tm_2O_3 \cdot 5Fe_2O_3$	Garnet	Cubic	12.325				Bertaut and Forrat [34].
Yb_2O_3–Fe_2O_3	66.7:33.3	800	20								
		1000	20								
		1350	6	$Yb_2O_3 + Yb_2O_3 \cdot Fe_2O_3$	C-type+perovskite	Cubic+orthorhombic					
	50:50	800	20								
		1000	65								
		1300	6								
		1500	6	$Yb_2O_3 \cdot Fe_2O_3$	Perovskite	Orthorhombic	5.22	7.56	5.58		
	37.5:62.5			$3Yb_2O_3 \cdot 5Fe_2O_3$	Garnet	Cubic	12.291				Bertaut and Forrat [34].
Lu_2O_3–Fe_2O_3	50:50	800	20								
		1000	65								
		1300	6	$Lu_2O_3 \cdot Fe_2O_3$	Perovskite	Orthorhombic	5.21	7.55	5.55		
		1500	6	do	do	do					
	37.5:62.5			$3Lu_2O_3 \cdot 5Fe_2O_3$	Garnet	Cubic	12.277				Bertaut and Forrat [34].
In_2O_3–Fe_2O_3	50:50	800	20								
		1000	65								
		1350	6	$In_2O_{3\ ss} + Fe_2O_{3\ ss}$	C-type+corundum	Cubic+rhombohedral					
		1500	6	do	do	do					
Sc_2O_3–Fe_2O_3[3j]	50:50	800	20								
		1000	65								
		1350	6	$Sc_2O_{3\ ss} + Fe_2O_{3\ ss}$	C-type+corundum	Cubic+rhombohedral				Nonequilibrium	
		1500	6	$Sc_2O_{3\ ss}$	C-type	Cubic					
	37.5:62.5	800	20								
		1000	20								
		1350	6	$Sc_2O_{3\ ss} + Fe_2O_{3\ ss}$	C-type+corundum	Cubic+rhombohedral					

Sc^{+3} and larger cations

La_2O_3–Sc_2O_3	50:50			$La_2O_3 \cdot Sc_2O_3$	Perovskite	Orthorhombic	5.678	5.787	8.098		Geller [6].
Pr_2O_3–Sc_2O_3	50:50			$Pr_2O_3 \cdot Sc_2O_3$	Perovskite	Orthorhombic	5.615	5.776	8.027		Geller [6].
Nd_2O_3–Sc_2O_3	50:50			$Nd_2O_3 \cdot Sc_2O_3$	Perovskite	Orthorhombic	5.574	5.771	7.998		Geller [6].

See footnotes at end of table.

TABLE 1.—*Binary oxide mixtures of the trivalent cations*—Continued

Sc^{+3} and larger cations—Continued

System	Composition	Heat[1] treatment		Phases identified by X-ray diffraction	Structure type	Symmetry	Unit cell dimensions				Remarks	References[2]
		Temp.	Time				a	b	c	α		
	Mole %	*°C*	*hr*				*A*	*A*	*A*	*deg*		
$Sm_2O_3-Sc_2O_3$	50:50	1350	6									
		1650	9.5	$Sm_2O_3 \cdot Sc_2O_3$	Perovskite	Orthorhombic	5.53	7.95	5.76			
$Eu_2O_3-Sc_2O_3$	50:50	1350	6									
		1650	9.5	$Eu_2O_3 \cdot Sc_2O_3$	Perovskite	Orthorhombic	5.51	7.94	5.76			
$Gd_2O_3-Sc_2O_3$	66.7:33.3	1350	6									
		1500	6									
		1650	6	Gd_2O_3 ss+$Gd_2O_3 \cdot Sc_2O_3$	B-type+perovskite	Monoclinic+orthorhombic						
	50:50			$Gd_2O_3 \cdot Sc_2O_3$	Perovskite	Orthorhombic	5.487	5.756	7.925		Results confirmed in present work for specimen heat treated at 1650 °C.	Geller [6].
	37.5:62.5	1350	6									
		1500	6	$Gd_2O_3 \cdot Sc_2O_3$+Sc_2O_3 ss	Perovskite+C-type	Orthorhombic+cubic						
		1650	6	do	do	do						
$Dy_2O_3-Sc_2O_3$	66.7:33.3	1350	6									
		1500	6	Dy_2O_3 ss+$Dy_2O_3 \cdot Sc_2O_3$	C-type+perovskite	Cubic-orthorhombic						
	50:50	1350	6									
		1650	9.5	$Dy_2O_3 \cdot Sc_2O_3$	Perovskite	Orthorhombic	5.43	7.89	5.71			
$Ho_2O_3-Sc_2O_3$	50:50	1350	6									
		1650	9.5									
		1875	0.3	Ho_2O_3 ss+$Ho_2O_3 \cdot Sc_2O_3$+Sc_2O_3 ss	C-type+perovskite+C-type	Cubic+orthorhombic+cubic	5.42	7.87	5.71		Nonequilibrium listed dimensions for perovskite phase in mixture.	
		1900	1	do	do	do					Nonequilibrium	
		1950	1	do	do	do					do	
		2000	0.3	$(1-x)Ho_2O_3 \cdot xSc_2O_3$ ss+$Ho_2O_3 \cdot Sc_2O_3$	C-type+perovskite	Cubic+orthorhombic					Nonequilibrium; amount of perovskite phase small. Equilibrium probably single phase C-type solid solution.	
$Y_2O_3-Sc_2O_3$	50:50	1350	6									
		1650	9.5	Y_2O_3 ss+$Y_2O_3 \cdot Sc_2O_3$+Sc_2O_3 ss	C-type+perovskite+C-type	Cubic+orthorhombic+cubic					Nonequilibrium	
		1890	0.3	$(1-x)Y_2O_3 \cdot xSc_2O_3$ ss	C-type	Cubic						
$Er_2O_3-Sc_2O_3$	50:50	1350	6									
		1650	9.5	Er_2O_3 ss+Sc_2O_3 ss	C-type+C-type	Cubic+cubic					Nonequilibrium	
		1850	0.7	$(1-x)Er_2O_3 \cdot xSc_2O_3$ ss	C-type	Cubic						
$Yb_2O_3-Sc_2O_3$	50:50	1350	6									
		1650	9.5	Yb_2O_3 ss+Sc_2O_3 ss	C-type+C-type	Cubic+cubic					Nonequilibrium	
		1850	0.3	$(1-x)Yb_2O_3 \cdot xSc_2O_3$ ss	C-type	Cubic						
$Lu_2O_3-Sc_2O_3$	50:50	1350	6									
		1650	9.5	$(1-x)Lu_2O_3 \cdot xSc_2O_3$ ss	C-type	Cubic						
$In_2O_3-Sc_2O_3$	50:50	800	20									
		1350	[4] 6	$(1-x)In_2O_3 \cdot xSc_2O_3$ ss	C-type	Cubic						

In^{+3} and larger cations

$La_2O_3-In_2O_3$	50:50	1350	0.5	$La_2O_3 \cdot In_2O_3$	Perovskite	Orthorhombic	5.723	8.207	5.914			Roth [4].
$Nd_2O_3-In_2O_3$	95:5	800	20									
		1350	6									
		1500	[4] 2	$(1-x)Nd_2O_3 \cdot xIn_2O_3$ ss	B-type	Monoclinic						
	85:15	800	20									
		1350	6									
		1500	[4] 2	$(1-x)Nd_2O_3 \cdot xIn_2O_3$ ss+$Nd_2O_3 \cdot In_2O_3$	B-type+perovskite	Monoclinic+orthorhombic.						
	75:25	800	20									
		1350	6									
		1500	[4] 2	$(1-x)Nd_2O_3 \cdot xIn_2O_3$ ss+$Nd_2O_3 \cdot In_2O_3$	B-type+perovskite	Monoclinic+orthorhombic.						
	66.7:33.3	800	20									
		1350	6									

		1350	6									
		1500	[4] 2	$(1-x)Nd_2O_3 \cdot xIn_2O_3$ ss + $Nd_2O_3 \cdot In_2O_3$	B-type+perovskite	Monoclinic+orthorhombic.						
	50:50	1350	0.5	$Nd_2O_3 \cdot In_2O_3$	Perovskite	Orthorhombic	5.627	8.121	5.891			Roth [4].
	33.3:66.7	800	20									
		1350	6									
		1500	[4] 2	$Nd_2O_3 \cdot In_2O_3 + In_2O_3$	Perovskite+C-type	Orthorhombic+cubic						
$Sm_2O_3-In_2O_3$	66.7:33.3	800	20									
		1350	6									
		1500	[4] 2	Sm_2O_3 ss + $Sm_2O_3 \cdot In_2O_3$	B-type+perovskite	Monoclinic+orthorhombic.						
	50:50	1350	0.5	$Sm_2O_3 \cdot In_2O_3$	Perovskite	Orthorhombic	5.589	8.082	5.886			Roth [4].
	33.3:66.7	800	20									
		1350	6									
		1500	[4] 2	$Sm_2O_3 \cdot In_2O_3 + In_2O_3$ ss	Perovskite+C-type	Orthorhombic+cubic						
$Eu_2O_3-In_2O_3$[3k]	50:50	800	20									
		1350	6									
		1650	[4] 2	$Eu_2O_3 \cdot In_2O_3$	Unknown	Unknown					Pseudo hexagonal symmetry	Schneider [23].
$Gd_2O_3-In_2O_3$	66.7:33.3	800	20									
		1350	6									
		1600	[4] 2	Gd_2O_3 ss + $Gd_2O_3 \cdot In_2O_3$	B-type+unknown	Monoclinic+unknown.						
	50:50	800	20									
		1350	6									
		1600	[4] 1	$Gd_2O_3 \cdot In_2O_3$	Unknown	Unknown					Isostructural with $Eu_2O_3 \cdot In_2O_3$	Schneider [23].
		1650	[4] 2	do	do	do						
	33.3:66.7	800	20									
		1350	6									
		1600	[4] 2	$Gd_2O_3 \cdot In_2O_3$ ss + In_2O_3 ss	Unknown+C-type	Unknown+cubic						
$Dy_2O_3-In_2O_3$	95:5	800	20									
		1350	6									
		1600	[4] 2	Dy_2O_3 ss + $(1-x)$ $Dy_2O_3 \cdot xIn_2O_3$ ss	C-type+B-type	Cubic+monoclinic						
	85:5	800	20									
		1350	6									
		1600	[4] 2	Dy_2O_3 ss + $(1-x)$ $Dy_2O_3 \cdot xIn_2O_3$ ss	C-type+B-type	Cubic+monoclinic						
	75:25	800	20									
		1350	6									
		1600	[4] 2	$(1-x)Dy_2O_3 \cdot xIn_2O_3$ ss	B-type	Monoclinic						
	66.7:33.3	800	20									
		1350	6									
		1600	[4] 2	$(1-x)Dy_2O_3 \cdot xIn_2O_3$ ss + $Dy_2O_3 \cdot In_2O_3$ ss	B-type+unknown	Monoclinic+unknown.						
	50:50	800	20									
		1350	6									
		1600	[4] 1	$Dy_2O_3 \cdot In_2O_3$	Unknown	Unknown					Isostructural with $Eu_2O_3 \cdot In_2O_3$ [23]	Schneider [23]
		1650	[4] 3	$(1-x)Dy_2O_3 \cdot xIn_2O_3$ ss + In_2O_3 ss	B-type+C-type	Monoclinic+cubic						
	33.3:66.7	800	20									
		1350	6									
		1600	[4] 2	$Dy_2O_3 \cdot In_2O_3$ ss + In_2O_3 ss	Unknown+C-type	Unknown+cubic						
$Ho_2O_3-In_2O_3$	50:50	800	20									
		1350	6									
		1600	[4] 1	$(1-x)Ho_2O_3 \cdot xIn_2O_3$ ss	C-type	Cubic						
$Er_2O_3-In_2O_3$	50:50	800	20									
		1350	6									
		1600	[4] 1	$(1-x)Er_2O_3 \cdot xIn_2O_3$ ss	C-type	Cubic						
$Tm_2O_3-In_2O_3$	50:50	800	20									
		1350	6									
		1600	[4] 1	$(1-x)Tm_2O_3 \cdot xIn_2O_3$ ss	C-type	Cubic						
$Yb_2O_3-In_2O_3$	50:50	800	20									
		1350	6									
		1600	[4] 1	$(1-x)Yb_2O_3 \cdot xIn_2O_3$ ss	C-type	Cubic						
$Lu_2O_3-In_2O_3$	50:50	800	20									
		1350	6									
		1600	[4] 1	$(1-x)Lu_2O_3 \cdot xIn_2O_3$ ss	C-type	Cubic						

[1] All specimens in present work slow cooled except where noted. Each heat treatment includes all previously listed lower temperature heatings given for the same composition.
[2] When no references are given, data was obtained in present investigation.
[3] The phase diagram for this system has been reported: (a) [22], (b) [10], (c) [26], (d) [27], (e) [28], (f) [10], (g) [29], (h) [22], (i) [18], (j) [30], (k) [23].
[4] Specimen heated in sealed Pt tubes and quenched.

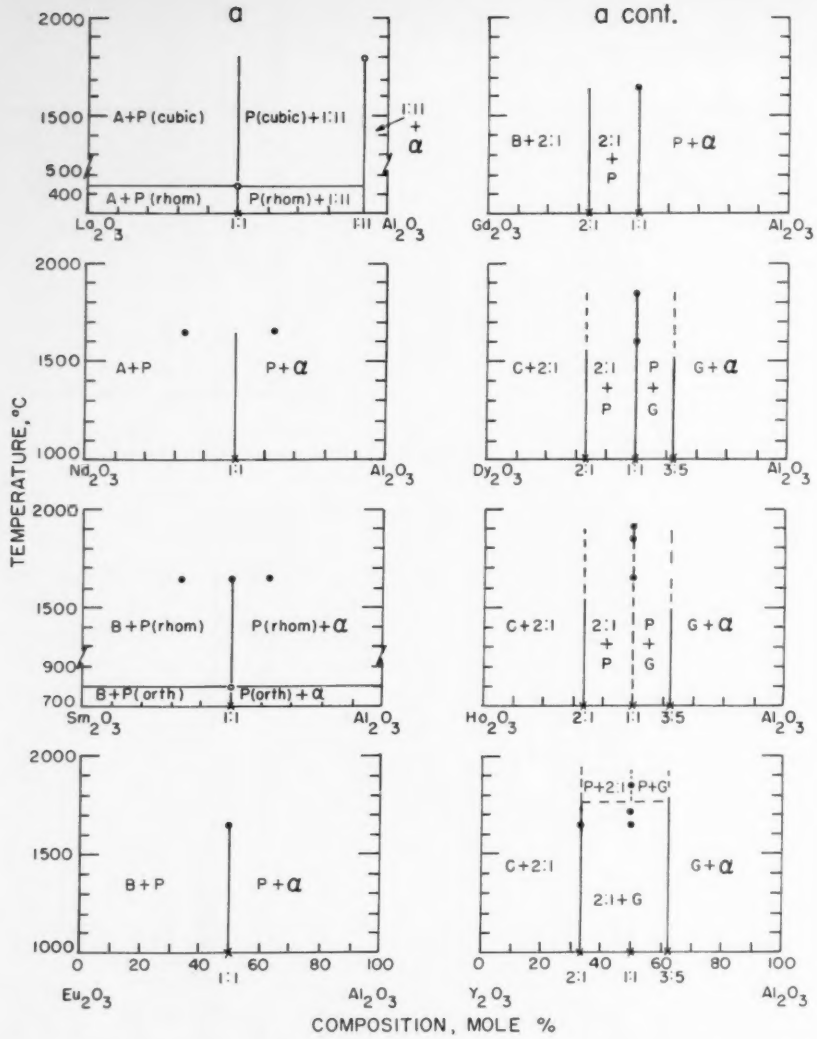

FIGURE 5. *Predicted subsolidus binary phase diagrams for systems involving oxides of the trivalent cations*

●—compositions studied in present work
○—data taken from literature
×—data taken from literature for which no temperature of heat treatment is given

A—A-type rare earth oxide structure
B—B-type rare earth oxide structure
C—C-type rare earth oxide structure
G—garnet type compound
1:11—beta alumina type structure
P—perovskite type compound
R—unknown type structure, rhombohedral symmetry
S—spinel type structure
α—corundum type structure
β—beta gallia type structure
K—kappa alumina type structure
u—unknown type structure similar to kappa alumina
ss—solid solution

(a) Binary oxide systems containing Al^{+3} and larger cations. The following systems pertinent to this series have been previously published.

1. Y_2O_3–Al_2O_3 [22]
2. Fe_2O_3–Al_2O_3 [10]
3. Cr_2O_3–Al_2O_3 [26]
4. Ga_2O_3–Al_2O_3 [27]

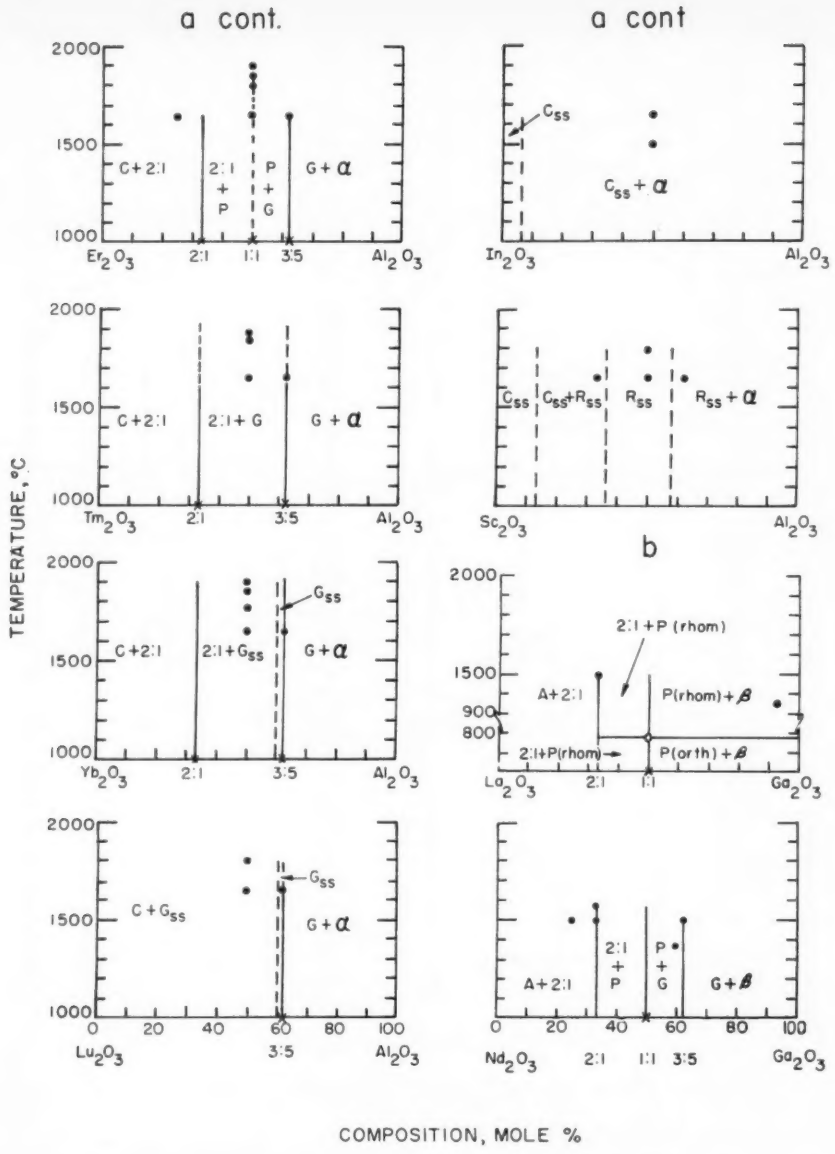

FIGURE 5. *Predicted subsolidus binary phase diagram for systems involving oxides of the trivalent cations*—Continued

●—compositions studied in present work
○—data taken from literature
×—data taken from literature for which no temperature of heat treatment is given

A—A-type rare earth oxide structure
B—B-type rare earth oxide structure
C—C-type rare earth oxide structure
G—garnet type compound
1:11—beta alumina type structure
P—perovskite type compound
R—unknown type structure, rhombohedral symmetry
S—spinel type structure
α—corundum type structure
β—beta gallia type structure
K—kappa alumina type structure
u—unknown type structure similar to kappa alumina
ss—solid solution

(a) Binary oxide systems containing Al^{+3} and larger cations. The following systems pertinent to this series have been previously published.

1. Y_2O_3–Al_2O_3 [22]
2. Fe_2O_3–Al_2O_3 [10]
3. Cr_2O_3–Al_2O_3 [26]
4. Ga_2O_3–Al_2O_3 [27]

(b) Binary oxide systems containing Ga^{+3} and larger cations. The In_2O_3–Ga_2O_3 system has been previously published [28]. Boundary limits of kappa alumina solid solution taken from Remeika [35].

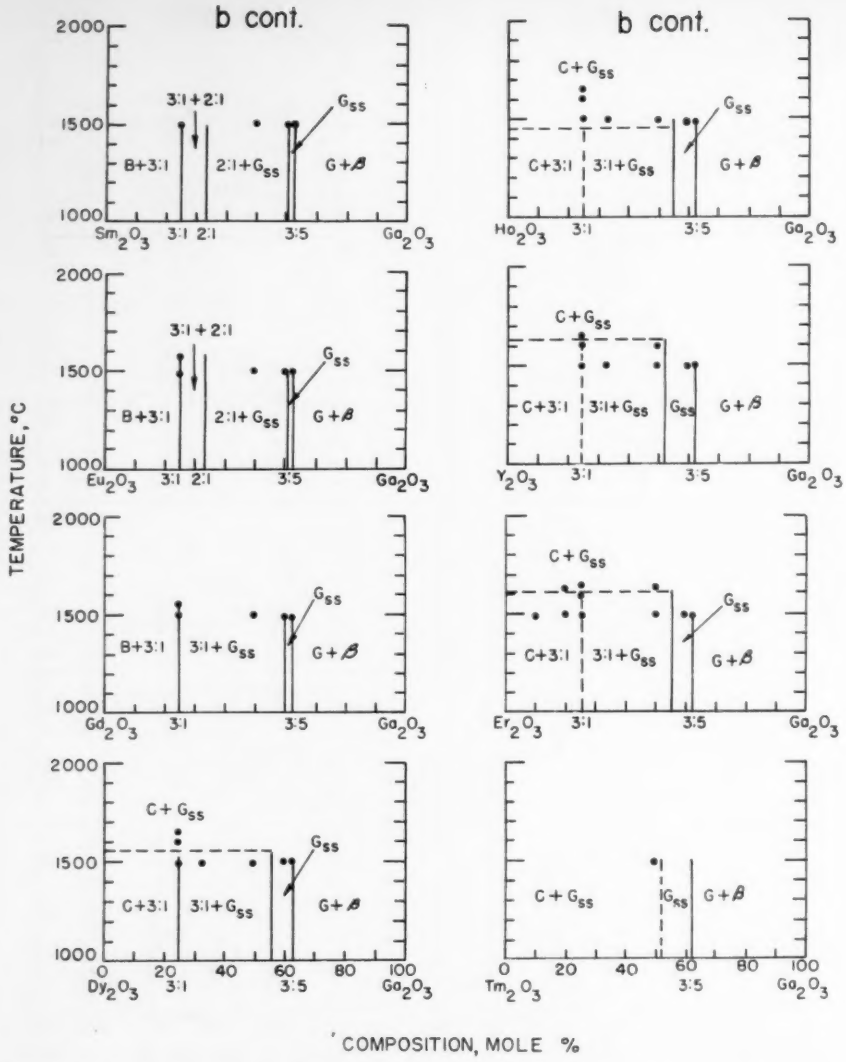

FIGURE 5. *Predicted subsolidus binary phase diagram for systems involving oxides of the trivalent cations*—Continued

●—compositions studied in present work
○—data taken from literature
×—data taken from literature for which no temperature of heat treatment is given

A—A-type rare earth oxide structure
B—B-type rare earth oxide structure
C—C-type rare earth oxide structure
G—garnet type compound
1:11—beta alumina type structure
P—perovskite type compound
R—unknown type structure, rhombohedral symmetry
S—spinel type structure
α—corundum type structure
β—beta gallia type structure
K—kappa alumina type structure
u—unknown type structure similar to kappa alumina
ss—solid solution

(b) Binary oxide systems containing Ga^{+3} and larger cations. The In_2O_3-Ga_2O_3 system has been previously published [28]. Boundary limits of kappa alumina solid solution taken from Remeika [35].

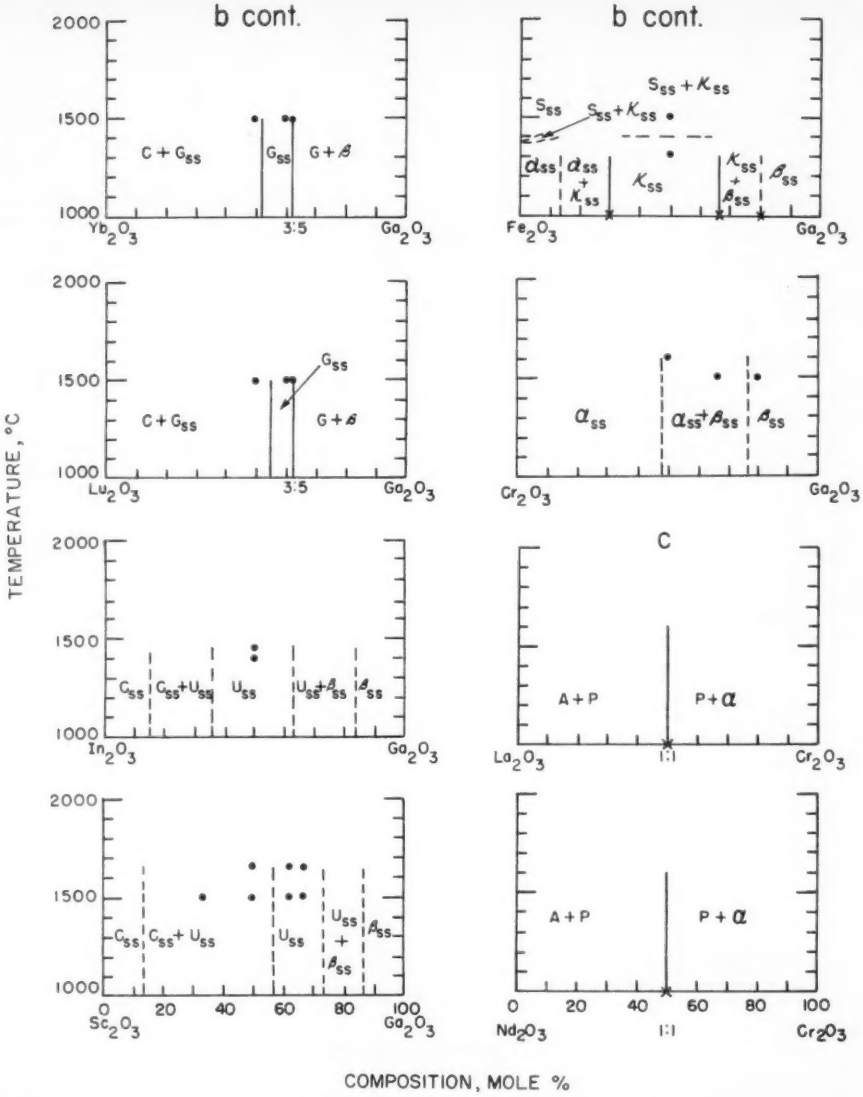

FIGURE 5. *Predicted subsolidus binary phase diagram for systems involving oxides of the trivalent cations*—Continued

●—compositions studied in present work
○—data taken from literature
×—data taken from literature for which no temperature of heat treatment is given

A—A-type rare earth oxide structure
B—B-type rare earth oxide structure
C—C-type rare earth oxide structure
G—garnet type compound
1:11—beta alumina type structure
P—perovskite type compound
R—unknown type structure, rhombohedral symmetry
S—spinel type structure
α—corundum type structure
β—beta gallia type structure
K—kappa alumina type structure
u—unknown type structure similar to kappa alumina
ss—solid solution

(b) Binary oxide systems containing Ga^{+3} and larger cations. The In_2O_3–Ga_2O_3 system has been previously published [28]. Boundary limits of kappa alumina solid solution taken from Remeika [35].

(c) Binary oxide systems containing Cr^{+3} and larger cations. The Fe_2O_3–Cr_2O_3 system has been previously published [10].

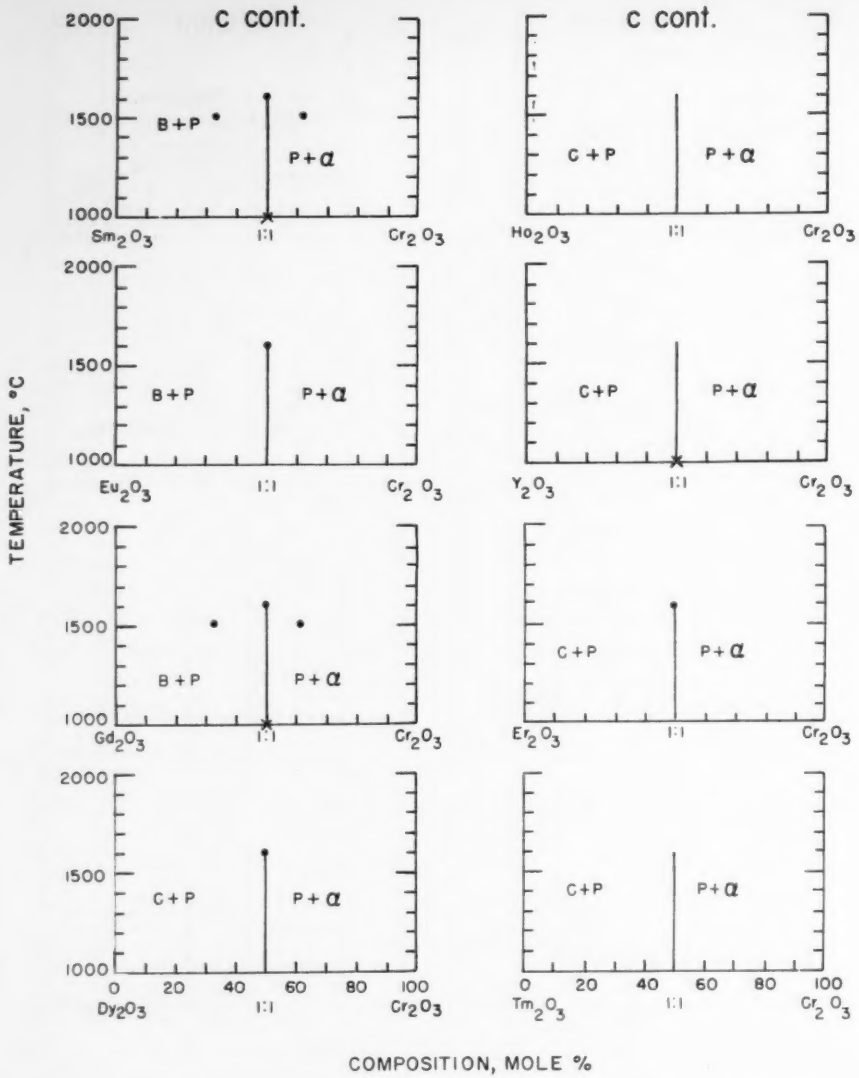

FIGURE 5. *Predicted subsolidus binary phase diagram for systems involving oxides of the trivalent cations*—Continued

●—compositions studied in present work
○—data taken from literature
×—data taken from literature for which no temperature of heat treatment is given

A—A-type rare earth oxide structure
B—B-type rare earth oxide structure
C—C-type rare earth oxide structure
G—garnet type compound
1:1—beta alumina type structure
P—perovskite type compound
R—unknown type structure, rhombohedral symmetry
S—spinel type structure
α—corundum type structure
β—beta gallia type structure
K—kappa alumina type structure
u—unknown type structure similar to kappa alumina
ss—solid solution

(c) Binary oxide systems containing Cr^{+3} and larger cations. The Fe_2O_3–Cr_2O_3 system has been previously published [10].

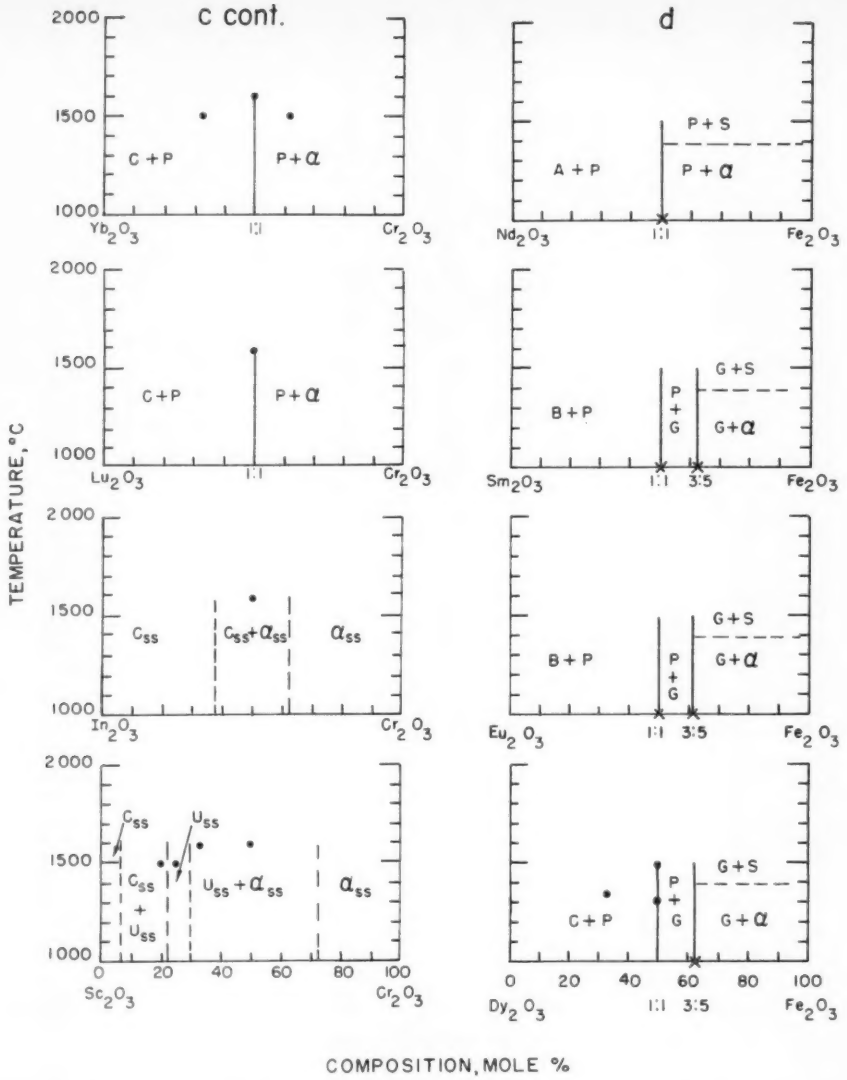

FIGURE 5. *Predicted subsolidus binary phase diagram for systems involving oxides of the trivalent cations*—Continued

●—compositions studied in present work
○—data taken from literature
×—data taken from literature for which no temperature of heat treatment is given

A—A-type rare earth oxide structure
B—B- ype rare earth oxide structure
C—C-type rare earth oxide structure
G—garnet type compound
1:1—beta alumina type structure
P—perovskite type compound
R—unknown type structure, rhombohedral symmetry
S—spinel type structure
α—corundum type structure
β—beta gallia type structure
K—kappa alumina type structure
n—unknown type structure similar to kappa alumina
ss—solid solution

(c) Binary oxide systems containing Cr^{+3} and larger cations. The Fe_2O_3–Cr_2O_3 system has been previously published [10].

(d) Binary oxide systems containing Fe^{+3} and larger cations. The transformation temperature of corundum to spinel type is taken as 1390 °C. [10]. The following systems pertinent to this series have been previously published:

1. La_2O_3–Fe_2O_3 [29]
2. Gd_2O_3–Fe_2O_3 [22]
3. Y_2O_3–Fe_2O_3 [18]
4. Sc_2O_3–Fe_2O_3 [30]

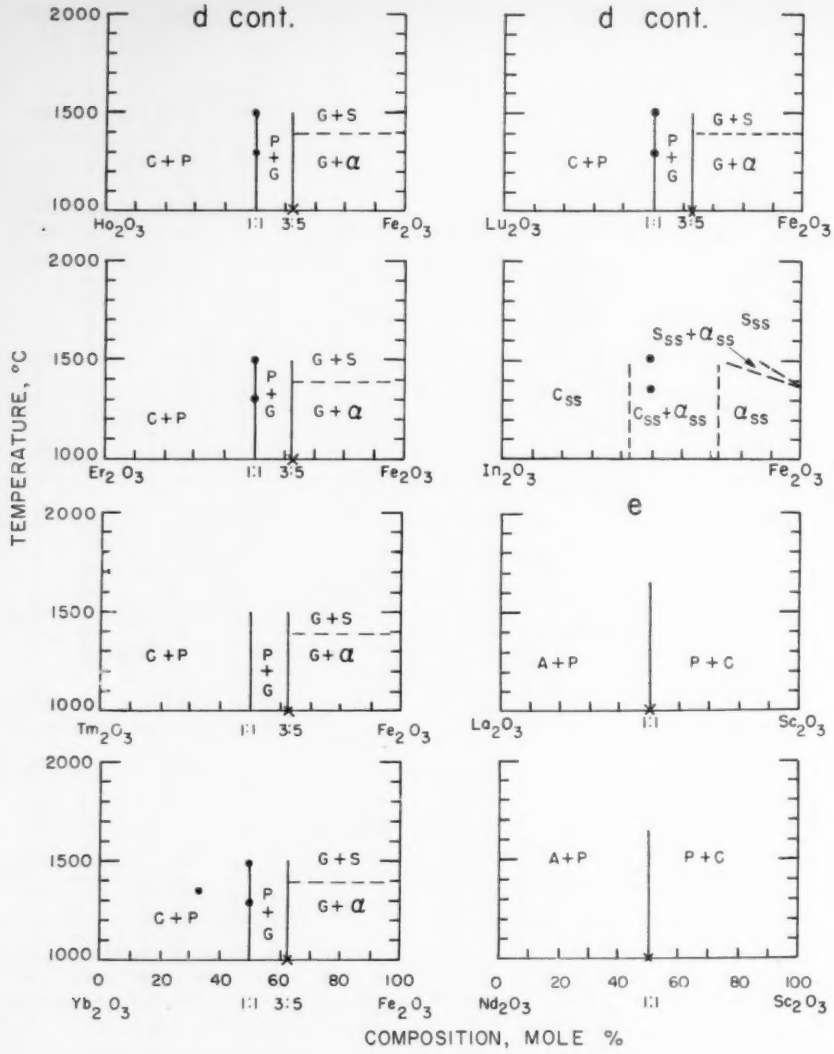

FIGURE 5. *Predicted subsolidus binary phase diagram for systems involving oxides of the trivalent cations*—Continued

●—compositions studied in present work
○—data taken from literature
×—data taken from literature for which no temperature of heat treatment is given

A—A-type rare earth oxide structure
B—B-type rare earth oxide structure
C—C-type rare earth oxide structure
G—garnet type compound
1:11—beta alumina type structure
P—perovskite type compound
R—unknown type structure, rhombohedral symmetry
S—spinel type structure
α—corundum type structure
β—beta gallia type structure
K—kappa alumina type structure
u—unknown type structure similar to kappa alumina
ss—solid solution

(d) Binary oxide systems containing Fe^{+3} and larger cations. The transformation temperature of corundum to spinel type is taken as 1390 °C. [10]. The following systems pertinent to this series have been previously published:

1. In_2O_3–Fe_2O_3 [29]
2. Gd_2O_3–Fe_2O_3 [22]
3. Y_2O_3–Fe_2O_3 [18]
4. Sc_2O_3–Fe_2O_3 [30]

(e) Binary oxide systems containing Sc^{+3} and larger cations.

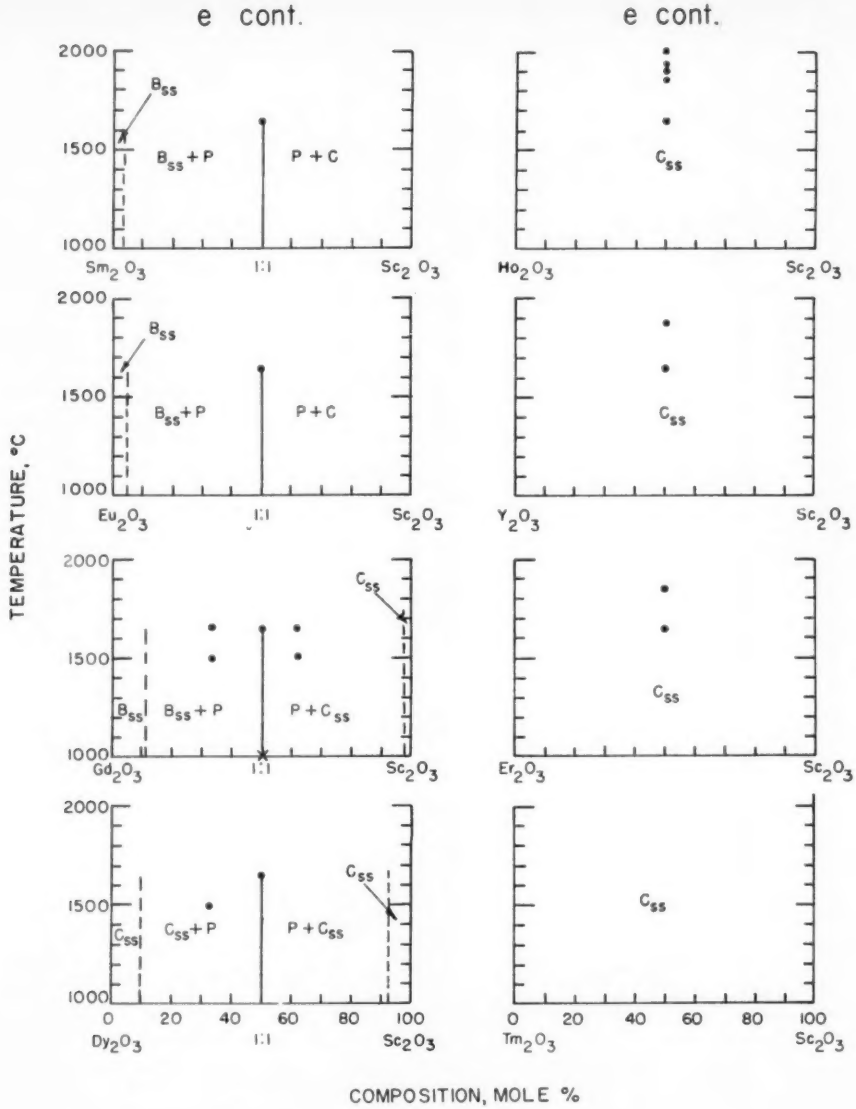

FIGURE 5. *Predicted subsolidus binary phase diagram for systems involving oxides of the trivalent cations*—Continued

●—compositions studied in present work
○—data taken from literature
×—data taken from literature for which no temperature of heat treatment is given

A—A-type rare earth oxide structure
B—B-type rare earth oxide structure
C—C-type rare earth oxide structure
G—garnet type compound
1:11—beta alumina type structure
P—perovskite type compound
R—unknown type structure, rhombohedral symmetry
S—spinel type structure
α—corundum type structure
β—beta gallia type structure
K—kappa alumina type structure
u—unknown type structure similar to kappa alumina
ss—solid solution

(e) Binary oxide systems containing Sc^{+3} and larger cations.

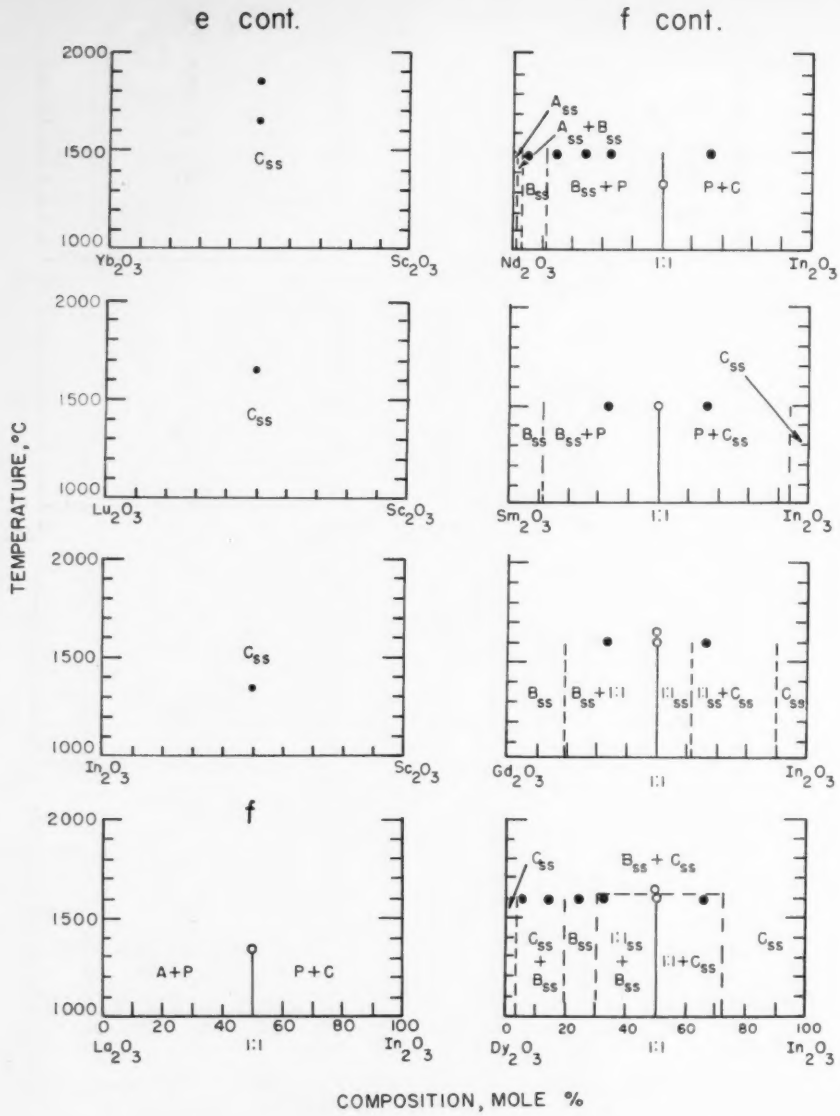

FIGURE 5. *Predicted subsolidus binary phase diagram for systems involving oxides of the trivalent cations*—Continued

●—compositions studied in present work
○—data taken from literature
✕—data taken from literature for which no temperature of heat treatment is given

A—A-type rare earth oxide structure
B—B-type rare earth oxide structure
C—C-type rare earth oxide structure
G—garnet type compound
1:11—beta alumina type structure
P—perovskite type compound
R—unknown type structure, rhombohedral symmetry
S—spinel type structure
α—corundum type structure
β—beta gallia type structure
K—kappa alumina type structure
u—unknown type structure similar to kappa alumina
ss—solid solution

(e) Binary oxide systems containing Sc^{+3} and larger cations.
(f) Binary oxide systems containing In^{+3} and larger cations. The Eu_2O_3–In_2O_3 system to be published [23].

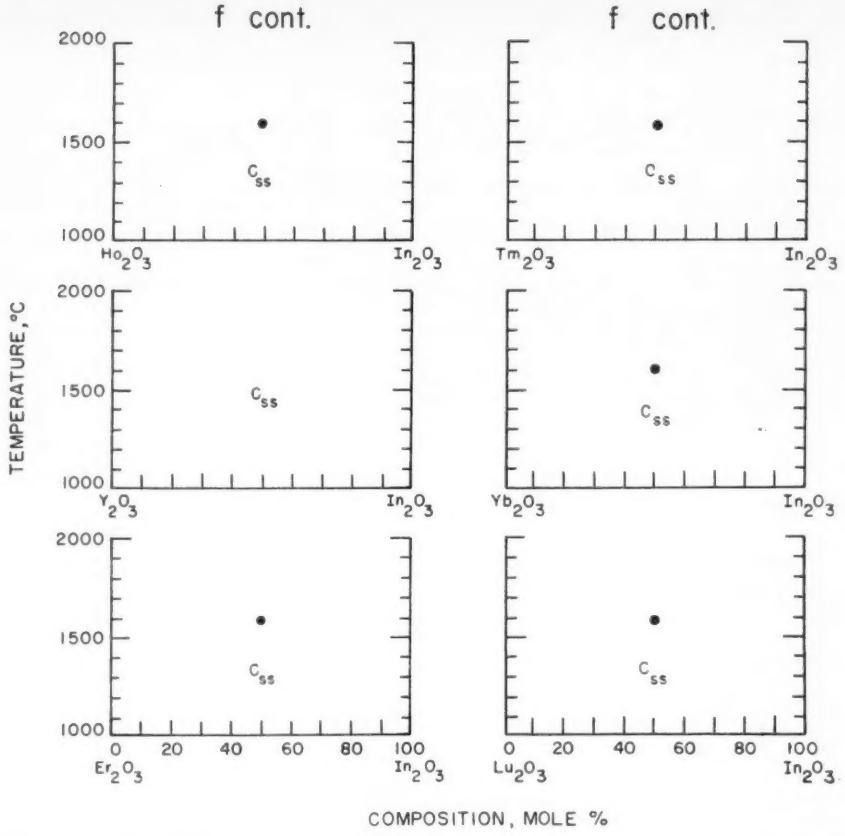

FIGURE 5. *Predicted subsolidus binary phase diagram for systems involving oxides of the trivalent cations*—Continued

●—compositions studied in present work
○—data taken from literature
×—data taken from literature for which no temperature o fheat treatment is given

A—A-type rare earth oxide structure
B—B-type rare earth oxide structure
C—C-type rare earth oxide structure
G—garnet type compound
H—beta alumina type structure
P—perovskite type compound
R—unknown type structure, rhombohedral symmetry
S—spinel type structure
α—corundum type structure
β—beta gallia type structure
K—kappa alumina type structure
u—unknown type structure similar to kappa alumina
ss—solid solution

(f) Binary oxide systems containing In^{+3} and larger cations. The Eu_2O_3–In_2O_3 system to be published [23].

6. References

[1] S. J. Schneider and R. S. Roth, J. Research NBS **64A,** 317–332 (1960).
[2] V. M. Goldschmidt, T. Barth, G. Lunde, and W. Zachariasen, Pt. VII Skrifter Norske Videnskaps-Akad. Oslo I. Mat-Naturv. K1 No. 2 (1926).
[3] M. L. Keith and R. Roy, Amer. Min. **39,** 1–23 (1954).
[4] R. S. Roth, J. Research NBS **58,** 75–88 (1957).
[5] S. Geller and E. A. Wood, Acta Cryst. **9,** 563–568 (1956).
[6] S. Geller, Acta Cryst. **10,** 243–248 (1957).
[7] S. Geller and V. B. Bala, Acta Cryst. **9,** 1019–1025 (1956).
[8] L. H. Ahrens, Geochim. et Cosmochim. Acta **2,** 155–169 (1952).
[9] R. S. Roth and S. J. Schneider, J. Research NBS **64A,** 309–316 (1960).
[10] A. Muan and S. Somiya, J. Am. Ceram. Soc. **42,** 603–613 (1959).
[11] E. Mooser and W. B. Pearson, Acta Cryst. **12,** 1015–1022 (1959).
[12] L. Pauling, The Nature of the Chemical Bond, 3d ed., Ithaca, N.Y., Cornell Univer. Press 98 (1960).
[13] W. Gordy and W. J. Orville, J. Chem. Phys. **24,** 439–444 (1956).
[14] M. W. Shafer and R. Roy, J. Am. Ceram. Soc. **42,** 563–570 (1959).
[15] R. Roy, V. G. Hill, and E. F. Osborn, Ind. and Eng. Chem. **45,** 819–820 (1953).
[16] J. A. W. Dalziel, J. Chem. Soc. Jun., 1993–1998 (1959).
[17] S. Geller and C. E. Miller, Acta Cryst. **13,** 179–186 (1960).
[18] H. J. Van Hook, J. Am. Ceram. Soc. **44,** 208–214 (1961).

[19] A. S. Russell, W. H. Gitzen, J. W. Newsome, R. W. Ricker, V. W. Stowe, H. E. Stumpf, J. R. Wall, and P. Wallace, Tech. Paper No. 10, Aluminum Co. of Amer. 1–65 (1956).
[20] H. M. Richardson, F. Ball, and G. R. Rigby, Trans. Intern. Cer. Congr., 3d Congr., Paris 173–181 (1954).
[21] E. A. Wood, Acta Cryst. **13,** 682 (1960).
[22] I. Warshaw and R. Roy, J. Am. Ceram. Soc. **42,** 434–438 (1959).
[23] S. J. Schneider, to be published in J. Research NBS **65A,** No. 5 (Sept–Oct 1961
[24] V. M. Goldschmidt, F. Ulrich, and T. Barth, Pt IV Skrifter Norske Videnskaps-Akad. Oslo I. Mat. Naturv. K1 No. 5 (1925).
[25] H. C. Stumpf, A. S. Russell, J. W. Newsome, and C. M. Tucker, Ind. and Eng. Chem. **42,** 1398–1403 (1950).
[26] E. N. Bunting, NBS J. Res. **6,** 947–949 (1931).
[27] V. G. Hill, R. Roy, and E. F. Osborn, J. Am. Ceram. Soc. **35,** 135–142 (1952).
[28] V. M. Goldschmidt, T. Barth, and G. Lunde, Pt V, Skrifter Norske Videnskaps-Akad. Oslo I. Mat. Naturv. K1 No. 7 (1925).
[29] V. L. Moruzzi and M. W. Shafer, J. Am. Ceram. Soc. **43,** 367–372 (1960).
[30] J. Cassedanne and H. Forestier, Compt. Rend. **250,** 2898–2900 (1960).
[31] R. S. Roth and S. Hasko, J. Am. Ceram. Soc. **41,** 146 (1958).
[32] I. Warshaw and R. Roy, Abstract Bull. Am. Ceram. Soc. **4,** 169 (1959).
Also: Presentation of paper, 61st Ann. Meet. Am. Ceram. Soc., Chicago, May 19 (1959).
[33] H. S. Yoder and M. L. Keith, Am. Min. **36,** 519–533 (1951).
[34] F. Bertaut and F. Forrat, Compt. Rend. **244,** 96–99 (1957).
[35] J. P. Remeika, Suppl. J. Appl. Phys. **315,** 263–264 (1960).

(Paper 65A4—116)

JOURNAL OF RESEARCH of the National Bureau of Standards—A. Physics and Chemistry
Vol. 65A, No. 4, July–August 1961

Gamma Irradiation of Fluorocarbon Polymers*

Roland E. Florin and Leo A. Wall

(April 10, 1961)

Several fluorocarbon polymers were irradiated with Co^{60} gamma radiation at doses up to 10^{22} ev/g. The polymers studied included polytetrafluoroethylene, polytrifluoroethylene, polychlorotrifluoroethylene, a copolymer of tetrafluoroethylene with hexafluoropropylene, and several rubbery vinylidene fluoride copolymers. *G*-values were measured for volatile products, for free radicals detected by electron spin resonance, and, in the case of polychlorotrifluoroethylene, for scissions. The course of degradation or crosslinking was followed by zero-strength-time and tensile-strength measurements. It was found that for polytetrafluoroethylene and its hexafluoropropylene copolymer the presence of air-accelerated scission drastically. The mechanism of the radiation-induced changes is discussed in terms of free-radical intermediates.

1. Introduction

In spite of their outstanding chemical and thermal stability, fluorocarbon polymers are usually classed among the poorest in resistance to radiation. They are considered to undergo degradation exclusively, and this degradation produces corrosive products [1–6].[1] If we include materials having some hydrocarbon groups, such as perfluoroalkyl-substituted silicones, hexafluorobutyl acrylate, and vinylidene fluoride copolymers, there is, however, a variation in behavior; for example, cross linking can occur [1]. The radiation dose at which most useful properties are lost ranges from a few megaroentgens for polytetrafluoroethylene to over 100 Mr for hexafluoropropylenevinylidene fluoride copolymers.

Aside from the striking contrast between the radiation resistance and the chemical and thermal resistance of these polymers, there are, however, other reasons for questioning the implication of extreme radiation sensitivity. An initial increase in impact strength of polytetrafluoroethylene was reported to take place prior to deterioration [3], and tensile strengths of 50 percent were retained under some circumstances [8] after 50 Mr of radiation. Most practical evaluations are made in the presence of air and moisture at 25 °C; results in vacuum can differ profoundly from these in some instances. Small fluorocarbon molecules studied in sealed containers [9, 10] have been found to be more stable towards radiation when air is absent. Because of the influence of diffusion (of oxygen inward and degradation products outward) the observed effects may depend upon the sample dimensions. Although radiation resistance approaching that of butadiene-styrene rubbers, marginally usable after a dosage of 10^3 Mr, is hardly to be expected of fluorocarbon materials, they may be superior in special combinations of dose, temperature, and environment.

More knowledge of the chemical mechanism of the radiation-induced changes was sought in this work by a study of volatile end products, intermediate radicals, and mechanical and flow properties related to molecular weight. Mass spectrometry and electron spin resonance (ESR) appeared adaptable for the first two. The study of molecular weight and cross linking would ordinarily be best conducted by the conventional methods of light scattering, solution viscosity, or swelling. However, since the measurement of any solution property of polytetrafluoroethylene offers extraordinary difficulties and the basic relations with molecular weight have not yet been established for most other fluorocarbon polymers, most reliance in this study was placed upon the semiquantitative indications furnished by tensile strength and zero-strength-time (ZST) determinations.

2. Experimental Procedure

The polymers studied were:

(1) PTFE (Polytetrafluoroethylene)
(2) TFE-HFP (Copolymer of tetrafluoroethylene and hexafluoropropylene)
(3) PCTFE (Polychlorotrifluoroethylene)
(4) PTrFE (Polytrifluoroethylene)
(5) CTFE-VF (Copolymer of chlorotrifluoroethylene and vinylidene fluoride)
(6) HFP-VF (Copolymer of hexafluoropropylene and vinylidene fluoride)
(7) PTFS (Poly-α, β, β-trifluorostyrene)
(8) PPFS (Poly-2,3,4,5,6-pentafluorostyrene)

Most of these polymers were supplied commercially; however, PTrFE was prepared in the laboratory in an aqueous persulfate system at 60 to 80 °C, PPFS was prepared in the laboratory, and the PTFS was supplied by R. S. Corley of Polaroid Corp.

*Based on research sponsored by the Aeronautical Research Laboratory, Wright Air Development Center, Wright-Patterson Air Force Base, Ohio.
[1] Figures in brackets indicate the literature references at the end of this paper.

Available analytical data on the copolymers are shown in table 1.

The radiation facility was a 2,000-curie Co^{60} source having an exposure dose rate near 0.5×10^6 R/hr. Methods for calculating the absorbed dose have been described [10]. Doses were in the range 1 to 200×10^6 R, and irradiations were made usually at a temperature of 20 ± 2 °C.

TABLE 1. *Copolymer compositions*

Copolymer	C	H	C	F	Monomer
	wt %	*wt %*	*wt %*	*wt %*	*Mole %*
PTFE-HFP					11%HFP
HFP-VF					
found	32.2	2.4	0	64.4	18%HFP
calc	32.8	2.1	0	65.1	
CTFE-VF (high Cl)					
found	27.0	1.3	15.5	52.5	44%CTFE
calc	27.6	1.3	17.9	53.3	
CTFE-VF (low Cl)					
found	29.6	1.7	11.3	56.4	30%CTFE
calc	30.1	1.8	13.4	54.8	

For observations of volatiles, about 0.1 g of the polymer was used in powered form, if possible, in an evacuated hard glass tube lined with foil of aluminum, silver, or nickel. Tubes were evacuated to pressures less than 10^{-4} mm of Hg before being sealed off. There was usually a delay of weeks to months before examination by mass spectrometer; thus any post-irradiation effects had generally taken place before the analysis was made. However, the effect of post-irradiation heating was studied for PTFE. The samples for zero-strength-time tests (ZST) [11, 12] were ordinarily pressed from molding powder, at the specified time and temperature, to the standard thickness and cut to usual size and notched shape. The ZST specimens of TFE-HFP copolymer were cut from commercial sheets of 0.060 in. and 0.040 in. thicknesses. Specimens were sealed in glass tubes, either in vacuum or in air, for the irradiation. The irradiated specimens were opened immediately before testing. Two to five replicate specimens were included in each tube. The conditions for molding and for the ZST determination are shown in table 2. Some specimens irradiated in air, rapidly became too fragile to handle; in other cases, supplementary ZST determinations were made upon weaker specimens at full cross section without notches.

TABLE 2. *Molding and ZST conditions* [a]

Polymer	Mold temperature	Time of heat	Time of press.	ZST temp
	°C	*min*	*min*	*°C*
PCTFE	260	4	2	250
TFE-HFP				280
CTFE-VF (high Cl)	177	5	15	214
CTFE-VF (low Cl)	163	5	15	211
HFP-VF	127	3	10	120

[a] Spacers 0.075 in.; test strip 2 in. long, 0.187 in. wide, 0.062 in. thick, except TFE-HFP copolymer, 0.060 and 0.040 in. thick; notch 0.047 in.

Samples for ESR measurements were usually cut in the form of a movable plug, sealed in 5-mm glass tubes after many hours of evacuation, and observed after briefly heating one end of the irradiated container to remove the signal due to glass, while cooling the other end with liquid nitrogen. PTFE samples were heated during evacuation, in some instances to 400 °C. Powdered or rubbery samples or those to be observed at very low temperature, were sealed in thin-walled tubes of Corning No. 7943 fused silica, a special high-purity grade prepared by a vapor-phase process. The signal from irradiated containers of this material is sharp and narrow, and its interference can often be ignored or corrected for. ESR observations were made with a Varian 4500 instrument at frequencies in the neighborhood of 9,000 to 9,600 Mc and fields in the neighborhood of 3,300 gauss. Rectangular cavities operating in the TE 012 mode were used; for low temperatures the cavity had a hole nearly 10 mm in diam and accommodated a Dewar-walled tube carrying a stream of cold nitrogen. Quantitative estimates were made by double integration of the first-derivative curves and comparison with those obtained with copper sulfate pentahydrate or diphenyl picryl hydrazyl.

3. Results

The *G*-values, in molecules per 100 ev, of the volatile products from irradiation of the polymers are shown in several tables: PTFE in table 3; copolymer TFE-HFP in table 4; PCTFE in table 5; PTrFE in table 6; and copolymer HFP-VF in table 7. All irradiations in these tables were made at 20 ± 2 °C in vacuum.

TABLE 3. *G-values of volatile products from polytetrafluoroethylene* [a]

Dose, (ev/g)$\times10^{-20}$	34.2	34.2	68.9	68.9	184	184	184
Container and treatment [b]	N	NP	N	NP	G	GQ	GR
SiF_4	0.16	0.12	0.16	0.31	0.15	0.21	0.005
CO_2	.12	.13	.11	.11	.06	.12	.02
CF_4	.004	.009	.007	.007	.009	.005	.006
C_2F_6	0	0	0	0	tr.	.007	0
C_2F_4	0	0	0	0.006	0	0	0
C_4F_8	0	0	0	.004	0	0.005	0
Total gas	0.32	0.31	0.30	.30			

[a] In powder form.
[b] Symbols:
G—glass tube, no liner;
N—nickel foil wrapper;
P—postheated 400 °C, 20 min;
Q—postheated 300 °C, 30 min;
R—further increment produced by air and heat; irradiated sample was opened to air, re-evacuated, then heated at 310 to 320°, 15 min.

TABLE 4. *G-values of volatile products from a tetrafluoroethylene-hexafluoropropylene copolymer* [a]

Dose, (ev/g)$\times10^{-20}$	9.0	34.4	34.4 [b]	69.3 [b]
SiF_4	0	0	0	0.0005
CO_2	0.022	0.008	0.026	.011
CF_4	.063	.085	.089	.113
C_2F_6	0	0	.005	.001
C_4F_8	0	0	.018	.022
C_3F_{12}	0	0	.006	.011
Total	0.102	0.107	.156	.169

[a] Beads of polymer, glass tubes, nickel foil liners.
[b] Heated after irradiation 280 °C, 15 min.

TABLE 5. *G-values of volatile products from polychlorotrifluoroethylene* [a]

Dose, (ev/g)×10⁻²⁰	21.8	66.1	66.1 [c]
Total gas [b]	0.11	>0.13	>0.14

[a] Glass tubes, silver foil wrapper.
[b] Mainly unidentified C, Cl, F compounds having up to 5 C and 2 Cl; no SiF_4; no Cl_2; little CO_2.
[c] Heated after irradiation 250 °C, 15 min.

TABLE 6. *G-values of volatile products from polytrifluoroethylene* [a,c]

Dose, (ev/g)×10⁻²⁰	12.2	39.5	67.3	67.3 [b]
SiF_4	0.668	0.767	0.864	0.94
CHF_3	.018	.025	.016	.029
CO_2	.092	.098	.113	.123
CO	.243	.147	.137	.14
H_2	.028	.033	.120	.091

[a] In powder form, glass tubes, aluminum foil wrapper.
[b] Heated after irradiation 100 °C, 1 hr.
[c] All samples also showed unidentified fragments of mass 82, but different from CF_2CFH.

TABLE 7. *G-values of volatile products from a hexafluoropropylene-vinylidene fluoride copolymer* [a]

Dose, (ev/g)×10⁻²⁰	9.23	35.1	35.1 [b]
SiF_4	0.29	>0.30	>0.26
CO_2	.091	>.011	>.007
H_2	.27	>.17	>.11
CF_4	.045	>.031	>.025
C_2F_6	.01	0	0
Total gas	.86	>0.54	>0.43

[a] Shreds of polymer, glass tubes, nickel foil liners.
[b] Heated after irradiation 100 °C, 30 min.

Evidence relative to molecular weight degradation and/or cross linking caused by high-energy radiation was obtained by zero-strength-time (ZST) measurements. No data were secured for PTFE. For PCTFE the molecular weight data derived from ZST-molecular weight correlations [11, 13, 14] are shown in table 8 and in figure 1. Correlations are not available for the other polymers, and the plots are of log ZST, which in general should have a linear relationship with molecular weight [11, 13]. The ZST data for TFE-HFP copolymer are given in table 9 and figure 2; for HFP-VF copolymer in table 9 and figure 3; and for two grades of CTFE-VF copolymer in table 9 and figure 4. All irradiations were made at 20±2 °C. The ZST data for PCTFE show a good linear relationship between the reciprocal of the number-average molecular weight, $1/M_n$ and the radiation dose, indicating a rather constant G(scissions) of 0.67, i.e., nearly 0.67 scissions per 100 electron-volts of energy absorbed from the radiation, independent of the presence of air. The scatter of individual determinations was of the order of 5 percent, in agreement with earlier experience [11, 13.] The G(scissions) is low compared to values for typical degrading polymers such as polymethyl methacrylate (PMMA) and polyisobutylene (PIB), for which G(scissions) are 1.6 and 5, respectively [15, 16]. The insensitivity to air is surprising in view of the great sensitivity of PTFE (in tensile tests [8]) and of the TFE-HFP copolymer (fig. 2) and the definite air sensitivity of the copolymer HFP-VF (table 9).

TABLE 8. *ZST and molecular weight data of irradiated polychlorotrifluoroethylene* [a]

Lot	Dose	ZST	M_n [b]
	ev/g×10⁻²⁰	sec	
A [c]	0	307	352,000
	0.198	250	314,000
	.602	197	271,000
	1.54	153	217,000
	3.71	111	150,000
A [d]	0.198	241	311,000
	.602	215	286,000
	1.54	139	196,000
	3.71	108	144,000
B [c]	0	347	373,000
	0	[e] 935	
	5.6	90	137,000
	5.6	[e] 146	
	27.8	[e] 95	([f] 50,000)
	72.3	[e] 70	([f] <10,000)

[a] ZST measured at 250 °C on standard notched strip [12, 13] unless otherwise indicated.
[b] From correlation chart [11, 13, 14].
[c] Irradiated in vacuum.
[d] Irradiated in air.
[e] ZST on whole strip without notch.
[f] Long extrapolation from chart.

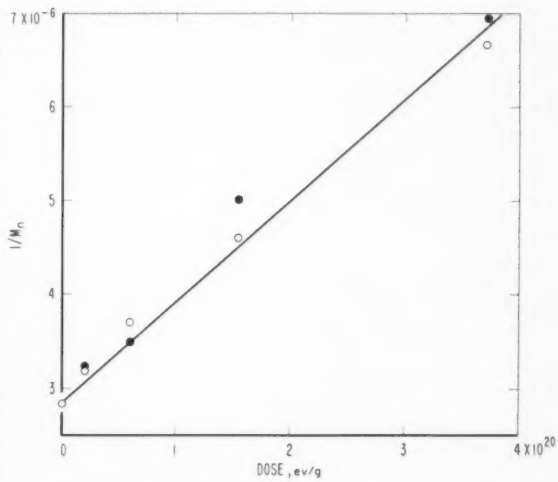

FIGURE 1. *Loss of molecular weight of polychlorotrifluoroethylene during irradiation.*

○, irradiated in vacuum.
●, irradiated in air.

Excepting possibly PTFE (for which ZST was not studied here) PCTFE was the only polymer in the group to show only scission. All the others, including even the pure fluorocarbon TFE–HFP copolymer, showed a period of rising ZST in the region up to 1–10×10²⁰ ev/g, after which degradation usually began to dominate, as indicated by a gradual lowering of ZST. The approach to the maximum ZST is not a convenient measure of gel-point phenomena, as prohibitively high ZST's, complicated by attendant thermal degradation of the sample, are reached

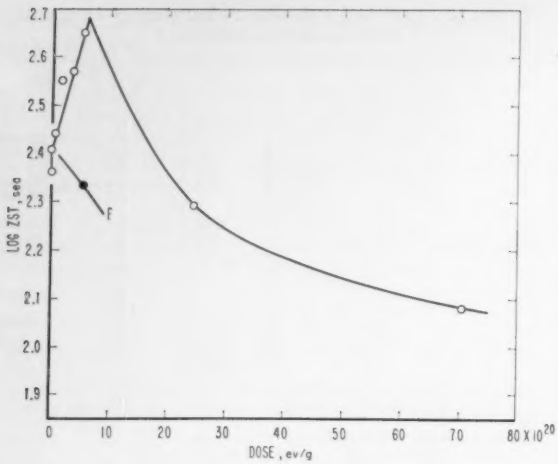

FIGURE 2. *Zero-strength-time of irradiated copolymer tetrafluoroethylene-hexafluoropropylene.*

○, irradiated in vacuum.
●, irradiated in air.
F, too weak to handle after 24×10^{20} ev/g.

TABLE 9. *ZST values of irradiated polymers*

Polymer	Dose	ZST
	ev/g $\times 10^{-20}$	*sec*
TFE-HFP [a,e]	0	256
	0.197	232
	.600	276
	1.54	243
	3.69	371
	5.52	448
	24.4	195
	70.6	[d] 123
TFE-HFP [b,e]	5.57	218
	24.4	(c)
HFP-VF [a,f]	0	356
	0.202	749
	.384	3275
	[g] .384	4030
	.616	49000
	5.72	[h] >260000
	28.4	[h] >260000
	74.0	[h] >260000
HFP-VF [b,f]	0.202	523
	.384	1080
	.616	3639
CTFE-VF [a,i] (15.5% Cl)	0	1001
	5.69	172
	28.2	21.6
	73.6	8
CTFE-VF [b,i] (15.5% Cl)	0.201	901
	.612	5988
	3.77	3330
CTFE-VF [a,i] (11.3% Cl)	0	960
	5.72	[h] >216000
	28.4	723
	74.0	67.6
CTFE-VF [b,i] (11.3% Cl)	0.202	[h] >6700
	3.79	[h] >80000

[a] Irradiated in vacuum.
[b] Irradiated in air.
[c] ZST at 280±0.5 °C. Thickness 0.060 in., or 0.040 in. converted to 0.060 in. basis.
[d] Rather brittle.
[e] Friable; could not be handled.
[f] ZST at 120°±0.5 °C.
[g] Heated after irradiation at 100 °C for 0.5 hr.
[h] No break; abandoned at time indicated.
[i] ZST at 214°±1 °C.

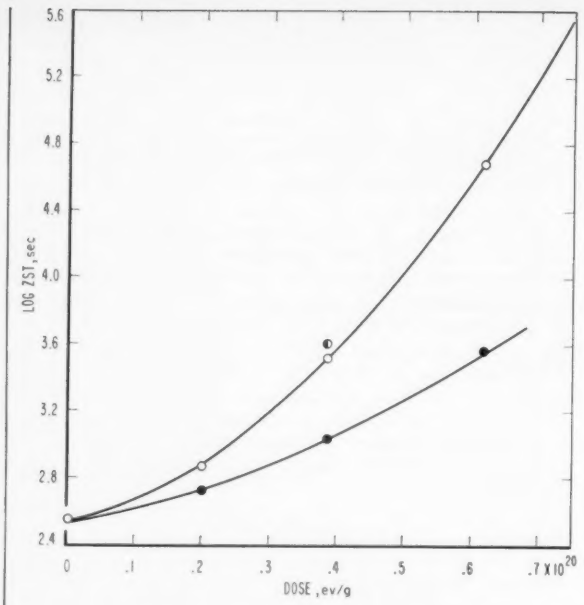

FIGURE 3. *Zero-strength-time of irradiated copolymer hexafluoropropylene-vinylidene fluoride.*

○, irradiated in vacuum.
◐, irradiated in vacuum, postheated 100 °C, 30 min.
●, irradiated in air.
Log ZST greater than 5.4 at doses of 5.7 and 74×10^{20} ev/g in vacuum.

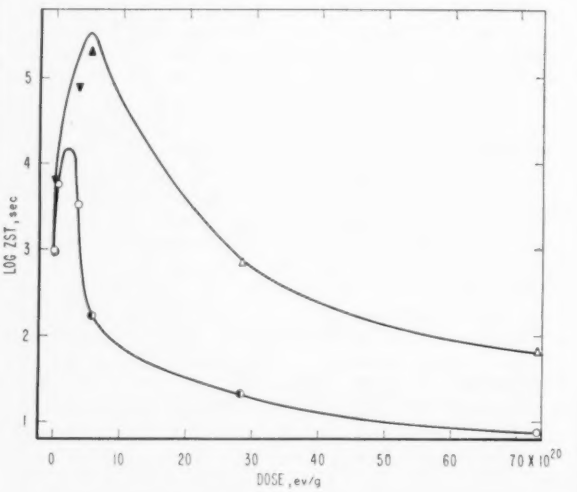

FIGURE 4. *Zero-strength-time of irradiated copolymers chlorotrifluorethylene-vinylidene fluoride.*

○, high chlorine content in air.
◐, high chlorine content in vacuum.
▲, low chlorine content in air.
△, low chlorine content in vacuum.
▼▲, no break at time indicated.

without any sharp break in the rising ZST curve. From the theory of crosslinked networks it appears unlikely that a sudden break in ZST should be expected. In the cross linking systems, ZST test specimens subsequent to the maximum often showed a transverse fracture rather than a fine drawn-out thread, and the scatter of individual determinations then became great, specimens within a small tube showing deviations of 50 percent. This phenomenon has been observed before [17], although not explicitly associated with cross linking. Some samples at high dose (table 9), despite a relatively high ZST, were quite brittle and required careful handling. Among the CTFE–VF elastomers, the relative rate of degradation was evidently much greater in the material of high chlorine content. If the difference in chemical analysis is due solely to monomer ratio in the copolymer, the change from about 30 to 44 mole-percent CTFE is accompanied by a drastic increase in ease of scission. Samples of irradiated PTrFE and PTFS, although not examined by ZST, appeared to cross link, as evidenced by swelling and insolubility in pyridine and methyl ethyl ketone.

The results on volatile products are subject to serious scatter; in some cases a given product is reported less abundant after a post-irradiation heating than before it, and inconsistencies approaching twofold appear for products of low yield, for example, CF_4 in table 3. Heating after irradiation had little demonstrable effect on yields of volatiles; however, a few products of higher molecular weight, absent before heating, appeared in trace amounts afterward, for example, C_4F_8 in table 3.

A major product was usually SiF_4; however, PCTFE and the copolymer TFE–HFP yielded none. In the copolymer the absence of SiF_4 may have been due to restricted diffusion of F atoms or other fragments from the polymer sample, which was in the form of 2-mm beads. The SiF_4 was accompanied by CO_2 of uncertain origin; CO may also have been present but was indistinguishable from small contaminations by atmospheric N_2 during analysis. Possible sources of the CO_2 are from the reactions of fluorocarbon radicals or unstable molecules with the glass walls of the vessel; carboxylic end groups in the polymer; or attack on radicals or double bonds by O_2 indirectly produced from container walls.

$$2\text{—Si—O—M}\rightsquigarrow\rightarrow 2\text{—Si—}+O_2,$$

or

$$2F_2+SiO_2\rightarrow SiF_4+O_2.$$

Since the use of loose metal-foil wrappers did not appreciably diminish the yields of SiF_4 and CO_2 (table 3), the formation of these products from radicals appears unlikely, as the species responsible has long enough life to diffuse through folds of the wrapper.

There is some uncertainty about the origin of H_2 from hydrogen-containing polymers. Possible sources are direct production from the polymer by an atomic or molecular mechanism, or reaction of initially produced HF with metal-foil wrappers. The reaction of HF with dry metal surfaces seems unlikely, however, and possibly all the H_2 recorded arises from the polymer.

In addition to the mass spectrometric determinations, HCl and a trace of Cl_2 were identified qualitatively from one tube of irradiated CTFE–VF copolymer; SiF_4 and H_2 may also have been present, and the pressure of more than one atmosphere would correspond to a total gas G-value in the neighborhood of 2 to 4.

No polymer yielded monomer as an important product. Some confusion was possible in the mass spectra of products from PTFE and PTrFE, where peaks were identified corresponding to the monomer mass numbers of 100 and 82, respectively; but in these instances the remainder of the mass spectrum was incorrect for the monomer, and the peaks in question were due to other products. Very small amounts of C_2F_4 corresponding to $G=0.006$ appeared from PTFE irradiated to 68.9×10^{20} ev/g and then heated at 400 °C for 20 min (table 3); and C_3F_6 equivalent to $G=0.005$ was present in irradiated TFE–HFP copolymer heated to 280 °C (table 4). A little C_3F_6 was also observed from the HFP–VF copolymer (table 7).

Both PTFE and PCTFE yielded numerous unidentified halocarbon products; however, the total of all volatile products was small, as the values of G (total gas) indicate (tables 3 and 5). In irradiated PTFE some material sublimes at 300 °C, producing a faint white ring, suggesting the presence of some products of intermediate molecular weight.

Any trend in the production of CF_4 from PTFE was obscured by the large scatter; the G-values were in the range 0.004 to 0.009 for doses up to 1.84×10^{22} ev/g, which are lower on the average than Charlesby's values [18] and do not seem to fit his dose-dependence formula requiring a regular linear increase from $G=0$ initially to $G=0.050$ at 1×10^{21} ev/g. At very high doses agreement might improve. The observations of Charlesby do not exclude some C_2F_6 and may have an uncertainty of nearly twofold based on uncertainties in the dosimetry.

ESR spectra for PTFE, TFE-HFP copolymer, PCTFE, PTrFE, PTFS, and PPFS are shown in figure 5, and data on yields and spacings are given in table 10. The rubbery VF copolymers had no ESR spectrum, at least when irradiated at room temperature. The spectra of the styrenes and of PTFE are shown only for comparison; the styrenes have been discussed elsewhere [19], and the ESR spectrum of PTFE has been investigated extensively by other workers [20–23], the more recent of whom are in essential agreement, except as to yield. All the spectra are quite broad. PTFE alone has a sharply resolved hyperfine structure (*hfs*), but the PTFE–HFP copolymer is similar in many respects, the main differences being associated with the poorer resolution. Figures 6 and 7 show the accumulation and decay of radicals in irradiated TFE–HFP copolymer. Single irradiations of PTFE were made at 77 °K and 4.2 °K; at 77 °K the *hfs* was lost by broadening, as

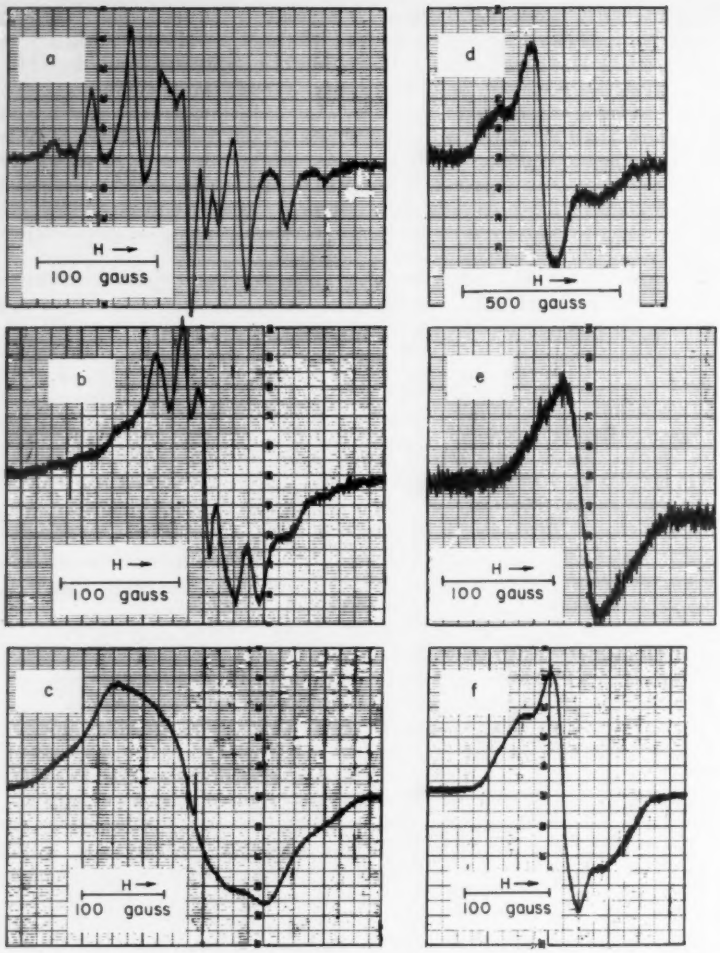

FIGURE 5. *Electron spin resonance spectra of irradiated fluorocarbon polymers.*

a. Polytetrafluoroethylene.
b. Tetrafluoroethylene-hexafluoropropylene copolymer.
c. Polytrifluoroethylene.
d. Polychlorotrifluoroethylene.
e. Poly-2,3,4,5,6-pentafluorostyrene.
f. Poly-α,β,β-trifluorostyrene.

mentioned by Voevodskii [21]; at 4.2 °K the main spectrum was distorted by relaxation effects and two hydrogen atom lines appeared, the origin of which could have been either in the container or in hydrogen-containing impurities such as soap.

4. ESR Spectra

The ESR spectra clearly show the presence of free-radical species, but, of course, yield no information as to their role in the mechanism of the chemical changes. The radical concentrations are known approximately, and the *hfs* gives clues to the identity; however, most of the identifications in polymers are tentative because of the possibility of unresolved or faint *hf* components.

For the radicals in irradiated PTFE all recent workers find an ESR spectrum of 10 lines (rarely 11) covering 225 gauss [20–22], in essential agreement with figure 5a. Earlier reported experiments indicated three lines [24], eight lines [25], or else no spectrum until air had been admitted [26]. The spectrum is very reasonably attributed to the secondary radical $\sim CF_2\dot{C}FCF_2 \sim$, where the *hf* interaction is with one α and four equal β fluorines [20]. There is no indication of any primary radicals $\sim \dot{C}F_2$, which would be intermediates in chain scission. A possible explanation is that pairs of primary radicals, if formed by C—C scission, are held in a cage until they recombine, while fluorine atoms that split off during formation of secondary radicals can diffuse away more easily because of their small

TABLE 10. *ESR data from irradiated fluorocarbon polymers*

Polymer	Number of peaks	Spacings	Width overall	Yield, G(R)
		Gauss [a]	*Gauss*	*Radicals/ 100 ev*
PTFE [b]	[c] 10 or 11	−96, −67, −40, −18, −13, (−3, +4) +13, +23, +42, +71, +97	220	0.15, 0.19
TFE-HFP [b]	11	−88, −67, −40, −20, −11, (−5, +2), +12, +22, +40, +67, +93	220	1.1
PCTFE [d]	3	−100, (−5, +5), +100	350	0.99
PTrFE [d]	[e] 5	−171 [e], −94, (−29, +29) [e], +94, +156 [e]	425	.74
PTFS [d]	3	−52, (−18, +19)+51	220	.57
PPFS [d]	1		140	.11

[a] Derivative peak locations; pair in parentheses due to single center component.
[b] Irradiated at 20 °C.
[c] Varies with orientation, identity and age.
[d] Irradiated at −80 °C; observed at 25 °C.
[e] Very weak shoulders.

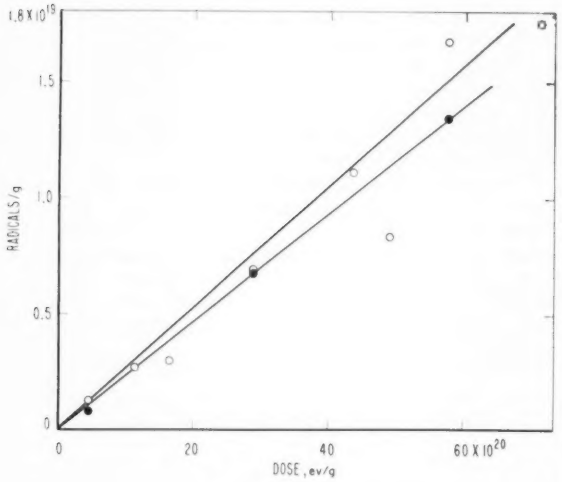

FIGURE 6. *Accumulation of radicals in irradiated polytetrafluoroethylene.*

○, stored 1 to 10 hr at 77 °K, error ±50 percent.
●, stored 5 mo at 300 °K, error ±20 percent.

size. The resolution of *hfs* is very good for a polymer at room temperature, but reversibly broadened out at 77 °K; the broadening is no doubt caused by the loss of motional freedom on cooling, in agreement with NMR studies [27]. The $\sim CF_2\dot{C}FCF_2 \sim$ radicals need not undergo scission and may form cross links.

The radicals combine readily with oxygen and several other agents, as might be expected of a free radical [20]. The peroxy radical has a much narrower spectrum than the parent fluorocarbon radical. There is some recent evidence that the combination with oxygen is partially reversed by heating, and that two kinds of peroxy radicals may exist [22].

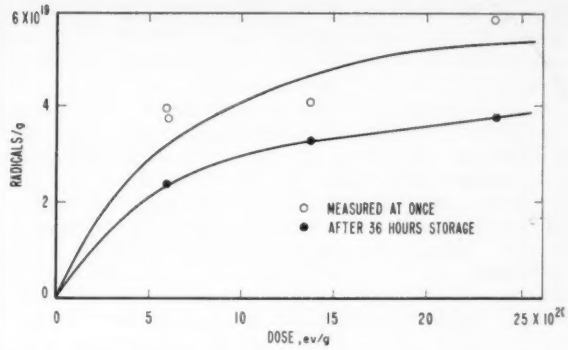

FIGURE 7. *Accumulation of free radicals in irradiated copolymer tetrafluoroethylene-hexafluoropropylene.*

○, stored 1 to 5 hr at 77 °K.
●, stored 36 hr at 300 °K.

The yields of radicals, $G(R) = 0.16$ to 0.19 for PTFE and $G(R) = 1.1$ for HFP copolymer, are comparable with the yields of volatile products, and the decay is quite slow (figs. 6 and 7). For PTFE the buildup of concentration was linear with dose to 64×10^{20} ev/g at least. The G-value, growth curve, and decay rate conflict somewhat with Watanabe's results from deuteron bombardment [23], where the initial G-value appears to be as low as 0.05 and the leveling off of radical concentration at higher doses fits a first-order decay constant of 2.8×10^{-3} sec^{-1}. It seems likely that Watanabe's low $G(R)$ may be due to a high local temperature and linear energy transfer associated with deuteron beams, and that the large first-order decay constant applies only while the irradiation is in progress.

Watanabe has suggested two mechanisms for a first-order disappearance: $\sim CF_2\dot{C}F_2 + \dot{C}F_2CF_2 \sim$ (in cage) $\longrightarrow \sim CF_2CF_2CF_2CF_2 \sim$ and $\sim CF_2\dot{C}F \sim \longrightarrow \sim CF{=}CF \sim + \dot{F}$. In the TFE–HFP copolymer the growth curve levels off (fig. 7), and a moderately rapid decay occurs initially. Both the more rapid decay and the greater diffuseness of *hfs*, compared with PTFE, may be attributed to lower crystallinity; some of the differences may also be due to the superposition of several radical spectra; for example,

$$\sim CF_2\dot{C}CF_2 \sim \quad \text{and} \quad \sim CF_2\dot{C}FCF_2 \sim$$
($\dot{C}F_3$ and $\dot{C}F_2$)

In irradiated PCTFE the initial $G(R)$ of about 1.0 is comparable with the estimated $G(\text{scissions}) = 0.67$ and much less than the $G(F^-)$ and $G(Cl^-)$ [5] of polymer irradiated in aqueous alkali and air. Previous studies indicated either no detectable radicals [26] or an *hfs* of several unresolved lines [28] if irradiated *in vacuum*, and a $G(R)$ of 0.5 [26] if exposed to air during or after irradiation. The three-peak structure here is too diffuse to support conjectures as to identity. The most favored radical energetically should be $\sim CF_2\dot{C}FCF_2CFCl \sim$

formed by removal of chlorine; it should have the same *hfs* as the radical from PTFE. In the ~~$CF_2\dot{C}FCF_2$~~ radical of PTFE, as analyzed by Rexroad and Gordy [20], the α fluorine interaction is 92 gauss and the β interaction 33 gauss. A radical ~~$CFCl\dot{C}F_2$~~ would have the requisite two α fluorines to produce the 3-peak structure with 100-gauss separation; the smaller splittings by the β fluorine could be obscured. Such a radical could be formed by a primary C—C scission or also by the breaking of an initial secondary radical formed by C—F splitting.

$$\sim\!CF_2CFCl\dot{C}FCFClCF_2CFCl\sim\!\longrightarrow$$

$$\sim\!CF_2CFClCF{=}CFCl+\dot{C}F_2CFCl\sim\!$$

The initial radical shown in this equation, although requiring more energy for formation, could be favored by greater mobility of the F atom removed. The diffuse spectrum actually found is compatible with the simultaneous existence of several kinds of radicals.

In the other irradiated polymers, as in PCTFE, the radical spectra are too diffuse to be very helpful for identification; the yields are moderately large in PTrFE and PTFS but very small in PPFS, suggesting stabilization against bond rupture by the pentafluorophenyl ring.

Besides the evidence for radicals, there are, in the literature, indications of the transient existence of both charged species and excited states. A temporary increase in electrical conductivity occurs during the irradiation of PTFE [7, 29, 30] and PCTFE [31], and persists for hours afterward, disappearing more rapidly at higher temperatures. A very weak phosphorescence also appears upon warming PTFE irradiated in vacuum at 77 °K [29]. The chemical importance of the species concerned is doubtful, and no definite speculations have been made regarding the emission process, nor is anything known of the identity, mobility, and concentration of the current-carrying species. Speculations have been made, however, concerning the possible role of ions in fluorocarbon radiation chemistry [32]. In irradiated PTFE the identification of the radicals as ~~$CF_2\dot{C}FCF_2$~~ is reasonably sure, and much of the known radiation behavior of the polymer can be explained in terms of them.

5. Products of Irradiation

Recent experiments on the irradiation of small fluorocarbon molecules do not indicate abnormally high G-values for products. The rapid polymerization of TFE and of CTFE by γ-rays may seem an exception, but in view of the high molecular weight of the polymer the *G*-value for initiation is not necessarily high. Gamma rays affect C_3F_6 remarkably slowly, and high polymer is not formed [33]. When perfluoroheptane is irradiated in vacuo in dry aluminum containers, scission products are present in small amounts only, no corrosion or inorganic fluoride is seen, and the irradiated material contains coupling products [9, 10]. In nickel tubes with glass capillary ends, small amounts of SiF_4 are seen also [10]. A few of the *G*-values of products from C_7F_{16} are given in table 11. Low *G*-values of products were found in CF_4 mixtures [32, 34]. From CF_4 mixed with C_6H_6, the *G*-values of C_6H_5F and $C_6H_5CF_3$ together amounted to about 1.

TABLE 11. *G-values of products from perfluoroheptane*

Product	G	Reference
C_7F_{16} (disappearance)	3.0	9
F	0	9
SiF_4	0.17	10
CF_4	.19	10
CF_4	0	9
C_2F_6	0.08	10
$<C_7$	~1	9
$>C_7$	~2	9
$\sim C_{11}$–C_{13}	1	9
C_{12}–C_{16}	2	10

The polymers studied fall into two distinct groups: (a) the hydrogen-containing polymers, which evolve HF or HCl and cross link rapidly, and (b) the pure halocarbon polymers, which cannot evolve HF or HCl and cross link more slowly, if at all. A special class may be constituted by the silicones containing perfluoroalkyl groups, which the literature reports to be quite sensitive to radiation [35].

Haszeldine has prepared copolymers of CF_3NO and C_2F_4 [36] and polymers of $CF_2{=}CF{-}NO$ [37], which show promise as elastomers. He has also prepared an unsaturated thermally stable polymer of structure $-CF{=}N-$ [37]. Although radiation stability of the first polymer would presumably be low, no data are available on these polymers or their analogs.

Fluoroaromatic polymers of several types have been made in small quantities. Representative types include PTFS (fluorocarbon main chain and hydrocarbon ring), PPFS (hydrocarbon chain an fluorocarbon ring), and polyperfluoropolyphenyl (perfluoroaromatic rings linked directly). The thermal stability of the latter two polymers appears to be good [38, 39]. Further aromatic systems such as perfluorophenylene ethers may be possible. Irradiation of the prototype molecule C_6F_6 resulted in coupling to form polymer as the main reaction, and produced almost no inorganic fluoride or small molecules [10]. The triazine polymers developed by H. C. Brown [40] have a quasi-aromatic ring structure, and some examples are thermally stable [38], but no radiation data are known. Among the pure halocarbon polymers, PTFE offers special problems and will be considered later.

5.1. PCTFE

For PCTFE the radiation resistance in terms of physical properties was rated low, similar to PTFE [3, 5]. There were high yields of ionic products from irradiations in dilute alkali and air; $G(F^-){=}G(Cl^-){=}3.5$, approximately [5]. In the present study an uncomplicated scission process seems established,

with constant G (scissions) of 0.67 (see fig. 1). This value is not high compared to those of such polymers as PMMA. The absence of SiF_4 from irradiated PCTFE (table 8) is curious and could be due to the easier breaking of C—Cl bonds. The low yields of any volatile products in vacuum irradiation contrast with the very high and equal yields of Cl^- and F^- for irradiations in the presence of water and oxygen [5]. A smaller discrepancy also exists between F^- yields from PTFE in aqueous and evacuated systems [4, 41, 42] (see table 12).

TABLE 12. *G-values of products from polychlorotrifluoroethylene and polytetrafluoroethylene*

Product	Condition	PCTFE	PTFE
Cl^-	in aq. alkali	3.5 [5]	
Cl	in vac	0 (table 5)	
F^-	in aq. alkali	3.5 [5]	2.0, 0.66 [4]
F	in vac (as SiF_4)	0 (table 5)	0.48 to 0.82 (table 3)

For PCTFE in vacuum, possible reactions are:

$$\sim CF_2CFClCF_2CFCl \sim \rightarrow \sim CF_2\text{—}\dot{C}F\text{—}CF_2CFCl \sim + Cl\cdot$$

$$\sim CF_2\text{—}\dot{C}F\text{—}CF_2CFCl \sim \longrightarrow \sim CF_2\text{—}CF{=}CF_2 + \sim \dot{C}FCl$$

$$\sim \dot{C}FCl + Cl\cdot \longrightarrow \sim CFCl_2$$

$$\sim \dot{C}FCl + \sim CF_2CFClCF_2 \longrightarrow \sim CF_2\dot{C}FCF_2 + \sim CFCl_2$$

If air and water are present, the radicals can be converted to peroxide radicals and ultimately hydrolyzed:

$$\sim \underset{Cl}{\overset{F}{C}}\cdot \xrightarrow{O_2} \sim \underset{Cl}{\overset{F}{C}}\text{—}O\text{—}O\cdot$$

$$\xrightarrow{H_2O} \sim \underset{Cl}{\overset{F}{C}}\text{—}O\text{—}O\text{—}H \xrightarrow{OH^-}$$

$$\sim \underset{Cl}{\overset{F}{C}}\text{—}O\text{—}O^-, \xrightarrow{OH^-} \sim \overset{O}{\overset{\|}{C}}\text{—}O^- + F^- + Cl^-.$$

In PTFE irradiated in air the reported development of appreciable water absorption [4] may be due likewise to the formation of carboxylic acid groups. The curious insensitivity of the PCTFE molecular weight to the presence of oxygen during irradiation may be due to the relative stability of peroxide radicals of this form, at least in the absence of water and alkali, or to the fact that the molecular weight drop is already occurring so rapidly in the absence of air.

5.2. Hydrogen-Containing Polymers

Polymers containing hydrogen have previously been found to undergo the changes associated with cross linking: vulcanization at 10 Mr or less [43, 44, 45], followed by a slow loss in elongation [46]. Copolymers of HFP and VF have marginal utility at 100 Mr according to evaluation studies. Similar results are shown for the PCTFE–VF copolymer and for perfluorodihydroacrylate polymers. The specific data quoted by Harrington [35, 46] at 100 Mr indicate a loss in tensile no greater than 36 percent for any of these three polymers, but about 85 percent loss of elongation for the acrylate and the HFP–VF copolymer.

In most of these hydrogen-containing polymers the evolution of hydrogen fluoride was observed qualitatively. Small molecules containing hydrogen as well as fluorocarbon groups have hardly been studied at all under irradiation; however, mixtures of fluorocarbons with hydrocarbons evolve hydrogen fluoride in large amounts [10], and the evolution of hydrogen fluoride is also reasonably expected if the hydrogen and fluorine are in the same molecule, as in VF. For fluorine-containing polymers the evolution of the highly stable molecule HF should be associated with cross linking as H_2 is for polyethylene.

The predominance of cross linking is shown by the trend of the ZST curves, figures 3 and 4. The associated high G(HF), (tables 6 and 7) and the implicit high G(HCl) are not surprising. Despite the well-developed cross linking, scission ultimately dominates. The greater tendency to scission (or smaller cross linking tendency) of the CTFE–VF copolymers is evident, especially for the copolymer of high Cl content. The HFP copolymer evolves a certain amount of C_3F_6, CF_4, and H_2, despite the competition of cross linking and HF evolution processes. For this class of polymers, especially the HFP–VF copolymer, it is interesting to note that long retention of useful properties [46] is not forbidden by a high rate of evolution of corrosive products.

In PTrFE the production of CF_3H is surprising. A possible but unconvincing route to it could exist in a mechanism similar to those quoted for CF_4 from PTFE [41, 42, 47]. For PTFE, either of the following reactions gives CF_4:

(1)
$$\sim \underset{F}{\overset{F}{C}}\text{—}\underset{F}{\overset{F}{C}}\text{—}\underset{F}{\overset{F}{C}}\cdot + F\cdot \longrightarrow$$

$$\left[\sim \underset{F}{\overset{F}{C}}\text{—}\underset{F}{\overset{F}{C}}\text{—}\underset{F}{\overset{F}{C}}\text{—}F\right]^* \longrightarrow$$

$$\sim \underset{F}{\overset{F}{C}}\text{—}\underset{F}{\overset{F}{C}}\cdot + FC\cdot \longrightarrow \sim \underset{F}{\overset{F}{C}}{=}\underset{F}{\overset{F}{C}} + CF_4,$$

(2)
$$CF_3\cdot + F\cdot \longrightarrow CF_4.$$

For PTrFE two of the three following reactions produce CF_3H:

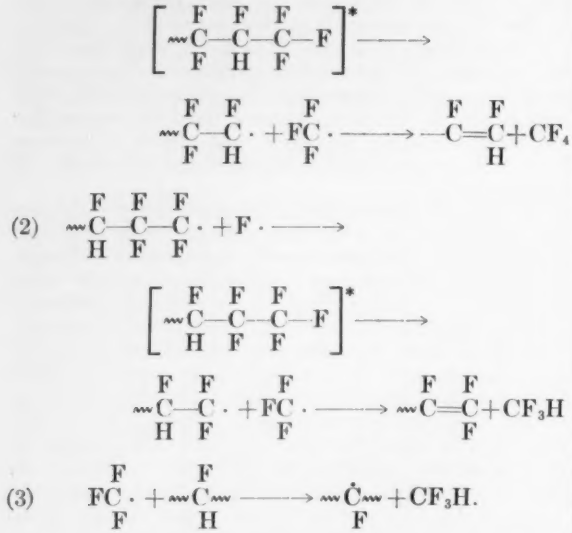

Both the above mechanisms for CF_3H and the high yields of SiF_4 (via HF) are favored by the probable frequent occurrence of head-to-head bonds $\sim CF_2—CFH—CFH—CF_2—CF_2—CFH,\sim$ a consequence of the nearly equal reactivity of the monomer for radical addition at either carbon atom [48].

5.3. PTFE

The radiation stability of PTFE remains an unsettled problem in several respects, although PTFE has been investigated for the longest time. Contributing factors to this situation are the extreme sensitivity to the presence of oxygen during irradiation [8] and the difficulty of measuring the properties related to molecular weight [17,49,50]. The tensile strength of PTFE film irradiated in air drops to zero after a few megaroentgens exposure, whereas with irradiation in vacuum there is an indefinitely long plateau at 50 percent of the original strength. Irradiation of thicker specimens, or irradiation in low vacuum, must show intermediate grades of behavior, depending upon the relation of dose rates, diffusion rates, and oxygen supply. The copolymer of PTFE and HFP, studied by ZST measurements, is also highly sensitive to irradiation atmosphere (table 9, fig. 2), whereas PCTFE is not (table 8, fig. 1).

The course of molecular-weight degradation and cross linking cannot be followed readily by the usual solution methods, as PTFE is insoluble except in special solvents at 320 °C and higher; observations of the usual properties including intrinsic viscosity, light scattering, osmotic pressure, and swelling in solvents have rarely been achieved. A few special molecular-weight methods have been calibrated by reference to end-group analysis as an ultimate standard. The reference standard involves assumptions about polymerization mechanism. Melt viscosity methods are available, but the most consistent methods at present appear to be based upon the density or crystallinity, following a carefully programmed annealing period [51]. In PTFE irradiation, some use has been made of crystallinity and density [41,42,52], but not as explicit measures of molecular weight. In the absence of more significant measurements much work has been done with mechanical properties, including impact strength [2], tensile strength and elongation [28,46], and creep rate [50,53]. The creep rate may have been rather closely connected with melt viscosity, which has been correlated with molecular weight. ZST measurements at 350 °C have been applied and correlated with molecular weight, but the behavior is not typical, and the results scatter badly [17,52,53]. The ZST measurement is more easily applied to the copolymer of TFE with HFP (see Experimental Procedures).

An undesirable feature of tensile strength measurements is that the property is generally sensitive to molecular weight in an intermediate range only, being zero at low molecular weights and reaching an upper limit at high molecular weights [54].

The observed changes of mechanical properties are, (1) a very early increase in impact strength at 3×10^{20} ev/g [2], (2) a loss of most elongation somewhere in the range $0.5–5\times10^{20}$ ev/g [2,46], (3) a loss of tensile strength, which may occur early or not be important until past 30×10^{20} ev/g [8,46], and finally (4) a disintegration of large pieces beginning around 300×10^{20} ev/g [18]. Thin pieces are more resistant to disintegration. The above observations apply to irradiations in which oxygen was usually not of major importance because of evacuation or of sample thickness. Irradiations conducted in air at room temperature caused a very rapid drop in ZST, melt viscosity, and activation energy for flow, and an increase in density and crystallinity [52,53,55].

To summarize, for PTFE specimens irradiated in evacuated containers there are many empirical data on properties but there is no information closely related to molecular weight, whereas for specimens irradiated in air the systematic data related to molecular weight indicate a very rapid degradation, important at doses as low as 0.2×10^{20} ev/g. For the related HFP copolymer the present ZST data are compatible with cross linking and very slow degradation in vacuum, and with very rapid degradation in air (fig. 2).

Volatile and ionic products sometimes show a dependence upon thickness [4,18] or upon storage after irradiation [4], which is attributed to slow diffusion. In the present study these effects were small because of the powdered form of the sample and the long storage before analysis. The initial G-value for evolution of F- in aqueous alkali and air was near 0.6 or 1.7 in different studies. A weight

loss proportional to the square of the radiation dose was found by Charlesby [18] when diffusion effects were eliminated. If the weight loss was principally CF_4, the $G(CF_4)$ should increase proportionally with dose. The identification of weight loss as CF_4 was only tentative.

In the present study CF_4 was not an especially abundant product, and $G(CF_4)$ did not increase notably with dose. The Charlesby relation may possibly hold for CF_4 at very high doses and higher temperatures. The CF_4 from the HFP copolymers (table 4) may indicate a tendency to break at branch points. No monomer was found after irradiation, and only a very little was found after heating irradiated polymer (table 3), in contrast with the reported behavior of poly(methyl methacrylate) [56]. The irradiation of PTFE in a furnace, however, is stated to yield monomer rapidly if irradiation is done above 325 °C [57]. Among incidental chemical or physical observations are an increased water absorption when irradiated in air [4], a change in X-ray spacing parameters [41], and permanganate titrations and infrared spectra suggestive of two kinds of double bonds. The double bonds and ionic fluoride mentioned earlier are not apparent in the irradiation of the chemically analogous perfluoroheptane. As mentioned earlier the ESR spectrum indicates the presence of a secondary radical $\sim\!\!\sim CF_2\dot{C}FCF_2\sim\!\!\sim$, which is quite stable in vacuum but reacts rapidly with oxygen.

The pertinent radiation yields from new and old work are listed in table 13. Earlier discussions of PTFE regarded the polymer as degrading exclusively, as much of the qualitative evidence seemed to imply. Thermochemical estimates of the several bond energies, F—F = 37 kcal/mole, C—C = 83 kcal/mole, C—F = 105 kcal/mole [58], made cross linking, with elimination of F_2, appear especially unfavorable energetically so that C—C scission would dominate in competition. The identification of radicals $\sim\!\!\sim CF_2\dot{C}F—CF_2\sim\!\!\sim$ shows that C—F splitting actually occurs; therefore, not energetics but cage effects and relative diffusion rates are the dominant factors, and C—C scission is no longer the only allowed process. From the parabolically increasing yields of gas (regarded as CF4) and a picture of random C—C scission, Charlesby had arrived at a G(C—C scission) = 2, of the same order as that found in polyethylene. Nishioka's melt viscosity data led to the much higher G(C—C scissions) ≈ 10 for degradation in air.

Detailed chemical steps suggested were the following:

(1) $\sim\!\!\sim CF_2CF_2CF_2\cdot + F\cdot \rightarrow \sim\!\!\sim CF_2CF_2CF_3 \rightarrow$
$\sim\!\!\sim CF_2CF_2\cdot + CF_3\cdot \rightarrow$
$\sim\!\!\sim CF{=}CF_2 + CF_4$ [41, 42, 47]

(2) $CF_3\cdot + F\cdot \rightarrow CF_4$ [47]

(3) $\sim\!\!\sim CF_2CF_2\sim\!\!\sim + F\cdot \rightarrow —CF_3 + \sim\!\!\sim CF_2\cdot$ [59]

The steps have accounted for the double bonds that were found [41]. A secondary effect was the distortion of crystal structure; since double bonds are shorter than single bonds and the angles are different, great strain is expected in the compound helix structure [41], and a disturbance of spacing was apparently found. The tendency to disintegrate was attributed either to the crystal strains [41] or to the pressure of relatively nondiffusing CF_4 accumulated in the solid [18,59].

Nothing more has been learned about the mechanisms of breakage. Indirectly, the analysis of volatile products from PTFE and of all products from the liquid n–C_7F_{16} [9,10] do not suggest important amounts of olefins. The superior retention of tensile strength in thin specimens of PTFE [8,18,60] may suggest that gas inclusions rather than crystal stresses cause the observed failures of thicker specimens.

The actual extent of molecular weight degradation is unsettled, largely because of the difficulties of measurement. The relatively careful measurements by Nishioka et al., [53] based largely on melt viscosity, were made upon samples irradiated in air, and the huge G (scission) value of 10 deduced from those measurements can apply only to the process in air. A more rigorous recalculation in terms of the best available molecular-weight relationships would be of interest. The tensile-strength measurements reported from this laboratory [47] suggest a very slow or zero rate of scission in vacuum. A few test data indicate a relatively slow loss of tensile strength but drastic loss of elongation [46]. These irradiations may have been performed in relatively good vacuum. However, the most favorable previous results indicate loss of most mechanical strength at a dose of about 0.5×10^{22} ev/g. A certain amount of cross linking is indicated by the ZST data for TFE–HFP copolymer, and possibly by the reported initial increase in impact strength of PTFE [2]. As has been mentioned, the free radical species $\sim\!\!\sim CF_2\dot{C}FCF_2\sim\!\!\sim$, which should be able to cross link, is the only one identified and is prominent.

Thermochemical considerations indicate very slight possibility for reaction by these radicals at ordinary temperatures, except possibly cross linking. Combination of small fluorocarbon radicals occurs readily enough, although perhaps more slowly than the

TABLE 13. *G-values of products from irradiation of polytetrafluoroethylene*

Product	Conditions	G	Reference
CF_4	Pile	0.005 to 0.05 [a]	18
CF_4	γ, vac; (30 to 84)x10^{20}ev/g	.004 to .009	Table 3
SiF_4	Pile	≤CF_4	18
SiF_4	γ, vac	0.12 to 0.16	Table 3
F	Water, air	2.0	41
C=C	Water, air; $KMnO_4$	~0.2	41
Scissions	Pile, vac	2	18
Do	Air	10	53
Radicals	Deuterons	0.05	50
Do	γ, vac	0.16 to 0.19	Table 10
Do	Vac., then air	Peroxy 0.2	26
Do	Irr. air	Peroxy 0.03	26

[a] Linear with dose, 0.05 at 10^{21}ev/g.

normal hydrocarbon rate [61]; (for other references see [10]).

Abstraction and disproportionation reactions have not been reported for fluorocarbon radicals and chain compounds up to high temperatures, and abstraction of F even by hydrogen atoms involves 17 kcal/mole or more (for references see [10]). The secondary radical could split at high temperature into an olefin and a primary radical, which could then split off monomer.

$$\sim\!CF_2CF_2\dot{C}FCF_2\sim\!\rightarrow\sim\!\dot{C}F_2+CF_2{=}CFCF_2\sim$$

$$\sim\!CF_2CF_2CF_2\dot{C}F_2\rightarrow\sim\!CF_2\dot{C}F_2+C_2F_4.$$

The last reaction is the reverse propagation step of polymer pyrolysis, for which the activation energy is necessarily greater than 46 kcal/mole, which is equivalent to the heat of polymerization [62]. Reverse propagation would occur to a negligible extent at room temperature, but one might have expected the formation of monomer at high temperatures, as is the case with PMMA [56]. Actually upon heating from 20 °C to 400 °C, a sample estimated to contain

$$3\times10^{18}\text{ radicals }((G_R/100)\cdot D\cdot W=\binom{0.2}{100}\times6.89\times10^{20}$$

ev/g$\times$0.2 g) (tables 13 and 3) evolved only 8.4×10^{16} molecules of C_2F_4 at 0.03 molecule per radical. The oxygenated radicals produced by exposure to air also give rise to very little decomposition of any kind when heated to 310 °C in vacuo (table 3, last column). Since the radicals disappear rapidly at 320 °C, most of them probably combine before the samples reach the temperature needed for rapid depropagation. If radicals could be produced continuously at 400 °C or so by irradiating a heated sample, a significant rate of depropagation might be found. Rapid depropagation evidently occurred in a sample of PTFE irradiated at a nominal temperature of 330 to 350 °C [57]. The weight loss of a PTFE sample irradiated to a dose of 12.7×10^{21} ev/ml, at a dose rate of 42×10^{18} ev/ml-sec, jumped from a level near 0.5 percent below 300° to 50 percent at 330 to 350 °C.

With more closely controlled temperatures, and observation of radicals under identical conditions, the constants of the depropagation process could be isolated. The data of Taubman et al., [57] indicate a $G(C_2F_4)$ of perhaps 30 molecules per 100 ev at 330 to 350 °C. If we assume that the rate of formation of depropagating radicals is given by the G-value of secondary radicals observed at room temperature, the data imply that each radical formed at 330 to 350 °C evolves on the average 150 molecules of C_2F_4 during its lifetime.

6. Conclusions

When fluorocarbon polymers are irradiated in vacuum, the observed yields of products from splitting the C—F and C—C bonds are often less than those from the C—H and C—C bonds in hydrocarbon polymers. The accompanying corrosion may, of course, be more serious. Cross linking, followed by degradation, occurs in polymers containing both F and H, and also in the pure fluorocarbon copolymer TFE–HFP. Chain scission alone occurs in PCTFE. Probably both processes occur in PTFE, with little net change in tensile strength. For both PTFE and its HFP copolymer the radiation behavior is very sensitive to the presence of oxygen. The radiation of PCTFE is insensitive to oxygen with respect to molecular weight degradation, which is moderately rapid in any event, but very sensitive with respect to loss of F and Cl in the presence of air, water, and alkali.

In many of the irradiated polymers free radicals can be observed, sometimes at G-values as large as 1. In the only perfluoroaromatic ring polymer studied, PPFS, the $G(R)$ was very low, similar to that in polystyrene, suggesting that perfluoroaromatic polymers would have superior radiation resistance.

There are many unsolved problems in the radiation chemistry of PTFE, particularly in regard to the true rates of scission and cross linking in vacuum, the possibility of predominant cross linking, and the ultimate fate and kinetic importance of the observed free radicals.

7. References

[1] E. J. Lawton, A. M. Bueche, and J. S. Balwit; Nature **172,** 76 (1953).

[2] C. D. Bopp and O. Sisman; Radiation stability of plastics and elastomers; Oak Ridge Natl. Lab. 1373 (July 1953).

[3] O. Sisman and C. D. Bopp; Oak Ridge Natl. Lab. 928, pp. 3, 85 (1951).

[4] J. C. Bresee, J. R. Flanary, J. H. Goode, C. D. Watson, and J. S. Watson, Nucleonics **14,** 74 (1956).

[5] J. Byrne, T. W. Costikyan, C. B. Hanford, D. L. Johnson, and W. L. Mann, Ind. Eng. Chem. **45,** 2549 (1953).

[6] J. G. Burr and W. M. Garrison, Atomic Energy Commission Document 2078 (1958).

[7] F. A. Bovey, The effects of ionizing radiation on natural and synthetic polymers, Polymer Reviews No. 1, Interscience, New York, 1958, pp. 67–69.

[8] L. A. Wall, and R. E. Florin, J. Appl. Polymer Sci. **2,** 251 (1959).

[9] J. H. Simons, and E. H. Taylor, J. Phys. Chem. **63,** 636 (1959).

[10] R. E. Florin, L. A. Wall, and D. W. Brown, J. Research NBS **64A,** 269 (1960).

[11] H. S. Kaufman, C. O. Kroncke, and C. R. Giannotta, Modern Plastics **32** (2), 146 (October 1954).

[12] A.S.T.M. D 1430–58T, A.S.T.M. Standards on Plastics, Dec. 1959, p. 55.

[13] E. K. Walsh and H. S. Kaufman, J. Polymer Sci. **26,** 1 (1957).

[14] H. S. Kaufman, E. K. Walsh, and H. L. Wagner; ZST-solution viscosity molecular weight correlations, Minnesota Mining and Manufacturing Co. Memorandum August 15, 1956.

[15] P. Alexander, R. M. Black, and A. Charlesby, Proc. Roy. Soc. **A232,** 31 (1955).

[16] P. Alexander, A. Charlesby, and M. Ross, Proc. Roy. Soc. **A223,** 392 (1954).

[17] A. Nishioka, J. Polymer Sci. **26,** 107 (1957).

[18] A. Charlesby, The decomposition of polytetrafluoroethylene by pile radiation, Great Britain Atomic Energy Research Establishment AERE M/R 978 (1952).

[19] R. E. Florin, L. A. Wall, and D. W. Brown, Trans. Faraday Soc. **56,** 1304 (1960).

[20] H. N. Rexroad and W. Gordy, J. Chem. Phys. **30,** 399 (1959).
[21] V. Voevodsky, EPR spectra of some hydrocarbon free radicals at 77 °K, paper presented at Faraday Society, Informal Discussion on Free Radical Stabilization, Sheffield, Sept. 4, 1958.
[22] T. Matsugashita, and K. Shinohara, J. Chem. Phys. **32,** 954 (1960).
[23] T. Watanabe, J. Phys. Soc. Japan **13,** 1063 (1958).
[24] E. E. Schneider, J. Chem. Phys. **23,** 978 (1955); Faraday Soc. Discussions **19,** 158 (1955).
[25] W. B. Ard, H. Shields, and W. Gordy, J. Chem. Phys. **23,** 1727 (1955); Faraday Soc. Discussions **19,** 158 (1955).
[26] R. L. Abraham and D. H. Whiffen, Trans. Faraday Soc. **54,** 1297 (1958).
[27] W. P. Slichter, J. Polymer Sci. **24,** 173 (1957).
[28] H. Shields, W. B. Ard, and W. Gordy, Bull. Am. Phys. Soc. II, **2,** 227 (1957).
[29] R. A. Meyer, F. L. Bouquet, and R. S. Alger, J. Appl. Phys. **27,** 1012 (1956).
[30] J. F. Fowler and F. T. Farmer, Nature **174,** 136 (1954).
[31] J. Goodman and J. H. Coleman, J. Polymer Sci. **25,** 253 (1957).
[32] P. Y. Feng, The radiation chemistry of fluorinated organic compounds, 2nd United Nations Conference on Atomic Energy (June 1958).
[33] D. S. Ballantine, P. Colombo, A. Glines, B. Manowitz, and D. J. Metz, Brookhaven Natl. Lab. 414 (T–81), (Oct. 3, 1956).
[34] P. Y. Feng, and L. Mamula, J. Chem. Phys. **28,** 507 (1958).
[35] R. Harrington, Rubber Age **83,** 472 (1958).
[36] D. A. Barr and R. N. Haszeldine, J. Chem. Soc. **1956,** 3416 (1956).
[37] C. E. Griffin and R. N. Haszeldine, J. Chem. Soc. **1960,** 1398 (1960).
[38] L. A. Wall and S. Straus, J. Research NBS **65A,** 227 (1961).
[39] P. Bradt and F. L. Mohler, Anal. Chem. **27,** 875 (1955).
[40] W. L. Reilly and H. C. Brown, J. Org. Chem. **22,** 698 (1957).
[41] J. W. Ryan, Modern Plastics **31,** (2), 152 (October 1953).
[42] J. W. Ryan, Soc. Plastics Engrs. Journal **10,** (4), 11 (1954).
[43] E. I. duPont de Nemours and Co., Inc.; Brochure on Viton A, p. 11 (1958).
[44] S. Dixon, D. R. Rexford, and J. S. Rugg, Ind. Eng. Chem. **49,** 1687 (1957).
[45] W. W. Jackson and D. Hale, Rubber Age **77,** 865 (1955).
[46] R. Harrington, Rubber Age **82,** 461 (1957).
[47] L. A. Wall, Atomic radiation and polymers, Conf. on effects of radiation on dielectric materials, Naval Research Lab., Dec. 14–15, 1950, Office of Naval Research Symposium rept. ACR–2, p. 139.
[48] R. N. Haszeldine and B. R. Steele, J. Chem. Soc. **1957,** 2800 (1957).
[49] P. E. Thomas, J. F. Lontz, C. A. Sperati, and J. L. McPherson, Soc. Plastics Engrs. Journal **12,** (6), 89 (1956).
[50] M. Watanabe, J. Polymer Sci. **24,** 298 (1957).
[51] C. Sperati, private communication.
[52] A. Nishioka, T. Moritaka, and O. Masakazu, J. Polymer Sci. **28,** 617 (1958).
[53] A. Nishioka, K. Matsumae, M. Watanabe, M. Tajima, and M. Owaki, J. Applied Polymer Sci. **2,** 114 (1959).
[54] H. Mark, Ind. Eng. Chem. **34,** 1343 (1942).
[55] K. Matsumae, M. Watanabe, A. Nishioka, and T. Ichimiga, J. Polymer Sci. **28,** 653 (1958).
[56] L. A. Wall and D. W. Brown, J. Phys. Chem. **61,** 132 (1957).
[57] A. B. Taubman and L. P. Ianova, All-Union Conf. on Radiation Chem. Moscow 1957, p. 287, dis. 306; tr. Consultants Bureau Inc. pp. 271, 291.
[58] L. Pauling, The nature of the chemical bond, 3d ed., 1960, Cornell Univ. Press, Ithaca, New York; p. 85.
[59] M. Burton, Conference on effects of radiation on dielectric materials, Naval Research Laboratory, December 14–15, 1954, p. 9.
[60] A. Charlesby, Radiation Research **2,** 96 (1955).
[61] G. A. Miller, G. O. Pritchard, and E. W. R. Steacie, Z. physik. Chem. **15,** 262 (1958).
[62] C. R. Patrick, Tetrahedron **4,** 34 (1958).

(Paper 65A4–117)

JOURNAL OF RESEARCH of the National Bureau of Standards—A. Physics and Chemistry
Vol. 65A, No. 4, July-August 1961

Inhibition of Diffusion Flames by Methyl Bromide and Trifluoromethyl Bromide Applied to the Fuel and Oxygen Sides of the Reaction Zone

E. C. Creitz

(March 9, 1961)

The difference in extinguishing effectiveness of an inhibitor introduced on the two sides of the reaction zone of diffusion flames has been measured as a function of oxygen concentration in the O_2-N_2 mixture supplied to the flames. Six fuels and two inhibitors were used. It was found that when the inhibitor was added to the fuel, the volume percentage required for extinguishment was much greater than when added to the oxygen side of the reaction zone, with the single exception of CO flames inhibited by trifluoromethyl bromide. In all cases except the latter, the amount required for extinction increased with increase of the oxygen concentration, being relatively less dependent on oxygen concentration above a certain threshold in the neighborhood of 21 percent when the inhibitor was added to the fuel. Above oxygen concentrations on the order of 25 percent, methyl bromide was completely ineffective when added to the oxygen side of the reaction zone, and above about 32 percent oxygen it was ineffective when added to the fuel, since at this oxygen concentration it burns without additional fuel.

1. Introduction

It was noted, in the course of some preliminary work on the inhibition of propane diffusion flames by methyl bromide, that extinguishment was more readily achieved when the inhibitor was supplied to the air side of the reaction zone than when added to the fuel. A search of the literature revealed that Simmons and Wolfhard [1] [1] had reported this effect in a paper devoted primarily to the spectroscopy of diffusion flames. Because of the possibility, suggested by this observation, that the inhibitor interferes with some reaction involving oxygen or oxygenated intermediates, it was decided to study the effect as a function of the oxygen concentration in the oxygen-nitrogen mixture supplied to the flame. In addition, it seemed desirable to inhibit the flames with nitrogen added to the fuel so that a datum could be established for estimating the relative efficiencies of the other inhibitors under similar conditions.

2. Apparatus and Procedures

No attempt was made to obtain gases of exceptionally high purity, since the study was aimed primarily toward obtaining information about the differences between the fuel and oxygen sides of diffusion flames. The hydrogen used was prepared commercially by electrolysis and contained [2] not more than 0.2 percent impurity which consisted almost entirely of oxygen and nitrogen. Mass spectrometer analysis of the natural gas used indicated that it consisted of 95.15 percent methane, 2.84 percent ethane, 0.63 percent propane, 0.62 percent CO_2, 0.42 percent N_2, and a number of heavier hydrocarbons totaling 0.34 percent. The following gases were of commercial purity, the percentage of the major component being specified with no indication of the nature of the minor components: ethane 95 percent, propane 99.5 percent, butane 99.5 percent, carbon monoxide 99.5 percent, methyl bromide 99.4 percent, trifluoromethyl bromide 94.0 percent.

A sketch of the burner is shown in figure 1. The diffusion flame burned on the end of a Pyrex glass tube 7 mm o.d. with 0.8 mm wall thickness. The burner jacket was of 5 cm i.d. and had 18 cm height above the glass beads used to distribute the air flow. The height of the jacket was approximately 15 cm above the burner tube. Flow rates of the various gases were metered through calibrated flow meters. Flows of secondary air in the jacket were maintained high enough so that concentration changes caused by the flames were restricted to the immediate vicinity of the flame and back diffusion of room air into the top of the jacket was avoided.

Extinction of a diffusion flame may be effected by a number of factors, among them being the rate at which the fuel is supplied to the burner and the velocity of the secondary air past the flame. The latter effect was found to be relatively unimportant except at rather low or very high flow rates and was ignored. However, when the rate of fuel supply was too low, for a given burner size, the flame would not burn, and conversely, when the rate was too high, lifting occurred and the flame tended to float off and be extinguished. Between these two extremes, an optimum rate of fuel supply was determined for each of the fuels and for each of the halogenated inhibitors. A typical extinguishment curve is shown in figure 2 (the extinction region lies above the line in each curve). It can be seen that considerable deviation

[1] Figures in brackets indicate the literature references at the end of this paper.
[2] Analyses furnished by the supplier.

from the optimum value of 220 cm^3 per minute (16 cm/sec lineal velocity) for ethane was permissible with this burner when the inhibitor was added to the fuel and the effect was very small when the inhibitor was added to the air supplied to the flame. Optimum rates for the other gases ranged between 100 and 360 cm^3/min.

In general, a set of conditions was established and inhibitor added slowly, either to the fuel or to the mixture supplied to the oxygen side of the flame, until the flame was extinguished. Under some conditions, the flame lifted and floated as much as 10 to 15 cm above the burner where it seemed to be quite stable and would return to the burner if the concentration of inhibitor was reduced. When this occurred, a very large amount of inhibitor was required to accomplish the extinguishment. Under these conditions, the flame was called extinguished at the inhibitor concentration which caused it to suddenly pull away from the burner and rise 1 to 2 cm above it.

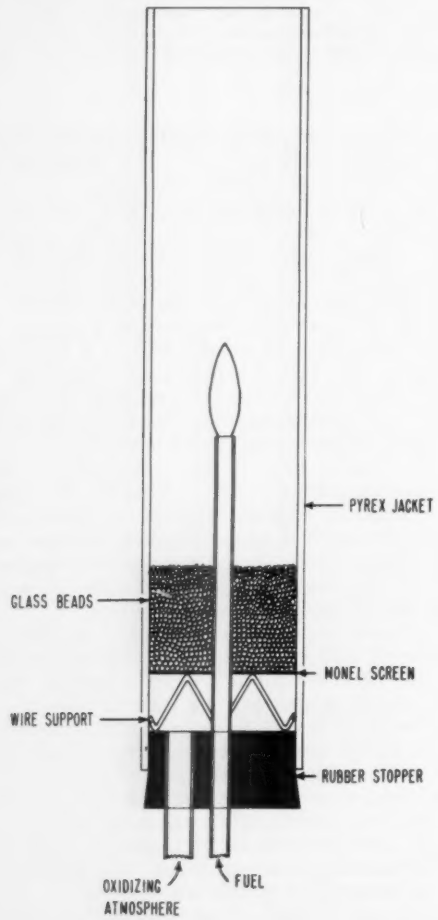

FIGURE 1. *The burner used to determine the extinction characteristics of methyl bromide and trifluromethyl bromide on diffusion flames of various fuels (shown in cross section).*

It was felt that, in cases of very high lifting, a certain amount of oxygen was mixing with the gas as primary oxygen and the flame was no longer a true diffusion flame.

3. Results

The results are presented in the form of curves which define the boundary between burning and extinguishment conditions. Figures 3 to 8 inclusive show these regions when the inhibitor was added to the oxygen side of the reaction zone. Burning regions are to the right and below the curves while extin-

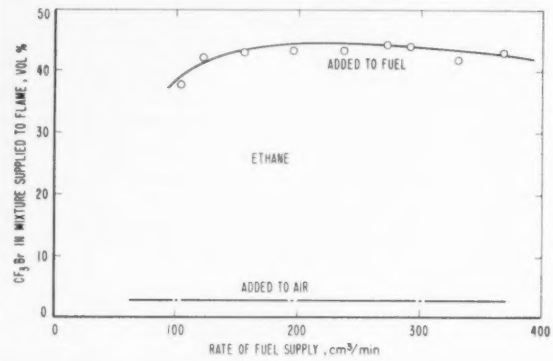

FIGURE 2. *Extinction characteristics of trifluoromethyl bromide when added to ethane and when added to the air supplied to the ethane diffusion flame, as a function of the fuel rate.*

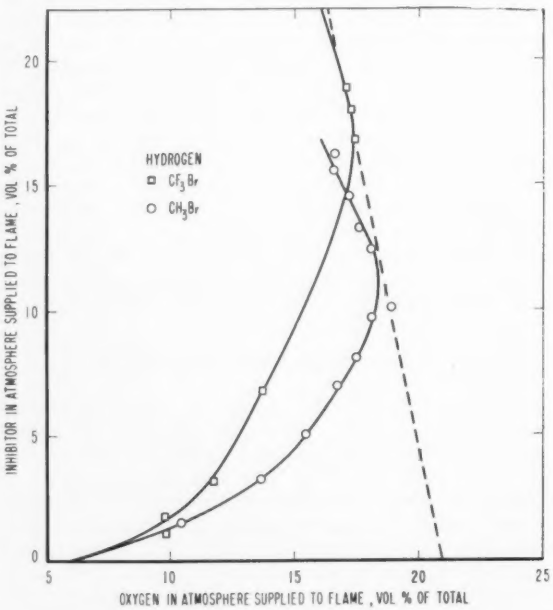

FIGURE 3. *Extinction of hydrogen diffusion flames by* CF_3Br (□) *and* CH_3Br (○) *when the inhibitor is added to the air supplied to the flame.*

Flames burn in areas to the right of each curve and are extinguished to the left.

guishment results for conditions represented to the left and above the curves. Dotted lines represent the decrease in oxygen concentration produced by dilution of air by the inhibitor. It was impossible to obtain curves similar to those of figure 2 for hydrogen. The reason for this is shown in figure 3, which indicates that this dilution effect was important in the extinguishment of hydrogen flames in air. If the oxygen concentration had been maintained at a constant 20.94 percent independent of the addition of inhibitor, neither of the agents would have been able to extinguish the flames.

The curves of figures 9 to 14, inclusive, show the results of adding methyl bromide, trifluoromethyl bromide or nitrogen to the fuels. As before, the curves are boundaries between regions in which diffusion flames burn or are extinguished, burning taking place under conditions represented to the right and below the curves with extinction above and to the left.

No curve is shown for the effect of CF_3Br added to CO as fuel. The amount required for extinguishment was too small to be measured with the apparatus available. It was estimated, however, to be approximately 1 percent by volume of the fuel rate. It thus appears that the CO diffusion flame was extinguished by a very small amount of CF_3Br regardless of whether it was added from the oxygen or from the fuel side of the reaction zone. There seemed to be no dependence of extinguishment on the oxygen concentration outside the reaction zone, regardless of whether the inhibitor was added to the fuel or oxygen side of it.

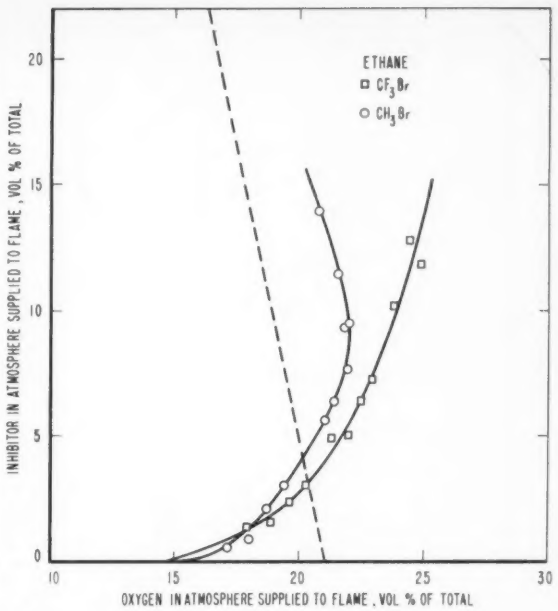

FIGURE 5. *Extinction of ethane diffusion flames by* CF_3Br (□) *and* CH_3Br (○) *when the inhibitor is added to the air supplied to the flame.*

Flames burn in areas to the right of each curve and are extinguished to the left.

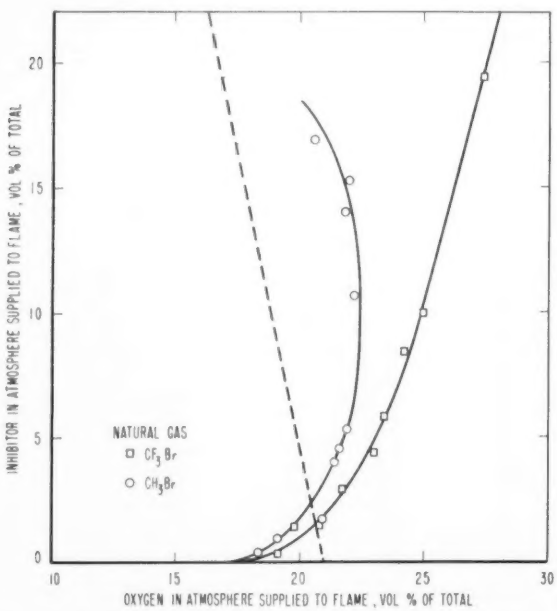

FIGURE 4. *Extinction of natural gas diffusion flames by* CF_3Br (□) *and* CH_3Br (○) *when the inhibitor is added to the air supplied to the flame.*

Flames burn in areas to the right of each curve and are extinguished to the left.

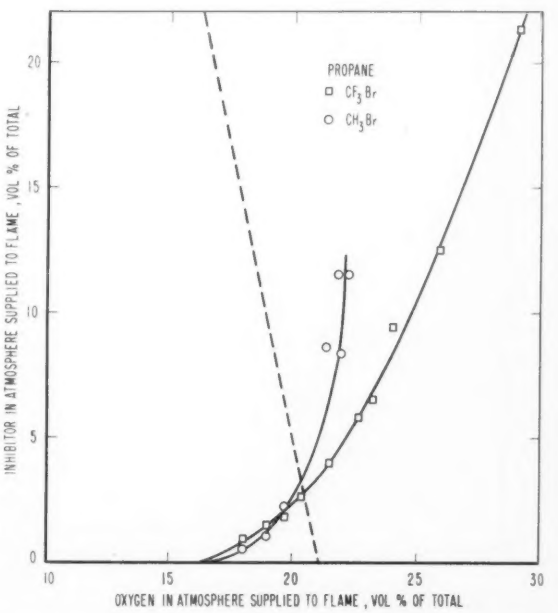

FIGURE 6. *Extinction of propane diffusion flames by* CF_3Br (□) *and* CH_3Br (○) *when the inhibitor is added to the air supplied to the flame.*

Flames burn in areas to the right of each curve and are extinguished to the left.

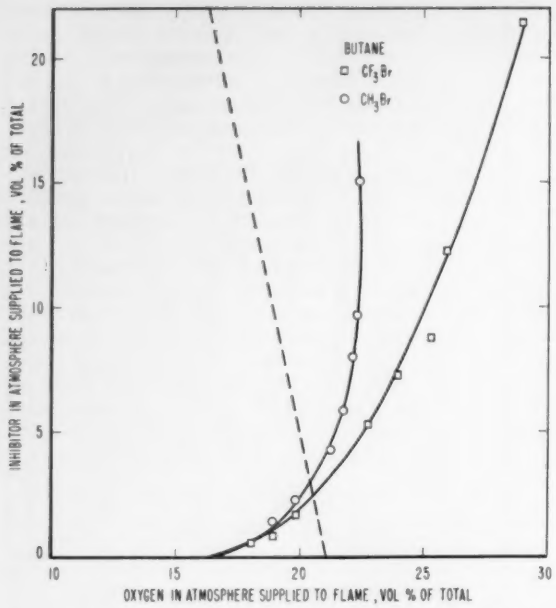

FIGURE 7. *Extinction of butane diffusion flames by* CF_3Br (□) *and* CH_3Br (○) *when the inhibitor is added to the air supplied to the flame.*

Flames burn in areas to the right of each curve and are extinguished to the left.

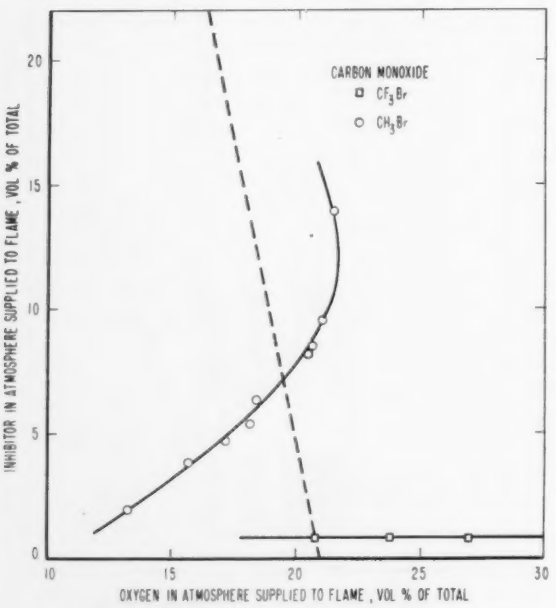

FIGURE 8. *Extinction of carbon monoxide diffusion flames by* CF_3Br (□) *and* CH_3Br (○) *when the inhibitor is added to the air supplied to the flame.*

Flames burn to the right of the CH_3Br curve and below the CF_3Br curve and are extinguished to the left of the CH_3Br curve and above the CF_3Br curve.

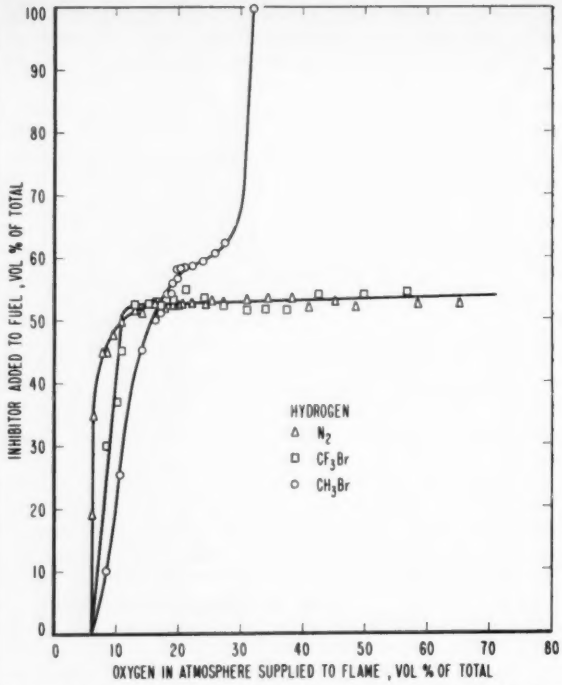

FIGURE 9. *Extinction of hydrogen diffusion flames by nitrogen* (△), CF_3Br (□) *and* CH_3Br (○) *when the inhibitor is added to the fuel.*

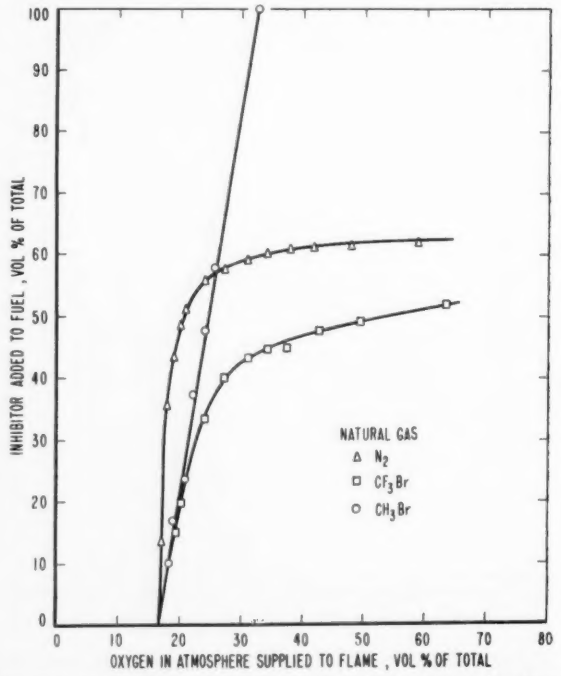

FIGURE 10. *Extinction of natural gas diffusion flames by nitrogen* (△), CF_3Br (□) *and* CH_3Br (○) *when the inhibitor is added to the fuel.*

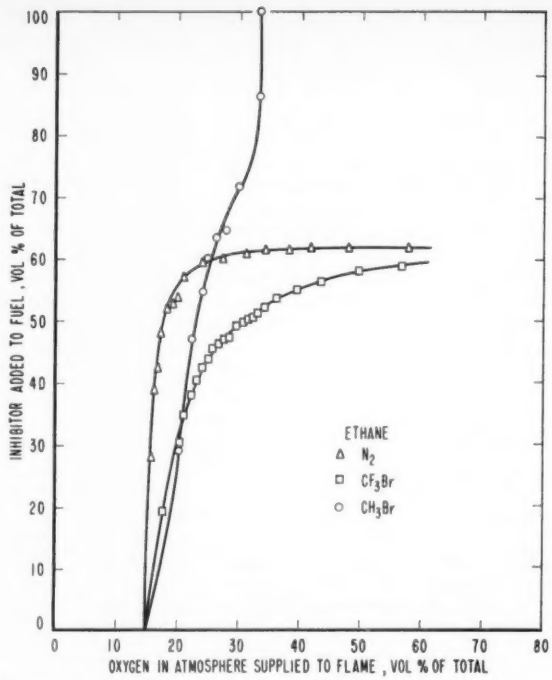

FIGURE 11. *Extinction of ethane diffusion flames by nitrogen (△), CF_3Br (□) CH_3Br (○) when the inhibitor is added to the fuel.*

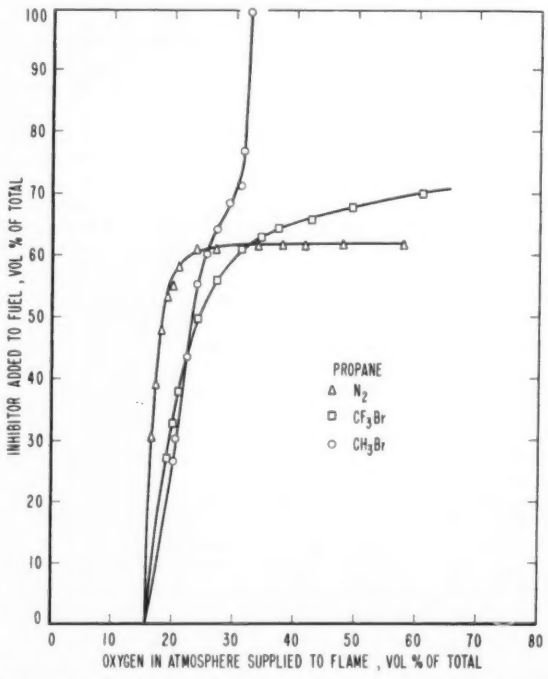

FIGURE 12. *Extinction of propane diffusion flames by nitrogen (△), CF_3Br (□) and CH_3Br (○) when the inhibitor is added to the fuel.*

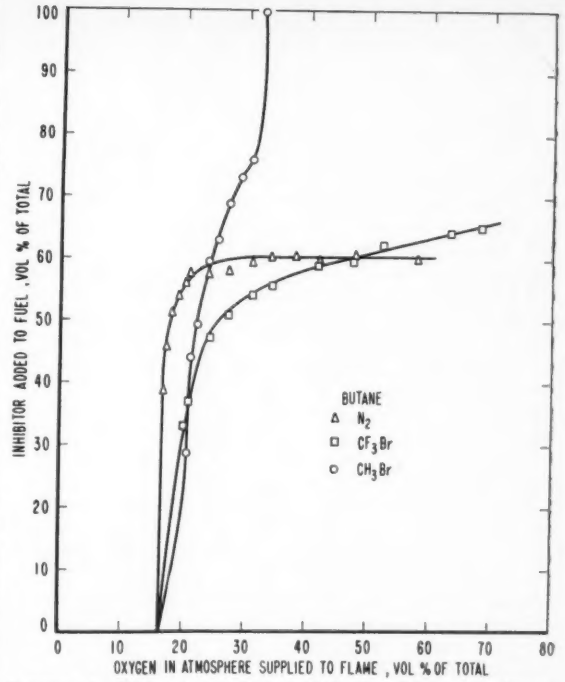

FIGURE 13. *Extinction of butane diffusion flames by nitrogen (△), CF_3Br (□) and CH_3Br (○) when the inhibitor is added to the fuel.*

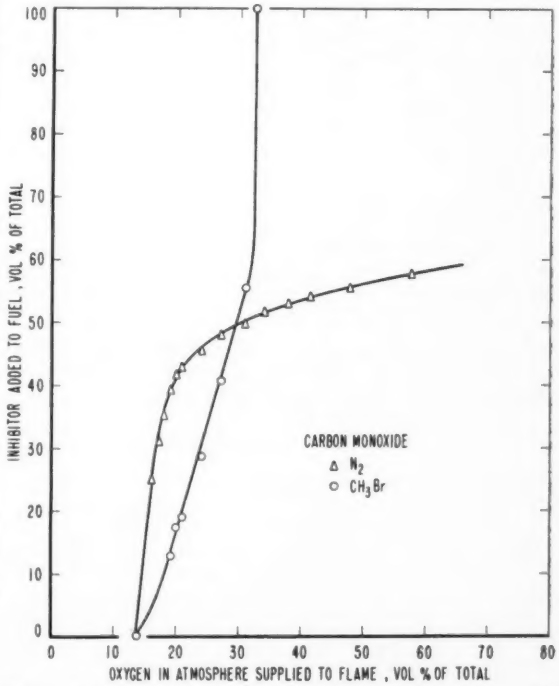

FIGURE 14. *Extinction of carbon monoxide diffusion flames by nitrogen (△) and by CH_3Br (○) when the inhibitor is added to the fuel.*

4. Discussion

Relative efficiencies of the three inhibitors for various concentrations of oxygen in the atmosphere supplied to the flame may be derived from the curves (fig. 9 to 14, inclusive) for the case where the inhibitor was added to the fuel. However, when the inhibitor was added to the atmosphere surrounding the flame, allowance had to be made for the reduction in oxygen concentration caused by the addition of inhibitor to the starting mixture of oxygen and nitrogen. Lines parallel to the dotted lines for air in figures 3 to 8, inclusive, give the oxygen concentration. Values for the percent inhibitor at extinction when normal air was the starting mixture were read from the curves at points where they crossed the dotted lines and are shown in table 1. Also shown in the table are the efficiencies of the two halogenated inhibitors compared to that of nitrogen. It is evident from the table and curves that, in spite of its inertness, the inhibiting effect of nitrogen is different on opposite sides of the reaction zone. Because of this fact, it was felt that nitrogen provided the best basis for a comparison of the efficiencies of the halogenated compounds when applied to the two sides of the reaction zone. The reaction zone of a diffusion flame may be considered as being bounded on one side by the rich combustible limit and on the other by the lean combustible limit, with the stoichiometric mixture somewhere in between, the whole flame being somewhat diluted by products of combustion and the inerts which accompany the reactants. The results of this study indicate that diffusion flames are peculiar in that the amount of nitrogen they will tolerate is dependent upon whether it appears at the lean or rich boundary. For example the hydrogen diffusion flame will not burn if more than 54 percent nitrogen is present in the fuel, even if the oxygen in the O_2–N_2 mixture supplied to the flame is increased to 70 percent (fig. 9). However, if the nitrogen is added with the oxygen, the mixture may contain as much as 94.1 percent nitrogen (fig. 3). In terms of the reaction $H_2+\frac{1}{2}\ O_2 \rightarrow H_2O$, 6.8 times as much nitrogen may be added with the oxygen as with the fuel. In the absence of chemical effects and neglecting differences in rates of diffusion, it would be expected that the halogenated inhibitors would behave similarly. The results show that, at 21 percent oxygen in the atmosphere supplied to the flame (where it will tolerate the most inhibitor), CF_3Br gives a value of 0.36 for the ratio of tolerable concentrations on the oxygen and fuel sides of the reaction zone. This value is only 5.4 percent of that for nitrogen, indicating that, while the hydrogen flame behaved similarly toward the addition of nitrogen and CF_3Br on the fuel side, the effects of these additives were quite different when added on the oxygen side. At lower oxygen concentrations these differences were even more pronounced, as they were for some of the hydrocarbon flames. The effect seems to be absent in CO flames; they behaved differently toward the addition of nitrogen, but CF_3Br appeared to differ little in its effect whether added to one side or the other.

Figures 3 and 9 and table 1 show that neither of the halogenated inhibitors was particularly effective in extinguishing a hydrogen diffusion flame, either when added to the air side or to the fuel side of the reaction zone. Their effectiveness increased when used on the oxygen side of hydrocarbon flames, CF_3Br being somewhat more effective than CH_3Br. However, for the CO diffusion flame there was a great difference not only between the effectiveness of the inhibitors, but also between their effects on the CO flame and the flames of the other fuels. The difference between the effectiveness of the two inhibitors for CO flames is, no doubt, connected with the hydrogen contained in the CH_3Br molecule and the well-known effects of hydrogen and hydrogen-containing compounds on the combustion of CO. The decreasing effectiveness of both inhibitors as the amount of free and bound hydrogen in the fuel increased suggests that some reaction of hydrogen opposes the action of the inhibitor.

Figures 3 to 14, inclusive, show that the oxygen concentration in the oxygen-nitrogen mixture supplied to the flame has a rather large effect on the efficiency of the inhibitors, particularly at oxygen concentrations below that found in air. The curves for methyl bromide may be interpreted as showing that the inhibitor starts to become a fuel at about 25 percent oxygen concentration and will burn unsupported as a diffusion flame when the oxygen concentration reaches about 32 percent. This result is not unexpected since Marsh [2] gives lower and upper limits of 14 and 19 percent for upward propa-

TABLE 1. *Comparison of extinguishment characteristics of* N_2, CH_3Br, and CF_3Br *for various fuels burning in air*

Fuel	Percentage of inhibitor in air or fuel at extinction						Efficiency relative to nitrogen			
	When added to air			When added to fuel			Added to air		Added to fuel	
	N_2	CH_3Br	CF_3Br	N_2	CH_3Br	CF_3Br	CH_3Br	CF_3Br	CH_3Br	CF_3Br
H_2	94.1	11.7	17.7	52.4	58.1	52.6	8.0	5.3	0.9	1.0
CH_4	83.1	2.5	1.5	51.0	28.1	22.9	33.2	55.4	1.8	2.2
C_2H_6	85.6	4.0	3.0	57.3	36.6	35.1	21.4	28.5	1.6	1.6
C_3H_8	83.7	3.1	2.7	58.3	34.0	37.6	27.0	31.0	1.7	1.6
C_4H_{10}	83.7	2.8	2.4	56.8	40.0	37.9	29.9	34.9	1.4	1.5
CO	90	7.2	0.8	42.8	19.9	----------	12.5	112	2.2	----------

gation in a 2-in. diameter tube when methyl bromide is mixed with oxygen. Figures 3 to 8, inclusive, show that methyl bromide is not effective as an inhibitor when supplied with an oxygen-nitrogen mixture containing more than 25 percent oxygen. This may be interpreted as evidence that combustion products of methyl bromide are ineffective as inhibitors when added on the oxygen side of the diffusion flame. Trifluoromethyl bromide seems to retain its effectiveness to considerably higher oxygen concentrations. When added to the fuel the inhibitors are most effective at oxygen concentrations below that found in air, but do not approach the corresponding efficiencies for the oxygen side of the reaction zone until the oxygen concentration approaches the minimum required to support the uninhibited flame.

The very low efficiency of the halogenated inhibitors when added to the fuel can probably be attributed to failure of the molecules to survive the combined effects of the reducing atmosphere and pyrolysis to which they are subjected as they enter the reaction zone. The results of this study suggest that there is less chance of survival when the inhibitor is added to the fuel than when added to the oxygen side of the reaction zone.

The lack of effectiveness of the decomposition products of CH_3Br and CF_3Br suggest that inhibition may be a result of some reaction or property of the intact inhibitor molecule, or of its freshly released decomposition products. The former concept is not consistent with the theory of Rosser [3] which postulates interference by halogen atoms with chain reactions involving hydrogen atoms. It seems likely that the inhibition reaction takes place in some particular region of the reaction zone, which requires that the inhibitor be stable enough to reach the area where its reaction takes place, but not so stable that it cannot react after it gets there.

TABLE 2. *Qualitative parallelism between extinguishing efficiency and dissociative resonance capture of electrons*

Compound	Concentration for extinguishment at peak flammability [7]	Electron attachment	Halogen ion formed	Reference
CH_3I	6.1	yes	yes	6
$CBrF_3$	6.1	yes	yes	5
CF_3I	6.8	yes	yes	5, 11
$CHBrF_2$	8.4	yes	yes	9
CH_3Br	9.7	yes	yes	6
$CClF_2\ CClF_2$	10.8	yes	yes	8
CCl_4	11.5	yes	yes	9, 8, 11
$CClF_3$	12.3	yes	yes	5
CF_3CF_3	13.4	yes	yes	9
CCl_2F_2	14.9	yes	yes	8, 11
C_4F_8	18.1	yes	yes	9
SF_6	20.5	yes	no	8
HCl	25.5	yes	yes	11
CF_4	26.0	yes	yes	5, 8
CH_3Cl	----	no	no	6
CH_3F	----	no	no	6
$C_8F_{16}O$	>8 [a]	yes	no	10

[a] Unpublished work from this laboratory.

The present study with halogenated inhibitors and much other unpublished work in this laboratory has brought to our attention the fact that gases known to capture electrons in other systems (mass spectrometer, discharge tubes, ionization detectors for gas chromatographs [4], etc.) have shown strong influences on the combustion processes when they are added to flames. These gases include oxygen, water vapor, nitrogen dioxide, and halogenated organic compounds. Of the many compounds which show this property, only those which form negative ions having a relatively high electron affinity, such as OH^-, O^- and the negative halogen ions, appear to have important effects. A list of halogenated compounds which are known to capture electrons is given in order of decreasing effectiveness as extinguishers, in table 2 [7]. Compounds in the lower half of the table are rather poor inhibitors and are known to either be strongly bonded or to produce no halogen ions in the mass spectrometer. The parallel between the yield of negative ions [5, 6] by dissociative resonance capture of electrons and the efficiency as a flame inhibitor for a number of these compounds is striking and is under investigation. The resonance dissociative capture of electrons may have something to do with the presence of the red and ultra-violet bromine recombination bands shown in the specta by Simmons and Wolfhard [1].

5. Summary

Methyl bromide and trifluoromethyl bromide are much more effective inhibitors when added to the oxygen side of the reaction zone of hydrogen or hydrocarbon diffusion flames than when added to the fuel side. In general, methyl bromide is less effective than trifluoromethyl bromide except at oxygen concentrations below that of air and when added to the fuel. Methyl bromide burns as a diffusion flame, unsupported by additional fuel, at oxygen concentrations above 33 percent. When added to the oxygen side of the reaction zone, it appears to burn as a premixed flame outside the main reaction zone at oxygen concentration above about 25 percent.

For the fuels studied, the difficulty of inhibition increases with the amount of hydrogen in the fuel, when the inhibitor is added to the oxygen side of the reaction zone, but shows no such effect when it is added to the fuel.

The effectiveness of the inhibitors when added to the oxygen side of the reaction zone is a function of the oxygen concentration, methyl bromide being completely ineffective above about 25 percent oxygen, trifluoromethyl bromide retaining some of its effectiveness at much higher oxygen concentrations except for the case of hydrogen as the fuel.

The results have practical application in that they show that the inhibitors are more effective under conditions of low oxygen concentrations and when mixed with the air supplied to a fire.

6. References

[1] Simmons, R. F. and M. G., Wolfhard, Trans Faraday Soc., **52,** 53–9 (1956).

[2] Marsh, D. F., Univ. Calif. publications in pharmacology **1,** 32–39 (1940).

[3] Rosser, W. A., H. Wise, and J. Miller, Seventh Symposium (International) on Combustion, p. 175–82, (Butterworth's (London) 1959).

[4] Lovelock, J. E., Anal. Chem. **33** 162–178 (1961).

[5] Dibeler, V. H., R. M. Reese, and F. L. Mohler, J. Research NBS **57,** 113 (1956) RP2700.

[6] Dibeler, V. H. and R. M. Reese, J. Research NBS **54.** 127 (1955) RP2573.

[7] Final report on fire extinguishing agents for the period Sept 1, 1947 to June 30, 1950, covering research conducted by Purdue Research Foundation and Dept. of Chemistry under contract M44–009 eng–507 with Army Engrs. Res. and Dev. Labs., Fort Belvoir, Va. Also contained in Engrs. Res. and Dev. Labs. Report 1177, Interim report on vaporizing fire extinguishing agents, by J. E. Malcolm.

[8] Hickam, W. M. and D. Berg, J. Chem. Phys. **29,** 517–23 (1958).

[9] Reese, R. M., V. H. Dibeler, and F. L., Mohler, J. Research NBS **57,** 367 (1956) RP2725.

[10] von Hoene, J. and W. M. Hickam, J. Chem. Phys. **32,** 876–9 (1960).

[11] Buchel'nikova, I.S., J. Exptl. Theoret. Phys. (USSR) **35,** 783 (1959).

(Paper 65A4–118)

JOURNAL OF RESEARCH of the National Bureau of Standards—A. Physics and Chemistry
Vol. 65A, No. 4, July–August 1961

Publications of the National Bureau of Standards*

(Including Papers in Outside Journals)

Selected Abstracts

Truncations in the method of intermediate problems for lower bounds to eigenvalues, N. W. Bazley and D. W. Fox, *J. Research NBS* **65B,** 105 (*Math. and Math. Phys.*), *No. 2, (June 1961).*
Two new procedures are developed for determining lower bounds to the eigenvalues of linear operators. The methods are based on the theory of semi-bounded self-adjoint operators in separable Hilbert space. Computation of the lower bounds is reduced to the solution of a matrix eigenvalue problem. The procedures have immediate application in the estimation of eigenvalues and eigenvectors of differential operators occurring in quantum mechanics.

Some boundary value problems involving plasma media J. R. Wait, *J. Research NBS* **65B,** (*Math. and Math. Phys.*). *No. 2,* 137 (*June 1961*).
A plasma, consisting of a neutral mixture of electrons, ions and molecules, in the presence of a constant magnetic field H_0, possesses a dielectric constant which is in the form of a tensor. Exact solutions of boundary value problems involving such media are obtained for two-dimensional configurations. Explicit results are given for the reflection coefficients of stratified plasma in planar and cylindrical geometry.

The electrically short antenna as a probe for measuring free electron densities and collision frequencies in an ionized region, R. W. P. King, C. W. Harrison, Jr., and D. H. Denton, Jr., *J. Research NBS* **65D,** (*Radio Propagation*), *No. 4,* 371 (*July 1961*).
If the admittance of a missile, satellite, or drone-aircraft antenna is monitored as the vehicle traverses an ionized region, it is possible to determine the free electron density and the collision frequency of the region if theoretical relations between these quantities are available. In this paper formulas are developed that relate the admittance of an electrically short center-driven dipole or a base-driven monopole when immersed in a conducting dielectric to the effective dielectric constant and conductivity of the medium. From well-known formulas relating these quantities to the free electron density and the collision frequency of an ionized region, these latter may be determined directly from measured admittances. The results obtained when the antenna is treated as a lumped capacitor are considered. It is shown that when the conductivity of the medium is increased to a value that is still quite small, the effect of radiation on the input admittance becomes negligible. The electrically short antenna immersed in sea water is discussed briefly.

Low even configurations in the first spectrum of thorium (Th I), R. E. Trees, *Physica* **26,** *353–360 (1960).*
Positions of 21 observed levels in the $6d^2\ 7s^2$ and $6d^3\ 7s$ configurations of Th I are calculated with a mean error of ± 143 cm^{-1}, by use of 7 adjustable parameters. This mean error is reduced to ± 47 cm^{-1} by use of the $L(L+1)$ correction in a calculation with 11 adjustable parameters. The agreement between observed and calculated g-values is satisfactory. The parameters are compared with ones already published for related configurations in the spectra of Th II and Th III. With one exception, similarly defined parameters show a roughly linear variation with the degree of ionization, in accordance with simple expectation. The effect of neglecting the $6d^4$ configuration in Th I is briefly discussed to explain this exception.

High-dispersion spectra of jupiter, C. C. Kiess, C. H. Corliss, and H. K. Kiess, *Astrophys. J.* **132,** *No. 1, 221–231 (July 1960).*
In May 1957 the spectrum of Jupiter was photographed with concave gratings of high dispersion at the Slope Observatory on Mauna Loa. The spectrograms covered the region from 3,600 to 8,900 A. Tables are presented listing the wavelengths and estimated intensities of lines that make up the structures of the ammonia bands at 6,450 and 7,900 A, and of the methane bands at 6,200, 7,250, 8,420, and 8,620 A. In the infrared four lines of the (3.0) band in the quadrupole rotation-vibration spectrum of H_2 were measured. In the violet and ultra-violet regions of the planet's spectrum a continuous absorption was recorded that closely resembles the continuous absorption of the nitrogen tetroxide molecule.

A prototype rubidium vapor frequency standard, R. J. Carpenter, E. C. Beaty, P. L. Bender, S. Saito, and R. O. Stone, *IRE Trans. Instrumentation* **I-9,** *No. 2 (Sept. 1960).*
A prototype rubidium vapor frequency standard has been developed for possible use in a satellite measurement of the gravitational frequency shift predicted by the Theory of Relativity. The relative transition frequencies of several optically pumped rubidium vapor absorption cells have been shown to remain stable to one part in 10^{11} or better for a period of one month. A crystal controlled oscillator is corrected to a subharmonic of the rubidium transition frequency by a fully electronic servo system. The standard is transistorized, small in size, low in weight, and requires less than 10 watts to operate.

Application of the method of polarized orbitals to the scattering of electrons from hydrogen, A. Temkin and J. C. Lamkin, *Phys. Rev.* **121,** *No. 3, 788–794 (Feb. 1961).*
The s-, p-, and d-wave scattering of slow electrons from atomic hydrogen is calculated by the method of polarized orbitals. Utilization of a transformation of Omidvar avoids the iterative procedure of solving the associated integro-differential equations. The s-wave scattering is smaller than that given by the exchange approximation, and the scattering lengths are within the upper bounds found by Rosenberg, Spruch, and O'Malley. The d-wave phase shifts are too small to explain a resonance in the total cross section. However they are much larger than those of the exchange or Born approximation, and they give considerable structure to the differential cross section curves. The p-wave phase shifts are not much increased by the polarization effects.

Atomic energy levels in crystals, J. L. Prather, *NBS Mono. 19 (1961) 60 cents.*
Discrete energy levels observed within certain crystals are treated as due to perturbations of the energy levels of the free ion by an electrostatic field arising from the crystal lattice. The analytic procedures for determining the field from the charge configuration are given, and the resulting fields are classified according to their symmetry. After a general survey of group-theoretical ideas, the applicable groups are analyzed in detail, and characters appropriate for both integral and half-integral angular momenta of the free ion are tabulated. These are applied to the determination of the number and type of levels arising from a free ion level with $J \leq 8$. The results of this analysis are tabulated, as are the selection rules for electric dipole, magnetic dipole, and electric quadrupole transitions. Calculation of the perturbation matrix elements by the use of Wigner and Racah coefficients is discussed. Examples of the application of these several techniques to specific problems are given.

Spectroscopy of fluorine flames. I. Hydrogen-fluorine flame and the vibration-rotation emission spectrum of HF, D. E. Mann, B. A. Thrush, D. R. Lide, J. J. Ball, and N. Acquista, *J. Chem. Phys.* **34,** *No. 2, 420–431 (Feb. 1961).*

The hydrogen fluoride vibration-rotation emission spectrum from a hydrogen-fluorine diffusion flame has been studied under high dispersion from 3,200 cm^{-1} in the infrared to about 5,500 A in the visible. Measurements were made on the rotational lines in 23 bands including (1–0), (2–1), and (3–2) of the $\Delta v=1$ sequence; (2–0), (3–1), (4–2), (5–3), and (6–4) of $\Delta v=2$; (3–0), (4–1), (5–2), and (6–3) of $\Delta v=3$; (4–0), (5–1), (6–2), (7–3), (8–4), and (9–5) of $\Delta v=4$; and (5–0), (6–1), (7–2), (8–3), and (9–4) of $\Delta v=5$. Complete rotational and vibrational analyses were carried out. The constants B_v, D_v, and H_v are given for v=0 to 9. The data were extensive and precise enough to require an extended Dunham treatment from which 18 coefficients could be determined, including those for terms in $(v+1/2)^5$ and $J^4\,(J+1)^4$. Band centers for 22 bands and the vibrational term values E for V=0 to 9 are given.

Mean motions in conditionally periodic separable systems, J. P. Vinti, *J. Research NBS* **65B,** *(Math. and Math. Phys.), No. 2,* 131 *(June 1961).*

A search of the literature failed to disclose any general statement or proof of a theorem informally current among dynamical astronomers. The present paper gives a proof of the theorem, which states that, in any conditionally-periodic, separable system, the mean frequency n_k of any separation coordinate q_k is equal to $\nu_k \equiv \partial\alpha_1/\partial J_k$. Here α_1 is the energy and J_k is the k'th action variable. The proof is carried out for nonsingular Staeckel systems, so that it is applicable to any nonpolar orbit of an artificial satellite, when the potential leads to separability.

On the absorption spectrum of CF_2 and its vibrational analysis, D. E. Mann and B. A. Thrush, *J. Chem. Phys.* **33,** *No. 6, 1732–1734 (Dec. 1960).*

The flash photolysis of CF_2Br_2 has been used to obtain the absorption spectrum of the CF_2 radical. The principal features of the spectrum are a progression of the upper state bending frequency, and a number of weak bands which are shown to arise from a vibrationally excited lower state. There is no evidence for transitions involving stretching vibrations. The vibrationless origin of the system ($v_1'=0$, $v_2'=0$; $v_1''=0$, $v_2''=0$) is shown to lie at approximately 37695 cm^{-1}. The deformation frequencies of the lower and upper states are about 660 and 500 cm^{-1}, respectively.

Microwave spectrum of cis-difluoroethylene, V. W. Laurie, *J. Chem. Phys.* **34,** *No. 1, (Jan. 1961).*

The microwave spectrum of *cis*-difluoroethylene, HFC=CHF, has been investigated in the region 17–36 kMc. Observed rotational constants (Mc) for the ground vibrational state of $C_2{}^{12}H_2F_2$ are $a_0=21103.31$, $b_0=5930.35$, $c_0=4622.27$; for $C^{13}C^{12}H_2F_2$, $a_0=20752.10$, $b_0=5900.17$, $C_0=4586.92$. From these constants a structure is obtained with $r_{cc}=1.324$ A, $r_{CF}=1.337$ A, rCH=1.080 A, $<$FCC=122°9′, and $<$HCC=121°16′. Rotational constants for $V_3=1$ have also been determined. A dipole moment of 2.42 D is calculated from the Stark effect.
Comparison with previously existing data for ethylene, vinyl fluoride, and vinylidene fluoride shows that there is a shortening of both the CF and the CC bonds with increasing fluorine substitution.

Electron scattering in high magnetic field, A. H. Kahn, *Phys. Rev.* **119,** *No. 4, 1189–1192 (Aug. 1960).*

Electrical conductivity in a strong magnetic field is calculated for the case of scattering by delta-function impurities. The impurity concentration is taken as sufficiently weak that collision broadening may be neglected. The scattering by an individual center is solved exactly rather than by perturbation theory. As a result, transition probabilities for an electron at the bottom of a Landau level vanish, rather than diverge. Expressions are given for the longitudinal and transverse conductivities in the oscillatory range, and in the quantum limit range for degenerate and nondegenerate statistics. The relation of this theory to those employing collision broadening is discussed.

Dielectric constant and dielectric loss of TiO_2 (Rutile) at low frequencies, R. A. Parker and J. H. Wasilik, *Phys. Rev.* **120,** *No. 5, 1631–1637 (Dec. 1960).*

Measurements have been made of the complex capacitance ($C=C'-iC''$) of undoped, high resistance, single crystal TiO_2 (rutile) in vacuum at 78, 195, 273, and 300°K as a function of frequency between 10^1 and 3×10^6 cps with a 0.1 volt ac signal. With the field in the c-direction, one low frequency loss peak is found at 200 cps. The capacitance C' and loss C'' of a 2 mm cube with the field in the c-direction are characterized by $\frac{1}{2}\pi\tau=200$ sec^{-1}, tan $\delta_{200\ cps}=0.8$, and a dielectric constant ϵ'_{1Mc} of 170, while $\epsilon'_{20\ cps}=30{,}000$. The loss and low frequency capacitance of the crystal are directly proportional to the area of the electrodes and depend but slightly on the sample thickness, electrode materials and surface treatment. C' and C'' have been measured at 300 °K as a function of the oxygen vacancy concentration in the crystal. C' and C'' have also been measured as a function of dc bias from 0 to 400 volts; $C'_{20\ cps}$, C''_{max} and τ are proportional to V^{-n} where n is between 0.3 and 0.8. The results of the experiments can be explained by an electron-deficient barrier layer whose thickness increases with increasing applied voltage. When the dc voltage in the c-direction is changed, effects are observed whose time constants are of the order of hours or even days.

Hydrogen-bonding in calcium-deficient hydroxyapatites, A. S. Posner, J. M. Stutman, and E. R. Lippincott, *Nature* **188,** *No. 4749, 486–487 (Nov. 1960).*

A quantitative infrared absorption spectrophotometric technique was developed for the analysis of the hydrogen bond content of a series of calcium-deficient hydroxyapatites. Index of refraction and X-ray diffraction techniques and chemical analysis were used to characterize the precipitated calcium phosphates as low-calcium hydroxyapatites. Using a sapphire pressure cell in the infrared spectrophotometer, the 3,400 cm^{-1} absorption band (i.e., the hydrogen bonded O–H stretching frequency) was used for hydrogen bond analysis in conjunction with a potassium ferricyanide internal standard band at 2,105 cm^{-1}. The absorbance due to hydrogen bonding, obtained from the spectrum by a base line method, was found to be directly proportional to the hydrogen bond content predicted from the low calcium content of the hydroxyapatite samples. To balance the electrical charges due to missing calciums in certain hydroxyapatites an earlier paper suggested hydrogen bonding between oxygen atoms of adjacent orthophosphate groups. The O–O distance of 2.85 A, calculated from the H–O stretching frequency, shows that this is a reasonable assumption for the location of the proton bond.

Amplitude and angular scintillations of the radio source Cygnus-A observed at Boulder, Colorado. R. S. Lawrence, J. L. Jespersen, and R. C. Lamb, *J. Research NBS* **65D,** *(Radio Prop.), No. 4,* 333 *(Aug. 1961).*

Variations in the apparent flux and position of the radio source Cygnus-A were recorded at 53 and 108 Mc/s using a two-element, phase-sweeping interferometer located at Boulder, Colorado. An ionospheric sounder operating at Ellsworth, Nebraska, provided, for a few hours each day, simultaneous vertical-incidence measurements on the ionosphere at its intersection with the line of sight from Boulder to the radio star. Amplitude scintillations observed at Boulder over a twelve-month period are compared with ionograms taken at Ellsworth. Positive correlation is found between amplitude scintillations and spread F, while no significant correlation is found with sporadic E.
Detailed analysis of the scintillations indicates that the probability distribution of the amplitude can be represented by the Rice probability distribution function. The zenith-angle dependence of the amplitude scintillations does not agree with a theory based upon isotropic ionospheric inhomogeneities.

Microtechnique for the infrared study of solids diamonds and sapphires as cell materials, E. R. Lippincott, F. E. Welsh and C. E. Weir, *Anal. Chem.* **33,** *137–143 (Jan. 1961).*
Difficulties are sometimes encountered in obtaining the infrared spectra of solids. Accordingly, it is desirable to supplement the available techniques for solids with new procedures which would increase the number and type of solids capable of being studied. A cell which has been used to obtain the infrared spectra of a wide variety of solids in the 2–35 micron region is described. Diamonds and sapphires are used as window materials. The method is essentially a microtechnique. Representative spectra utilizing sample weights as small as 4γ (4×10^{-6}g) have been obtained. The cell can be used in a routine manner to obtain the infrared spectra of corrosive liquids and, as far as is known, of all solids. In addition, the visible and ultraviolet regions can be studied by means of this cell.

On the properties of the vapor pressure curve, E. H. Brown, *Cryogenics* **1,** *No. 1, 37–40 (Sept. 1960).*
Some general mathematical properties of the vapor pressure as a function of temperature are investigated by rigorous methods. In particular, the limiting shape of the vapor pressure curve is shown to be determined by the vanishing of the limits of the derivatives of all orders in the neighborhood of absolute zero. Some comments on the inapplicability of the Third Law of Thermodynamics to the sublimation curve are included.

Digital methods for the extraction of phase and amplitude information from a modulated signal, R. S. Lawrence, J. L. Jespersen, and R. C. Lamb, *J Research, NBS* **65D** *(Radio Prop.), No. 4,* 351 *(Aug. 1961).*
A description is given of three digital methods which have been used to recover amplitude and phase information from a modulated sinusoidal signal sampled at equal intervals of not more than one-sixth of a period. The first method, the "zero-crossing" method, is economical of computer time and for modulation which is not too deep and does not contain frequencies near the carrier frequency, accurately recovers the phase and amplitude modulation. The second method, the "filter" method, is more laborious but it gives better accuracy and will operate with deeper and more rapid modulation. The third method, a statistical approach, will work with severely overmodulated signals, but it yields only a statistical summary of the modulation. The methods were designed specifically for analysis of radio-star scintillation records but they may be applied to many other modulated signals.

A spectrophotometric atlas of the spectrum of CH from 3,000 A, to 5,000 A, A. M. Vass and H. P. Broida, *NBS Mono. 24 (1961) 20 cents.*
The near ultraviolet and visible emission spectrum of CH was recorded and presented in the form of a spectrophotometric atlas. The spectrum was recorded photoelectrically from an acetylene-oxygen flame in the region 4,900 to 3,000 Å by use of a high-resolution grating monochromator. Each of the lines in the CH spectrum is identified.

Measurement of reflections and losses of waveguide joints and connectors using microwave reflectometer techniques, R. W. Beatty, G. F. Engen, and W. J. Anson, *IRE Trans. Instrumentation* **I–9,** *No. 2, 219–226* (Sept. 1960).
The reflection and loss of a waveguide joint are quantified by its VSWR and efficiency, respectively. These are conveniently and accurately determined by techniques which employ a reflectometer with auxiliary tuners and an adjustable sliding termination. Depending upon the stability and gain of the associated apparatus, measurements of VSWR's of 1.001 and lower, and of efficiencies of 99.99 percent and higher may be obtained. The attenuations of short lengths of waveguide may be determined at the same time that the efficiency measurement is made.

Propagation of electromagnetic waves along a thin plasma sheet, J. R. Wait, *Can. J. Phys.* **38,** *1586–1594 (1960).*
It is shown that a thin ionized sheet will support a trapped surface wave. The effect of a constant and uniform magnetic field is to modify the phase velocity and polarization of the surface wave. The essential features are illustrated by numerical results for selected values of the electron density, collision frequency and gyro frequency. The effect of locating the plasma sheet near and parallel to a conducting plane is also considered. In this situation other modes of a wave-guide type are possible in addition to the surface wave.

The sensitivity of photographic film to 3-mev neutrons and to thermal neutrons, M. Ehrlich, *Health Phys.* **4,** *113–128 (1960).*
Measurements were made to determine the sensitivity to 3-Mev neutrons and to thermal neutrons of three commercial photographic films (DuPont film types 502, 510, and 606). The films were exposed in the conventional "NBS holders", consisting of Bakelite covered with thin layers of lead and tin. The results of the measurements were compared with results obtained by rough theoretical estimates. The sensitivity of the films to neutrons was found to be relatively low. On the least sensitive film, a photographic density of 0.1 was obtained with a fast-neutron exposure of 6.8×10^{10} n/cm^2. On the most sensitive film, the exposure for the same density was 4.9×10^{9} n/cm^2. The ratios of the films' fast neutron-to-gamma-ray sensitivities were found to be roughly equal to the reciprocal of the ratios of their average grain diameters. The thermal neutron sensitivity of the films was of the same order as the 3-Mev sensitivity, and was roughly the same for all three film types. In the few cases in which values for the neutron sensitivity could be obtained theoretically, they showed order-of-magnitude agreement with the experimental values.

Other NBS Publications

Journal of Research, Section 65B, No. 2, April–June 1961. 75 cents.

Optimal approximation for functions prescribed at equally spaced points. H. F. Weinberger.
Truncations in the method of intermediate problems for lower bounds to eigenvalues. N. W. Bazley and D. W. Fox. (See above abstract.)
Comparison theorems for symmetric functions of characteristic roots. M. Marcus.
Some properties of the empirical distribution function of a random process. M. M. Siddiqui.
Another extension of Heinz's inequality. M. Marcus.
Mean motions in conditionally periodic separable systems. J. P. Vinti. (See above abstract.)
Some boundary value problems involving plasma media. J. R. Wait. (See above abstract.)
A new decomposition formula in the theory of elasticity. J. H. Bramble and L. E. Payne.
Pointwise bounds in the Cauchy problem of elastic plates. L. E. Payne.

Journal of Research, Section 65D, No. 4, July–August 1961. 70 cents.

Almost fifty years of URSI. J. H. Dellinger.
Power density requirements for airglow excitation by gyro-waves. V. A. Bailey.
On the validity of some approximations to the Appleton-Hartree formula. K. Davies and G. A. M. King.
Amplitude and angular scintillations of the radio source Cygnus-A observed at Boulder, Colorado. R. S. Lawrence, J. L. Jespersen, and R. C. Lamb. (See above abstract.)
Digital methods for the extraction of phase and amplitude information from a modulated signal. R. S. Lawrence, J. L. Jespersen, and R. C. Lamb. (See above abstract.)
Comparison between mode theory and ray theory of VLF propagation. H. Volland.
Antenna coupling error in direction finders. C. W. Harrison, Jr.
The electrically short antenna as a probe for measuring free electron densities and collision frequencies in an ionized region. R. W. P. King, C. W. Harrison, Jr., and D. H. Denton, Jr. (See above abstract.)
Effect of multiple atmospheric inversions on tropospheric radio propagation. F. H. Northover.
A few observations of the perturbations in the phase of the low-frequency ground wave. J. M. Ross and J. E. Kirch.
Smooth earth diffraction calculations for horizontal polarization. L. E. Vogler.

On the theory of mixed-path ground-wave propagation on a spherical earth. J. R. Wait.

Development of high-temperature strain gages, J. W. Pitts and D. G. Moore, NBS Mono. 26 (1961) 20 cents.

Units of weight and measure (United States customary and metric) definitions and tables of equivalents, L. V. Judson, NBS Misc. Publ. 233 (1960) 40 cents.

Measurement of absorbed dose of neutrons, and of mixtures of neutrons and gamma rays, NBS Handb. H75 (1961) 35 cents.

Medical X-ray protection up to three million volts, NBS Handb. H76 (1961) 25 cents.

Precision measurement and calibration, S. F. Booth: Electricity and electronics, NBS Handb. 77, Vol. I (1961) $6.00; Heat and mechanics, NBS Handb. 77, Vol. II (1961) $6.75; Optics, metrology, and radiation, NBS Handb. 77, Vol. III (1961) $7.00.

Quarterly radio noise data, September, October, November 1960, W. Q. Crichlow, R. T. Disney and M. A. Jenkins, NBS TN18–8 (PB151377–8) (1961) $1.75.

Prolonged space-wave fadeouts in tropospheric propagation, A. F. Barsis and M. E. Johnson, NBS TN88 (PB161589) (1961) $2.00.

Physical metallurgy and mechanical properties of materials: Ductility and the strength of metallic structures, J. M. Frankland, J. Eng. Mech. Div. Proc. Am. Soc. Civil Eng. **86,** No. EM 6, 45–52 (Dec. 1960).

Cryogenic impurity adsorption from hydrogen, M. J. Hiza, Chem. Engr. Progress **55,** No. 10, 68–71 (Oct. 1960).

Nomenclature for standards of radioactivity, A. G. McNish, Intern. J. Appl. Radiation and Isotopes **8,** 145–146 (Jan. 1960).

Lithium, M. R. Meyerson, Am. Soc. for Metals Handbook 1, 1213 (1961).

Tensile cryostat for the temperature range 4° to 300° Kelvin, R. M. McClintock and K. A. Warren, ASTM Bull. **1,** No. 2, 95–98 (Feb. 1961).

The minima of cyclic sums, K. Goldberg, J. London Math. Soc. **35,** 262–264 (1960).

Normal approximation to the chi-square and non-central F probability functions, N. C. Severo and M. Zelen, Biometrika **47,** No. 3 & 4, 411–416 (1960).

Definitions relating to metals and metalworking, M. R. Meyerson and S. J. Rosenberg, Am. Soc. Metals Handb. **1,** 1–41 (1961).

Stress-rupture tests at 1350° F on type 304 stainless steel, W. D. Jenkins, W. A. Willard and W. J. Youden, ASTM Bull. **1,** No. 2, 104–108 (Feb. 1961).

Techniques in calorimetry. I. A Noble-metal thermocouple for differential use, E. D. West, Rev. Sci. Inst. **31,** No. 8, 896–897 (Aug. 1960).

Paratellurite, a new mineral from Mexico, G. Switzer and H. E. Swanson, Am. Mineralogist **45,** 1272 (Nov.–Dec. 1960).

Evaluation of micrometer and microscopical methods for measuring thickness of floor coverings, E. Horowitz, J. Mandel, R. J. Capott, and T. H. Boone, ASTM Bull. **1,** No. 2, 99–102 (Feb. 1961).

Electrodeposition of metals from nonaqueous media, A. Brenner, Chapter on Electrodeposition, Encyclopedia Chem. Tech. 2d Suppl., 315–324 (Jan. 1961).

The nature, cause, and effect of porosity of electrodeposits VI. Note on a magnetic method of detecting corrosion currents, F. Ogburn and W. H. Roberts, Plating **48,** No. 2, 168–169 (Feb. 1961).

The height of maximum luminosity in an auroral arc, F. E. Roach, J. G. Moore, E. C. Bruner, Jr., H. Cronin and S. M. Silverman, J. Geophys. Research **64,** No. 11, 3575–3580 (Nov. 1960).

Standards and testing, the key to quality, B. E. Foster, Eng. Bull., Purdue Univ. **XLIV,** No. 6, 54–62 (Nov. 1960).

A radio-frequency permittimeter, R. C. Powell and A. L. Rasmussen, IRE Trans. Instrumentation **I-9,** No. 2, 179–184 (Sept. 1960).

Subgroups of the modular group and sums of squares, M. Newman, Am. J. Math. **82,** No. 4, 761–778 (Oct. 1960).

Phase equilibria in the system cadmium oxide-niobium oxide, R. S. Roth, J. Am. Ceram. Soc. **44,** No. 1, 49–50 (Jan. 1961).

Redetermination of the chromium and nickel solvuses in the chromium-nickel system, C. J. Bechtoldt and H. C. Vacher, Trans. Metallurgical Soc., Am. Inst. Mining Engrs. **221,** 14–18 (Feb. 1961).

A modulated subcarrier technique of measuring microwave phase shifts, G. E. Schafer, IRE Trans. Instrumentation **I-9,** No. 2, 217–219 (Sept. 1960).

An analysis of the accumulated error in a hierarchy of calibrations, E. L. Crow, IRE Trans. Instrumentation **I-9,** No. 2, 105–114 (Sept. 1960).

Hydrogen sulfide precipitation of the elements from 0.2–0.5 normal hydrochloric acid, J. I. Hoffman, Chemist Analyst **50,** No. 1, 30 (Mar. 1961).

Generating functions for formal power series in non-commuting variables, K. Goldberg, Proc. Am. Math. Soc. **11,** No. 6, 988–991 (Dec. 1960).

Tests for regression coefficients when errors are correlated, M. M. Siddiqui, Ann. Math. Stat. **31,** No. 4, 929–938 (Dec. 1960).

A recommended standard resistor-noise test system, G. T. Conrad, Jr., N. Newman and A. P. Stansbury, IRE Trans. Component Parts **CP-7,** No. 3, 71–88 (Sept. 1960).

A transfer instrument for the intercomparison of microwave power meters, G. F. Engen, IRE Trans. Instrumentation **I-9,** No. 2, 202–208 (Sept. 1960).

Standards and measurements of microwave surface impedance, skin depth, conductivity and Q, H. E. Bussey, IRE Trans. Instrumentation **I-9,** No. 2, 171–175 (Sept. 1960).

Plating gun bores, V. A. Lamb and J. P. Young, Ordnance **XLV,** No. 245, 725–727 (Mar.–Apr. 1961).

Integrated starlight over the sky, F. E. Roach and L. R. Magill, Astrophys. J. **133,** No. 1, 228–242 (Jan. 1961).

Low temperature static seals using elastomers and plastics, D. H. Weitzel, R. F. Robbins, G. R. Bopp, and W. R. Bjorklund, Rev. Sci. Inst. **31,** No. 12, 1350–1351 (Dec. 1960).

Electrodeposition of metals from nonaqueous media, A. Brenner, Encyclopedia of Chemical Technology, 2d Suppl., 315–324 (Interscience Encyclopedia 1960).

FM and SSB radiotelephone tests on a VHF ionospheric scatter link during multipath conditions, J. W. Koch, W. B. Harding and R. J. Jansen, IRE Trans. Commun. Systems **CS-8,** No. 3, 183–186 (Sept. 1960).

Propagation of error in a chain of standards, A. G. McNish and J. M. Cameron, IRE Trans. Instrumentation **I-9,** No. 2, 101–104 (Sept. 1960).

Absolute measurement of temperatures of microwave noise sources, A. J. Estin, C. L. Trembath, J. S. Wells, and W. C. Daywitt, IRE Trans. Instrumentation **I-9,** No. 2, 209–213 (Sept. 1960).

Surface roughness of gold castings, J. J. Barone, R. L. Huff and G. Dickson, Dental Progr. **1,** No. 2, 78–84 (Jan. 1961).

Comparison measurements with intensity standards for high energy bremsstrahlung, J. S. Pruitt and W. Pohlit, Z. Naturforschung **15b,** No. 9, 617–619 (1960).

Stability of thermoset plastics at high temperatures, S. L. Madorsky and S. Straus, Modern Plastics **38,** 134–140 (Feb. 1961).

Immiscibility and the system lanthanum oxide boric-oxide, E. M. Levin, C. R. Robbins and J. L. Waring, J. Am. Ceram. Soc. **44,** No. 2, 87–91 (Feb. 1961).

Absorption and scattering of photons by holmiun and orbium, E. G. Fuller and E. Hayward, Proc. Intern. Conf. Nuclear Structure, 761–766 (Kingston, Canada 1960).

**Publications for which a price is indicated (except for Technical Notes) are available only from the Superintendent of Documents, U.S. Government Printing Office, Washington 25, D.C. (foreign postage, one-fourth additional). Reprints from outside journals and the NBS Journal of Research may often be obtained directly from the authors.*

UNIVERSITY OF MICHIGAN
ORD # 56-160074
PHYSICS LIBRARY, 2035 RANDALL LAB.
ANN ARBOR MICH
S.JR-A DEC D-18220 BA

UNITED STATES
GOVERNMENT PRINTING OFFICE
DIVISION OF PUBLIC DOCUMENTS
WASHINGTON 25, D.C.

OFFICIAL BUSINESS

PENALTY FOR PRIVATE USE TO AVOID
PAYMENT OF POSTAGE, $300
(GPO)

JOURNAL OF RESEARCH of the National Bureau of Standards
A. Physics and Chemistry

Vol. 65A, No. 4 July–August 1961

Contents

	Page
Electrical properties and kinetics of electrode reactions. Ralph J. Brodd.	275
Effect of hydrostatic pressure upon the relaxation of birefrigence in amorphous solids. Roy M. Waxler and Leason H. Adams	283
Vapor pressures of platinum, iridium, and rhodium. R. F. Hampson, Jr., and R. F. Walker	289
Crystallization of bulk polymers with chain folding: theory of growth of lamellar spherulites. John D. Hoffman and John I. Lauritzen, Jr.	297
Phase equilibrium relations in the binary system barium oxide-niobium pentoxide. R. S. Roth and J. L. Waring	337
Solid state reactions involving oxides of trivalent cations. S. J. Schneider, R. S. Roth, and J. L. Waring	345
Gamma irradiation of fluorocarbon polymers. Roland E. Florin and Leo A. Wall	375
Inhibition of diffusion flames of methyl bromide and trifluoromethyl bromide applied to the fuel and oxygen sides of the reaction zone. E. C. Creitz	389
Publications of the National Bureau of Standards	397

For sale by the Superintendent of Documents, U.S. Government Printing Office, Washington 25, D.C. Price 70 cents (single copy). Subscription price $4.00 a year; 75 cents additional for foreign mailing.

UNITED STATES GOVERNMENT PRINTING OFFICE, WASHINGTON : 1961